Grafted organic monolayer for single electron transport and for quantum dots solar cells

Louis Caillard

GRAFTED ORGANIC MONOLAYER FOR SINGLE ELECTRON TRANSPORT AND FOR QUANTUM DOTS SOLAR CELLS

by

Louis M. Caillard

APPROVED BY SUPERVISORY COMMITTEE:

Dr Yves J. Chabal, Chair

Dr Olivier Pluchery, Chair

Dr Eric L. Garfunkel, Referee

Dr Robert L. Opila, Referee

Dr Julia W. P. Hsu

Dr Anton V. Malko

Dr William Sacks

Dr Manuel A. Quevedo-Lopez

Dr Philippe Dollfus

A tous ceux qui m'ont soutenu et cru en moi

PREFACE

This dissertation was produced in accordance with guidelines which permit the inclusion as part of the dissertation the text of an original paper or papers submitted for publication. The dissertation must still conform to all other requirements explained in the "Guide for the Preparation of Masters Theses and Doctoral Dissertations at The University of Texas at Dallas." It must include a comprehensive abstract, a full introduction and literature review, and a final conclusion. Additional material (procedural and design data as well as descriptions of equipment) must be provided in sufficient detail to allow a clear and precise judgment to be made of the importance and originality of the research reported.

It is acceptable for this dissertation to include as chapters authentic copies of papers already published, provided these meet type size, margin, and legibility requirements. In such cases, connecting texts which provide logical bridges between different manuscripts are mandatory. Where the student is not the sole author of a manuscript, the student is required to make an explicit statement in the introductory material to that manuscript describing the student's contribution to the work and acknowledging the contribution of the other author(s). The signature of the Supervising Committee which precedes all other material in the dissertation attests to the accuracy of this statement.

GRAFTED ORGANIC MONOLAYER FOR SINGLE ELECTRON TRANSPORT AND QUANTUM DOTS SOLAR CELLS

by

LOUIS MARIE CAILLARD MS

DISSERTATION

Presented to the Faculty of

The University of Texas at Dallas and Université Pierre et Marie Curie

in Partial Fulfillment

of the Requirements

for the Degree of

DOCTOR OF PHILOSOPHY IN

MATERIAL SCIENCE AND ENGINEERING

THE UNIVERSITY OF TEXAS AT DALLAS
UNIVERSITE PIERRE ET MARIE CURIE

November 2014

ACKNOWLEDGMENTS

I would like to thank Olivier Pluchery and Yves Chabal who granted me the opportunity to work in their respective lab. In the framework of my thesis, I had the chance to work in two different countries with their whole set of experiences. Thanks to their support, the four years I spent working with them were immensely enriching whether it was scientifically, professionally or humanely. I would not have been able to go this far without their guidance. Similarly I would like to give a special thanks to those who worked along with me in Dallas in the different projects I had the chance to work on. A special thank to Oliver Seitz who was kind enough to share his wisdom and knowledge with me when I was just an inexperienced graduate student. But I also want to acknowledge the help of Philip, Will, Sara, Anton Malko, Michael, Minh, Niels, Weina, Collin, Katy, Frederick and Natis for their inestimable help in my work. And those who didn't work with me but with whom I shared so many things in the lab. Special thank to Saeedeh who has been a dear friend all this time. But also Don, Tatiana, Gautam, Jean Francois, Lindsay, Nour, karla, wilfredo, Audrey, Yingzhen, Peter, Irinder, Anna, Kui, Abraham,… Of course I need to thank those who work with me in France to help me better my work and shared with me their experience. Anne Felicie, Philippe, Emmanuelle, Suchinda, Romain, Herve, Sebastien. And also the one with whom I didn't have the chance to work but who were still here to make this thesis enjoyable. Delphine, Axel, Bernard, Piotr, Yves, Jean Noel, Iryna, Geoffroy, Laurent, Michel, Nadine, Denis,… I would also like to thank the members of my committee,

Anton Malko with whom we add a collaboration, like with Philippe Dollfus. Also Manuel Quevedo who taught me an outstanding class. Robert Opila and Eric Garfunkel, who accepted to be my referees. And of course William Sacks and Julia Hsu. I thank them for their kind acceptance to review this work and they all are great inspiration for achievement of greatness. Also I thank the special organism that funded me during my thesis. They made all this possible: NSF, Chateaubriand scholarship and Nanotwinning. Of course, nothing would be possible if not for my close family that have supported me for all these years. Mom, dad, Romain, Anaïs and Alexis, even when I was several thousands of kilometers away from them, I always had their support in moments of joy and as well as moments of doubts. I also received kind word from the rest of my huge family. The same could be said about all my friends, their support was crucial during all my student years, whether they are from France or from Dallas. In France, my friends who share the same passion with science have always inspired me to go further. Armand, Eric, Barbara, Romain, Simeon, Caroline and all others. But also those who followed different path gave me the support that I needed during all these years. Adrien, Johan, Gad, Olivia, Raphaelle, Alex, Reda.... My more recent friends in Dallas allowed me to experience this new culture. They shared with me a part of their life. Collin, Jordan, Jeremy, Udi, Brenda, Christy… Lastly, many thanks to the ones I forgot.

November 2014

GRAFTED ORGANIC MONOLAYER FOR SINGLE ELECTRON TRANSPORT AND QUANTUM DOTS SOLAR CELLS

Publication No. _____

Louis Marie Caillard, PhD
The University of Texas at Dallas, 2014
Université Pierre et Marie Curie, 2014

Supervising Professors: Dr Yves Chabal
Dr Olivier Pluchery

Functionalization of oxide-free silicon and silicon oxide surfaces is important for a number of applications. In this work, organic monolayers are grafted (GOM) on oxide-free silicon surfaces using thermal and ultraviolet-activated hydrosilylation of hydrogen-terminated silicon surfaces, primarily using Fourier transform infrared spectroscopy and X-ray photoelectron spectroscopy for characterization. The resulting amine-terminated GOM have been used for depositing nanoparticles, selecting the end group for two very specific applications: single electron devices and nano-quantum-dot (NQD) enhanced Si photovoltaic cells.

To perform single-electron transport measurements, colloidal gold nanoparticles have been deposited on amine-functionalized silicon surfaces and tunneling measurements performed with a scanning tunneling microscope in an ultra-high vacuum chamber. Using a double-barrier tunneling junction (with the GOM as the first barrier and the vacuum between the scanning tip

and the gold nanoparticle as the second one), single-electron transport was observed at 30K through a Coulomb staircase phenomenon. The critical parameters were identified to improve reproducibility. Finally, recently developed advanced modeling, based on traditional "orthodox" theory, was optimized to account for the observations (*e.g. I-V* dependence on band bending). This work provides a basis for the development of single-electron transistors that are compatible with current silicon based technology.

To enhance standard silicon-based solar cells, GOM is also needed to graft strongly absorbing II-VI NQDs and optimize their energy transfer to the silicon substrate. Recent photoluminescence spectroscopy has demonstrated that energy transfer occurs through both radiative and non-radiative mechanisms between NQDs and the substrate. With grafting technology, the aim was to optimize absorption, as probed by photoluminescence, in two ways. First, silicon nanopillars were fabricated to increase the surface area, with a careful investigation of the attachment of the NQDs to the walls of the nanopillars. Second, multilayers were deposited, using a diamine linker between layers. In the case of bilayers of NQDs with a size gradient, the PL measurements confirm directed energy transfer from the top to the second layer and then to the substrate. These two approaches are shown to increase the efficiency of energy transfer of current Si solar cells, and will require more work to implement in actual device fabrication.

TABLE OF CONTENTS

LIST OF FIGURES

LIST OF TABLES

INTRODUCTION

0.1 General introduction

Understanding of Silicon substrate properties and optimization of its application have been leading research topic these past 50 years. As the main substrate used in microelectronic industry, there has been a growing interest in a better understanding of the physics involved in past, present and future silicon based technologies. As a topic of interest in this thesis, we study some phenomena occurring at its interface, *i.e.* the geometric frontier, with other materials. In the framework of electric transport, the interface plays a crucial role for charge exchange. The fabrication of perfect interface (*i.e.* flat and defect-free) has always been a challenge in semiconductor industry. In the case of monocrystalline silicon, defects can be due to contamination, uncontrolled oxidation or defects in the crystallographic structure. A lot of devices rely on the electronic transport through an interface; this is why their performances can be hindered when there is a creation of charge traps that can capture electrons, surface dipoles that can induce a localized electric field or parasitic resistance and capacitance.

One of the reasons why silicon is a widely used material is the quality and the stability of its oxide: SiO_2, when thermally grown in a controlled atmosphere, has excellent dielectric properties and a low amount of defects compared to other mainstream semiconductors' oxides[1]. However, the attachment of a molecular layer on top of it (*i.e.* silicon oxide functionalization) often leads to surfaces that are unstable and lack in reproducibility[2,3]. The reason is the amorphous nature of SiO_2 and because of the relative instability of Si-O-R liaison. This is why oxide free silicon functionalization has been considered as an alternative path. Ever since the

discovery of hydrogenated silicon (111) obtained after hydrofluoric acid and ammonium fluoride treatment in 1989[4], silicon functionalization has known an ever growing interest from the scientific community. The evaluation of the amount of defects on a treated Si(111) surface was shown to be consistent with the amount of defects due to the miscut of the sample[5]. That is to say that the defects observed are on the steps of the silicon and a part from that, the resulting surface is atomically flat and provides an ideal starting surface for further modifications. Contrary to amorphous silicon oxide, whose surface is usually atomically rough, oxide free silicon benefits from its crystallographic nature. Its functionalization leads to an ordered molecular layer that provides control over electronic properties and the morphology of the insulating layer. Several functionalization techniques have been investigated in order to provide defects-free and stable grafted organic monolayers (GOMs) on silicon. The main approach consists in replacing the H termination of the hydrogenated silicon with another molecule. Several routes have been explored to do so, such as thermal activation[6,7,8] UV activation[9,10], electrochemical activation[11,12], and chlorination[8,13]. In the Laboratory for Surface and Nanostructure Modification (LSNM), we are able to fabricate an oxide-free passivated silicon surface prepared with thermal or UV hydrosilylation that shows outstanding chemical stability (*i.e.*, the molecule remains stable with time in air and after all additional chemical steps to graft nanoparticles[7,14,15]) and provides a protection of the underlying silicon bulk[16,17] (*i.e.* prevents contamination and oxidation). The functionality of the surface can also be tuned by changing the GOM termination to promote grafting of nanoparticles on the surface.

In this work, we take advantage of the properties of these surfaces to investigate two main areas, reflected in the two main parts of the thesis. The first one is a collaboration between Yves Chabal at the University of Texas at Dallas (UTD) and Olivier Pluchery from the Institute for NanoScience in Paris (INSP) focused on single electron transport using Coulomb blockade. The second project is a collaboration between Yves Chabal's group in Material Science with Anton Malko's group in Physics at UT Dallas focused on energy transfer mechanism from Nanoquantum dots (NQDs) to silicon for photovoltaic (PV) cells applications.

0.2 Oxide-free silicon functionalization for single electron transport

This thesis is a co-tutelle between UTD and the university Pierre et Marie Curie (UPMC). INSP is an important laboratory of UPMC, with expertise in solid state physics and physical chemistry. INSP comprises 82 researchers, 38 technical staff and 47 PhD and post-docs. This is the result of the agreement between the two universities to propose a joint program that fulfills the requirements for a doctoral degree for each doctoral school. This international collaboration started with the idea of using the knowledge on silicon surfaces available in the American laboratory in combination with the fundamental physics knowledge and the state of the art equipment for which the French laboratory is renowned for. The schedule of my thesis was set according to this project: I spent two year and a half in Dallas in Yves Chabal's lab and after that I spent one year and a half in Paris in INSP (with some travelling exchange in between).

There is no other field that has known more progress than electronic and computer science these past few decades. From the ENIAC, sixty years ago, to nowadays, the same operation can be done one million times faster, cost 100 000 times lower in term of energy and 10 000 lower in term of price and weight. Today, CMOS (complementary metal oxide semiconductor) technology is used by most semiconductor companies. This is why a lot of efforts have been done on performance optimization and in the MOSFET (metal oxide semiconductor field effect transistor) integration and miniaturization these past thirty years. However we have reached a point in term of miniaturization where difficulties not only come from fabrication processes but also from new phenomena that render the technology less viable (heating, leaking…). This is why a call for alternative technologies has been launched. Single electron transport is a phenomenon that attracts a strong interest from the research community as well as the industry community because of its promising outcome in the field of SCs. The ability to control the amount of electron being stored in a three dimension confinement (such as a nanoparticle) can be taken advantage of in multiple applications such as single electron transistor (SET), memory cells, single electron detection and so on. Minimal current consumption and further reduction of transistor size are the two major expectations from this technology. Observation of single electron transport can be achieved with the fabrication of two insulating barriers in series through which electrons are going to tunnel. To make such structure, we fabricate in Dallas passivated oxide free silicon samples and ship them in Paris to characterize them using a scanning tunneling microscope (STM). The architecture of the investigated system is shown in **figure 0.1** and is called a double barrier tunneling junction (DBTJ). It is formed by the positioning of a tip on a gold nanoparticle (AuNP) grafted on a silicon surface passivated

with a GOM. The two tunneling barriers of this structure are 1- the vacuum gap between the STM tip and the AuNP and 2- the insulating GOM. The quality and the stability of the GOM are critical parameters of this work because of the extreme sensitivity of this phenomenon: it has three main purposes:

- It passivates the silicon bulk to avoid its oxidation. Uncontrolled oxidation of silicon -or "native" oxides- generates electrical traps that negatively affect electronic device performance[18].
- It provides an active termination (an amine group -NH_2) that allows the stable and accurate grafting of AuNP on the surface.
- It is used as an insulator with a tailored and reproducible thickness between the AuNP and the silicon bulk.

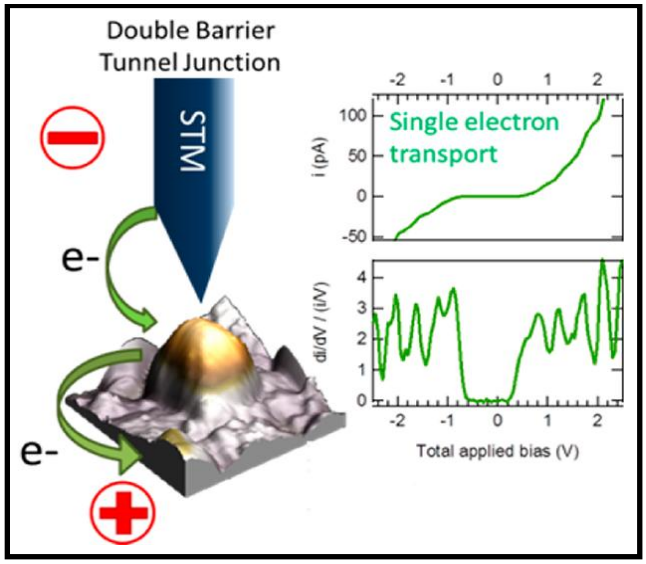

Figure 0.1: *three dimensional view of the double barrier tunneling junction used in order to observe single electron transport. The inset shows a sweep of voltage done on the AuNP and its derivative. Each peak on the derivative corresponds to an additional electron tunneling in the AuNP. From Caillard et al. Langmuir (2013).*

The topic of this project is to investigate the feasibility and the reliability of such architecture for single electron transport. **CHAPTER 1** will focus on the state of the art and the expertise available in UTD in terms of oxide free silicon and SiO_2 functionalization. This knowledge will be applied in the fabrication of the GOM. **CHAPTER 2** will give a theoretical input on the phenomena that allow single electron transport: Coulomb blockade effect. Consequences of this phenomenon and specificity of our architecture will be discussed and a short state of the art of the technology will be exposed. **CHAPTER 4** is an overview of the experimental techniques employed in this thesis. We will identify what are the advantages of the selected techniques in the framework of this project. The fabrication of our architecture will be detailed in **CHAPTER 5** (published in Langmuir).We are going to show preliminary results that are going to be used as proof of concept. **CHAPTER 6** (submitted in Nanotechnology) will focus on the parameters that affect the reproducibility of our results. To have a better idea of the viability of this technology we will show a study which results in an optimized protocol for reliable observation of single electron transport. **CHAPTER 7** will be mainly focused on the interpretation of obtained data. We are going to used simulation software and correlate simulated results with experimental data. Specificity of our structure as discussed in **CHAPTER 2** will be considered in this study.

0.3 Oxide free silicon functionalization for NQDs based solar cells

This collaboration takes advantage of the ability to chemically modify silicon surfaces developed in Yves Chabal's lab and the capability to probe NQDs energy transfer by time resolved photoluminescence in Anton Malko's group. The latter group possesses the equipment for sample characterization and an extensive knowledge of quantum photonics, and collaborates with Yuri Garstein for theoretical interpretation.

It was in the 1970s that the world realized that their energy resources (fossil fuels and fissile uranium) were not limitless. Ever since, people have taken notice of the inevitable shortage of traditional resources and looked for alternative ways to produce the energy needed for the society. Solar cells technology research has benefited from this realization and great progresses have been made. The amount of energy provided by the sun in only one second is estimated to be around 10^{17} Joules/sec.m^2 (1000 Watts m^{-2}). According to G.W. Crabtree, the sun provides us in 1.5 days the equivalent energy of the world recoverable resources in oil. In one hour it provides an energy equivalent to what all humans combined use in one year[19]. The first generation of solar cells is based on monocrystalline silicon and represents 85% of the overall market[19]. They still dominate the market because they are durable and have relatively high efficiency, in contrast to more recent technologies that have not been successful yet into entering the market despites higher efficiency. However, Si-based cells are still expensive to make because they require high quality monocrystalline Si, which represents 70% of the total manufacturing cost[20]. More recent thin film silicon solar cells are cheaper to make but they suffer from insufficient light absorption (*i.e.* poor efficiency). In this work, we are investigating the use of highly absorbing quantum dots to enhance the efficiency of Si-based solar cells.

As stated earlier, GOMs help maintain the quality and enhance the stability of oxide-free silicon surfaces. They can provide an excellent interface between the silicon bulk and another component, such as quantum dots. In PV structures, the energy transfer is a critical parameter that influences the performance of a device: a defect-free interface will optimize this energy transfer. In order to enhance the absorption of silicon, we attach NQDs on top of a functionalized surface as shown in **Figure 0.2** so that most of their energy (produced by photon absorption) can be transferred into the silicon substrate, without substantial loss in interface states thanks to the high quality of the Si/GOM interface, resulting in an enhanced overall light absorption. Once NQDs are excited by an incoming light, they can transfer their energy to the bulk either through radiative decay (radiative energy transfer, RET) or non-radiative decay (non-radiative energy transfer, NRET; or Förster resonant energy transfer, FRET). In summary, the GOM fulfills several critical requirements for this project:

- It protects the silicon surface by avoiding charge traps associated with oxidation.
- It remains stable and therefore protects the Si during all chemical steps needed for NQDs attachment on the surface.
- It provides a well-defined separation distance between the NQDs and the surface, *i.e.* afford good control over the distance between the NQDs and the substrate.

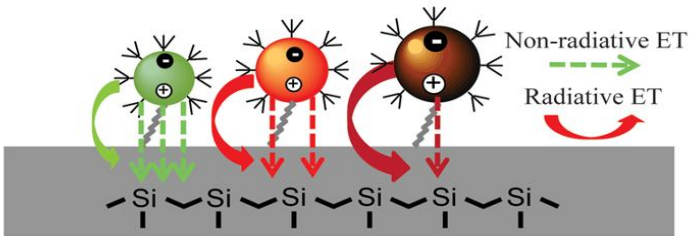

Figure 0.2: *Sketch of the hybrid device, showing schematically the different energy transfer mechanisms from NQDs to Si. From Nimmo et al. ACS Nano (2013).*

This part of the work, focused on enhancing the efficiency of NQDs-based solar cells, is based on the ability to functionalize both oxide-free silicon and SiO_2 surfaces, as presented in **CHAPTER 1**. The basic theory behind our approach is discussed in **CHAPTER 3**, which is helpful to understand the physical phenomena probed experimentally. The basic energy transfer between NQDs and silicon substrate has been observed and explained for flat surfaces in our lab as briefly summarized in this chapter[21]. The experimental characterization methods are also presented in **CHAPTER 4** with a brief discussion of relative advantages of each technique. Two approaches are considered for the optimization of quantum dots-based solar cells. The first one is silicon patterning by formation of Si nanopillars with tailorable shapes, as discussed in **CHAPTER 8** (the last part is published in Applied Physics Letters). The second is multilayer stacking by use of chemical linker, as discussed in **CHAPTER 9**. **CHAPTER 10** (published in Advanced Functional Materials) constitutes an extension of **CHAPTER 9** by describing a method for directed energy transfer from NQDs with increasing size (*i.e.* decreasing energy) all the way to the Silicon substrate using bilayers of NQDs with a size-gradient.

CHAPTER 1

SILICON FUNCTIONALIZATION

1.1 Introduction

Silicon is one of the best studied materials, not only for its bulk properties but also for its surface quality thanks to the low density of electronic surface states at the Si/oxide interface. Therefore, even though germanium has better intrinsic electrical properties (*e.g.* carrier mobility), it has not been adopted because its oxide is unstable oxide (GeO_2 is water soluble at standard temperature and pressure). The Si/oxide interface is of great interest in the framework of PV cells, sensors, transistors, and so on… Silicon oxide interfaces can also be stabilized and functionalized using chemical compounds. Another method to get a stabilized interface is to directly graft molecule on an oxide-free silicon surface. Such layers are usually obtained by wet chemistry and are sometimes called self-assembled monolayers (SAMs) or grafted organic monolayers (GOMs). Since the molecular layer is chemically grafted on our surface and not self-assembled in the strict sense, we adopt the second term in this thesis, in which different kinds of GOMs are used on both oxidized and oxide-free silicon surfaces.

1.2 Functionalization of silicon oxide surfaces

Silicon is well known for the quality and the stability of its oxide. When properly grown silicon oxide is a stable dielectric that has very few defects and so is well suited for electronics application. We first review the different types of oxide encountered in this work and describe how these can be functionalized.

1.2.1 Different types of silicon oxide

Silicon dioxide can be encountered in many forms, crystalline or amorphous. In this thesis, we encounter primarily two types of amorphous SiO_2. These differ in the way they were formed, which affects their electrical properties:

"Native" oxide

Pristine silicon surface in unstable in air: if not protected with a GOM or kept in Ultra High Vacuum (UHV), the surface oxidizes, forming a thin layer of SiO_2 on the surface. Because it is a spontaneous reaction in an uncontrolled environment, the quality of this oxide is ill-defined. This type of oxide is typically ~2nm thick and not homogeneous. It may also have defects and contamination coming from the ambient air, which means that it is not suited for most electronic devices application[18]. Prior to the deposition of another material or the growth of another oxide, one often removes this "native" oxide first.

Thermal oxide

Thermal oxide is obtained by putting a cleaned sample in a furnace with a controlled atmosphere of oxygen (O_2). This type of oxide is obtained in the UTD cleanroom and the equipment is operated by the cleanroom staff. The growth temperature is typically 900°C in a

horizontal diffusion tube (see **Figure 1.1**). The oxidation of the silicon occurs at the interface of the silicon and the SiO_2 through oxygen diffusion. High temperature is required to enhance the diffusion, as at room temperature the oxide cannot be thicker than 2nm. Thermally grown oxides, with a post-anneal in an inert gas, are of high quality with an excellent Si/SiO_2 interface (low density of interface traps), compared to SiO_2 deposited with other techniques like evaporation or sputtering. It can be used as a protective layer, as a dielectric or as a substrate.

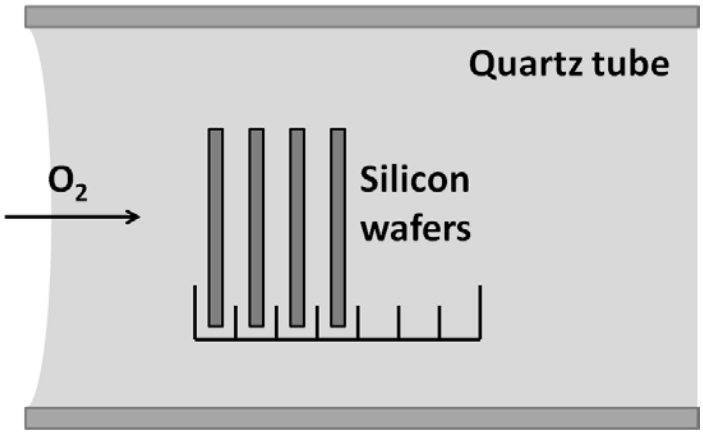

Figure 1.1: *Horizontal diffusion tube for silicon wafer oxidation*

Thermal silicon oxides are terminated with hydroxyl groups albeit with a variable density because of the amorphous nature of these oxides as shown in **Figure 1.2**[22]. It is however possible to use a piranha cleaning solution (H_2O_2/H_2SO_4; 2/3; v/v) to eliminates hydrocarbons and metal ions contamination, and increase the density of hydroxyl groups on the SiO_2 surface[14,23,24].

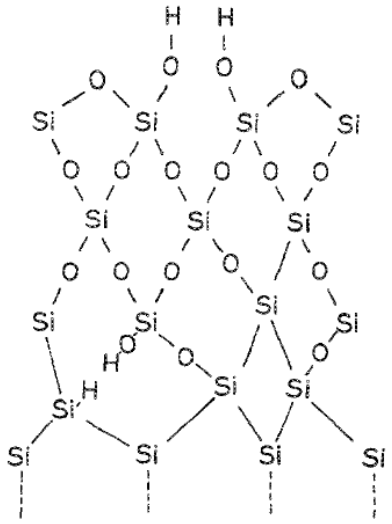

Figure 1.2: *A model of native oxide growth in ultrapure water. From Morata et al. Journal of Applied Physics (1990).*

1.2.2 Different types of molecules used

Glass or oxidized silicon are cheap flat substrates that can have excellent dielectric and optical properties For that reasons, silicon oxide functionalization is a natural topic that has been thoroughly studied for different applications like biosensors[23] or solar cells development[21]. Since the pioneering work of Sagiv *et al.* in the 1980s[25,26,27], two main types of molecules have been traditionally used. Silanization of organic chains with silane termination on SiO_2 surface is the most common[28,29] and it is the one used in this thesis. The attachment is made through the formation of a Si-O-Si bond between the silanol group and the surface. The reaction is performed in two steps: first there is the hydrolysis of the alkoxy group to form a hydroxysilane; this product is then covalently adsorbed on the surface[30]. The presence of water is needed for the first step to occur, but to avoid unwanted polymerization, it is best to perform the attachment in a

water free environment and rely only on the water previously physisorbed on the hydrophilic sample[2]. A serious problem is the reproducibility of results because of the variable –OH termination and water concentration on the surface where the reaction takes place[31,32]. This is why usually a prior cleaning with a piranha solution is performed. To functionalize SiO_2 surfaces, four silane molecules have been used in this work:

- 3-Aminopropyltriethoxysilane (APTES) a short molecule with an amine termination at the other end, used for nanoparticle attachment[7,23].
- 11-aminoundecyltriethoxysilane (AUTES). This longer chain molecule typically leads to a better ordered monolayer and it is more stable as shown in **Figure 1.3**[23].
- 11-mercaptoundecyltrimethoxysilane (MUTS). This molecule has the same chain length as AUTES but with a thiol terminal group that has a special affinity with gold and ZnS and allows effective attachment of nanoparticles[33,34].
- triethoxysilyl undecanal (C11-Ald). This is a similar molecule than AUTES, but with an aldehyde termination.

The experimental protocol is the same for all these molecules and is described in the beginning of **CHAPTER 9**.

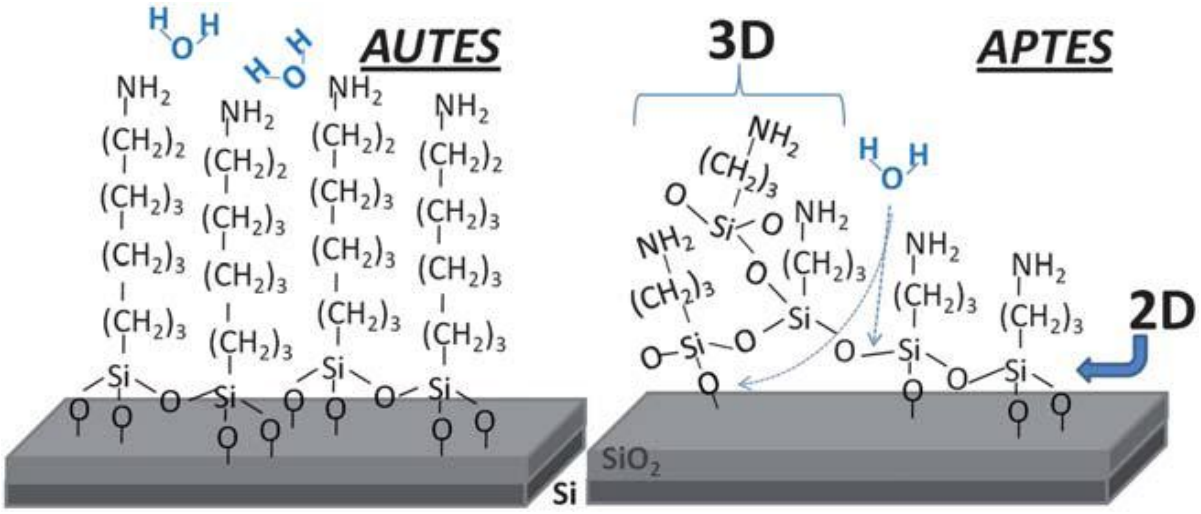

Figure 1.3: *Schematic figure highlighting the different configurations of APTES and AUTES attachment to the surface. While AUTES is mainly attached to the silicon oxide surface and can polymerize in a 2 dimensional direction, APTES molecules form a 3 dimensional attachment due to the 3-D polymerization. Such arrangement enables water molecules to reach the interface and can lead to (molecule) Si–O---Si–O (SiO_2) bond breakage i.e. APTES layer removal. Seitz et al., J. Mater. Chem., 2011.*

For completeness, phosphonate molecules need to be mentioned because, although they are not used in our work, they can be effectively grafted on silicon oxide. The grafting technique was developed by Hanson *et al.* in 2003[3] and recently optimized in Yves Chabal's group by Vega *et al.* in 2012[35]. They can be grafted on a SiO_2 surface with a method called: "tethering by aggregation and growth" or T-BAG. Initially the molecules are physisorbed, forming an ordered array because of the interaction between phosphonate headgroups. A bond is then formed with the substrate after a long annealing (~2 days, 140°C). However, the GOM layer is not very stable because the Si-O-P bond is relatively weak and can be easily hydrolyzed especially in basic and neutral solutions.

1.3 Oxide-free silicon surface functionalization

Oxide-free silicon surface functionalization technology was developed in light of the previously mentioned issues regarding oxidized silicon. Most of the chemical routes involve the covalent attachment of molecules to hydrogen terminated Si surfaces. Comprehensive reviews have been done on this topic by Thissen *et al.* in 2012[15] and De Benedetti *et al.* in 2013[36]. The following provides only a brief overview.

1.3.1 Oxide-free silicon surfaces

Hydrogen terminated silicon surfaces

Oxide-free Si functionalization takes advantage of the relatively easy chemical process (*i.e.* HF etching) that removes surface oxide and leads to hydrogen termination. Specifically, a aqueous solution of hydrofluoric acid (1-40%) efficiently removes the oxide. For a long time it was thought that the resulting surface was F-terminated[37] because F was detected with x-ray photoelectron spectroscopy (XPS), but it has been shown using infrared spectroscopy in 1990 that it is H-terminated instead[5]. The etching mechanism is shown in **Figure 1.4**[38]. Even if the strength of the Si-F (~5eV) bond is higher than the one of the Si-H bond (~3.5eV), the Si-F bond is highly polarized, weakening the underlying Si-Si bond (because of the eletronegativity of the neighboring bonded fluorine atom) and leading to the removal of the surface Si atom in the form of SiF_X (mainly SiF_4 or H_2SiF_6) molecules. The resulting surface is then H-terminated and is stable because the underlying Si-Si is less polarized. **Figure 1.5**[39] shows that the removal of the

Si-F is only possible if the surface is rough (**Figure 1.5a**). If the surface is smooth, the Si-Si bond under the Si-F is protected because of the steric hindrance of neighboring atoms (**Figure 1.5b**).

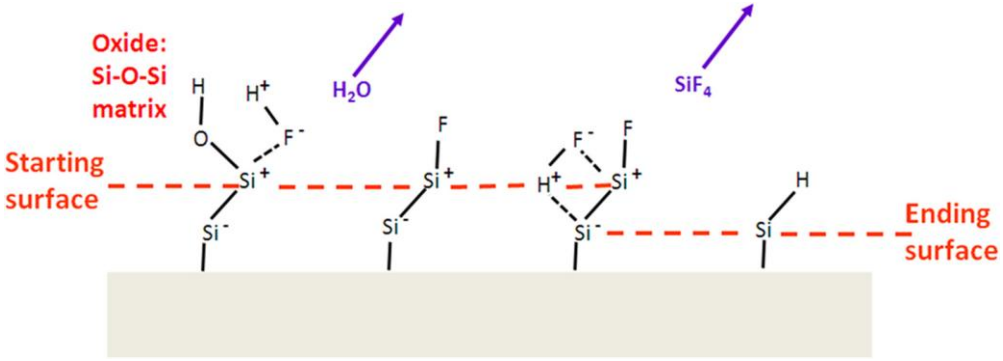

Figure 1.4: *Mechanism leading to the formation of H-terminated Si surface by HF etching: The last step of oxygen removal from SiO_2 involves HF attack of the Si-O bond, with removal of OH as H_2O and termination of the surface Si atom with fluorine. Further attack of the polarized $Si^{\delta-}$-$Si^{\delta+}$ leads to H-termination. From Ubara et al. Solid State Communications (1984).*

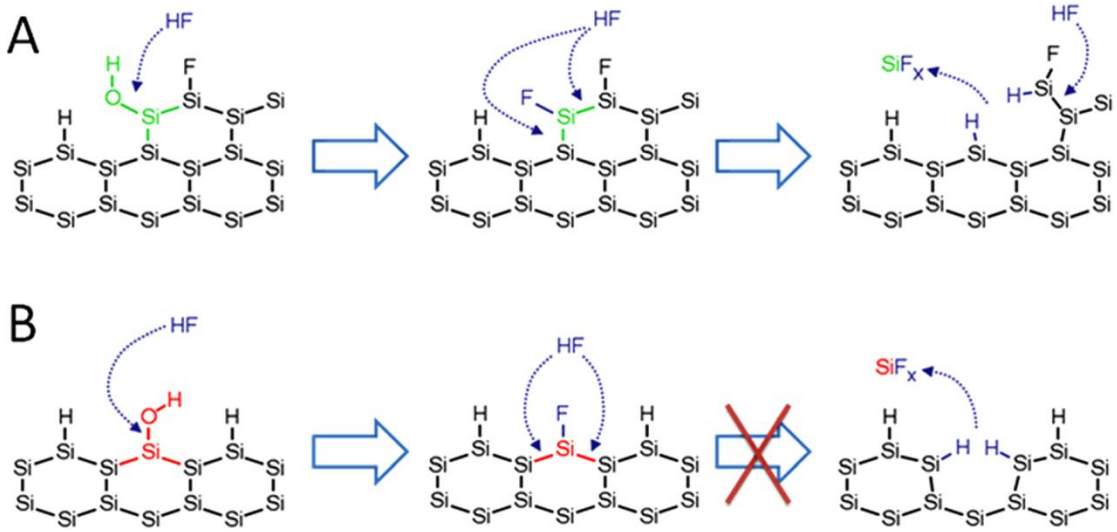

Figure 1.5: *Mechanism of HF attack on (a) an atomically rough, partially F-terminated surface, and (b) an atomically flat, partially F-terminated surface. From Michalak et al. Nat Mater (2010).*

Atomically smooth Si(111)surfaces

Using an HF solution removes the oxide and H-terminates the silicon surface, but the resulting oxide-free surface is atomically rough because the initial interface between the silicon and the native SiO_2 is rough. An atomically rough surface is characterized by several hydrides: monohydride, dihydride and –rarely- trihydride[5,4,40,41]. With a basic solution of HF, however, it has been shown that an atomically flat Si(111) surface can be obtained by removing most of the defect on the (111) face because of preferential etching (through slow reoxidation/removal of defect Si atoms), leading to ideal monohydride termination[5]. Practically, 40% NH_4F solution with a pH equal to 8 is optimum. Fourier Transform Infrared Spectroscopy (FTIR) is used characterize the treated sample, exhibiting a single stretch mode at 2083.7cm^{-1} with a very narrow Full width at half maximum (FWHM <1cm^{-1}), characteristic of a high quality monohydride surface termination[42]. FTIR results are displayed in **Figure 1.6**[43].

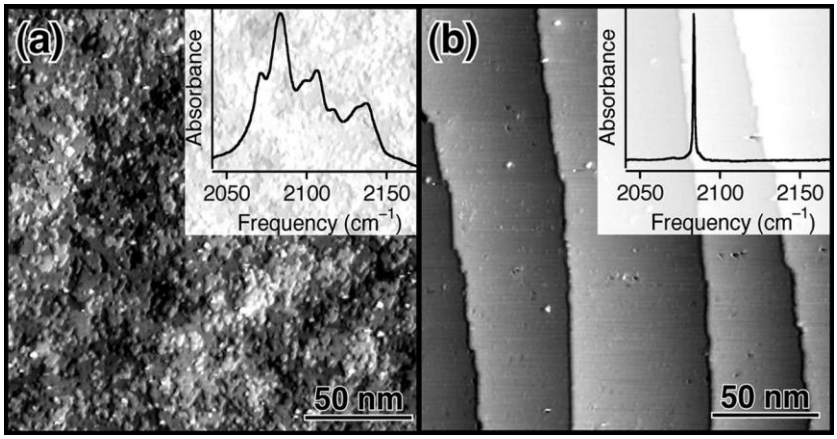

Figure 1.6: *FTIR Spectra and STM images of surfaces obtained by (a) low pH etching (HF, pH<3) leading to rough inhomogeneous surfaces with mono- and dihydride terminated silicon species, and (b) high pH etching (NH_4F/HF buffer system, pH>8) leading to ideally H-terminated homogenous and atomically flat silicon surface. From M. A. Hines, Annu. Rev. Phys. Chem. (2003).*

One of the main advantages of this process is that an ideal Si(111) hydrogen-terminated surface is a remarkably stable surface. It can remain stable indefinitely when kept in controlled atmosphere at room temperature. Controlled atmosphere means ultra-pure gases, including water vapor and oxygen (*e.g.* water or oxygen can only induce oxidation at high temperature, >300K[44]). Initial stages of oxidation are usually caused by free radicals and Ozone (O_3) found in air (the concentration can vary from one place to another). Some initial surface degradation can occur right after exposition to air that can only detected by charge recombination techniques[45]. However, initial detectable oxidation (with FTIR or XPS, see **CHAPTER 4**) of an ideal surface only starts to appear after a few hours depending on the air composition.

1.3.2 Functionalization methods

Because of their remarkable stability, the atomically flat oxide-free silicon surfaces cannot easily be chemically modified. There have been several techniques that have been developed for that purpose, as describe in the section.

Hydrosilylation

Linford *et al.* proposed in 1993 a novel method that enabled the hydrosilylation of a hydrogen terminated silicon surface. The product of such reaction was the covalent attachment of an alkyl group on a Si(111) surface though a Si-C bond[6,46]. This achievement offered surface scientists a way to protect a silicon surface with a stable molecular layer with a density close to

that of crystalline hydrocarbons (~90%)[6]. This reaction can be done using a wide variety of activation: thermally[17,24], catalytically[47,48], photochemically[8,49] or radically[46]. The reaction is as follow:

$$-Si-H+CH_2=CH-R \rightarrow Si-CH_2-CH_2-R \qquad Eq\ 1.1$$

The radical R can be a long carbon chain terminated with an active group on top, as long as it does not affect the hydrosilylation itself[16,17]. Several processes, like the one involved in this thesis rely on the attachment of a protected group (like a protected carboxylic acid: an ester) which is then "deprotected" after the grafting on the surface[7,16]. Two techniques have been used in this thesis: thermal hydrosilylation and UV-activated hydrosilylation. The first one, which relies on elevated temperatures to start the hydrosilylation reaction, has been extensively used and reported in the literature mainly because of its relative ease of use. Contrary to lots of other techniques it does not require catalytic compounds that can oxidize and contaminate the surface. The experimental protocol is presented in **CHAPTER 5.** UV activated hydrosilylation is only slightly more complicated, involving the formation of a radical because the energy of the incoming light (~200-300nm so ~4-6eV) is higher than the energy of the Si-H bound (~3.5eV). The silyl radical created can then react with the alkene of the molecule inducing the formation of a Si-C bond. This technique has the advantage over the thermal one that it allows the attachment of smaller molecules that would evaporate during thermal hydrosililation. On the other hand, smaller molecules are prone to polymerization, so dilution, or introduction of inhibitors compounds is sometime needed. Chidsey et al. first reported the use of UV-initiated hydrosilylation to graft 1-pentene on a oxide free Si(111) surface in 1993[46]. Possible mechanisms are shown in **Figure 1.7** and the experimental protocol is shown in **CHAPTER 6**.

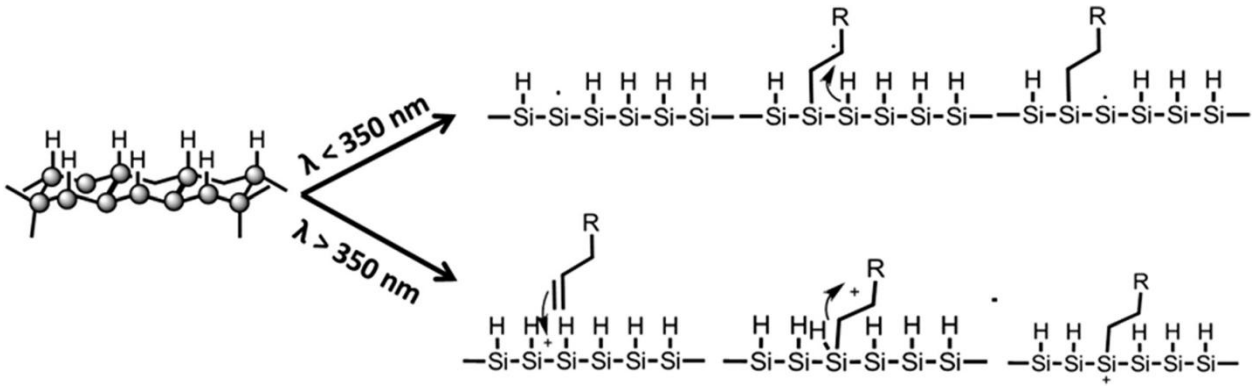

Figure 1.7: *Proposed mechanisms for thermal and radical initiated hydrosilylation. From W. J. I. De Benedetti et al. Journal of Vacuum Science & Technology A (2013).*

Quantities that are often associated with the overall quality of the resulting GOM, such as coverage, density or level of substrate oxidation, need to be monitored using several techniques such as contact measurement[50], FTIR[17,24], X-ray photoelectron spectroscopy (XPS)[7,16] or ellipsometry[50] in order to investigate the impact of each parameter. The difficulty in this task is that several physical factors can have an effect on the initial GOM quality such as doping level, miscut of the sample or preparation condition[15,36]. Unfortunately, this initial quality controls the ability to deposit an additional layer on top a GOM without damaging, which is really important for semiconductor industry. Encouraging results come from recent work that has shown that atomically flat, H-terminated Si(111) surfaces, passivated with a GOM, can withstand the deposition of several nm of Al_2O_3 deposited with atomic layer deposition. Furthermore, such a hybrid heterostructure is characterized by a very low surface defect density ($D \sim 10^{11}/cm^2$)[51], which is actually comparable with the interface between Si(111) and a thermally grown SiO_2.

Halogenation for Grignard functionalization.

Complementing thermal and photo-initiated hydrosilylation, the use of Grignard reagents is also attractive, particularly to graft small hydrocarbons to silicon. The technique was first implemented for surfaces by Nate Lewis *et al.* at Caltech in 1996[52]. The process is based on the reaction between halogenated silicon and organo-magnesium compounds of the form R-MgX - with X being a halogen (usually Cl or Br) - which leads to the formation of a Si-R bond leaving MgX_2 as a side product as shown in **Figure 1.8**. The initial halogenation step, *e.g.* chlorination using PCl_5, can replace 99% Si-H with the corresponding Si-X termination, with only a relatively low concentration of chemical defects arising from minority reaction with the solvent[53]. IR absorption measurements after the two-step process confirms that nearly 95% of the surface is covered by Si-R, as determined in the case of R=methyl radical[54]. With bigger molecules, the coverage is similar as the one encountered with hydrosilylation (~50%)[54].

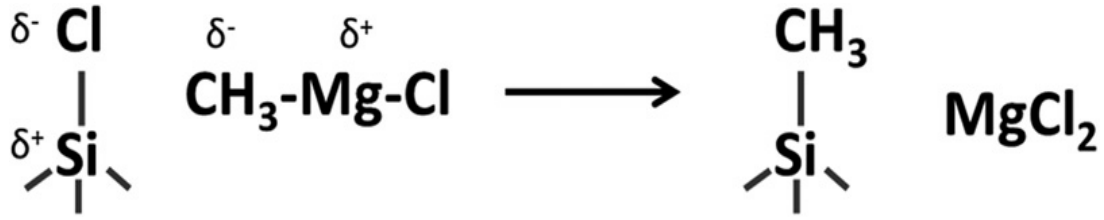

Figure 1.8: *Schematic representation of Grignard functionalization on halogen-terminated Si(111) surfaces. From W. J. I. De Benedetti et al. Journal of Vacuum Science & Technology A (2013).*

Nanopatterning with methanol

Oxide-free H-terminated Si(111) surfaces can also be modified with alcohols, leading to the formation of alkoxy termination. Usually oxidation occurs with the process[55], but is has been shown by Michalak *et al.* in 2010 that immersion of monohydride-terminated Si(111) surfaces in an anhydrous solution of methanol at 65°C yields a well-ordered methoxy nanopattern, with no detectable oxidation on the resulting surface[39]. The reaction is highly dependent on the temperature of the solution: coverage of 1/3 of the surface is obtained at 65°C and 2/3 at 120°C. The reaction mechanism is still under study[15] buts presumed to be as shown in **Figure 1.9**, with methoxy attachment and molecular hydrogen release. The reaction is highly dependent on the chemical potential of the methanol and local hydrogen concentration, potentially allowing the back reaction, hence the establishment of a dynamic equilibrium.

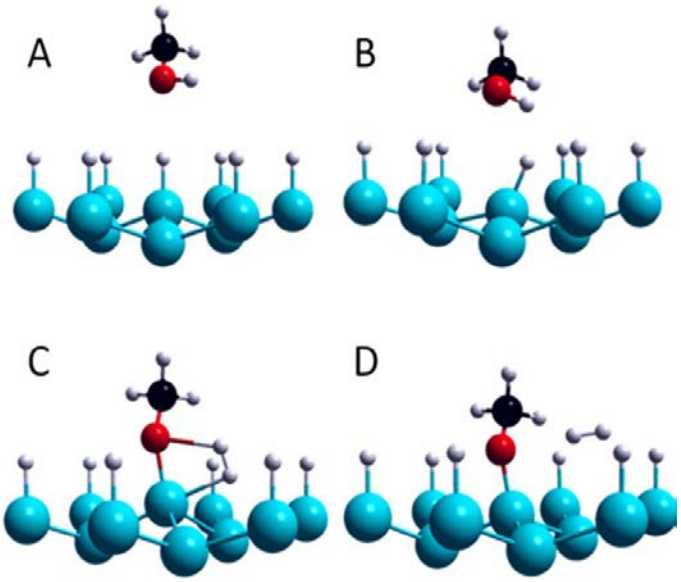

***Figure 1.9**: Representation of the reaction mechanism leading to methoxy grafting of H-terminated Si(111) surfaces. From P. Thissen et al. Prog. Surf. Sci. (2012).*

The methoxy surface can be further processed by replacing the $–OCH_3$ group with fluorine in a 49% HF solution. The Si-F bond can then be transformed into Si-OH by placing the sample in ultrapure water as depicted in **Figure 1.10**. The resulting nanopatterned Si-OH surface is ideal to explore surface chemistry.

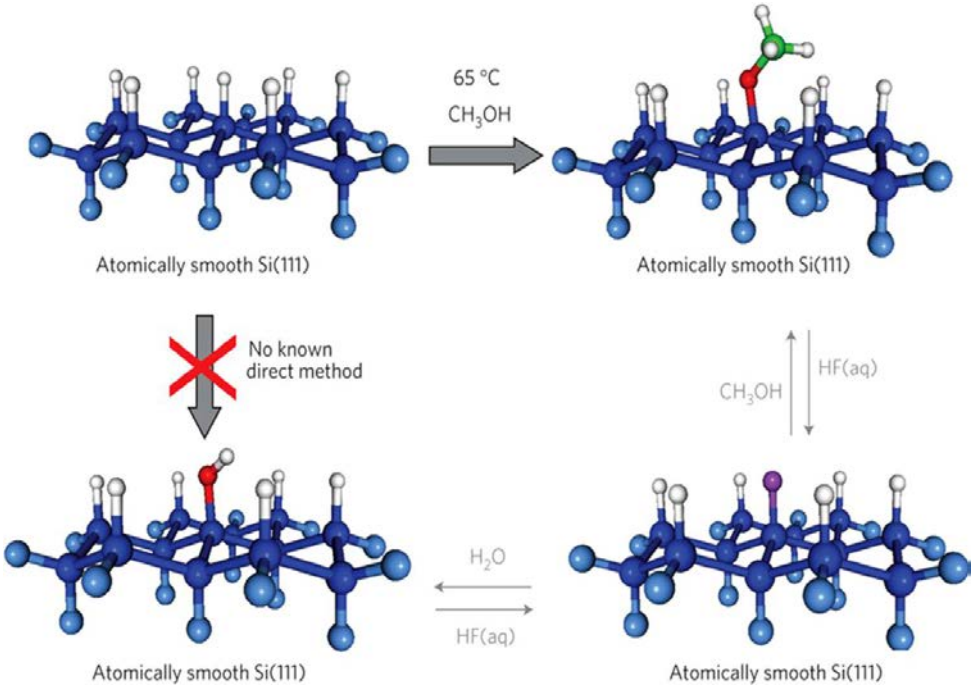

Figure 1.10: *Selective chemistry on nanopatterned, methoxy-terminated Si(111) surfaces, leading to OH-terminated, oxide-free Si(111) surfaces. From Michalak et al., Nat. Mater. (2010).*

1.4 Conclusion

All these examples show the potential of oxide-free silicon functionalization, which permits the preparation of well-controlled, defect-free and reproducible surfaces that can be used to explore new surface chemistry. UV and thermal hydrosilylation are proven and reliable

techniques that have been selected in this work. Two molecules have been considered: the long chain ethyl undecylenate (SiC_{11}) and the short chain ethyl 6-heptenoate (SiC_7). These two esters, once attached, can be deprotected into a carboxylic acid that can then be used for the attachment of a di-amine[7,16]. This last step provides an amine termination to the GOM, which is ideal for nanoparticle attachment[7,16]. Experimental processes are described in detail in **CHAPTER 5.**

CHAPTER 2

GRAFTED ORGANIC MONOLAYER ON OXIDE-FREE SILICON FOR SINGLE ELECTRON TRANSPORT

2.1 Introduction

In 1965, the president of Intel, Gordon Moore made a simple observation that, since then, has been known under the name of Moore's law: the number of transistors on a chip doubles approximately every 18 months. This law has been accurately describing the progress made in the SC industry these past few decades effectively bringing an exponential growth of computers performances in shorts periods of time. This law has also been used in research and development in order to foresee and plan future technology in a wide variety of technological fields (camera, sensors, memory and so on). This observation is an interesting tool that can describe technological progresses made in this field at the end of the 20th century and the beginning of the 21st. But one may wonder whether such trend can be sustained for much longer. Two main issues are being considered:

- The smaller a transistor is, the more expensive it becomes to build it. Will there be a market for the latest transistor technology knowing that a corollary of the Moore's law states that equipment used in SC industry quadruple in price every four years (Rock's law).
- Decreasing transistors in size eventually leads to new technological challenges. Some effects are being enhanced at extremely small scale (heat generation, charge leaking…), making them not compatible with today's technology.

In the framework of these challenges, new technologies have been considered in order to eventually replace existing ones. One of these technologies is the single-electron electronic. Under this self-explanatory name is an electrical phenomenon that occurs in the nanometer scale which, under certain circumstances, allows us to have a degree of control over the number of

electrons stored in a nanoparticle: Coulomb blockade. This phenomenon is the cornerstone that leads to the apparition of a new type of transistor: single electron transistor (SET) which standard schematic is based on Field Effect Transistor and shown in **Figure 2.1**. The current between the source and the drain can be set by the amount of supplemental free electrons stored in the nanoparticle. This number can be set from zero to one depending on the voltage bias applied on the gate as shown by the I_{DS}-V_G curve. When varying the voltage between the source and the drain, we obtain a current flowing through the device that is made of events where a discrete number of electrons cross the nanoparticle simultaneously (from 1 to an integer n). It will be discussed in the following section. Expected advantages of such technology are a decrease in the current consumption with the use of minimal number of charge carrier, and the decrease of transistor size (minimal heat being generated). Moreover it opens new paradigms for designing a new kind of electronics intrinsically based on logic electronics and no longer on analogic signals. This might prove a decisive advantage to implement directly logic electronics in the basic device of a microprocessor[56,57]. An example of single charge memory was demonstrated in 2009[58] where the authors embedded gold nanoparticles inside a thin layer of HfO_2. For example an exact model for a single-electron transistor was developed within the circuit simulation package SPICE and made possible to study how to integrate this new device in more complex circuitry[59].

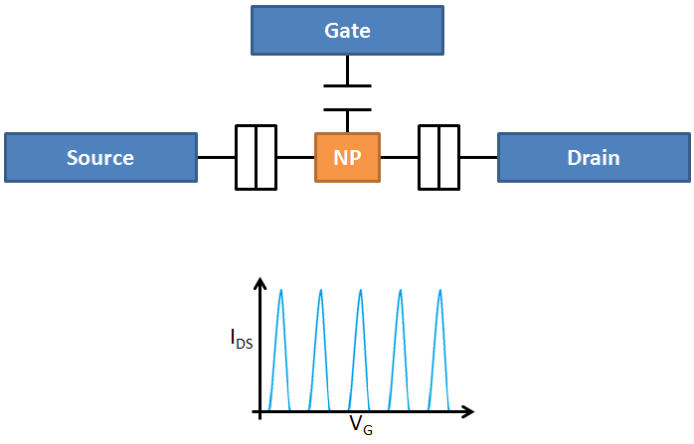

Figure 2.1: *Schematic of a single electron transistor with its Id-Vg characteristic curve.*

As we will see later in this chapter, in order to observe single electron phenomena at room temperature, dimension of the device must be in the order of a few nanometers. In theory capacitance of the storage nanoparticle must not be higher than 3aF, which roughly corresponds to nanoparticle smaller than 53nm (practically speaking, nanoparticle size should be 10 times smaller). This means that only a handful of type of fabrication techniques can be considered for such small dimensions, where the control of the morphology has to be achieved at a nanometer scale:

- new generation lithography, such as extreme UV[60], X-ray[61], E-beam[62], ion beam[63] or nanoimprint[64].
- direct etching techniques with STM[65] or AFM.
- self assembly techniques[16].

In order to effectively develop this technology in large scale, a lot of challenges have to be overcome. Prediction and control of the behavior of manufactured devices require a deep understanding of the physics governing the flow of electrons. Also, Fabrication techniques have

to be optimized in order to provide a cheap and reliable way to build reproducible and stable devices. Indeed, today it is still difficult and costly to build sub-100nm structure. In order to tackle some of these challenges, organic materials have been considered as promising alternatives to standard inorganic structures. As shown in **CHAPTER 1**, oxide free silicon functionalization can provide a controlled and defect free interface between the silicon bulk and the organic layer. This is possible thanks to the chemical process that controls the fabrication of atomically flat silicon (111). We will demonstrate that the interface obtained using hydrosilylation can be used for cutting-edge nanoelectronics such as Coulomb blockade. We take advantage of the possibility to use a GOM to passivate and protect the silicon surface and to attach a gold nanoparticle with the help of an anchoring group (NH_2). The GOM is also used for its dielectric properties to create a tunneling junction: this is why we need to assess some of its electrical properties in order to effectively propose a simulation model that can be used to describe and predict the behavior of our system. In order to build our structure, only self assembled techniques are being used: we wish to investigate the feasibility for cheap chemical process to compete with costly sub-100nm technology.

2.2 Coulomb blockade and Coulomb staircase for single electron transistor

2.2.1 Orthodox theory

Before going any further, we must go over the phenomenon on which is based the single electron transport: Coulomb blockade. In usual current flux occurring in metallic wires, the

discrete nature of electrons is masked. But in some structure, such as tunneling junctions, it can be unraveled. The tunneling junction is an insulating barrier between two conducting contacts that charges can cross thanks to the tunnel effect. From an electric standpoint, and in static, a tunneling junction can be electrically modeled as a capacitance C and a resistance R in parallel as seen in **Figure 2.2**.

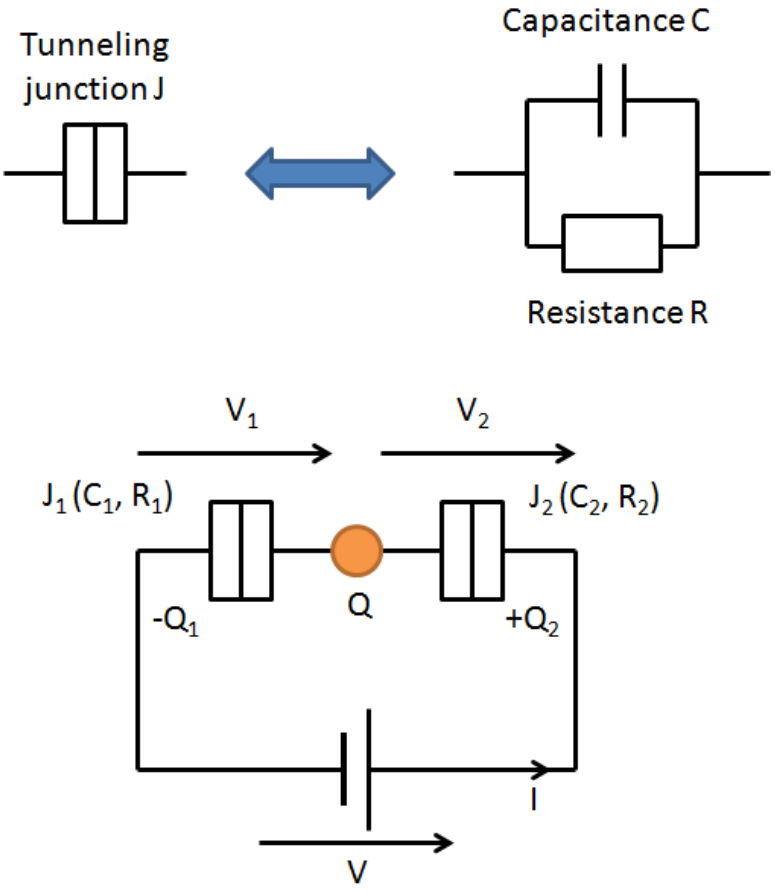

Figure 2.2: *Equivalent electronic circuit of a tunneling junction with the schematic of a double barrier tunneling junction.*

When two of these tunneling junctions are placed in series we create the architecture of a physical island in which electrons can be stored. Usually, the island is a metallic nanoparticle

where electrons can be confined, but can also be small capacitances that are sometime the results of unwanted contamination or defects[66]. The equivalent electronic schematic of the system is shown in **Figure 2.2**. If voltage is applied on such structure, it is possible to lower the barrier and introduce a new electron in the island. The energy needed to add an extra electron in the island is directly related to the capacitances of the two tunneling junctions: The crossing of an electron through J_1 or J_2 is only possible if the energy provided by the source is higher than the electrostatic energy. The work of the voltage source W must be compared with the electrostatic energy in the capacitances E_p.

From the circuit we have the following equations:

$$\begin{cases} Q = Q_1 - Q_2 \\ Q = -ne \\ Q_1 = C_1 V_1 \\ Q_2 = C_2 V_2 \\ V = V_1 + V_2 \end{cases} \rightarrow \begin{cases} V_1 = (C_2 V - ne)/C_{eq} \\ V_2 = (C_1 V + ne)/C_{eq} \end{cases} \qquad \textit{Eq 2.1}$$

With $C_{eq} = C_1 + C_2$

We can then deduce the electrostatic potential in the capacitances

$$E_p = \frac{{Q_1}^2}{2C_1} + \frac{{Q_2}^2}{2C_2} = \frac{C_1 {V_1}^2}{2} + \frac{C_2 {V_2}^2}{2}$$

$$E_p = \frac{1}{2C_{eq}} [C_2 C_1 V^2 + (ne)^2] \qquad \textit{Eq 2.2}$$

Let's consider now the work:

$W = \int V(t) I(t) dt = V \Delta Q$ with $\mathrm{V(t)} = \mathrm{V} = \mathrm{Constant}$

Looking at **Figure 2.3**, we now have two cases:

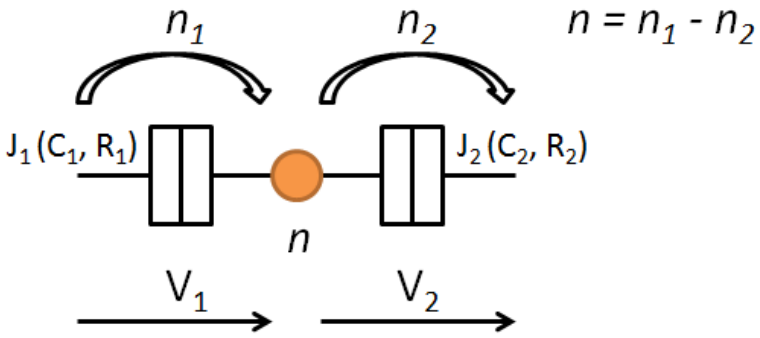

Figure 2.3: *Junctions J_1 and J_2 forming a DBTJ. n is the total number of electrons in the island. n_1 is the number of electron stored in the positive plate of the first capacitor and similarly for n_2.*

Case 1: When one electron goes out of the nanoparticle through J_2 (*i.e.* $n_2 \to n_2 + 1 \Longrightarrow n \to n - 1$):

In that case J_1 is equivalent to a capacitor and J_2 is equivalent to a resistor which gives us a change in voltage $V_1 \to V_1 + e/C_{eq}$ so

$$\Delta V_1 = \frac{e}{C_{eq}} \Longrightarrow e\frac{C_1}{C_{eq}} \qquad \textit{Eq 2.3}$$

The voltage source compensates by applying ΔQ_1: it applies the necessary charge on J_1's left plate corresponding to a positive current *I*. So, for n_2 electrons, we have the work given by the voltage source:

$$W_1 = e\frac{C_1}{C_{eq}} n_2 V \qquad \textit{Eq 2.4}$$

Case 2: When one electron goes in the nanoparticle through J_1 (*i.e.* $n_1 \to n_1 + 1 \Longrightarrow n \to n - 1$):

In that case J_1 is equivalent to a resistor and J_2 is equivalent to a capacitor. Using the same approach we get for n_1 introduced electrons:

$$W_2 = -e\frac{C_2}{C_{eq}} n_1 V \qquad \textit{Eq 2.5}$$

Combining **Eq 2.4** and **Eq 2.5**, we end up having in the end:

$$E_p = \frac{1}{2C_{eq}}[C_1C_2V^2 + (ne)^2] \quad ; \quad W = e\frac{V}{C_{eq}}(n_1C_2 + n_2C_1) \qquad \textit{Eq 2.6}$$

A transition is then possible if $E_p < W$ *i.e.* $\Delta E = E_p - W < 0$

This gives us:

$$\textit{1st junction} \begin{cases} n_2 \to n_2 + 1 \implies n \to n - 1 \implies \Delta E_{n_2+1} = \frac{e}{2C_{eq}}[-(2n-1)e - 2VC_1] \\ n_2 \to n_2 - 1 \implies n \to n + 1 \implies \Delta E_{n_2-1} = \frac{e}{2C_{eq}}[+(2n+1)e + 2VC_1] \end{cases} \qquad \textit{Eq 2.7}$$

$$\textit{2nd junction} \begin{cases} n_1 \to n_1 + 1 \implies n \to n + 1 \implies \Delta E_{n_1+1} = \frac{e}{2C_{eq}}[+(2n+1)e - 2VC_1] \\ n_1 \to n_1 - 1 \implies n \to n - 1 \implies \Delta E_{n_1-1} = \frac{e}{2C_{eq}}[-(2n-1)e + 2VC_1] \end{cases} \qquad \textit{Eq 2.8}$$

Effectively giving us as threshold voltages:

$$\begin{cases} \Delta E_{n_2+1} < 0 \Longrightarrow V > -(2n-1)e/2C_1 \\ \Delta E_{n_2-1} < 0 \Longrightarrow V < -(2n+1)e/2C_1 \\ \Delta E_{n_1+1} < 0 \Longrightarrow V > +(2n+1)e/2C_2 \\ \Delta E_{n_1-1} < 0 \Longrightarrow V < +(2n-1)e/2C_2 \end{cases} \qquad \textit{Eq 2.9}$$

So, if we consider that $C_1 = C_2 = C$ and that there is initially no free electron in the gold nanoparticle (*n=0*), we have no energy transfer unless:

$$|V| < V_{th} = \frac{e}{2C}$$

This correspond to the energy

$$\Delta E_c = \frac{e^2}{C_{eq}} \qquad \textit{Eq 2.10}$$

This is the energy needed for an electron to enter or leave the island. Now we can use **Eq 2.10** to determine which are the conditions of observation. For the phenomena to occur at room

temperature, the energy from the medium must be lower that the needed electrostatic energy. To avoid any spontaneous transfer of electron we need:

$$\frac{e^2}{2C} \gg k_B T \implies \frac{e^2}{2C} > 10 k_B T \qquad \textit{Eq 2.11}$$

With $k_B T$= 0.0256eV this leads to a capacitance of the order of 10^{-18} F (aF).

Let's now consider the link between capacitance and the dimensions of the nanoparticle. We can either use the equation for the self capacitance of the nanoparticle (**Eq 2.12**) or the capacitance between the nanoparticle and the bulk (here we consider they are both plane surfaces, **Eq 2.13**) to give an order of magnitude:

$$C = 2\pi\varepsilon d \qquad \textit{Eq 2.12}$$

where ε is the permittivity of the medium around the nanoparticle. Taking ε= $8.854.10^{-12}$ F.m^{-1} (permittivity of the vacuum) the diameter is then: d~10^{-8}m.

$$C = \varepsilon \frac{d^2}{h} \Longrightarrow d = \sqrt{\frac{Ch}{\varepsilon}} \qquad \textit{Eq 2.13}$$

where ε is the permittivity of the medium between the susbtrate and the nanoparticle and h, the distance between the nanoparticle and the substrate. For h~2nm, which is the typical thickness of a GOM, we obtain the same order of magnitude: d~10^{-8}m. We can conclude that the nanoparticle must have a diameter in the order of magnitude of several nanometers for room temperature observation. But practically speaking it is easier to observe single electron transport at very low temperature. Experiments show that even at low temperature, small nanoparticles with a diameter between 5-10 nm are usually considered for better results[67].

Another condition must be fulfilled: for the charge to be well defined, it must remain on the island long enough. That is to say the controlled charge that goes through the junction must be higher than the charge leakage. By looking back at the RC schematic in **Figure 2.2** we can determine that the charging time depends on the time constant of the junction. Combining the Heisenberg uncertainty principle $\Delta t \Delta E > h$ and the **Eq 2.10**, we can obtain

$$R > \frac{h}{e^2} \qquad \textit{Eq 2.14}$$

This gives us a condition on the value of the tunnel resistances of the barriers: $R > 25k\Omega$.

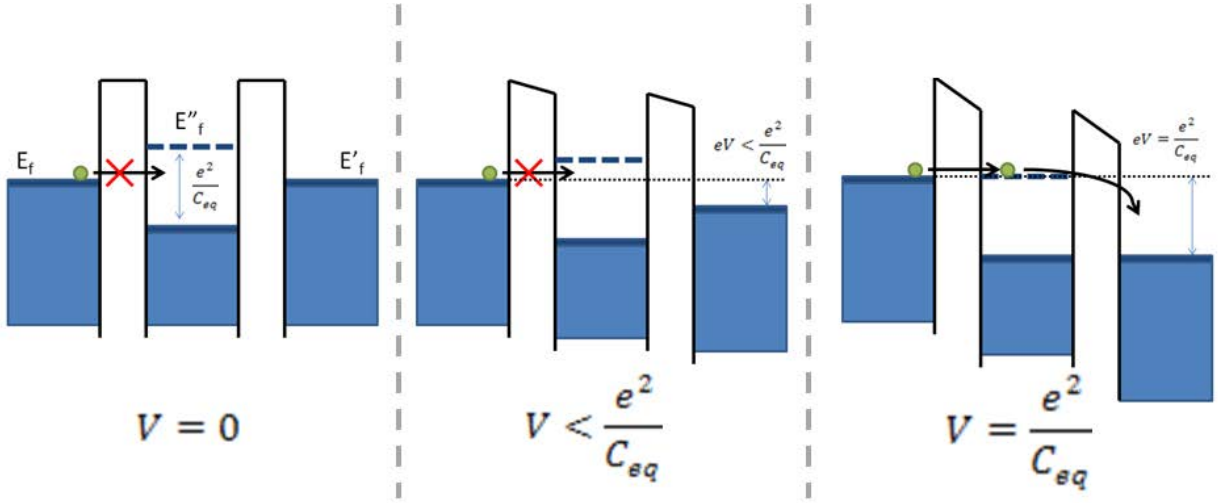

Figure 2.4: *Band diagram of a symmetrical DBTJ with different applied voltage*

Once we apply a voltage on the DBTJ we lower the barrier and allow electrons to go through the junctions as shown in **Figure 2.4**. There can be two cases occurring. If the DBTJ is symmetric (*i.e.* with equivalent tunnel resistance and capacitance for both junctions), then once an electron has enough energy to go through one barrier, it has enough energy to go through the other one. In that case, there is no discrete number of electron in the nanoparticle and the *I-V*

curves shows a non conducting behavior when the voltage is under the threshold voltage (Coulomb blockade), and a linear curve once the threshold is reached (see **Figure 2.5**a). However, in the case of an asymmetric DBTJ (*e.g.* $R_1 \ll R_2$ and $C_1 < C_2$), once an electron is introduced in the island, it doesn't have enough energy to go through the other one and is effectively "trapped" in the nanoparticle for a specific time. If the electron tunnel through the other barrier it is replaced by another one immediately leading to a constant current for a given number of electron. If the voltage is increased, additional electrons can be introduced in the island: the *I-V* curve ends up having a staircase shape where each step corresponds to an additional electron being introduced in the island (Coulomb staircase) as shown in **Figure 2.5**b. in **Figure 2.5**b we can also see the influence of temperature that smooth the steps because of spontaneous transport of electrons[68].

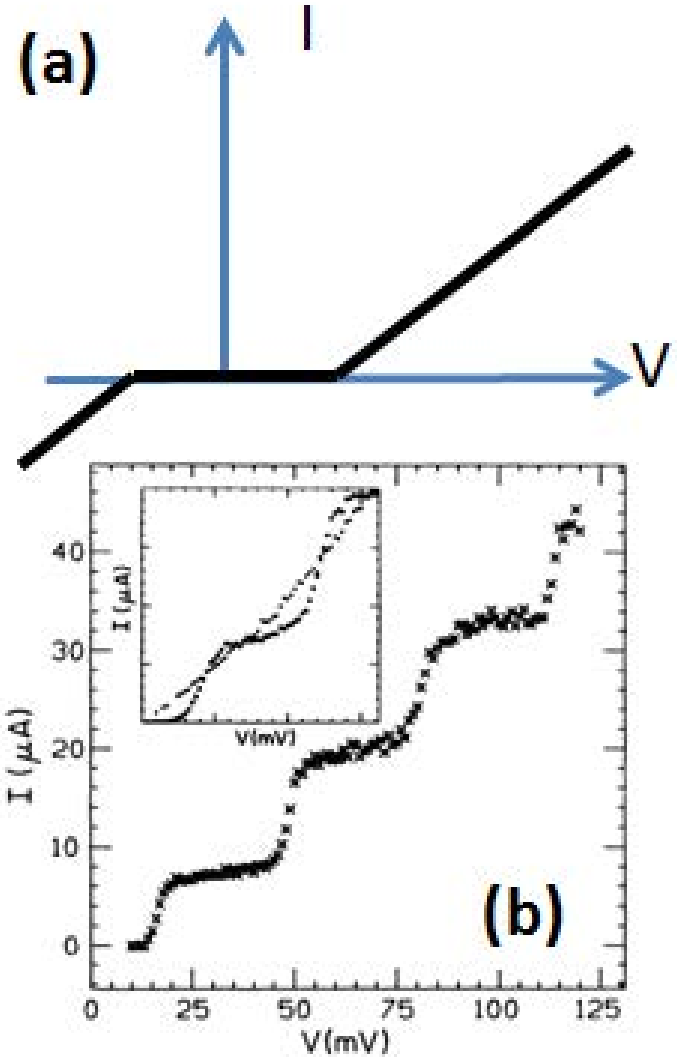

Figure 2.5: *Characteristic I-V curve when the DBTJ is symmetric (a) and when the two junctions are different (b): Calculated I-V characteristic for two ultrasmall-capacitance tunnel junctions in series driven by an external voltage source when $C_1 < C_2$ and $R_1 << R_2$. The steps are $\Delta V = e/C_2 = 32$ mV wide and have a height of $\Delta I = e/R_2(C_1+C_2) = 10.67$ μA. The parameters are $R_1 = 25\Omega$, $R_2 = 2500\Omega$, $C_1 = 0.001$fF, $C_2 = 0.005$fF, and T=10 K. Inset: The temperature dependence of the voltage steps. The steps and the voltage offset are no longer visible when kT is on the order of $e^2/2C_2$. The temperatures are T =40 K (squares) and 80 K (crosses). From Mullen et al. Phys. Rev. B (1988).*

2.2.2 Single electron transistor (SET)

In order to fabricate a SET, an additional contact has to be made: the gate contact can be modeled as an additional capacitance on which a voltage can be applied. The equivalent electronic circuit is shown in **Figure 2.6**.

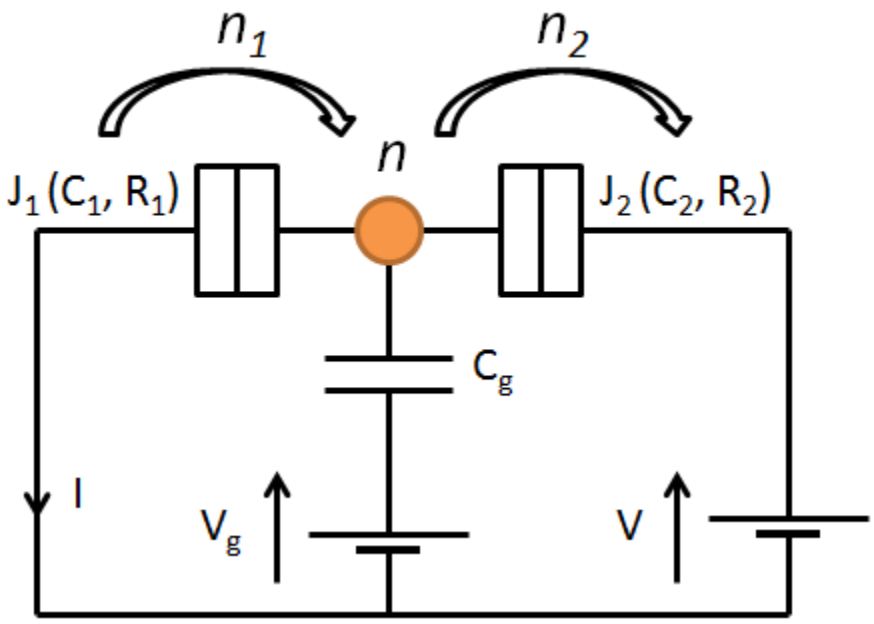

Figure 2.6: *Schematic of the single electron transistor*

In this case, we can go back to **Eq 2.7** and **Eq 2.8** and adjust them with the addition of the new capacitance C_g and the new voltage V_g

$$\Delta E_{n_2 \pm 1} = \frac{e}{2C_{eq}}\left[e \mp 2\left(n + V(C_1 + C_g) - V_g C_g\right)\right] \qquad \textit{Eq 2.15}$$

$$\Delta E_{n_1 \pm 1} = \frac{e}{2C_{eq}}\left[e \pm 2\left(ne - VC_2 - V_g C_g\right)\right] \qquad \textit{Eq 2.16}$$

It is hard to evaluate the influence of V_g on the circuit using these equations. So we will consider two different conditions in order to extract what is called, the stability diagram. The first condition is when we have the variation of energy being equal to zero. **Eq 2.15** and **Eq 2.16** give us:

$$\begin{cases}\Delta E_{n_2\pm1}=0\\ \Delta E_{n_1\pm1}=0\end{cases}\Rightarrow\begin{cases}e\mp2(n+V(C_1+C_g)-V_gC_g)=0\\ e\pm2(ne-VC_2-V_gC_g)=0\end{cases} \qquad \textit{Eq 2.17}$$

This equation leads to $V=f(V_g)$ curves for every value of n which are all parallels lines for the same type of transfer ($n_2\pm1$ or $n_1\pm1$) shown in **Figure 2.7**. When we consider the transfer through the two junctions we have curves that form parallelograms (or diamond).

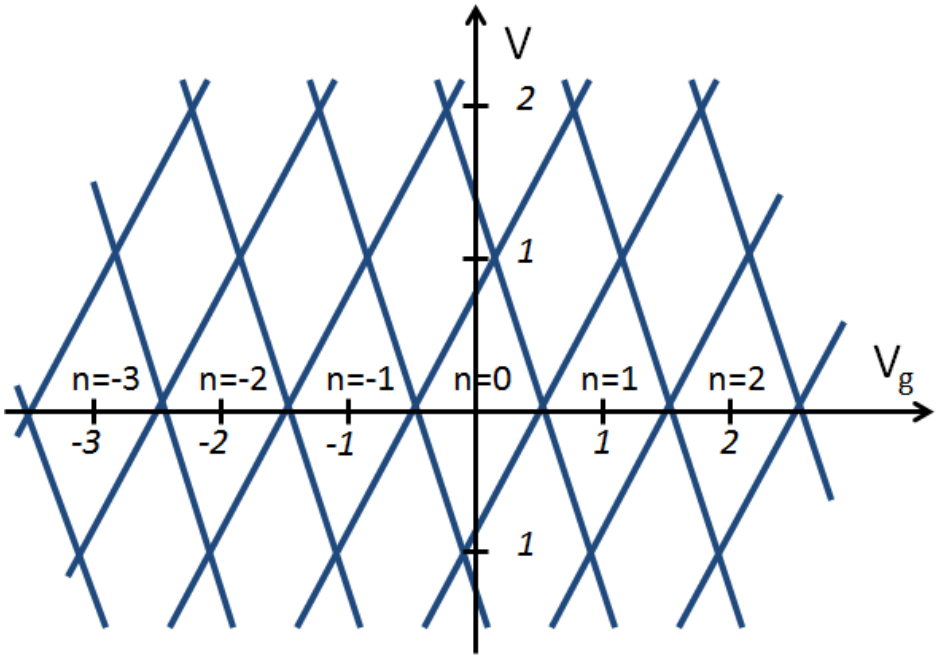

Figure 2.7: *Parallel lines corresponding to the variation of energy being equal to zero*

We also need to identify when the current doesn't go through. So we must consider when $\Delta E>0$. So we obtain

$$\begin{cases}\Delta E_{n_2\pm1} > 0 \\ \Delta E_{n_1\pm1} > 0\end{cases} \Rightarrow \begin{cases} -\frac{e}{2} - ne + C_g V_g < V(C_1 + C_g) < -\frac{e}{2} - ne + C_g V_g \\ -\frac{e}{2} + ne - C_g V_g < VC_2 < \frac{e}{2} + ne - C_g V_g \end{cases} \qquad \textit{Eq 2.18}$$

This effectively shows that the zones that are in light blue in **Figure 2.8** are the zone where no current pass through (Coulomb blockade). There is a threshold value for V above which there cannot be any Coulomb blockade whatever V_g is.

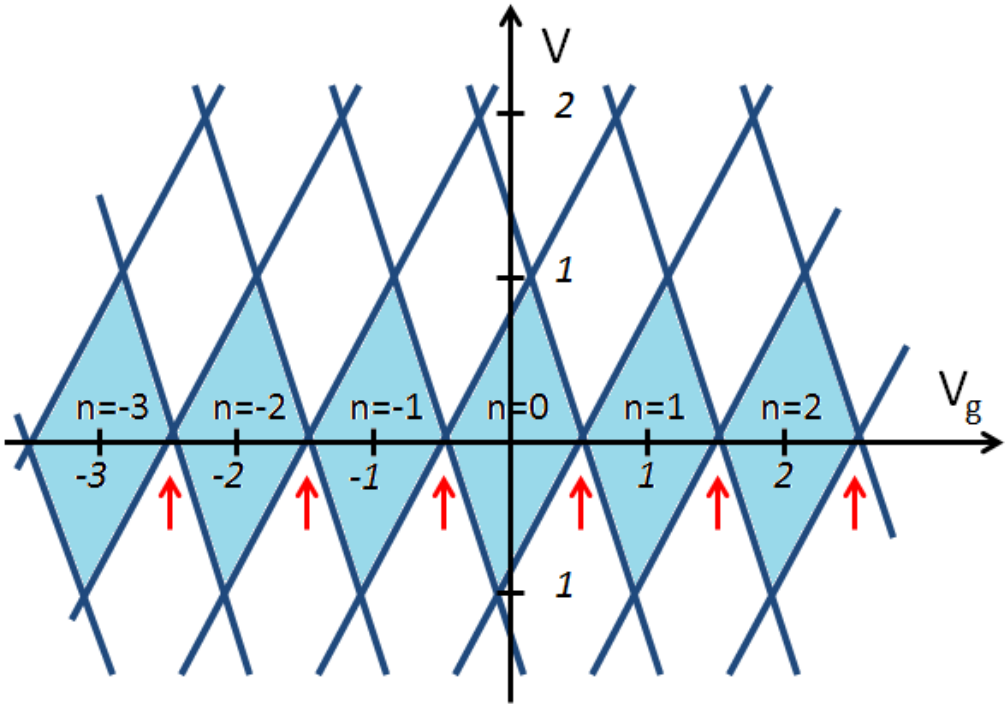

Figure 2.8: *Stability diagram or Coulomb diamond of the single electron transistor*

When V=0 we can vary Vg and obtain the Ids/Vg curve shown in **Figure 2.1**. This can be identified on the stability diagram when V=0: each peak corresponds to the current going through at equidistant point when two "diamond" touch (red arrows in **Figure 2.8**).

2.2.3 Experimental studies

The first experimental single electron transistor was made by Fulton and Dolan in 1987[69]. The principle was based on a relatively simple technique that uses a mask done with e-beam lithography through which they evaporated aluminum from two angles. A lot of successful experiments have been done since then, producing single electron transistors with various architecture and materials. In the late nineties a lot of progresses were made in the fabrication of sub 10nm devices[70,71,72,73,74,75,76,77] as summarized in **Table 2.1**.

Materials Island/barrier	**Fabrication method**	**Highest ΔE_c(meV)**	**year**	**ref**
Al/AlO_x	Evaporation through an e-beam-formed mask	23	1996	71
CdSe/organics	Nanocrystal binding to prepatterned Au electrodes	60	1997	72
Al/AlO_x	Evaporation on a Si3N4 membrane with a nm-scale orifice	92	1997	73
Ti/Si	Metal deposition on prepatterned silicon substrate	120	1997	74
Carboran molecule	E-beam patterned, thin-film gate: STM electrode	130	1996	75
Si/SiO_2	E-beam patterning + oxidation of a SIMOX layer	150	1996	76
Nb/NbO_x	Anodic oxidation using scanning probe	1000	1998	77

***Table 2.1**: Some High-ΔE_c Single-Electron Transistors. From Likharev et al., Proceedings of the IEEE (1999).*

Most of them were based on inorganic materials and were not capable of producing reliable and reproducible single electron transistor that were compatible with standards of fabrication. This is why new approaches are being investigated. As seen earlier, new techniques have been developed in chemistry for providing new tools that can be used in this framework.

Organic monolayers, because of their potential stability, their size, their versatility and their insulating properties can be used in order to provide another degree of control on the fabrication of single electron transistor. A lot of work has been done along that path. A DBTJ was fabricated using gold nanoparticles and amino-based organic layer on gold by Jacobsen *et al.*[78] using an STM. I-V characteristics were acquired using scanning tunneling spectroscopy (STS). Step-like behaviors were not clearly obtained in ambient condition leading up to the conclusion that using an STM induces a lot of surface modification (rearrangement, chemical reaction, drift) that hinders reproducibility of results. More recent work used gold nanoparticle on nanogap fabricated using a GOM[79] and had experimental observation of size dependence of Coulomb staircase shape. A recent work shows Coulomb staircase behaviors in a vertically engineered silicon nanopillar[80]. This demonstrates that silicon can be used as the island for electron storage as well as the contacts (source, drain and gate). The same conclusion can be obtained from a study from Tan *et al.* reporting SET behavior using silicon nanocrystal films that were selectively oxidized at the grains boundary to create DBTJs[81]. The first CMOS-compatible SET was built by Ray *et al.* in 2008[82]. The fabrication of the device relies on the heavy use of lithography and the attachment of a gold nanoparticle on a manufactured pillar (see **Figure 2.9**). It is an impressive achievement with clear Coulomb staircases and Coulomb diamond but they do not use a silicon electrode but chromium ones. The yield remains however too low for (1%) for any industrial application yet.

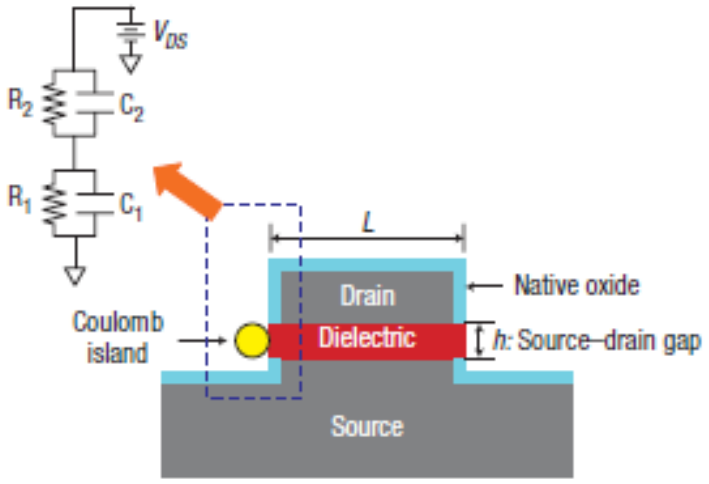

Figure 2.9: *The single-electron device architecture. The source and drain electrodes are vertically and self-aligned so that the source-drain gap is defined by controlling the dielectric thickness. The top left depicts an equivalent circuit representation of the single-electron transport inside the dashed box. From Ray et al. Nature Nanotechnology (2008).*

2.3 Case of an electrode being a semiconductor

In the orthodox approach being discussed in the first part of this chapter, the system is considered to be made of inorganic dielectrics and metals. But in this thesis, we wish to use the silicon bulk as one of the electrode. Therefore we need to identify the differences induced by the use of a SC instead of an ideal metal.

Using a SC as one of the contact has an influence on the DBTJ: several factors have to be taken into account for a good characterization and understanding of the system. Due to the formation of a depletion region of a SC, an additional insulating distance must be considered: the

electron have to tunnel through a longer distance to reach the nanoparticle. Also, in the theoretical approach, we must consider that the surface potential of the bulk has an influence on the voltage effectively applied on the tunneling junction. The charging state of the SC surface (inversion, accumulation or depletion), depends on the applied voltage, and has a great influence on its surface potential. Of course, this is dependent on the doping level of the substrate as well as the electrical properties and homogeneity of the GOM. Depending on the nature of the GOM various effects arise, such as formation of molecular dipoles that have an influence on transport[83] or Fermi level pinning[84].

Some works have already been published and investigate some of the issues that are the consequences of the use of SC instead of metal in a DBTJ. Feenstra *et al.* explored the effect of the dopant type and doping level on the voltage drop across the substrate and calculated the band bending induced by the very close vicinity of the metallic tip of the STM tip. This voltage drop is linked to the band bending at the surface of the SC and Feenstra proposed in 1987 a graph showing this effect for p- an n-doped GaAs(110)[85]. It is displayed in **Figure 2.10**. For example, when a bias of +2V is applied on the sample relative to the tip, the potential drop across the depletion region (noted band bending ϕ_S) reaches 1.5 V for the n-doped GaAs. The potential drop across the tip-vacuum-GaAs junction is therefore reduced to 0.5 V. We will tackle this issue for the more complex geometry of our DBTJ in **CHAPTER 7**.

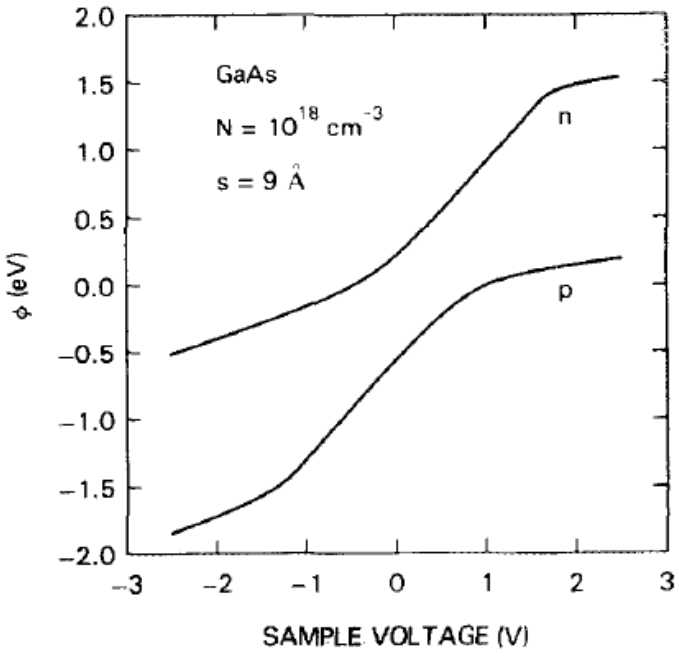

Figure 2.10: *Band bending as a function of sample voltage for n- and p- type GaAs with a doping of 10^{18} cm^{-3}. The quantity plotted is computed using numerical integration of Poisson's equation through the space-charge region that forms in the GaAs. A metal probe tip, biased at 0 V, is placed 9 Å from the surface. Feenstra and al. Am. Vac. Soc. (1987).*

2.4 Specificity of using an organic dielectric

2.4.1 Electronic transport in molecules

Using a GOM as one of the tunneling junction can have some effect on the overall system compared to using a regular inorganic dielectric like Al_2O_3 or SiO_2. In order to explore this phenomenon, we need to identify the different electronic transport mechanism occurring in a molecular junction. We can consider four fundamental conduction mechanisms which are summarized in **Table 2.2**.

Conduction mechanism	Characteristic behavior	Temperature dependence	Voltage dependence
Direct tunneling	$J \sim V \exp\left(-\frac{2d}{\hbar}\sqrt{2m\varphi_{\mathrm{B}}}\right)$	none	$J \sim V$
Fowler-Nordheim tunneling	$J \sim V^2 \exp\left(-\frac{4d\sqrt{2m}\varphi_{\mathrm{B}}^{3/2}}{3q\hbar V}\right)$	none	$\ln(\frac{J}{V^2}) \sim \frac{1}{V}$
Thermionic emission	$J \sim T^2 \exp\left(-\frac{\varphi_{\mathrm{B}} - q\sqrt{qV/4\pi\epsilon d}}{k_{\mathrm{B}}T}\right)$	$\ln\left(\frac{J}{T^2}\right) \sim \frac{1}{T}$	$\ln(J) \sim V^{1/2}$
Hopping conduction	$J \sim V \exp\left(-\frac{\varphi_{\mathrm{B}}}{k_{\mathrm{B}}T}\right)$	$\ln\left(\frac{J}{V}\right) \sim \frac{1}{T}$	$J \sim V$

Table 2.2: *Possible conduction mechanisms. Here, J is the current density, V is the bias voltage, φ_B is the barrier height, d is the barrier length and T the temperature. From Cuevas and Scheer,* Molecular Electronics*, World Scientific (2010).*

Coherent transport

A strict definition of coherent transport (or tunneling), is a transport regime where the information of the phase of the wavefunction of conduction electrons is preserved through the molecular junction. However, when people mention coherent tunneling through a potential barrier they usually refer to the first two mechanisms in **Table 2.2**, Direct Tunneling and Fowler-Nordheim Tunneling. The first one refers to what happen when dealing with low bias (when the voltage is much smaller than the barrier height), and the latter is when the applied voltage is

larger than the average barrier's height. I-V curves of both regimes are not dependent on the temperature of the medium.

Thermionic emission

When electrons are excited they can go over a potential barrier. This is a different conduction mechanism than tunneling and it is called thermionic emission. Since it depends on the excitation of the incoming electrons, this is very dependent on the temperature and it can become a dominant transport mechanism when the potential barrier is small. Electrons cross the barrier elastically and their wavefunction phase is preserved, so strictly speaking, it can be considered as a coherent mechanism.

Hopping conduction

This mechanism is an incoherent transport mechanism based on the successive hopping of electrons between different localized points within a molecule. This means that this transport is usually dominant in long molecule (*e.g.* DNA) because the conductance decays linearly with the length of the conducting wire as opposed to coherent mechanism transport where it decays exponentially[86,87]. This is also a process that is highly dependent on the temperature[88].

In the framework of this thesis, we wish to observe the single electron transport at low temperature in order to avoid temperature dependent conduction mechanism. We also use low voltage bias, ensuring that coherent direct tunneling transport is the dominant conduction

mechanism. This is consistent with what can be found in the literature[87,89,90]. However, it should be noted that this is a simplifying approach as other mechanisms can be considered but it is a good first introduction. Other possible transport mechanism (that shouldn't apply to our system because of the very low temperature) such as thermal transport or vibrationally-induced inelastic current are developed in the book *Molecular Electronics: An Introduction to Theory and Experiment*[86].

2.4.2 Metal anchoring contact, the role of the GOM termination

When building a molecular-metal junction, one must consider the end group of the molecular junction that will bear the functionalities of the interface. Choosing the correct terminal moiety is a compromise between the functionality of this group and the constraints set by its chemical reactivity. In the framework of this project, we aim at attaching gold nanoparticles to a GOM. Only a few terminations can firmly attach AuNP, and among them we have decided to consider thiol and amine moieties. But other parameters must be considered when an anchor is chosen. They highly depend on the desired functionality of the system. Indeed, if the goal is to maximize conductivity, then the strength of the metal-molecule coupling must be optimized[91], the stability and robustness of the junction also have to be considered as well as the variability of the bonding between the anchor group and the metal which can be an issue for reproducibility of experimental results.

Some studies have been done in regards of the adaptability of thiol-gold bonding for electrical measurements. It has been determined that the variability in the bonding tends to be harmful for the reliability of these measurements, especially on single molecules[92]. Amine group has been identified as a viable alternative by Venkataraman *et al.*[92]: when they conducted experiment regarding the measurement of molecular conductance, the variability of the results with an amine group was much lower than those with thiol groups. Another group, Tao *et al.* have compared conductivity of thiol, amine and carboxylic acid (COOH) groups[90] and concluded that they were independent of temperature and that the decay with the tunneling length was under the form: $G = Ae^{(-\beta L)}$. L is the molecule length and β the attenuation factor. Typically, β's value ranges from 0.2-0.4 $Å^{-1}$ for conjugated molecules to 0.8-1.2 $Å^{-1}$ for aromatic compounds[87]. These results suggest a coherent tunneling mechanism. The exponential factor A is experimentally highly dependent on the nature of the anchoring group. In their study they demonstrated that it varies in the following order: SH > NH_2 > COOH. It was attributed to the coupling strength of each group with gold. For our study, we have decided to use an amine group since it provides more reproducible results than the thiol group even if thiol seems to provide a higher electron conductance. The coupling strength is also lower for amine, but it has been shown to be enough for a good attachment of colloidal AuNP[7].

2.4.3 Effective electron mass

Most experimental I-V characteristics of a molecule or a molecular layer can be fitted using a standard double polynomial curve. It is then easy to superpose a fit and experimental data

without offering a model consistent with the experimental condition: Some works have done so[89], the extracted parameters were very different from those predicted by theory, like the barrier height. That's why some interpretation work must be done: some additional effects have to be taken into account, such as effect of electron effective mass. when Akkerman *et al.* were able to determine the effective mass of electron in their molecular layer by including in their Au-alkane model an image charge effect[93]. Basically they considered a single effective mass and a barrier height. The barrier height obtained were in the order of 4-5eV, which is not dependent on the length of the molecules, and an effective mass of $0.28m$. These results were in agreement with theoretical predictions[94]. For more information about the determination of the effective electron mass, please refer to **CHAPTER 7**.

2.4.4 How to more accurately model a molecular junction

In the framework of our project, we use an organic layer as one of the junction of the DBTJ. We wish to consider modeling tools introduced by the book *Molecular Electronics: An Introduction to Theory and Experiment*[86] in order to understand the behavior of our GOM when dealing with small voltage bias like it is the case with Coulomb staircase. One could argue that modeling a molecular junction as a single barrier is not accurate enough. At least a double barrier junction seems appropriate as a molecular junction has two interfaces.

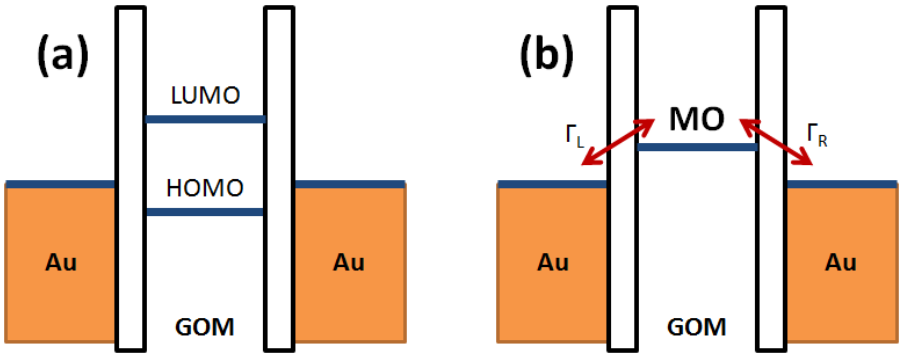

Figure 2.11: *(a) Level scheme of a molecular junction. (b) Same junction when the transport is dominated by one level in the molecular layer MO.*

We have then a band diagram which resembles the one displayed in **Figure 2.11a**. The molecular junction is a series of discrete levels (here only Highest Occupied Molecular Orbital, HOMO and Lowest Unoccupied Molecular Orbital, LUMO are represented) whereas the metal possess a continuum of states that is filled up to the Fermi energy of the metal. When one level (HOMO or LUMO, at a level MO) is close to the Fermi level of the metal, it will dominate the transport at certain voltage range. In that case **Figure 2.11b** gives a good idea of the resulting case. The energy level of the molecule depends on the voltage applied on the system and should be noted *MO(V)*. Other important parameters are scattering rates Γ_R and Γ_L of respectively the right and left barriers. They depend on the nature and quality of the bonding of the molecular with each electrode. This regime correspond to the resonant tunneling model where the *I-V* characteristic is shown in **Figure 2.12** when the system is symmetric (*i.e.*, the scattering rates are equals)[86]. Once a voltage threshold is reached (*MO(V)*), the dominant transport is a coherent tunneling through the LUMO or the HOMO that is characterized by a peak in the conductance. After the peak the current saturate as shown in **Figure 2.13** and we reach another plateau[86].

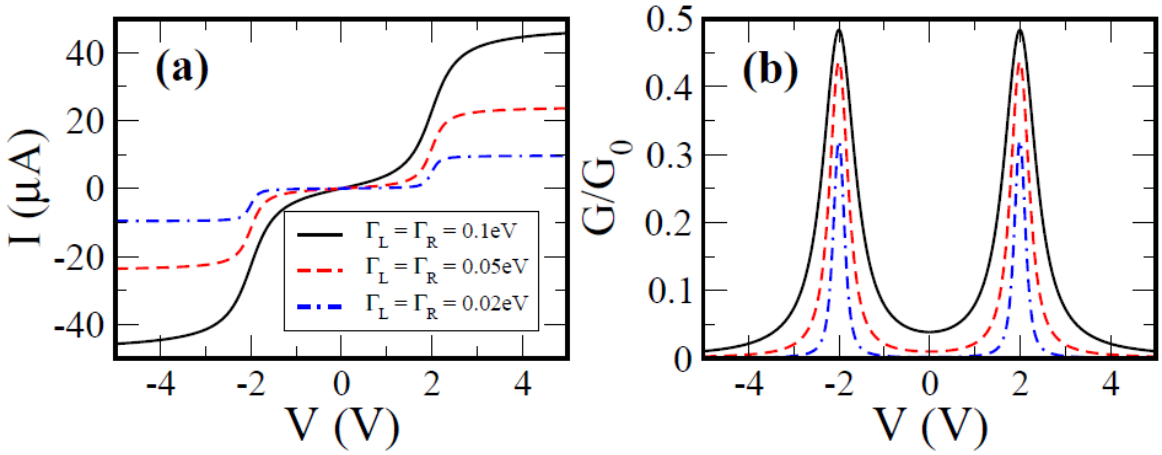

Figure 2.12: *(a) Current vs. bias voltage in the resonant tunneling model for a level position MO = 1 eV (measured with respect to the Fermi energy of the electrodes) and at room temperature (k_BT = 0.025 eV). The different curves correspond to different values of the scattering rates that are assumed to be equal for both interfaces. (b) The corresponding differential conductance G = dI/dV normalized by $G_0 = 2e^2/h$. Cuevas and Scheer,* Molecular Electronics*, World Scientific (2010).*

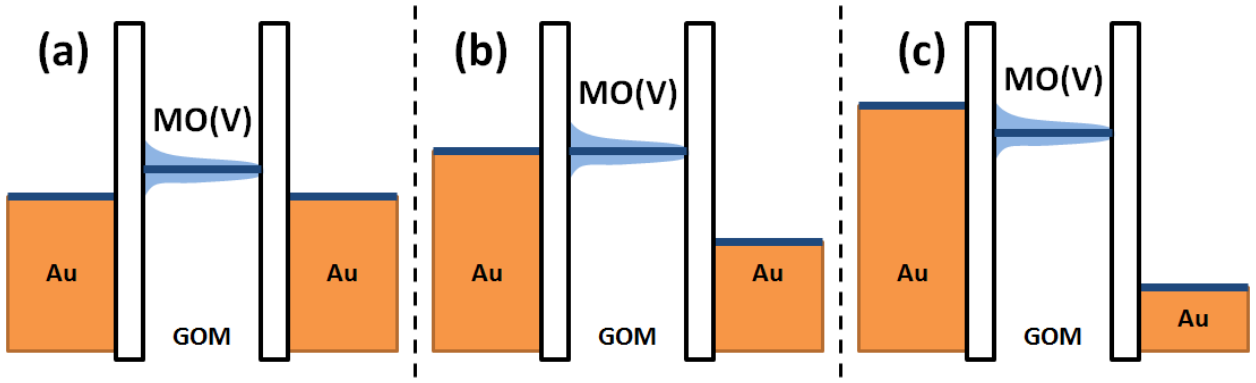

Figure 2.13: *Voltage dependence of the level alignment at zero bias (a), in a resonant situation (b) and at large bias (c) when the current saturates.*

But the double junction still behaves like a regular tunneling junction as shown in **Figure 2.14** when dealing with small bias.

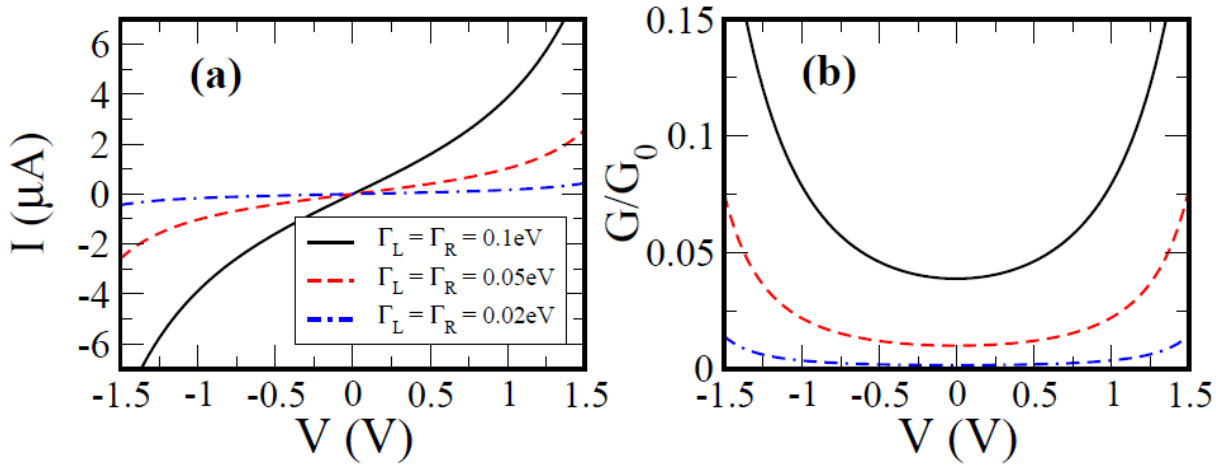

***Figure 2.14**: The same as in **Figure 2.12** for low bias (|eV| < MO(V)). Cuevas and Scheer,* Molecular Electronics*, World Scientific (2010).*

The molecular junctions involved in this thesis are not symmetrical. Even if we replace the silicon bulk with a metallic contact (gold), one of the contacts, is a plane surface, the other one is a gold nanoparticle. Moreover the anchoring group is an amine, and the junction between the GOM and the bulk is made through a Si-C bond. We can then consider that our molecular junction is asymmetrical and we must look into how this model can take that into account. If Γ_L and Γ_R are different then, there can be a voltage drop that will have an influence on the level of the GOM. In the book *Molecular Electronics: An Introduction to Theory and Experiment* [86], they model this variation to the form: $MO(v) = MO + (eV/2)\ (\Gamma_L - \Gamma_R) / (\Gamma_L + \Gamma_R)$. This expression is based on the fact the energy level will shift toward the electrode where the rate is higher. The *I-V* curve is then dramatically changed and is displayed in **Figure 2.15**. We can qualitatively understand it by seeing that, for example, if $\Gamma_L << \Gamma_R$ we have a shift of the energy level of $-eV/2$. The junction will then follow the chemical potential of the right electrode and the peak

corresponding to the resonant condition can only be observed in positive bias: the current is then really low for negative bias.

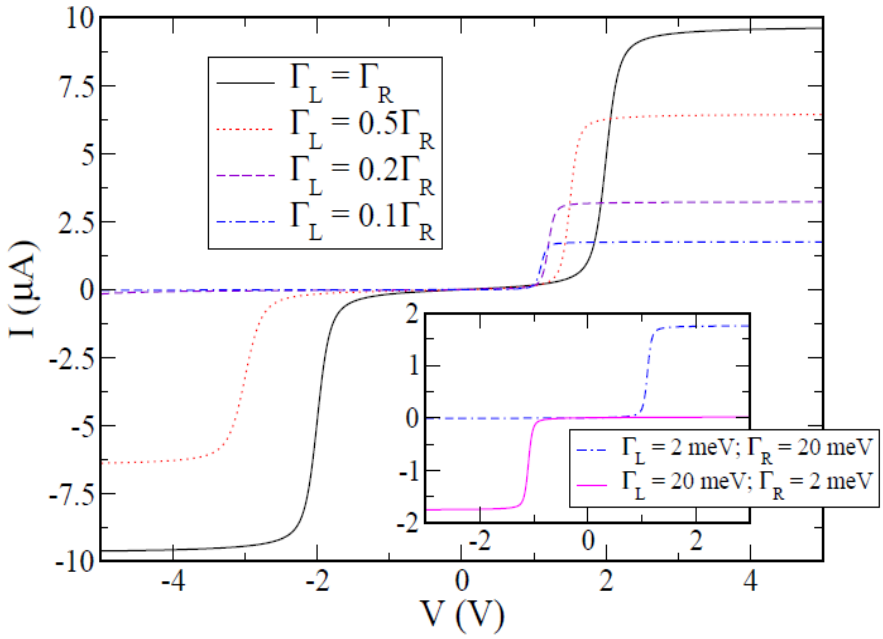

Figure 2.15: *Current-voltage characteristics in the resonant tunneling model for an asymmetric situation for MO = 1 eV, Γ_R = 20 meV and at room temperature (k_BT = 25meV). The different curves correspond to different values of the left scattering rate. The inset shows very asymmetric situations where the scattering rates have been interchanged. Cuevas and Scheer,* Molecular Electronics*, World Scientific (2010).*

Experimental results usually evaluate bandgap of alkyl based GOM to be in the order of 6-8eV. This is a relatively high value: this means that HOMO and LUMO of our GOM are far apart and that the voltage bias has to be in the order of 3-4V for the conduction to be dominated by either the HOMO or the HOMO. Therefore it is expected that our GOM should behave like a regular dielectric and can be modeled as a regular tunnel junction. However, experimental characterization must be done to confirm it (see **CHAPTER 7**).

2.5 Conclusion

In this chapter we introduced the concept of Coulomb blockade and Coulomb staircase and showed the potential of such technology to replace current transistor technology (such as current consumption and size). We have studied this phenomenon using self assembly techniques on functionalized silicon. We have shown that using a SC bulk as one of the electrodes introduce new effects like band bending that affect the resulting behavior of our system. The use of a molecular layer also introduces new parameters that can be difficult to control and model. However, all parameters cannot be taken into account because of the complexity of such models. Akkerman *et al.* showed that, with molecular electronic, it is really difficult to obtain experimental data that are consistent with an accurate simulation and that are reproducible[87] so we are going to address this issue in the next chapters. That's why some work has been done to study reproducibility of our results. **CHAPTER 5** is going to focus on the experimental protocol involved in the fabrication of the architecture and the results obtained as a proof of concept. **CHAPTER 6** is mainly going to focus on parameters that affect the reproducibility of said results and **CHAPTER 7** is providing simulation tools that offers good model for our architecture with an opening toward working devices.

CHAPTER 3

NANOQUANTUM DOTS ON SILICON FOR HYBRID SOLAR CELLS

3.1 Introduction

3.1.1 Overview of solar cell technology

In light of recent challenges regarding the need to find new ways of harvesting energy in a non-polluting way, solar cells technologies have received a lot of media attention. A lot of work has been done to create environmentally and economically sustainable solar cells. A wide variety of technologies have been investigated, from the fabrication of expensive but very efficient devices (*e.g.* for space applications) to inexpensive but much less efficient devices (for low-end applications). Conversion of energy in solar cells usually occurs in two steps. Light is first absorbed in a material, creating electron-hole pairs. The electrons and holes are then separated and collected at the anode for electrons and the cathode for holes, creating a current. In **Figure 3.1** this process is pictured for different types of solar cells technologies in use today. Most technologies rely on a P/N junction to create a natural field without external bias: charges are created in the depletion region when excited by an incoming light and the current is extracted to the contacts by the built-in electric field. The first silicon solar cell was reported by Chapin *et al.* in 1954 with a reported efficiency of 6% which was six times higher than the best previous attempt. The solar cell efficiency is defined as the ratio of the electrical output of the device to the incident energy from the sunlight. It is basically the percentage of the solar energy that is converted into electrical energy. It is obtain with the equation:

$$\eta = \frac{P_m}{EA_c} \qquad \textit{Eq 3.1}$$

where P_m is the cell power output in watts, E the input light flux (in $W.m^{-2}$) and A_c the surface area of the solar cell (in m^2). **Figure 3.2** summarizes the progress made over the past decades. It gives a good overview of the recent trends in PV cells technologies. Notable examples of technologies are:

- Silicon is the most prevalent material used. Either as a monocrystalline bulk (most efficient see **Figure 3.1**a), or as polycrystalline or amorphous (**Figure 3.1**c) thin films (cheaper and potentially flexible). The theoretical maximum efficiency of Silicon solar cell cannot exceed ~31%.
- A way to go over the 31% efficiency limit is to use more than one SC by stacking several SCs with different bandgaps for an optimized absorption. Such multijunctions are the most expensive and efficient solar cells. They are located in the top part of **Figure 3.2**.
- Organic photovoltaic cells (OPV) are located at the low end of **Figure 3.2**. They are usually flexible cells based on organic SCs. They are cheap but have low efficiency and limited durability.
- Dye sensitized solar cells (**Figure 3.1**g-h). The light is absorbed in dye molecules transferring an electron from ground state to excited state through contacts that involve a molecular electron acceptor at the anode and a molecular electron donor at the cathode. Despite much work to optimize such promising structures, their efficiency is still lower than traditional Si solar cells, although the cost could be lower.

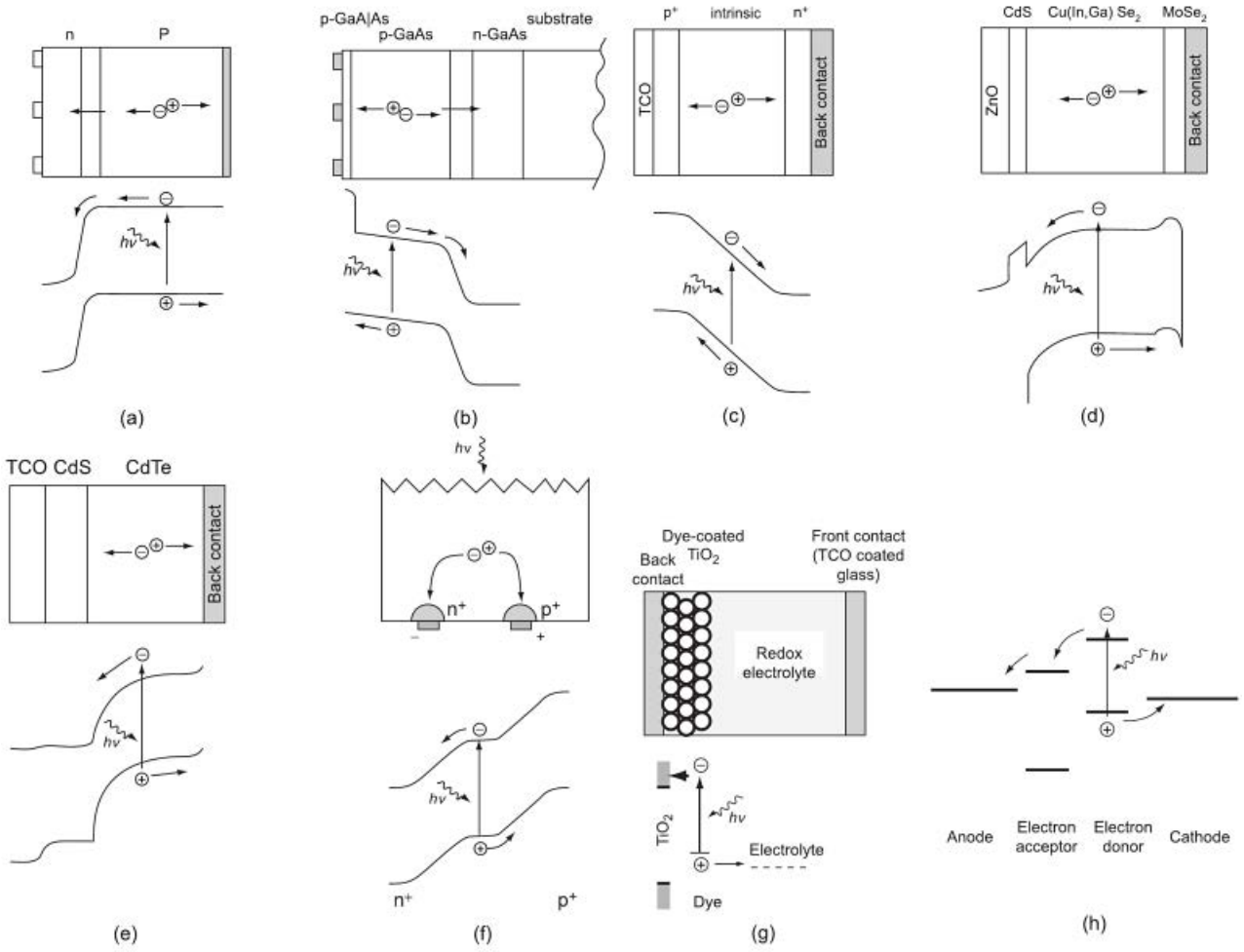

Figure 3.1: *(a) Structure of typical crystalline silicon solar cell. The bulk is usually a thick p-type base where most of the incident light is absorbed. (b) Gallium arsenide heterojunction that works similarly to silicon bulk solar cells. (c) Silicon amorphous solar cell based on a p-i-n junction. (d)-(e) solar cells based on compounds SCs. (d) contacts can be arranged on the same side, the n-type bulk silicon is usually thinner than in (a) for charges extraction, so to make up for the lack of absorption, it is usually patterned. (g)-(h) dye sensitized cells that rely on energy transfer from molecular based electron acceptor and donor for charge extraction. From the book "Solar cells: materials Manufacture and operation by McEvoy et al. (2013)*[95].

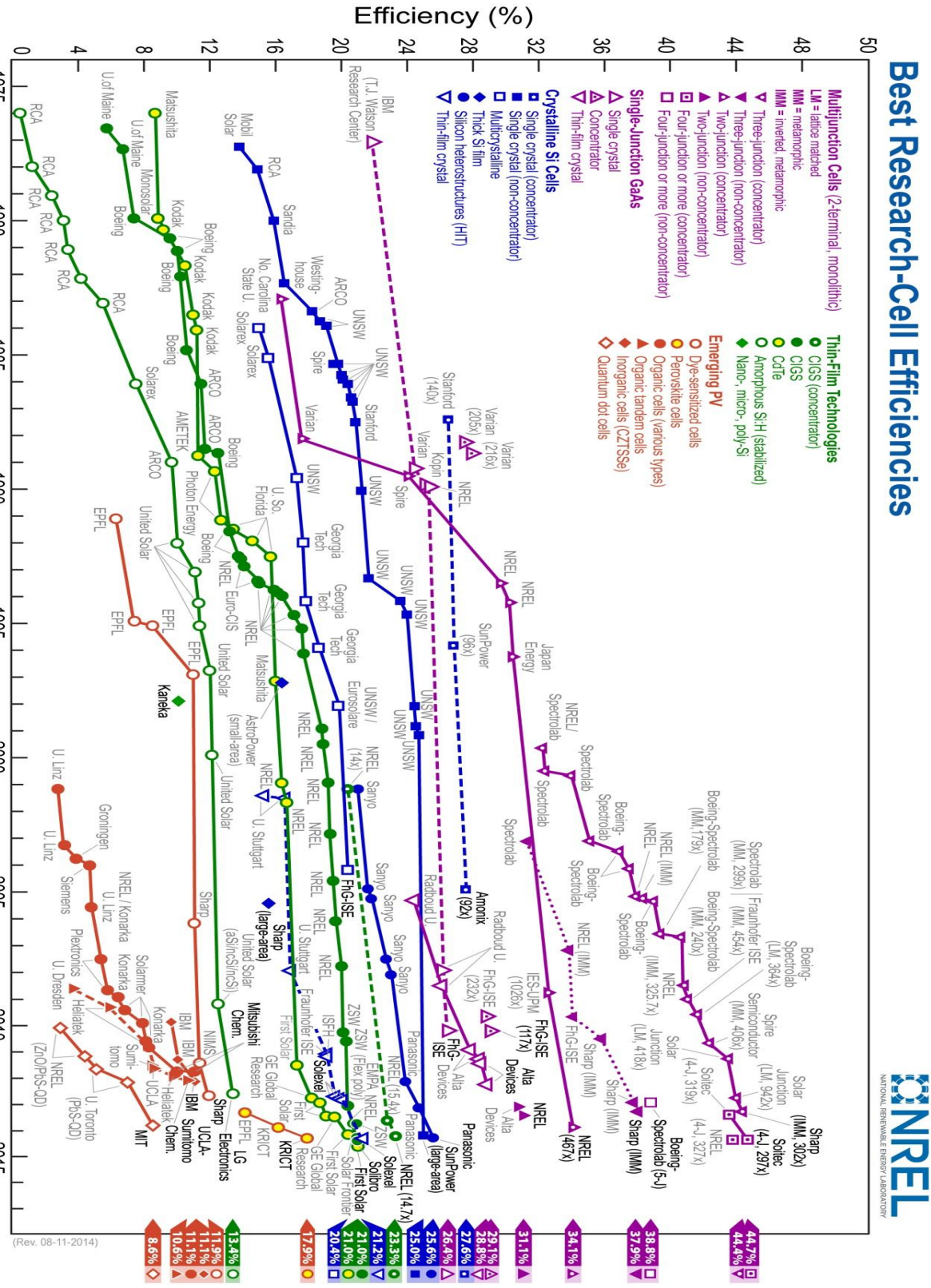

Figure 3.2: *Reported timeline of solar cell energy conversion efficiencies. From National Renewable Energy Laboratory,USA (2014).*

3.1.2 Hybrid nanoquantum dot technology

Still currently at the lowest end in **Figure 3.2** (*i.e.* low efficiency), there is a new emerging technology that is showing promising results: nanoquantum dots (NQDs) solar cells. They are based on the same principle as dye sensitized solar cells (**Figure 3.1**g and **Figure 3.1**h) but with inorganic compounds (NQDs) as electron donors and acceptors. The quantum dots bandgap can be tuned in order to cover a wide range of energy level[96], which is done by changing the NQDs size. Originally the goal was to replace the thick bulk with NQDs as an absorbing PV material. For instance, Ip *et al.* proposed in 2012 a device with a thick film of NQDs embedded between a metallic contact (MoO_x/au/Ag) and a transparent conducting contact (FTO)[97]. The reported efficiency was 7%. This has been surpassed in 2014 by Chuang *et al.* who used passivating ligand (ethylenedithiol) on the NQDs while removing the MoO_x interfacial layer, and achieved an efficiency of 8.6%[98]. This efficiency is still quite low compared to inorganic crystalline devices because of the poor interface quality, carrier transport and collection efficiency. **Figure 3.3**a shows that charges have a high chance of recombination before reaching contacts.

We follow another approach: we use a combination of the strongly absorbing inorganic NQDs grated onto high mobility SC layers (*e.g.* Si). Such devices rely on the *energy* transfer (instead of *charge* transfer) across the interface from the NQDs to the SC bulk where the separation and transport of charge carriers occurs as shown in **Figure 3.3**. Doing so requires the presence of a passivating layer between the NQDs and the SC that also plays a role for the

quality of the interface. This is done in order to avoid energy loss phenomena such as charge trapping and recombination. Another advantage of this technology is the fact that NQDs that active and chemically stable in the near infrared region (NIR) can be used, which is a region where silicon absorption is low. Grafting NQDs will then effectively enhance the absorption of the overall structure, which is usually one of the drawbacks of silicon thin films solar cells compared to monocrystalline bulk silicon solar cells. This thesis describes how we use our knowledge to prepare well-controlled GOM on Si(111) surfaces to attach NQDs. We then optimize solar cells efficiency with silicon patterning and multilayer grafting. In this chapter, we provide the basics of energy transfer between NQDs and an acceptor. We also review some of the progress that has previously been made in our lab identify and quantify these processes experimentally.

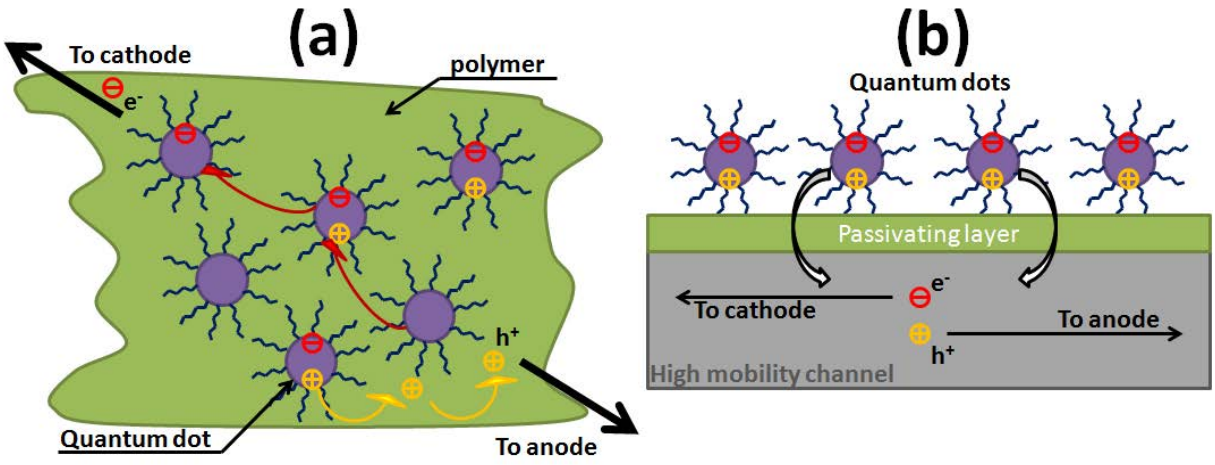

Figure 3.3: *(a) Schematics of a typical organic (NC/polymer) solar cell. Upon exciton break-up at the interface, electrons and holes travel through separate charge transfer mechanism. Recombination and charge trapping are hindering cell efficiency. (b) Schematics of the proposed energy transfer based device that avoids the influence of the interface and directly delivers electron-hole pairs into the high mobility SC layer.*

3.2 Properties of Nanoquantum dots

3.2.1 What is a Nanoquantum dots?

NQDs are crystalline nanoparticle made of a semiconductor that can exhibit some quantum mechanical properties (see **Figure 3.4**). Their small size (nanometer scale) leads to three-dimensional confinement of excitons, which gives them discrete properties (they are sometimes referred as "artificial atoms"). These specific properties are closely related to their size and shape: for instance, the bandgap of a NQD can be tuned depending on its size. It determines the wavelength of the emitted light when the quantum dot is photoexcited. The frequency of the emitted light decreases (*i.e.* shifts from blue to red) when the size of the NQD increases (see **Figure 3.4**). NQDs can be manufactured with a wide variety of sizes which gives control over their optical properties without changing the underlying material or the deposition/grafting techniques[96]. For NQDs made using wet chemistry, simple parameters like temperature or reaction time can be used to tailor their final sizes. NQDs used in this thesis have a SC core made of cadmium selenide (CdSe) and are usually protected by a zinc sulfide (ZnS) layer. Typically, organic capping and ligands surround the NQDs, which helps tune their chemical properties such as solubility in different solvent (see **Figure 3.4**). Some large CdSeTe NQDs have also been synthesized, which is useful for higher wavelength emission.

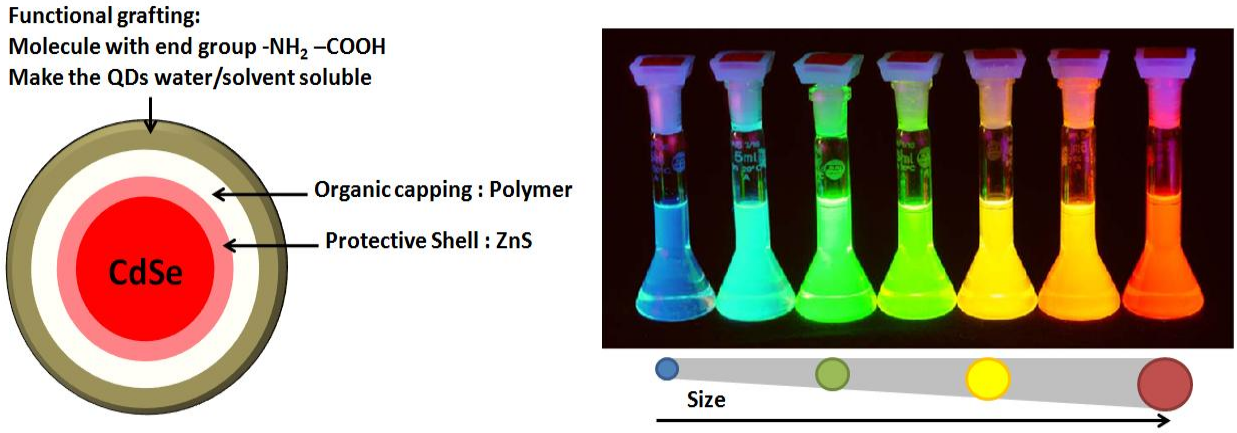

Figure 3.4: *Scheme of a CdSe NQD with a visual representation of emission wavelength size dependence. Different NQD solutions are excited with a UV light.*

3.2.2 Energy transfer

The excitation of NQDs by photons or electrons generates excitons in its core (i.e., electron-hole pairs). Such e-h pairs in excited NQDs can decay by capture by surface traps, radiative decay, or by energy transfer into a substrated through radiative and non-radiative energy transfer mechanisms (RET and NRET), creating e-h pairs in the substrate. NRET is also referred to as Förster resonant energy transfer (FRET) and only involve dipole-dipole coupling. These different decay mechanisms are discussed in more detail below by focusing on the nature of the substrate and its role as an acceptor, the actual non-radiative energy transfer and the coupling that exists between NQDs within a layer or layers.

Role of an acceptor

Once excited by a source, isolated NQDs will transfer all their energy through radiation that can be picked up by a detector (see **Figure 3.5**a), assuming there are no surface or bulk traps for the emitted radiation. When NQDs are far enough from each other (> several times their diameters), they do not affect with their local decay mechanism (i.e., there is no energy diffusion from dot to dot). As the concentration of isolated NQDs increases, so does the photoluminescence (PL) intensity. This is because there is no acceptor to "harvest" the energy. Once an acceptor is brought in close proximity of NQDs, the PL count drastically decreases (see **Figure 3.5**b) because there are new decay channels: (i) absorption of emitted radiation by the substrate (RET), and (ii) excitation of image dipoles in the substrate leading to dipole-dipole energy transfer (*i.e.*, non-radiative energy transfer) NRET. In our case, the acceptor substrate is silicon.

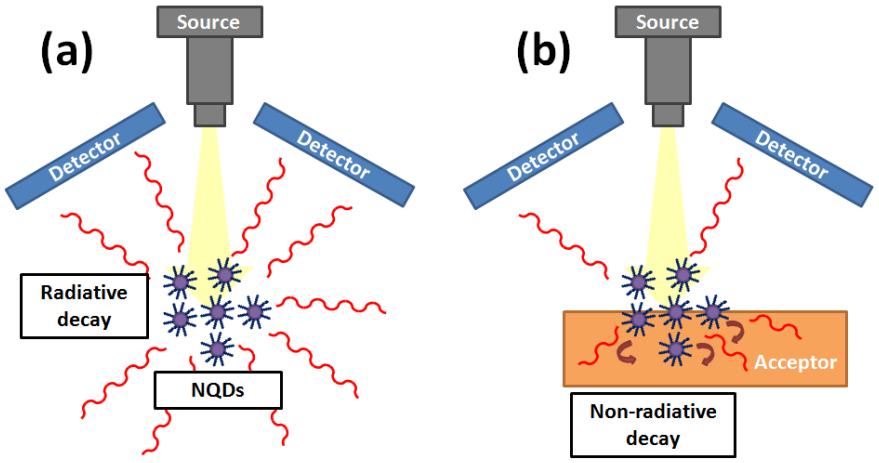

Figure 3.5: *Visual representation of NQDs decay without (a) and with an acceptor (b). Without an acceptor the decay is mostly radiative. With an acceptor, the decay is a combination of radiative decay, RET and NRET.*

Non-radiative energy transfer

NRET involves the direct interaction of oscillating dipolar field generated in the NQDs by photon absorption with the dipolar field of the dipole within the SC substrate induced by image charge [99,100]. This is basically the non-radiative transfer of an electron-hole pair from a donor to an acceptor through dipole-dipole interaction as shown in **Figure 3.6**. The dipole coupling is much shorter range than any radiative coupling, even when only nearfields are involved. This is why NRET is a faster process than regular RET (*i.e.* characterized by faster decay times). The transfer rate is strongly dependent on the distance between the acceptor and the donor, although, in contrast to dot-to-dot dependence of $\sim 1/d^6$, it is $\sim 1/d^3$ for dot-to-substrate, when the substrate is three-dimensional (see **Figure 3.7**). If the NQD is further away from the acceptor, RET dominates because its distance dependence is weaker than $\sim 1/d^3$. This process has first been discovered and explored in the case of molecular systems[101,102]. The case of hybrid organic-inorganic system has been considered more recently, especially by Agranovich *et al.*[103] who suggested the exploitation of NRET based architecture for light emitting devices. As an inverse process than for solar cells, the SC bulk would be used to excite NQDs through NRET which would in turn emit light.

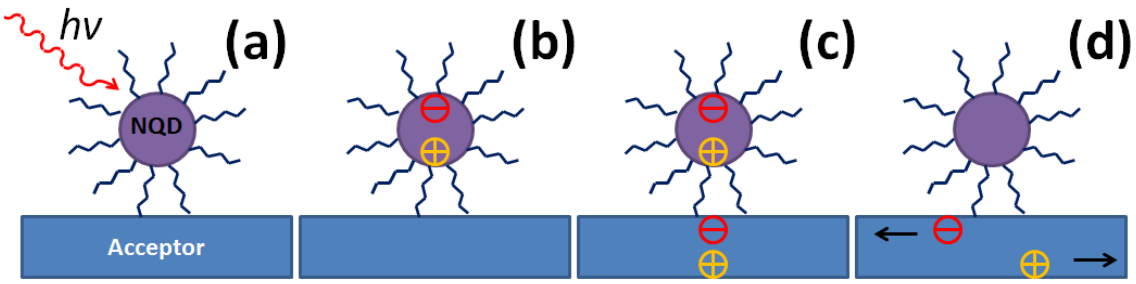

Figure 3.6: *Visualization of NRET. The NQD is excited by a source (a) which leads to the formation of an exciton (b). The electron-hole pair is transferred to the neighboring acceptor because of a dipole-dipole electrostatic interaction (c) where it can be separated and harvested in the form of a current (d).*

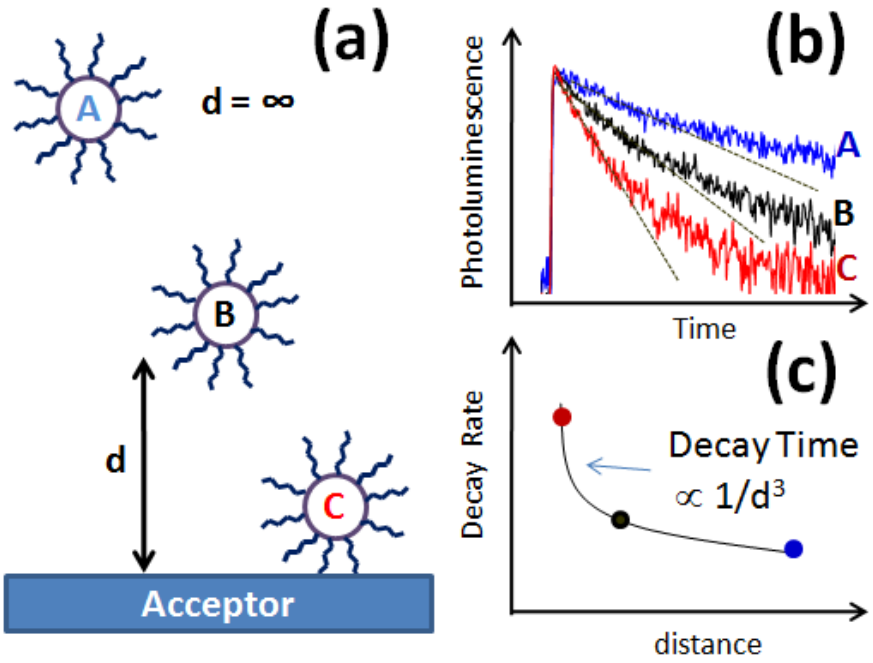

Figure 3.7: *Transfer rate dependence on acceptor/donor distance. Different NQD/acceptor distances have been evaluated (a) and their PL at the NQDs wavelength measured with respect to time (b). Decay time has been extracted and a relation between decay time and distance has been determined (c).*

Inter-dot energy transfer

We have seen that NQDs can transfer their energy non-radiatively to an acceptor such as a SC bulk. But the acceptor can also be another NQD assuming that its absorption wavelength is equal or longer than the one of the donor. This means that the donor is able to provide enough energy for the acceptor to be excited. This phenomenon needs to be taken into account and managed in any system with close NQD packing. Practically, colloidal solutions of NQDs have a range of sizes of nanoparticle, with a size distribution (usually 5-10%). The smallest NQDs in the solution (highest energy) can transfer their energy to larger NQDs in the solution (lower energy), but the opposite is not possible (see **Figure 3.8**a). Because of this, and the fact that NRET between two NQDs is a fast process, there is a difference in the decay time when looking at the PL at slightly different wavelengths. When the distance between NQDs is close enough for inter-dot energy transfer to occur, the highest energy NQDs transfer their energy to lowest energy NQDs, resulting in a shorter decay time of the shortest wavelengths. Lower energy NQDs have a longer decay time because energy cannot be transferred into other NQDs, and they feature an initial rise in the PL count because of the energy received from the other NQDs (this is however difficult to observe). If the decay time remains approximately constant over the band spectral range (low dispersion), the inter-dot energy transfer is negligible, *i.e.* the NQDs are not "talking" to each other (see **Figure 3.8**b and c). In summary, the wavelength dependence of PL decay can be used to estimate the average distance between NQDs in monolayers [104,105].

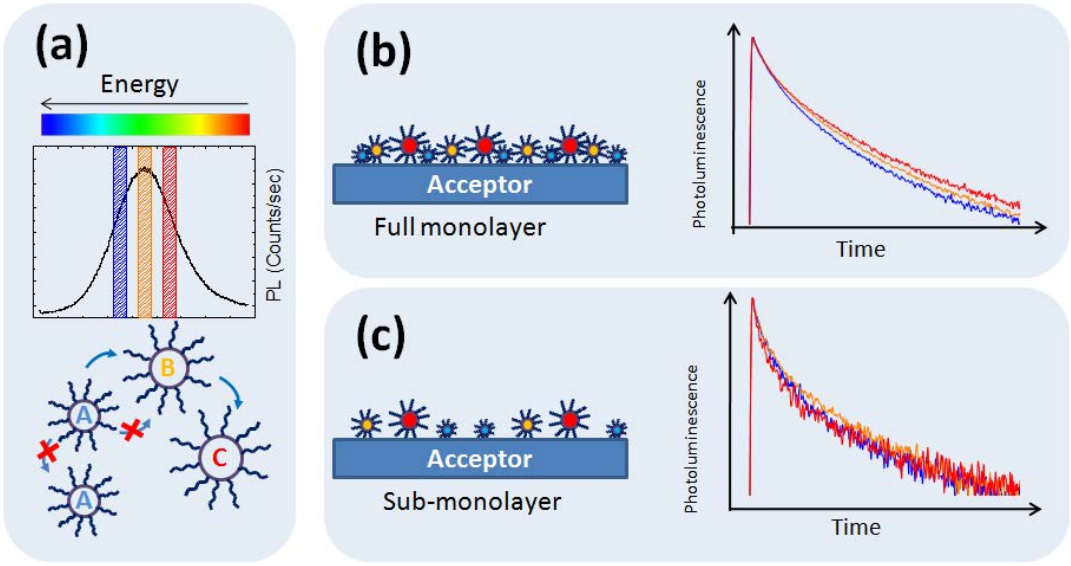

Figure 3.8: *Visual representation of inter-dot energy transfer. (a) In a NQD colloidal solution there is a size distribution, in this case we have NQDs with a wavelength of 555 (A), 565 (B) and 575 (C). NRET can only be done from NQDs of higher energy to lower energy. (b) In the case of a dense layer, NQDs "talk" to each other and they have a different decay time. (c) If the density is lower, NQDs are far enough to not interact with each other.*

This phenomenon can be used to channel the energy transfer from higher to lower energy all the way to the substrate. To do so, one must be able to fabricate multilayers of NQDs where each layer is made of a different type of quantum dots. The top layer should have the highest energy NDQs and the bottom layer the lowest energy NDQs (*i.e.* the gradient is from smallest to biggest diameters). In this way, the energy is transferred from the top layer to the substrate through NRET as pictured in **Figure 3.9**. This promising structure for NQDs solar cells[106], is the topic of **CHAPTER 10**.

Figure 3.9: *Schematic of a multilayer channel of quantum dots. Energy is transferred from the top layer all the way the acceptor substrate.*

3.3 Experimental progress toward NQDs based solar cells

This section summarizes the experimental progress made to graft NDQs and uncover the fundamental energy transfer mechanisms, taking advantage of well controlled GOMs.

3.3.1 Grafting of NQDs on planar surfaces

Following the work of Nguyen *et al.*, a GOM was used to graft monolayers of NQDs on a Si/SiO_2 substrates[21]. As pictured on **Figure 3.10**a, three cases were investigated:

- NQDs directly grafted on an oxide-free silicon substrate ($d=0$).
- NQDs grafted on a 4.7nm thick thermally grown oxide layer (d=4.7nm).
- NQDs grafted on a pure glass sample ($d\sim\infty$).

Pure glass sample is a material with "no acceptor" for the NQDs to transfer their energy into. Silicon, on the other hand, is an acceptor in which electron-hole pairs can be excited. The goal of

this study is to derive experimental evidence of NRET and RET processes from the NQDs/acceptor distance *d*, and to estimate the resulting efficiency. The selected NQDs have an emission wavelength of 565nm, which corresponds to a region where the Si absorption is rather low as seen in **Figure 3.10**b. This work takes advantage of the quality and stability of GOMs on oxide-free silicon, with a density of defects and charge traps at the interface that is low enough to unravel the intrinsic energy transfer mechanisms.

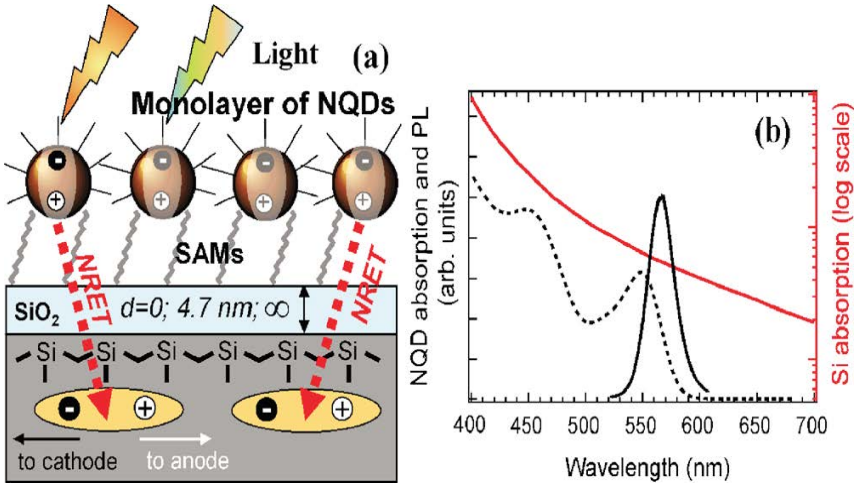

Figure 3.10: *(a) Sketch of the hybrid device, showing schematically the NRET from NQDs to Si. Thickness of SiO_2 is presented for three situations: d=0 (no oxide, NQDs grafted on Si), d=4.7 nm and d=∞ (NQDs are grafted on pure glass) and (b) PL and absorption spectra of NQDs (dashed and solid lines) and absorption spectrum of Si (monotonous curve plotted against right axis). From Nguyen et al. Appl. Phys. Lett. (2011).*

Molecules used to graft these layers are AUTES for SiO_2 surface and SiC_{11} for oxide free surface. AUTES is an amine terminated silane (the silane allows grafting on SiO_2) and SiC_{11} is an amine terminated molecule that has been attached on oxide-free silicon through thermal hydrosilylation. These two molecules were briefly introduced in the **CHAPTER 2**. After attachment of NQDs, atomic force microscopy (AFM) characterization was performed and inter-

dot effect monitored using PL measurements (see **Figure 3.11**). Only a small difference in decay time was measured for dense layer so it was assumed that Inter-dot energy transfer was negligible for both dense monolayers and sub-monolayers.

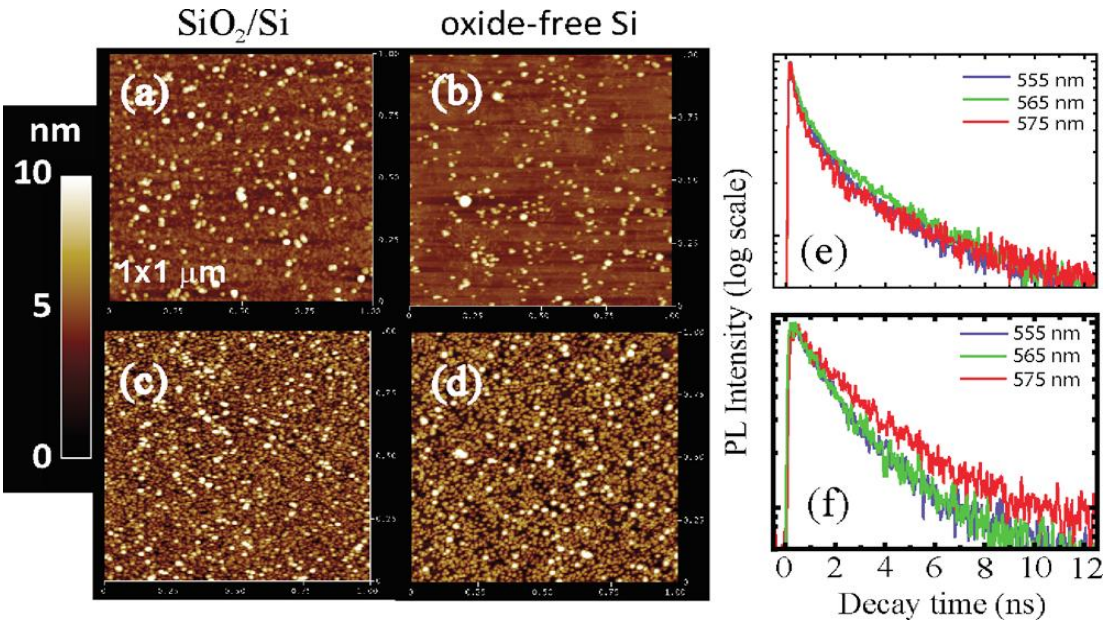

Figure 3.11: *AFM images of sub-monolayers of NQDs grafted on SiO_2 / Si (panel a) and pure Si (panel b), same for dense layers on panels (c) and (d). PL dynamics at various spectral positions within the imhomogeniously broadened spectrum for sublayer (e) and dense layer (f) on SiO_2 / Si. From Nguyen et al. Appl. Phys. Lett. (2011).*

PL lifetimes of each architectures (d=0, 4.7nm or ∞) have been compared in order to assess contribution of NRET and RET in the NQDs decay. There is a clear dependence of the PL dynamics on separation distance, with the fastest relaxation when $d=0$ (pure Si) as expected. The slowest one (pure glass, $d\sim\infty$) is used as a reference to compare the two others, because it is assumed that there is no energy transfer into the substrate in this case, only into space (natural radiative decay). With an acceptor substrate, varying d is supposed to have an influence on the

decay dynamics. This is shown in the inset of **Figure 3.12**b: that displays the calculated variation of purely radiative decay time τ_{rad} (compared to τ_0, in vacuum) as a function of the SiO_2 thickness d. This graph shows that the decay time should be 2.5 faster on silicon that on glass. However, the experimental results presented in **Figure 3.12**a show a ratio of τ_{glass}/τ_{SiO2}=3.8 for d=4.7nm and τ_{glass}/τ_{Si}=7.5 for $d=0$. The difference is explained with the occurrence of NRET. **Figure 3.12**b shows the calculated total width Γ/Γ_{glass} with $\Gamma=\hbar/\tau$ for a dipole situated at a distance z from the SiO_2 layer (z is taking into account the size of the GOM and the NQDs' sizes) as a function of d. different Silicon absorption are being considered from $Im(\varepsilon)=0$ (purely radiative) to $Im(\varepsilon)$=0.4 (NRET is taken more and more into account). Points A and B correspond to experimental results for respectively d=0 and d=4.7nm and can only be fitted in the model if NRET is taken into account. The obtained silicon absorption $Im(\varepsilon)$=0.4 is in good agreement with published data[107]. Using the **Figure 3.12**b inset and the measured τ_{glass}=12.8ns we assume that for d=0, τ_{rad}~12.8/2.5=5.1ns. We also have τ_{Si}=1.7ns and $1/\tau_{Si}=1/\tau_{rad}+1/\tau_{NRET}$, which gives us τ_{NRET}~2.5ns. A quantum efficiency for NRET can then be extracted $E_{NRET}=100*\tau_{Si}/\tau_{NRET}$~65%. It is important to note that a substantial amount of light emitted by the NQDs can be absorbed by the silicon (RET).

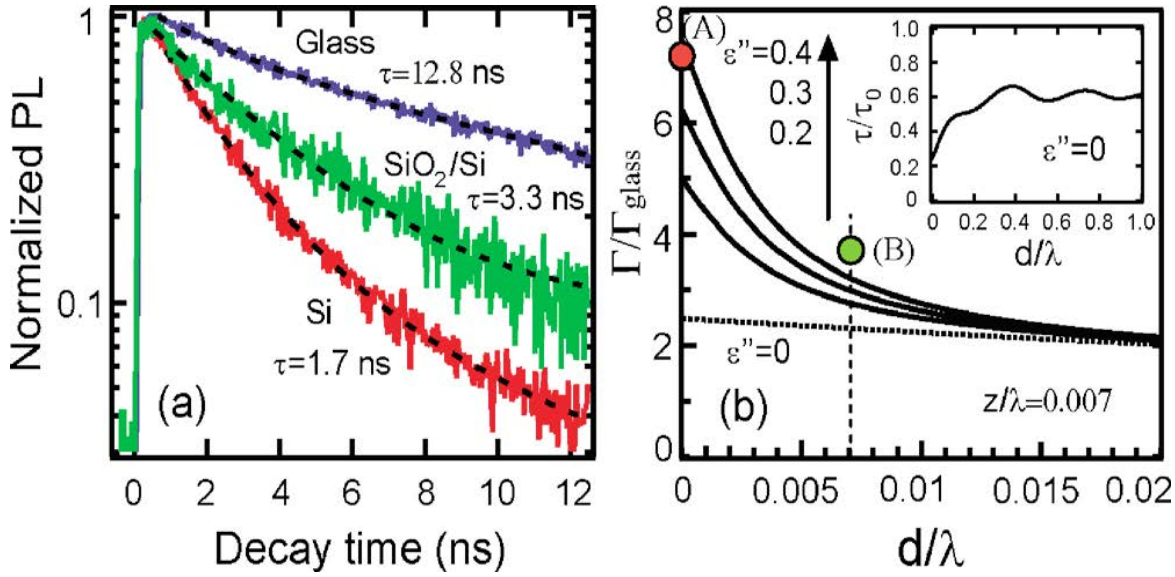

Figure 3.12: *(a) PL dynamics of dense NQD layers deposited on different substrates; (b) calculations of the total width Γ, with NRET included for various values of ε" (dashed line for ε"=0, solid lines are in the increasing order for ε"=0.2; 0.3; 0.4). Solid dots show experimental values for $\Gamma_{Si}/\Gamma_{glass}$ (dot A) and for $\Gamma_{SiO2}/\Gamma_{glass}$ (dot B). Inset: variation in purely radiative lifetimes as a function of the thickness d of the SiO2 layer above Si surface. From Nguyen et al. Appl. Phys. Lett. (2011).*

3.3.2 NQDs with silicon absorption

Another study, for which I performed all the experiments (except PL measurements), was to obtain spectroscopic evidence for energy transfer mechanisms between NQDs and a silicon substrate[108]. This has been done with the grafting of NQDs with a wide range of emission wavelengths going from visible 545nm to NIR 800nm. The experimental protocol was as follows: all the CdSe/ZnS (from 545 to 605nm) and CdSeTe/ZnS (705 and 800nm) NQDs were grafted on three different substrates.

- Directly on bare silicon using SiC_{11} molecule as mentioned earlier

- On a thin SiO_2 layer (10nm) using an AUTES molecule.
- On a thick SiO_2 layer (2µm) that is assumed to behave as a pure glass sample (no acceptor). This last sample as also been functionalized with AUTES and used as a reference.

PL measurements have been performed on each sample after AFM characterization in order to estimate the density of the investigated layers (see **Figure 3.13**). Note that only sub-monolayers are used in this study, with negligible inter-dot energy transfer.

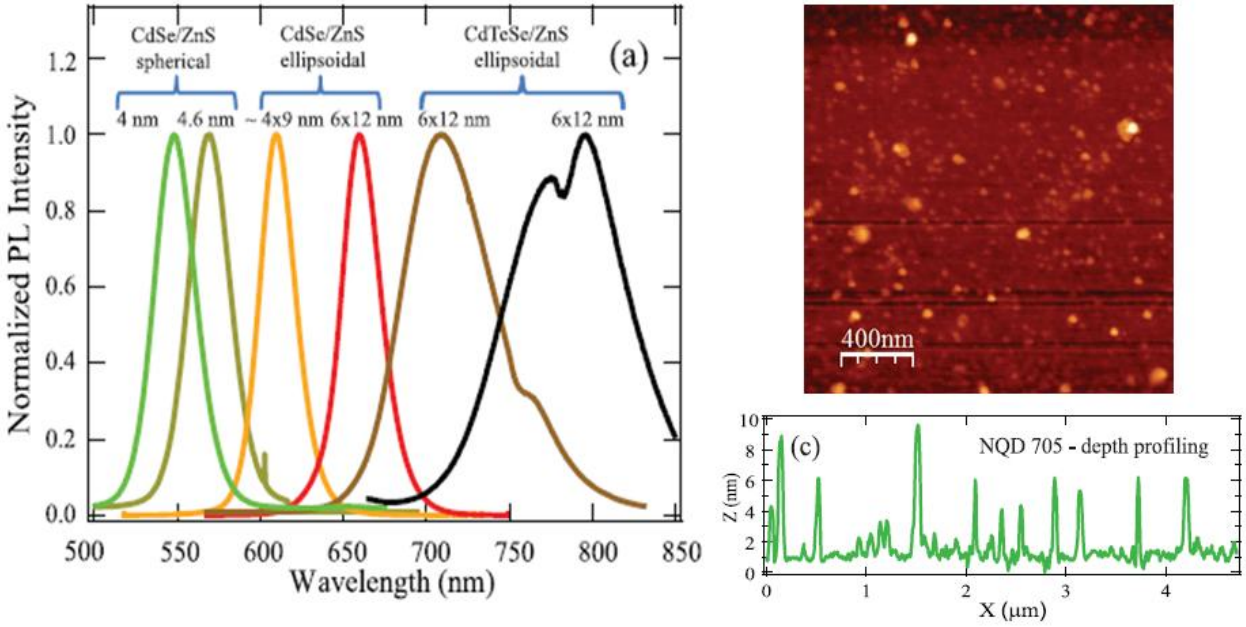

Figure 3.13: *(a) PL emission spectra of different NQDs emitting from 545 to 800 nm as grafted on SiO_2. NQDs on Si exhibit the same PL profile. (b) AFM image of a sample with NQD-705 grafted on the Si surface. (c) AFM depth profiling extracted from (b) that indicates the preferential positioning of ellipsoidal NQDs with their longer axis parallel to the surface. From Nimmo et al. ACS Nano (2013).*

Theoretical model developed by Gartstein *et al.* detailed in this paper predict that NRET is a dominant mechanism at short distance, but once the NQD is situated more than 6nm away from the acceptor, NRET become less important as shown in **Figure 3.14**. Panels (a) and (b) show the different mechanisms involved in the total decay rate (Γ_{Si}) and their contributions as a function of NQDs emission wavelength at different distances (4 and 6nm). Mechanisms mentioned are NRET (Γ_{NRET}), RET to the silicon (Γ_{RET}) and unabsorbed radiative decay (Γ_v). It shows that radiative decay (Γ_v) is suppressed when the distance is very small and that NRET and RET are responsible for most of the decay. If NRET dominates in the middle of the visible range, it is predicted to be on par with RET in the NIR as shown in panel (c). But when the distance is greater than 6nm, the NRET contribution decreases and the energy transfer to silicon is mainly due to RET. The two mechanisms have very different distance dependences. Panel (d) shows the efficiency of energy transfer to the silicon substrate: $E_{TOTAL}=100*(\Gamma_{RET}+\Gamma_{NRET})/\Gamma_{Si}$ which is high when NRET is still dominating but reduced when the NQDs are located further from the surface.

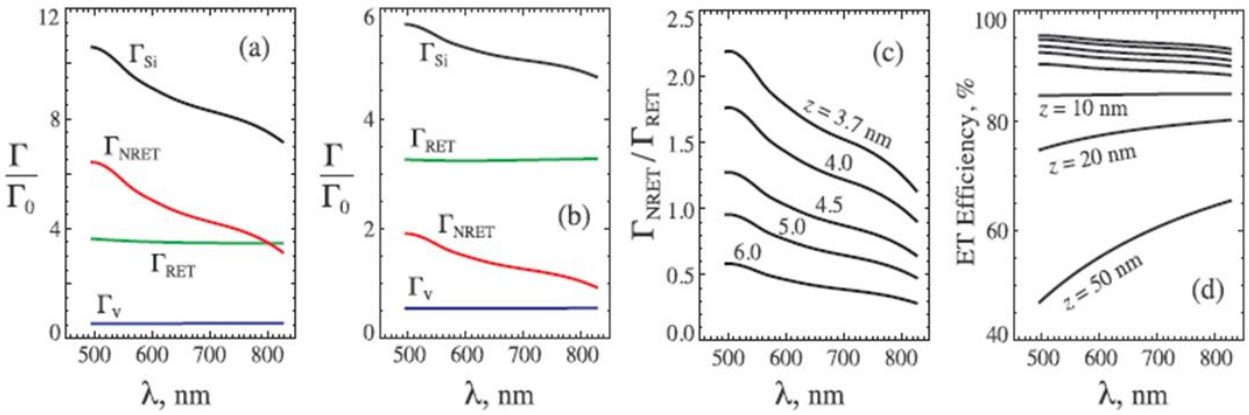

Figure 3.14: *Theoretical results illustrating modification of the decay time as a function of vacuum wavelength for a randomly oriented electric dipole transition in the vicinity of the Si substrate. Panels (a) and (b) display the total decay rate and its contributions from different channels in terms of the vacuum rate: (a) for distance z = 4 nm and (b) z = 6 nm from the substrate. (c) Ratio of contributions from NRET and RET for a series of indicated distances from the substrate. (d) Corresponding total efficiencies of energy transfer into the substrate for distances shown in panel c and, in addition, for larger separations as indicated. From Nimmo et al. ACS Nano (2013).*

When the NQDs are situated at a distance larger than 6nm, NRET becomes a negligible process and transfer from NQDs to silicon is mainly due to NRET. In the following experimental work, NQDs are situated at more than 10nm from the silicon bulk: this means that NRET is negligible. Results are shown in **Figure 3.15** and decay time can be extracted with exponential fits. RET contribution is estimated from sample with a 10nm SiO_2 layer and compared to NRET contribution which is estimated on bare silicon samples (where both RET and NRET occur). Contribution of NRET and RET in the overall energy transfer is then plotted in **Figure 3.16** with $E_{NRET}=100*\Gamma_{NRET}/\Gamma_{Si}$ and $E_{RET}=100*\Gamma_{RET}/\Gamma_{Si}$. We can see that experimental data confirm the fact that NRET is a dominant mechanism in the middle of the visible range, but toward the NIR, RET and NRET contributions become comparable.

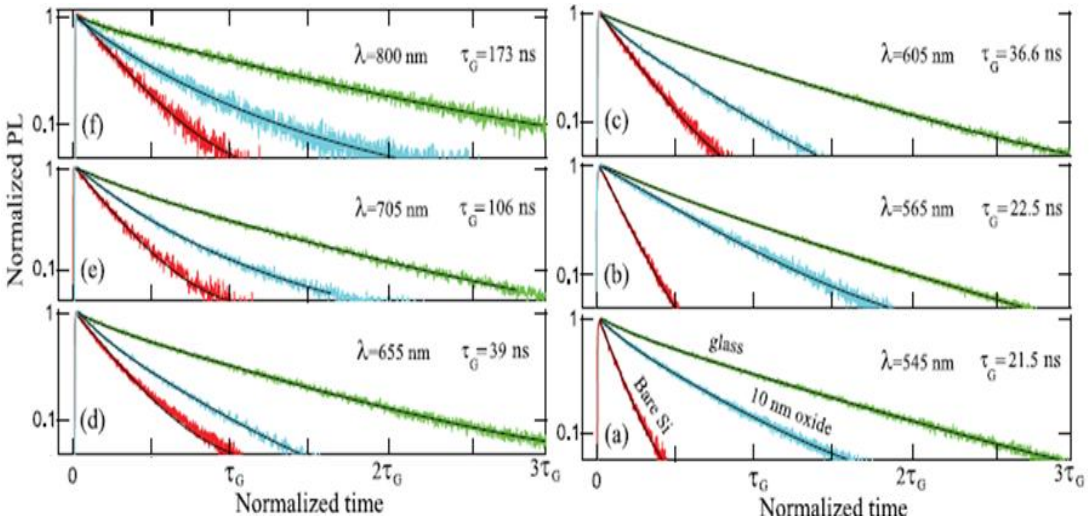

Figure 3.15: *(a-f) PL dynamics for nanocrystals emitting at different wavelengths spanning the range from (a) 545 nm to (f) 800 nm. Shown on the panels are the respective PL measurement wavelengths. The horizontal scale (time) for each panel is normalized to the specific NQD lifetime (from double exponential fits) as measured on glass, τ_G, indicated on the panels, and extends to $t_{max} = 3\tau_G$. Green traces (top) show measured NQD PL decays on reference glass substrates, red traces (bottom) on bulk Si substrates, and light blue traces (middle) on Si substrates with a d = 10 nm thick interfacial SiO_2 spacer. Black curves on the top of the traces show the fits used to extract the lifetime values. A relative slowdown of the PL decays on Si substrates toward longer emission wavelengths is clearly visible. From Nimmo et al. ACS Nano (2013).*

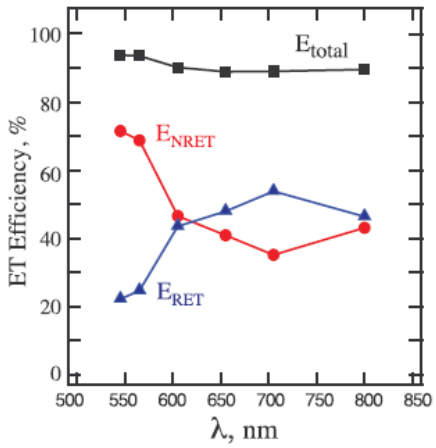

Figure 3.16: *Total ET efficiency E_{total} shown by black squares along with separate contributions E_{NRET} from NRET (red circles) and E_{RET} from RET (blue triangles). The efficiencies were estimated the same way as in* ***part 3.3.1.*** *From Nimmo et al. ACS Nano (2013).*

3.4 Conclusion

In this chapter we gave a brief overview of the status of solar cell technology. We introduced solar cells enhanced with Quantum dots. This is an emerging technology and, before being able to make a working device, we wish to explore and understand mechanisms that are involved. This allows us to identify the goals that need to be achieved in order to optimize the proposed structures. This chapter summarized the basic mechanisms and described recent experimental support of the theoretical work of Gartstein *et al.*[109] These tools are useful to understand the different optimization ways studied in this thesis: **CHAPTER 8** focuses on the optimization of PL generation through silicon patterning and **CHAPTER 9** provides experimental evidence for optimization through multilayer grafting. **CHAPTER 10** uses the structure developed in **CHAPTER 9** to study energy transfer in gradient multilayer nanofilms.

CHAPTER 4

EXPERIMENTAL TECHNIQUES

This chapter provides an overview of the experimental techniques and procedures that have been used in this work. I have performed all measurements with these characterization techniques unless stated otherwise.

4.1 Fourier Transform Infrared Spectroscopy (FTIR)

Fourier transform infrared spectroscopy is a characterization tool that can identify chemical bonding in materials or at surfaces by direct excitation of the normal modes with an infrared light. All the spectra in this thesis were taken in a transmission mode, which means that the exciting infrared beam goes through the whole sample at a specific incidence angle. In order to analyze the bonding present on the surface of the sample as unambiguously as possible, both sides are polished and treated in the same way. FTIR was primarily used to investigate the presence and the quality of the GOM on a surface by cleaning and functionalizing both sides at the same time and under the same conditions (*i.e.* in the same solutions). The basic apparatus of a FTIR is shown in **Figure 4.1** It consists of an interferometer (Michelson) that allows the detection of all the wavelengths as a function of the moving mirror displacement (*i.e.* path difference in the two beams) as an interferogram. This interferogram is then digitized, apodized, and Fourier transformed to extract the spectrum of the transmitted broadband radiation. Each bond on the surface has a series of resonant frequencies at their respective normal modes and the transmitted light is absorbed accordingly. These frequencies are characteristic of the type of bond. For instance, for di-hydrides, there are bending (scissoring, rocking, twisting and wagging) or stretching (asymmetric or symmetric) vibrations.

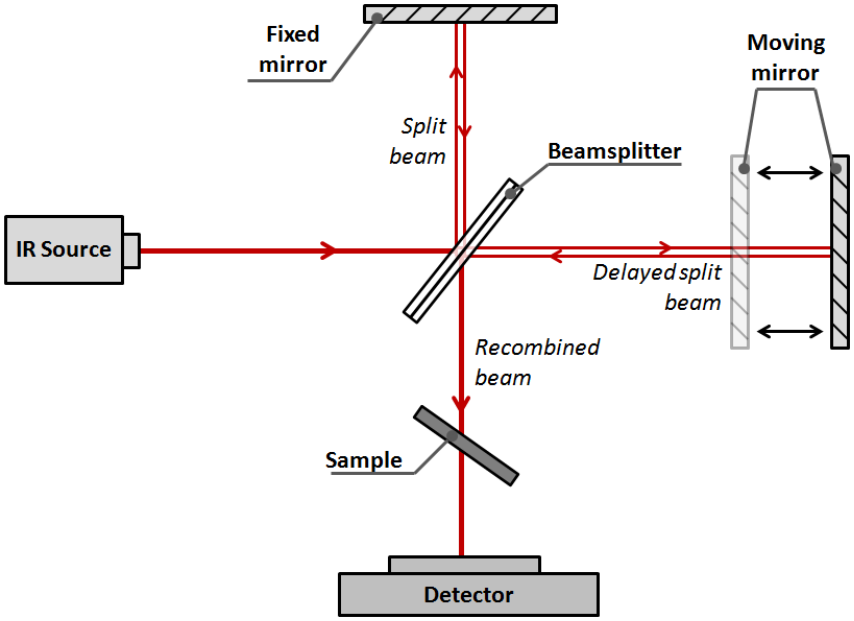

Figure 4.1: *Diagram showing the IR beam path through the Michelson interferometer.*

In contrast to most techniques, infrared absorption spectra require a reference spectrum. Sometimes such a reference is the transmission in the absence of sample. However, in most cases, the reference is the same sample without the specific species under study. For instance, to study the surface of oxide-free silicon, the initial reference is the previously oxidized surface. Similarly, to investigate a GOM obtained by modifying a H-terminated Si surface, the reference is the H-terminated surface. The absorbance is defined as follows[110]:

$$A = -log_{10}T \qquad \textit{Eq 4.1}$$

where T is the transmittance and defined as

$$T = \frac{I_{measured}}{I_O} \qquad \textit{Eq 4.2}$$

This is the ratio of the intensity of the beam transmitted through the sample ($I_{measured}$) to the intensity of the beam without the sample (I_0). So when we reference a signal 2 with a signal 1, we obtain:

$$\Delta A = log_{10} T_{measured,1} - log_{10} T_{measured,2} \qquad \textit{Eq 4.3}$$

This gives us

$$\Delta A = log_{10} \frac{I_{measured,1}}{I_{measured,2}} \qquad \textit{Eq 4.4}$$

From this technique it is possible to have a qualitative idea of how the surface changed between the two spectra. A negative peak in a spectrum indicates the loss of a specific bond on the surface, from either bond breaking or reaction. Positive peaks are associated with the formation of a bond. It is then possible to deduce the chemical nature of compounds on the surface at each step of an investigated process. Specifically it is possible to detect the apparition of oxidation on a silicon substrate (TO and LO mode at 1080 and 1240 cm^{-1}), which is an important measure of quality of the GOM grafting process. *In situ* real-time measurements can also reveal the mechanism of some reactions. FTIR also have a quantitative aspect: it is possible to measure the integrated area of absorption bands and relate it to the concentration (or coverage) of a species at the surface. Such a correlation assumes that the dynamic dipole moment of the species is not changed and that the overall screening of the mode remains constant, which is a fair approximation in most cases. For instance, it is possible to check how many Si-H bonds remain on the surface after a functionalization. The ratio of the two peaks (before and after functionalization) gives a good estimation of the coverage of the molecular layer. All data in this thesis have been acquired using a Nicolet 6700 FTIR spectrometer with a DTGS detector located

inside a Mbraun Glove box with a dry N_2 environment for the sample to remain stable throughout the whole measurement. Measurements, as mentioned before, were taken in transmission mode with an incidence angle of 74°. Samples investigated have to be double side polished so that the light is not scattered and to optimize the signal-to-noise ratio.

4.2 X-ray Photoelectron Spectroscopy (XPS)

XPS is a characterization tool that relies on the interaction of X-rays with core electrons of elements in materials. The electrons excited/generated by the X-rays (called photoelectrons) are then collected. Their binding energy is then deduced from their kinetic energy (see **Figure 4.2**). From the binding energy, one can extract information about the nature of the investigated elements. Because of the low escape depth of photoelectrons (≤10nm), this technique is very surface sensitive. It is a good complement for a FTIR study because it is sensitive to elements that are difficult to detect with FTIR, such as heavy atoms (*e.g.* metals) since their vibrations are below 400 cm^{-1} (lower limit of the FTIR spectral range with standard KBr beam splitters).

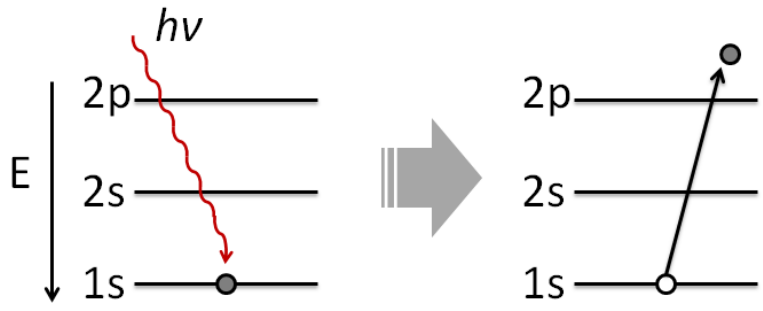

Figure 4.2: *Schematic of the photoemission process occurring in XPS measurements.*

The X-ray source excites the core electrons with an energy *hv* which is enough for them to escape the atom. Their kinetic energy E_{KE} is then measured with a detector and then the binding energy E_B can be deduced using the following equation:

$$E_{KE} = h\nu - E_B - \varphi \qquad \textit{Eq 4.5}$$

where φ is the work function of the material. The detection is made using a hemisphere detector that filters incoming electron for a specific kinetic energy and counts them. The electrons are accelerated with an electric field into a curved trajectory and only the one with the selected kinetic energy reach the detector. The others hit the walls (bottom or the top) of the hemisphere if their energy is too high or too low, respectively. Each kinetic energy is then investigated and a spectrum can then be obtained when plotting the count of electron for each pass energy. Kinetic energy can also be altered if there is an accumulation of charge at the surface of the sample (*i.e.* an additional field due to charging). In the case of surface charging (typically positive), an electron beam is used to neutralize the surface charges when dealing for instance with non-conducting samples. The binding energy can also vary depending on the chemical environment of the investigated elements, which makes it possible to extract chemical bonding information from subtle but detectable core level shifts. For instance, deconvolution of the carbon 1s core level peak, it is possible to distinguish carbon atoms in a C-C and C-O bonding configurations, which is important when identification of a specific molecule is needed. Another useful example is the detection of the presence of native oxide on a surface: the Si2p peak corresponding to the amorphous Si-O liaisons is detected at 103eV, which is easily distinguishable from the regular Si2p peak for elemental silicon (99eV). XPS is also a quantitative method: the peaks ratio can be used to estimate the amount of each element on the surface. This is useful to determine the ratio

of bonding present in one molecule (*e.g.* how many C-C bonds are present, compared to C-O bonds), which provide information for a molecule or material. An estimation of a GOM coverage can be done using this technique. In this work, XPS analysis was performed with a Quantum 2000 Scanning ESCA Microprobe (Physical Electronics, USA) spectrometer equipped with a concentric hemispherical analyzer under ultrahigh vacuum conditions (10^{-10} mbar) and a monochromatic Al Kα X-ray source (1.5keV, filament current 20mA). Spectra were recorded at a 45° takeoff angle with respect to the surface. A sample area of 100μm × 100μm was analyzed with a pass energy of 46.95eV for survey and 11.75eV for detailed elemental scans.

4.3 Scanning Tunneling Microscopy (STM)

STM-VT from Omicron, acquired in 2008, equipped with cooling (40K) and heating (up to 500°C) capabilities. The instrument is shared between 5 regular users. Our group had access to the instrument 2 months per year.

4.3.1 Imaging

STM has been used in the single electron transport project as a way to investigate electronic properties of our system. But at first it is essential as it provides a topographic image of our sample. It relies on the interaction of an atomic sharp tip with a conducting sample. The

tip scans a reduced portion of the sample, typically 50x50nm², and probes the surface by applying a bias voltage and measuring the resulting tunneling current. The distance between the tip and the sample is roughly 5-10 Å, but this distance remains unknown because it depends on the current setpoint, on the voltage and on the nature of the investigated material. Actually the detected current is given by:

$$I_{tunnel} = A.eV_{bias}e^{-2\sqrt{\frac{2mW}{\hbar}}.d} = A.eV_{bias}e^{-1,025\sqrt{W}.d} \qquad \textit{Eq 4.6}$$

Where W is the work function (energy barrier), e is the electron charge, m is the electron mass, h is the Planck's constant, V_{bias} is the applied voltage, d is the tip-sample distance and A is a constant (unknown). From this formula, it can be deduced that the tunneling current reduces by a factor 10 for every 0.1 nm increase in d if we have W = 4 eV (metal). This means that over a typical atomic diameter of *e.g.* 0.3 nm, the tunneling current changes by a factor 1000! This is what makes the STM so sensitive. The tunneling current depends so strongly on the distance that it is dominated by the contribution flowing between the last atom of the tip and the nearest atom in the sample! A raster scan of the surface is done with a feedback system to keep the current constant (*i.e.* also a constant distance between the tip and the sample if the sample as a homogeneous conductivity). The obtained image is not a topographic image per se: more accurately it is a convolution of topography and electronic density image. Also, it only works if the scanned material is conductive. A change in conductivity on the surface can induce change in observed topography, even if there is no actual topographic change. That's why STM is not the best tool to accurately measure the size of AuNP on a GOM, from the equation given above (**Eq 4.6**) we can estimate that the accuracy of the topography obtained with STM is about 0.5 nm.

Images depend on the voltage bias: when a positive bias is applied on the tip (relative to the grounded sample) electrons tunnel from the filled states of the sample to the empty states of the tip: the image will depend on the superposition of filled states on the surface and empty state on the tip. If a negative bias is applied, electron from filled states of the tip tunnel to the empty states of the sample. STM measurements were taken using an Omicron VT-STM under UHV conditions. The chamber pressure was typically on the order of 10^{-10} - 10^{-11} mbar. We usually use a voltage bias of V_{STM} = 1.5 V and a current setpoint (current measured and set constant through adjusting the tip position with a feedback system) $I_{setpoint}$ = 40pA.

4.3.2 Fabrication of STM tip

STM tips were prepared electrochemically using the etching reaction of potassium hydroxide on a tungsten wire. With the application of a voltage, the reaction is as follows[111]:

-Cathode *(metal ring immersed on KOH):* $6\,H_2O + 6e^- \rightarrow 3H_2\,(g) + 6OH^-$ *Eq 4.7*

-Anode *(tungsten wire):* $W(s) + 8\,OH^- \rightarrow WO_4^{2-} + 4H_2O + 6e^-$ *Eq 4.8*

The tungsten wire is etched by the solution and more efficiency close to the solution surface. The weight of the immersed part of the tip eventually tears off the etched metallic wires and this maximizes the chance to obtain a tip with only a couple of atoms at its apex. At this stage, the current drops and the voltage is automatically cut. The extremity of the wire is then gently rinsed in alcohol and water. The obtain tungsten tip is extremely sharp and can then be entered in the UHV chamber where it is going to be “degassed” by heating it up for half an hour. The tip is

then “flashed” which effectively remove the tungsten oxide. This last step increases the quality of the measurement.

4.3.3 Scanning Tunneling Spectroscopy (STS)

A special operation mode provided by an STM is the STS: it is used in order to obtain electrical measurement on a designated part of a sample. In many single electron experiments, a STM tip is used as one of the electrode of a DBTJ[78,112,113,114,115] which has the advantage of allowing the characterization of a relatively large number of different devices. STS works as follows: the user set a position on a previously obtained image and the tip is positioning on top of the desired location. Once stabilized, the feedback loop is opened (no more control of tip-sample distance) and a voltage sweep is done: the resulting current is acquired. The time taken by one sweep is about the raster time (typically 5ms) x the number of points (typically 250) and it is possible to average over series of several measurements. Usually averaging is not carried out over more than 20 sweeps. Actually STS conditions can vary during this acquisition due to a mechanical drift, or a change of temperature, a contamination or reaction on the surface (especially with the GOM). A thermal drift can be very important (10^{th} of nanometer per seconds) when we decrease the temperature to 40K, this is why we need to wait 2-3h for it to reach lower and more stable values (<1nm/s) which can be roughly compensated by the STM. Using this technique, it is possible to observe Coulomb staircase as described in **CHAPTER 2** by looking at the I/V curve. Another factor that must be considered is the noise of the system. The signal to noise ratio must be high enough to be able to detect single electron transport (*i.e.*

the current noise must be lower than 2-3pA). In our case we usually perform STS at very low temperature (~30K). The sample can be cooled down with a cold finger in contact with liquid helium. The liquid helium is pumped and the system is given time to stabilize (several hours) to avoid thermal drift of piezoresistors.

4.3.4 Other modifications

In order to do experimental prototypes of SET using an STM, it is critical to add another contact on the system. We have modified the STM (see **Figure 4.3**) to be able to apply a gate voltage on devices with an external DC voltage box. The added system didn't introduce any additional noise and the atomic resolution usually obtained on a flashed Si(111) sample with 7x7 reconstruction was preserved.

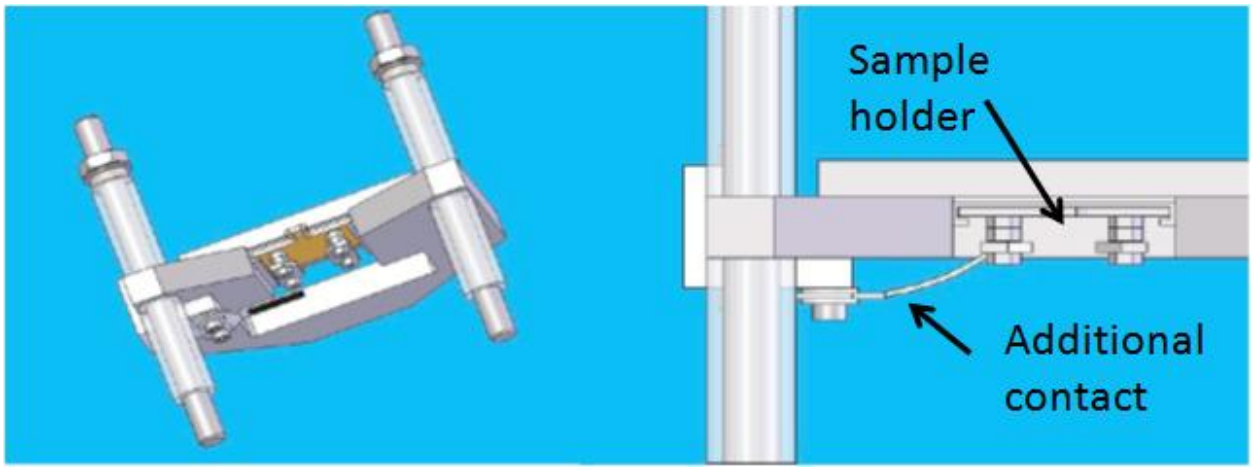

Figure 4.3: *3D sketch of the modified STM heads with the sample holder and the additional contact. The additional contact is connected to a DC voltage box that can deliver up to 12V.*

4.4 Atomic Force Microscopy (AFM)

AFM is a technique that we have used in order to monitor coverage and density of nanoparticles grafted on a GOM. Contrary to our STM, the AFM used allows measurement in air which makes it an easier way to characterize the topology of our sample. Apart from the density, AFM images provide a good estimation of the size distribution of the grafted nanoparticles when looking at the Z axis. This is assuming that the density is low enough for the tip to effectively go all the way to the substrate in between two particles. Measurements are taken in tapping mode: the tip is oscillating at a frequency close to its resonance frequency. The frequency of the oscillations will vary depending on the topology of the sample because of the interaction between the tip and the surface. A reflected laser on the cantilever (see **Figure 4.4**) is going to allow the detection of this change in frequency with the help of a four quadrant photodetector. With a feedback system, the height of the tip is constantly readjusted so that the oscillation and the tip height remain constant. AFM provide an exceptionally good resolution in the Z axis (sub nanometer), and can then give a very good estimation of features' height. That's why it is an interesting tool for the determination of AuNPs or NQDs size. However, its lateral resolution is limited by the tip radius which is usually in the order of magnitude of 10nm. Features usually appear larger than they actually are. A lateral resolution of tens of nanometers is usually achieved. Another advantage of AFM compared to STM for a quick characterization is the fact that it does not require the substrate to be conductive. In our case, this means that, if we wish to characterize size distribution and coverage, we do not need to go through the long process of making an oxide free GOM. A simple organic layer on native oxide is enough for a proper

characterization. AFM gives also a good idea of nanoparticles stability on the surface: if the AuNP or NQDs are not strongly attached, AFM tip is going to drag the nanoparticles on the surface. AFM was performed with a Digital Instrument DI-3000 or a Multimode-8 instrument from Veeco and images were processed with the software WSxM. Another type of measurement have also been done, but not by me, in Salmeron's *et al.* laboratory in Berkeley. They have access to a conducting AFM that allows voltage sweep with the tip directly in contact of the GOM in UHV. This can be used to extract the HOMO-LUMO of the GOM.

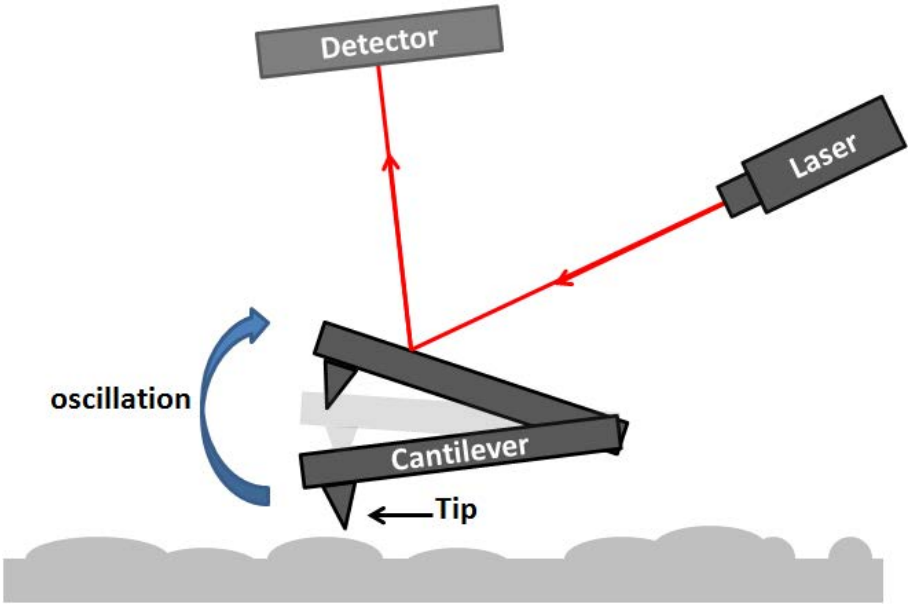

Figure 4.4: *Simplified schematic of an AFM on tapping mode.*

4.5 Scanning Electron Microscopy (SEM)

SEM was used for the project on the NQDs-based solar cells. For instance, it was used to examine structures such as nanopillars developed to enhance absorption in Si solar cells[116,117,118].

Other microscopy methods like AFM or STM are not as appropriate to examine such patterned surfaces when features heights are in the order of several micrometers. SEM provides an efficient and easy way to look at patterns and therefore feedback for our fabrication method.

SEM is based in part on the excitation of secondary electrons by a primary high-energy electron beam which is focused on the surface. The beam is then rasterized on a wanted area and information is extracted from the byproducts of the reaction of the electrons on the surface. Several byproducts are possible and are pictured in **Figure 4.5**.

- **Secondary electrons** are electrons that are ejected from the atoms at the surface (usually from the conduction band) after a collision with incident electrons. They have a low energy (~50eV) so they have a low escape depth and are harvested with the help of an electric field. They provide good information about the topology of the sample with a good lateral resolution (up to several nanometers).
- **Backscattered electrons** are incident electron that have been scattered in a direction close to their incident one after a quasi-elastic interaction with the atom nucleus. In that case they lose a very small amount of energy so they have a high kinetic energy. This is why they have a longer penetration depth and do not provide a good resolution (up to tens of micrometers). However they depend on the nature of the nucleus so they can provide qualitative information about the nature of the sample.
- **Auger electrons** can also be formed after the removal of a core electron in an atom. They are a possible byproduct of the relaxation of the atom (transfer of an electron from an outer shell). These are dependent on the nature of the atom and can be harvested to identify

compounds on the sample. They have low energy, so they essentially provide information about compounds situated at or near the surface.

- **Emission of X-rays** is another byproduct of relaxation of an ionized atom. It can be detected to have information about the nature of the bulk of the sample. Additional equipment is required for this technique (Energy Dispersive X-ray analysis or EDAX).

In our case, we only used the SEM for the topological information it can provide. Therefore only the technique based on the detection of secondary electrons is considered in this thesis. One of the advantage of SEM is also the fact that sample can be tilted so the sample can be seen from different angle. For silicon patterning studies, we often cut samples in half so that samples can be seen from the side. This is referred to as “cross section view” or “side-view”. SEM has a good enough resolution to allow us to estimate coverage of NQDs after their attachments on plane and patterned silicon surfaces. Oxide surfaces were not looked at with SEM because the sample needs to be conductive in order to avoid charging effect. A usual way to look at insulating sample is to evaporate a thin gold layer on top: but that will not work with very small features. A Zeiss Supra40 instrument located in a cleanroom was usually used and operated at 20-30kV. In this thesis, it is sometimes specified that a low resolution JEOL Tabletop SEM is used instead: this equipment has a low working voltage (up to 5kV) and a low resolution (200nm).

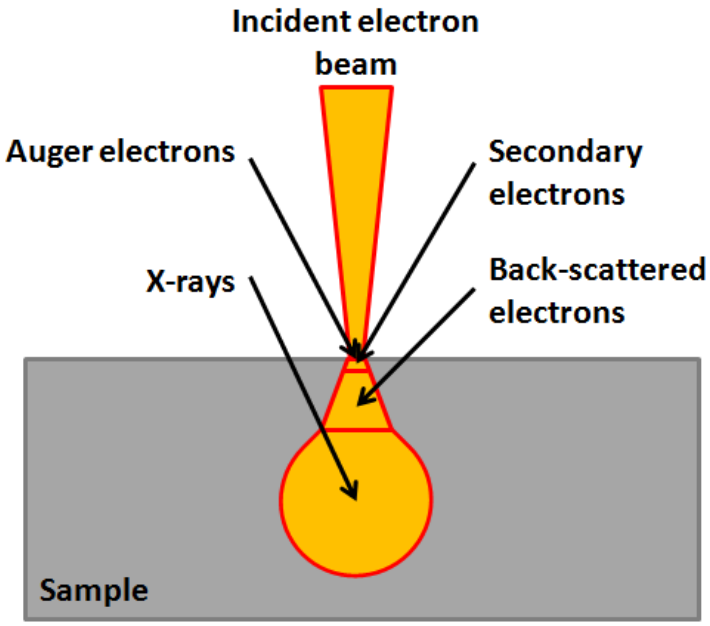

Figure 4.5: *Possible byproduct of the interaction of the electron beam with the sample.*

4.6 Photoluminescence spectroscopy (PL)

PL measurements have been performed in Anton Malko's laboratory by his students, not by me. PL is used for the NQDs-based solar cells project in order to monitor NQDs deposition and emission. NQDs are excited with a monochromatic source and their luminescence detected at longer wavelengths. In principle, the PL intensity scales with the NQDs coverage, although the absolute PL intensity is very sensitive on alignment and is also affected by other decay processes, hence the error bars substantial. When processes other than radiative decay occur, it is best to measure the normalized PL time dependence in order to extract the decay time at a specific wavelength. The decay time is extracted using exponential fits of the measured time resolved intensities. It provides information on the nature of the decay mechanism. Indeed, decay

time can vary from a few femtoseconds for emission involving free carrier plasma in inorganic semiconductors[119] up to milliseconds for phosphorescent processes (sometimes even more). A typical, microscope-based μPL system designed for high collection efficiency is used. The samples are mounted on the microscope table and excited by 50 ps laser pulses at 405 nm with a 2.5 MHz repetition rate using a Picoquant diode laser (focused through a numerical aperture = 0.6 objective). NQD emission is collected by a sensitive photon detector (MicroPhoton Devices) after passing through a spectrometer for wavelength-dependent PL lifetime analysis. μPL decays were collected via time-correlated single photon counting performed on board of Pico300E photon counting hardware (PicoQuant GmbH). The overall time resolution was less than 50ps.

4.7 Transmission Electron Microscopy (TEM)

TEM measurements were performed in the "Laboratoire de Reactivite de Surfaces" in Paris by people other than me. TEM is a technique in which an electron beam is focused on a very thin sample. It differs from SEM on the fact that the detected electron are not "reflected" on the surface but transmitted through it and detected behind it. Therefore the investigated sample needs to be extremely thin (~50nm). This is a very powerful technique that can potentially provide sub-atomic resolution (because of the small de Broglie wavelength of electrons) but usually requires a long and demanding sample preparation. In our case we used TEM to study the crystallinity of AuNPs. Our use of it is therefore much simpler: we drop cast a solution of AuNPs on a TEM grid and place the grid in the instrument. With proper orientation of the NQDs with respect to the electron beam, it is possible to determine whether a nanoparticle is

monocrystalline, polycrystalline or amorphous. However, since control of the orientation of the deposited AuNP is difficult, it is impossible to be sure if an AuNP appear amorphous because of its non-crystalline nature or because of the fact that its crystallographic plan are not aligned with the electron beam. TEM images are collected with a JEOL 2010 microscope operating at 200 kV equipped with a charge-coupled device camera. Particle size measurements are performed by "particle ImageJ" (Image processing and analysis in Java, Open source). The limit of size detection is about 1 nm.

4.8 Other techniques

Very basic spectroscopic ellipsometry measurements have been performed in order to estimate the thickness of organic layers, using a "De Cauchy" layer modeling with a HORIBA Jobin Yvon ellipsometer (iHR320). UV-Absorption measurements were also performed, but not by me, in order to quantitatively monitor the amount of NQDs grafted on a surface. Also, an extensive amount of deposition and etching techniques in a cleanroom environment have been used in this thesis for silicon patterning which are more detailed in **CHAPTER 8**.

CHAPTER 5

GOLD NANOPARTICLES ON OXIDE-FREE SILICON−MOLECULE INTERFACE FOR SINGLE ELECTRON TRANSPORT

This chapter is a direct reproduction of a study that has been published in the Langmuir journal in 2013[16]:

Caillard, Louis, *Oliver Seitz, Philip M. Campbell, Rachel P. Doherty, Anne-Félicie Lamic-Humblot, Emmanuelle Lacaze, Yves J. Chabal, and Olivier Pluchery. "Gold Nanoparticles on Oxide-Free Silicon–Molecule Interface for Single Electron Transport." Langmuir 29, no. 16 (April 23, 2013): 5066–73.*

This work focuses essentially on the fabrication of the architecture introduced in the general introduction. Preliminary STS results serve as proof of concept of the observation of single electron transport using our system.

5.1 Introduction

This chapter shows that a Grafted Organic Monolayer on Si(111) as described in **CHAPTER 2**, is not only a extremely well controlled layer but can also serve as a functional layer. A functional organic layer should also be able to carry out electrical functions such as driving charges with a high mobility, storing electrons in a memory device[120], or controlling their flow in a transistor[121,122]. However, this requires a high degree of morphologic organization close to what is achieved in a silicon crystal. If not, the memory will leak and exhibit a poor retention time, the electrons will be trapped[123], or the Fermi level will be pinned in a noncontrollable way[84]. Therefore, it is crucial to succeed in assembling molecules on silicon with atomic precision. Here we start with the most straightforward functionality and we aim at achieving an ultrathin insulating layer, with homogeneous quality. We describe a chemical route for building

two different organic monolayers grafted on silicon. In order to probe the electrical quality of the organic layer, gold nanoparticles (AuNP) from colloidal solutions are covalently attached on top of the monolayer. The whole process is achieved by wet chemistry. It preserves an oxide-free silicon substrate that remains stable under ambient conditions. This architecture serves as a first tunnel junction (silicon/organic layer/AuNP junction) and is completed by a second tunnel junction established with an STM tip (AuNP/vacuum/tip junction). Such a double barrier tunnel junction (DBTJ) exhibits an electric behavior characterized by Coulomb blockade which is detectable at 40 K in UHV. This work focuses on the fabrication and initial electrical characterization of this double barrier tunnel junction. Coulomb blockade is a typical single charge phenomenon where electrons can be controlled one by one by adjusting the potential applied to the DBTJ. It is based on the fact that the system is mostly capacitive and the value of the capacitance is roughly proportional to the nanoparticle diameter. The electrostatic energy needed to add one more electron to the nanoparticle (called the island) is expressed as $e^2/2C$, where e is the unit charge and C the capacitance. For very small nanoparticles this energy becomes larger than kT and the electrostatic energy overcomes the thermal noise, so that the electron flux can be controlled by an external applied potential. At room temperature, this condition is fulfilled for nanoparticles smaller than 5 nm. In order to observe single electron phenomena, the targeted device is the DBTJ. Given that the tunnel current depends exponentially on the barrier thickness, an accurate control of the samples geometry is necessary. Moreover, the typical thickness of such junctions lies between 0.8 and 2 nm, which requires that the tunnel barrier thickness must be controlled at the atomic level. Such a control can best be achieved with self-assembled monolayers. Highly ordered monolayers on silicon have been explored for

decades, particularly after the discovery of a process to form atomically flat hydrogen-terminated silicon surfaces in 1989[5]. As explained previously in **CHAPTER 1** this H−Si(111)-(1 × 1) surface can be modified following many chemical routes[124] for replacing the terminal hydrogen by other molecules: thermal activation[6,7,8,125], UV activation[8,10,9,126], electrochemical activation[11,12], and chlorination[8,13,127]. More recently, some of these groups started investigating the electrical quality of these organic layers in order to integrate them within future functional architectures[128,129]. The monolayer is probed either globally, with the mercury drop method[14,130], with electrochemistry[126], by depositing an oxide layer[51] or a metallic electrode, or sometimes local probes such as Kelvin Probe Force Microscopy (KPFM) or conductive AFM are used[9]. From these studies, it appears that the Si−organics interface can be made with a notably low amount of surface defects, in line with expectations based on the H−Si(111) interface[14,17,51]. Interestingly silicon surfaces functionalized with organics are usually much more stable against oxidation[123] (*e.g.*, up to 1 month) than H − Si(111) surfaces, which is encouraging for implementing a robust functional molecular passivation of silicon surfaces.

5.2 Experimental method

5.2.1 Preparation of Highly Ordered Monolayers on Si(111).

Samples of 5 × 12 mm^2 were cut from n-doped silicon (111) wafers with different level of resistivity. Resistivity of either 0.03 Ω·cm (~1.10^{18} cm^{-3}), 7 Ω·cm (~6.10^{14} cm^{-3}) have been tested. Float zone (FZ) grown samples were chosen in order to minimize the amount of oxygen

and allow an accurate monitoring of potential surface oxidation with FTIR[7,131,127]. It should be noted that the chemistry described here works equally well with Czochralski grown wafers but depends on the level of doping[9]. Functional organic monolayers were prepared within four steps (see **Figure 5.1**). In step 1, samples were initially cleaned in a piranha solution at 80 °C (3:1 H_2SO_4 98%: H_2O_2 30%) and copiously rinsed with ultrapure water (18 MΩ·cm, Millipore). Atomically flat, hydrogen-terminated Si(111)-(1 × 1) surfaces were prepared by oxide removal in a concentrated HF solution for 30 sec, followed by a 150 sec immersion in 40% NH_4F solution and thorough rinsing in deionized water[9,5,132]. Caution is recommended because the piranha solution reacts strongly with organics, and the HF solution is extremely harmful. Both solutions should be handled with due protection: goggles and suitable gloves. Starting from a set of two different hydrogen-terminated Si(111)-(1 × 1) surfaces, step 2 consists of covalently attaching the organic layer by direct thermal hydrosilylation with either a long alkyl chain of 11 carbon atoms (SiC_{11} samples) or a shorter chain with 7 carbon atoms (SiC_7 samples).

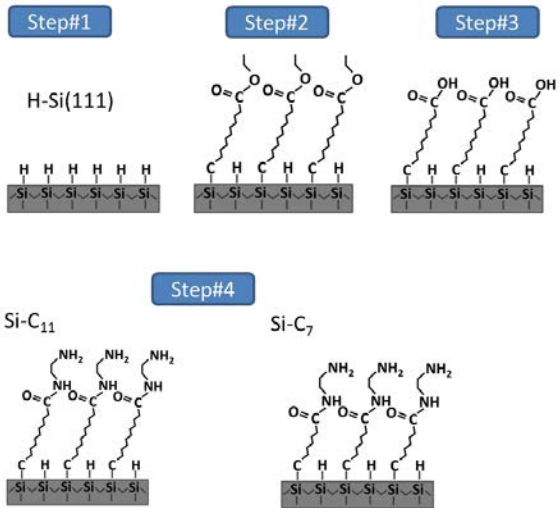

Figure 5.1: *The four steps for preparing the two kinds of the grafted organic monolayer considered in this study. From Caillard et al. Langmuir (2013).*

SiC_{11}. 10-Carboxydecyl organic monolayers were grafted on the hydrogenated silicon via direct thermal hydrosilylation of ethyl undecylenate. The neat alkene was outgassed three times by freezing it using liquid nitrogen under low vacuum (10^{-2} Torr) in a Schlenk tube. It was then heated up to 200 °C under continuous argon bubbling when inserting the freshly prepared H-terminated silicon sample. Grafting was performed for 4 h.

SiC_7. 6-Carboxydecyl organic monolayers were grafted on the hydrogenated silicon via direct thermal hydrosilylation of ethyl 6-heptenoate diluted (1:1) in mesitylene following the same procedure described above. Notable differences are the use of a lower vacuum during the outgassing step (10 Torr) with liquid N_2, and thermal hydrosilylation is performed at 170°C. Both modifications are done to avoid evaporation of the molecule and most of the solvent during the preparation and the reaction. At the end of this second step both organic monolayers are terminated with a protected carboxylic acid.

At the end of this second step both organic monolayers are terminated with a protected carboxylic acid. In step 3, the functionalized surfaces were sonicated in ethyl acetate and rinsed in boiling dichloromethane (40 °C). The carboxylic acids groups were then deprotected by using potassium tert-butoxide in DMSO (for 90 s and then rinsed thoroughly with DMSO) and by finally using an acid solution (HCl) to protonate the active group. Finally, step 4 is the transformation of the functional headgroup into succinimidyl ester-terminated. This was performed by reaction with an aqueous solution of N-ethyl-N′-(3-(dimethylamino)propyl)-carbodiimide (EDC) and 2-morpholinoethanesulfonic acid (MES). After a few minutes in EDC solution, 1 mL of ethylenediamine is added to the solution for 1 h 30 min at room temperature.

Finally, the surface was rinsed with ultrapure water. During the last step, one amine group of the ethylenediamine molecule ($H_2N{-}CH_2{-}CH_2{-}NH_2$) reacts with the activated ester, leading to the attachment of the molecule via an amide bond ($-(C{=}O){-}NH{-}CH_2{-}CH_2{-}NH_2$). It is very unlikely that the ethylenediamine binds in a bridging configuration through its two amine ends because the molecule length (2.99 Å) is shorter than the typical distance between two COOH groups estimated from the Si−Si distance. Therefore, at the end of step 4, the resulting surface presents amine groups on top of the layer[24,133,17].

5.2.2 Attachment of gold nanoparticles

Two different methods were used to prepare colloidal gold nanoparticles (AuNP):

Turkevich AuNP.

The citrate reduction method for synthesizing gold nanoparticles in water was pioneered by Turkevich *et al.* in 1951[134] and modified by Frens in 1973[135]. It remains one of the most popular methods for producing spherical monodisperse gold nanoparticles. An aqueous solution of $HAuCl_4$ (20 mL, 0.25 mM) was boiled under refluxing conditions and vigorous stirring. Sodium citrate was quickly added (1 mL, 18 mM), and the solution color changed from faintly yellowish to clear gray, purple, and finally dark purple within 2−3 min. The resulting AuNP have a diameter of typically 15 nm as already established[136,137] and demonstrated below by AFM. In this reaction, citrate first acts as a reducing agent and tends to adsorb onto the metallic gold

clusters, slowing down their growth and resulting in size regulation. Moreover, citrate ions are negatively charged such that the nanoparticles repel each other[138,139].

Ascorbic Acid Nanoparticles (asc-AuNP).

The asc-AuNP were synthesized following a method described elsewhere[140]. Typically, 200 μL of an aqueous solution of $HAuCl_4+3H_2O$ (10 g. L^{-1} of gold) was added to 25 mL of water at around 2 °C (ice-cooled) in a beaker. Then, 1.5 mL of a Na2CO3 solution (21.2 $g.L^{-1}$) and 1 mL of an ascorbic acid solution (7 $g.L^{-1}$) were added under vigorous stirring. The solution became instantaneously dark red.

Attachment on the surface

Deposition of AuNP on the organic monolayer was performed by dipping the functionalized silicon substrate into the colloidal solutions. The attachment occurs through the interaction between the $-NH_2$ moiety of the organic layer and gold surface. In the case of Turkevich AuNP the maximum nanoparticle coverage is reached after 1 h and occurs with an initial step of electrostatic attraction between the negatively charged citrate and the $-NH_3^+$ end group which is protonated due to the acidity of the Turkevich solution (pH = 5). In the case of the asc-AuNP, the solution was first acidified to pH = 6 with a 0.1 M hydrochloric acid solution. The solution color remained unchanged. The functionalized silicon surface was dipped into the AuNP solutions for 12 min, allowing the particles to become grafted onto the amino-terminated

surface while remaining well separated. In both cases, the substrate was cleaned after the dipping by several rinses in deionized water and dried with a nitrogen gas stream.

5.3 Characterization

5.3.1 Characterization of the SAM

FTIR characterization of the GOM

All FTIR spectra were taken using a Nicolet 6700 FTIR spectrometer from Thermo Scientific equipped with a DTGS detector in transmission mode at an angle of incidence of 64° with respect to the Si surface normal in a dry N2(g)-purged atmosphere and with an unpolarized IR beam. The spectra were obtained after the initial molecular attachment and deprotection of the carboxylic acid, *i.e.*, after step 3. The reference spectra were recorded in both cases using the oxide-free, fully hydrogen-terminated Si(111) surfaces. In the case of SiC_{11}, no oxide was detected. This surface remains robust against oxidation as evidenced by the absence of any detectable absorption at 1080 and 1240 cm^{-1} (TO and LO modes of SiO_2 oxide) in **Figure 5.2**. In the case of SiC_7 a negligible amount of oxide shows up at 1080 cm^{-1}. This oxide uptake is due to the time spent by the sample in air, needed for recording the FTIR spectra, and this characterization step was discarded for the samples used for STM measures. The negative peak at 2093 cm^{-1} is due to the replacement of Si−H bonds with Si−C bonds in the hydrosilylation process. Knowing that a fully hydrogen-terminated Si surface exhibits a Si−H line with an area of 0.08 cm^{-1}, an area comparison between the Si−H peak before and after molecular grafting shows that a coverage of roughly 1/2 of the surface is obtained for the SiC11 and slightly more

for the SiC_7. Half of the hydrogen atoms remain on the unreacted silicon atoms as depicted in **Figure 5.1**. The peak at 1713 cm^{-1} is assigned to the terminal C=O bond. The two peaks at 1280 and 1410 cm^{-1} correspond to the C−O bonds, and the 1461 cm^{-1} band is due to the bending mode of the methylene groups of the alkyl chains. The positive peaks in the range of 2880 and 2920 cm^{-1} are due to the CH_2 chains. They exhibit a higher area in the case of SiC_{11}, confirming the presence of a longer chain.

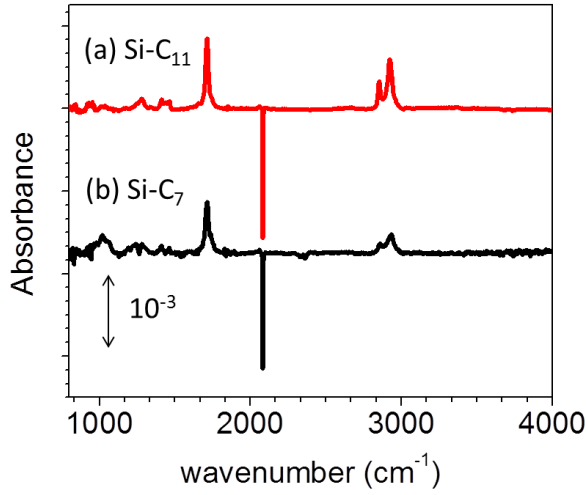

Figure 5.2: *FTIR transmission spectra showing the organic monolayer fabrication when the surface is terminated with carboxylic acid at step 3 (see Scheme 3). The monolayer was obtained by hydrosilylation with ethyl undecylenate (abbreviated SiC_{11}, spectrum a) and ethyl 6-heptenoate (SiC_7, spectrum b). The reference spectra were recorded in both cases using the oxide-free, fully hydrogenated Si(111)-(1 × 1) surface. These spectra demonstrate that the hydrosilylation process occurs without oxidizing the silicon substrate. From Caillard et al. Langmuir (2013).*

XPS characterization of the GOM

Surface analysis after molecular grafting using X-ray photoelectron spectroscopy after step 2 confirms that there is no oxide present (see **Figure 5.3**) and gave almost identical results

for both monolayers: in the vicinity of Si 2p core level shift, there is no evidence of Si oxidation (*i.e.*, at 103.2 eV). Moreover, the C1s region shows the specific peaks corresponding to the ester (290.0 eV), the C−O bond (288.0 eV), the C−C bond (285.0 eV), and the Si−C bond (284.5 eV). This last peak is less intense than the C−O and the ester peaks because it corresponds to carbon located deeper in the sample; *i.e.*, fewer photoelectrons can escape. An additional peak is also observed at 286 eV and is attributed to organic contamination because of exposure to air after surface chemistry during transport to the XPS chamber.

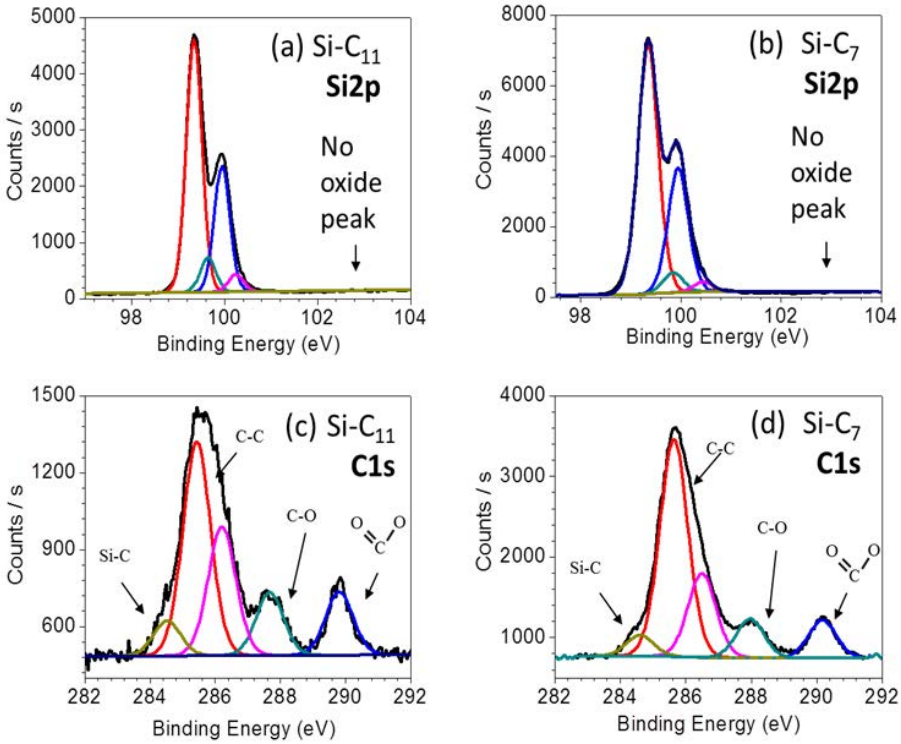

Figure 5.3: *XPS characterization of SiC_{11} and SiC_7 molecules after hydrosilylation. The C1s peaks between 284.5 and 290.0 eV observed for both SiC_7 (a) and SiC_{11} (b) confirm that the molecules are grafted on the surface. The Si 2p regions for SiC_7 (c) and SiC_{11} (d) contain no evidence of oxidation. From Caillard et al. Langmuir (2013).*

Ellipsometry characterization of the GOM

Spectroscopic ellipsometry measurements were also performed on the samples using an HORIBA Jobin Yvon ellipsometer (iHR320). After organic modification, the thickness and the dielectric constant of each organic layer are determined using a simple two-layer model similarly to previous study[7]. The thicknesses of the layers derived from the results are 1.6 nm for the SiC_{11} and 1.3 nm for the SiC_7. These results are in agreement with the expected values (1.67 and 1.28 nm, respectively) calculated from the geometric considerations: bond lengths and orientation of the molecule.

5.3.2 AuNP characterization

AFM was performed on these surfaces using the tapping mode with a Digital Instrument DI-3000 (**Figure 5.4**a) or a Multimode-8 instrument from Veeco (**Figure 5.4**b) and were processed with the software WSxM[141]. In the case of the Turkevich AuNP, the deposition was carried out as a test experiment to make sure that attachment occurred on the oxide-free monolayer investigated here similarly to what had been previously demonstrated in other publications dealing with monolayer on oxidized silanized silicon surfaces[142,136]. The amino-terminated monolayer layer was confirmed as being very efficient at immobilizing the nanoparticles[7], and the AFM images acquired in tapping mode showed no indication that the AuNP were moved by the tip. However, Turkevich nanoparticles are too large (diameter ~15 nm)

to exhibit Coulomb blockade at room temperature since this phenomenon requires NPs diameter around 5 nm. Therefore, we concentrate on the asc-AuNP. As shown in **Figure 5.4**b, the asc-AuNP are randomly distributed over the organic layer and there was no aggregation. Based on their profile height, the average size of the nanoparticles is 9.5 nm (standard deviation of 2.5 nm). Practically, this means that it is possible to find nanoparticles with a diameter between 4 and 15 nm on a typical AFM or STM image. The roughness of the underlying substrate without nanoparticles was measured to be 0.36 nm.

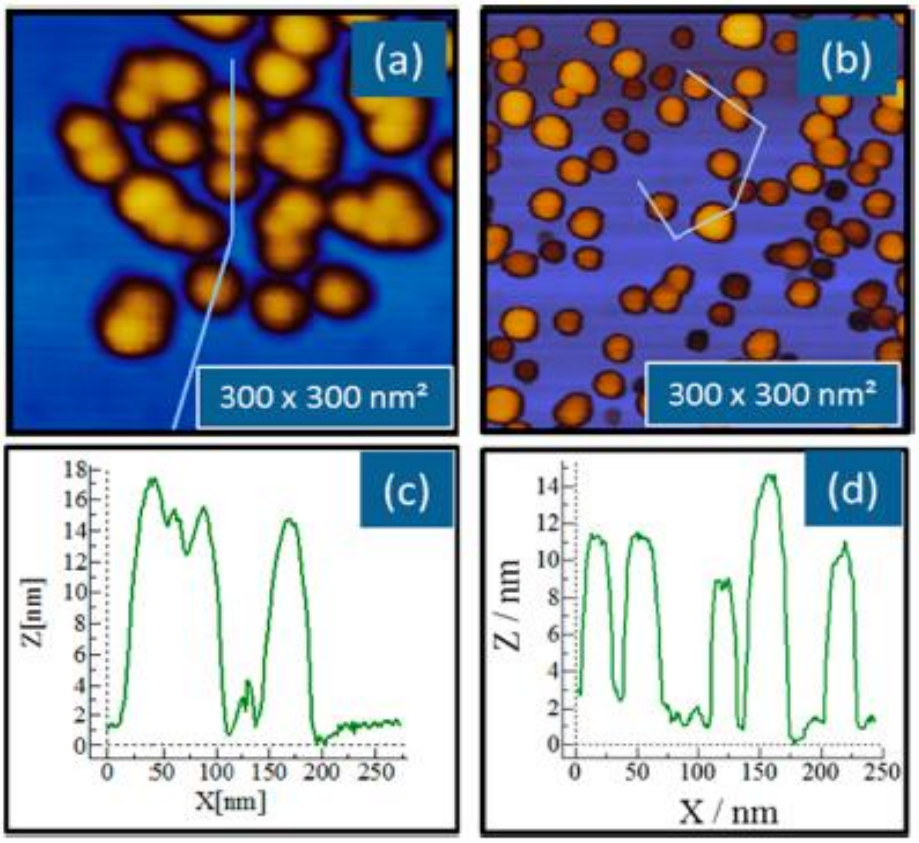

Figure 5.4: *AFM images in tapping mode of AuNP deposited on highly ordered monolayers on Si(111)-(1 × 1) surfaces. The Turkevich nanoparticles (a, c) were deposited on the SiC_{11} organic layer and the asc-AuNP (b, d) on a SiC_7 organic layer. From Caillard et al. Langmuir (2013).*

5.3.3 STM characterization of the assembled system

STM images of the two kinds of organic-functionalized surfaces (see **Figure 5.1**) were recorded in UHV at room temperature prior to AuNP deposition, as shown in **Figure 5.5**a and b. The surfaces are remarkably flat with a rms roughness of 0.33 and 0.38 nm, respectively, in agreement with AFM experiments, which indicates that the monolayer is very well ordered. The surface shown in **Figure 5.5**a exhibits parallel lines that are attributed to the silicon terraces[9]. The inset in **Figure 5.5**b shows that 3 nm large protrusions can be resolved, corresponding to bundles of ~10 molecules[142]. STM imaging found no notable differences between SiC_7 and SiC_{11} surfaces.

After the asc-AuNPs were grafted ex situ as described above, the samples were analyzed again by STM. As evidenced in **Figure 5.5**c and **Figure 5.5**d, AuNP are clearly visible, with a topographic distribution comparable to what was measured by AFM (**Figure 5.4**). The AuNP were strongly attached and could not been displaced by the STM tip as might occur on other systems such as self-assembled monolayer on Au(111). The diameters of two particles (marked with a cross in **Figure 5.5**c and **Figure 5.5**d) were evaluated, taking advantage of their height and found to be 7.5 nm for both particles.

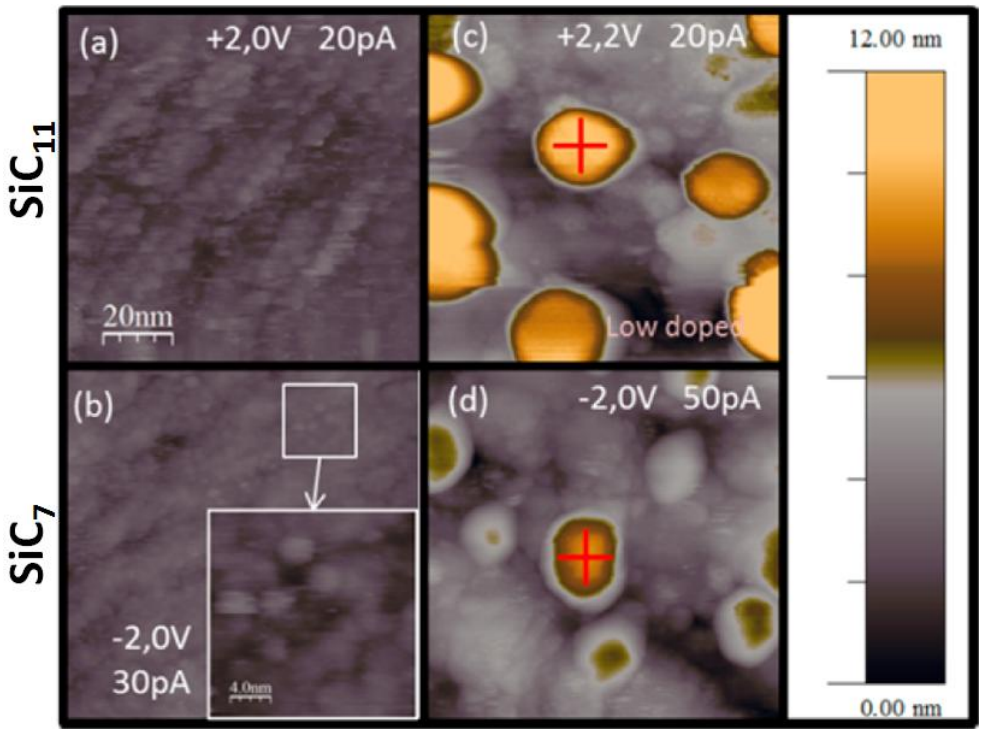

Figure 5.5: *STM images (100 × 100 nm^2) of different surfaces of organic layers grafted with a Si−C bond to the Si(111) substrate. Surfaces (a) and (c) were prepared with the long chain molecule (SiC_{11}) and surfaces (b) and (d) with the shorter chain (SiC_7). Inset in image (b) is a 20 × 20 nm^2 zoom of the surface with an enhanced contrast showing the molecular bundles on the surface. On both surfaces, asc-AuNPs have been grafted through the $-NH_2$ terminal group of the organic monolayer (images c and d). The cross indicates the AuNP where STS was performed. Images (a) and (b) have been recorded at room temperature and images (c) and (d) at low temperatures (25 and 37 K, respectively). Scanning conditions are given on the images (gap voltage and current set point). From Caillard et al. Langmuir (2013).*

5.4 Results and discussion

5.4.1 STS measurements

After acquiring an STM image, the current−voltage spectra I(V) were recorded on various AuNP selected on the basis of their size (closest to 5 nm) and having sufficient

separation from neighboring particles. The tip was placed above each AuNP at a distance determined by the current set point used for imaging, typically between 20 and 50pA. At ca. 40 K, the typical lateral drift was 0.4 nm/min after 1h stabilization time. For each image and before I(V) acquisition, this drift was precisely calculated, and a correction was applied so that the tip did not move more than 0.01 nm over a nanoparticle during data acquisition. After having switched off the feedback loop, a series of 40 spectra were acquired and averaged. However, a few curves were usually dropped from the averages because of tip mechanical instability. As depicted in **Figure 5.6**, positioning the STM tip over a gold nanoparticle creates a double barrier tunnel junction (DBTJ). The first barrier is composed of the organic layer and the second of the vacuum gap between the tip and the nanoparticle. This system can be electrically modeled by the circuit represented in **Figure 5.6** where each tunnel junction is represented by a capacitance and a resistance in parallel. If the two junctions are symmetric, the *I=f(V)* curve exhibits a Coulomb blockade region *(−e/2C < V < e/2C)* where no current flows through the DBTJ, and an Ohmic behavior is expected outside this region. On the other hand, if the DBTJ is asymmetric, the *I=f(V)* curve is staircase-like, and the number of extra electrons simultaneously present in the island is a discrete number directly controlled by V[68]. About 100 AuNPs were investigated under different conditions: three different temperature ranges (room temperature, 100 K with liquid nitrogen, and 25−40 K with liquid helium cooling), two different monolayer thicknesses (C_7 and C_{11}), two different substrate doping, and several AuNP diameters ranging from 4 to 10 nm. In this chapter, we select a few examples to illustrate the performance of this organic monolayer-based system, and we restrict ourselves to nanoparticles of one size. Further considerations regarding the dependence of STS with NP size will be given in **CHAPTER 7**.

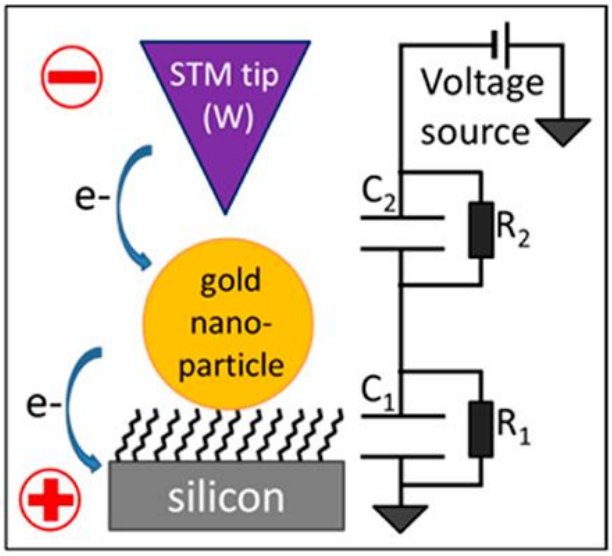

Figure 5.6: *Configuration Used To Build a Double Barrier Tunnel Junction with the Tip of the STM Placed above a Nanoparticle. From Caillard et al. Langmuir (2013).*

5.4.2 Coulomb blockade

I(V) spectra on three AuNP of similar size (8 nm) are presented in **Figure 5.7**: two spectra were recorded with the same SiC_{11} monolayer, but with two different substrate doping levels. The third spectrum was taken on the thinner SiC_7 layer. They illustrate the understanding of the influence of the thickness of the tunnel barrier and the influence of the semiconductor doping level on electron transport. The spectra were recorded at low temperatures (25, 37, and 100 K, respectively). In all three samples, Coulomb staircases were clearly observed (top graph of **Figure 5.7**) and are evidenced by differentiating the *i(V)* spectrum and calculating *(di/dV)/(i/V)*. The quantity *di/dV* is proportional to the local density of states (LDOS) and allows detecting the electrostatic energy levels generated by Coulomb blockade in the metallic island[143].

Each Coulomb oscillation in the differentiated curve corresponds to a step of the Coulomb staircase, indicative of an additional electron stored in the nanoparticle. These results demonstrate that the quality of an organic monolayer on silicon can be such that they act as a local tunnel barrier between the substrate and a metallic nanoparticle and that it is possible to prevent an insulating oxide from being spontaneously formed. However, the exact Coulomb blockade behavior depends on many parameters such as the size and shape of nanoparticles, their crystallinity[144], the presence of an organic surfactant on the nanoparticle, and the actual bonding between the nanoparticle and the organic layer. These delicate issues have barely been investigated in the literature so far, and we do not address them in detail in the present chapter. A further analysis of our acquired data set will be reported in **CHAPTER 6** and will focus on the transport measurements in a more statistical approach. Nevertheless, we checked that on the three nanoparticles discussed herein Coulomb blockade was repeatedly observed during a measurement campaign and that for a given particle the positions of the *di/dV* peaks were reproduced within an interval of 0.08 V.

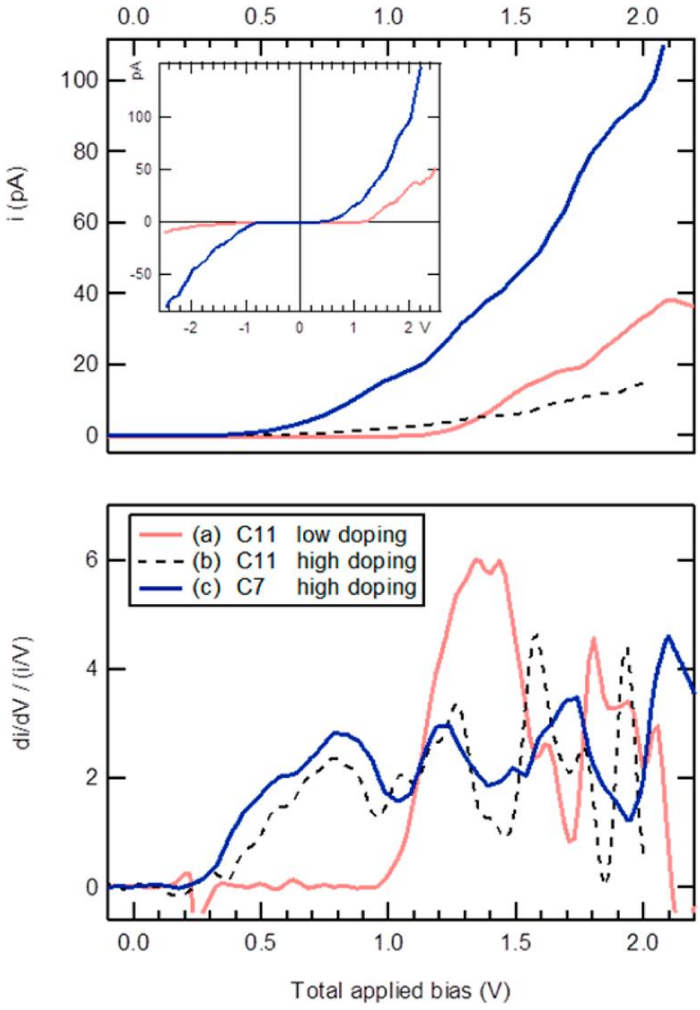

Figure 5.7: *Tunnel spectroscopy on 8 nm nanoparticles at low temperatures (25, 100, and 37 K, respectively) showing Coulomb staircases (upper graph) and its derivative (di/dV)/(i/V) (lower graph). Each peak of the derivative corresponds to a supplemental electron added to the nanoparticles. Spectra (a) and (c) were recorded on the AuNP marked with a cross in* ***Figure 5.5****c and* ***Figure 5.5****d, respectively. The silicon substrates were n-doped in all cases with a carrier density of* 4.10^{14} cm^{-3}, 7.10^{17} cm^{-3}, *and* 2.10^{18} cm^{-3}, *respectively. From Caillard et al. Langmuir (2013).*

In the case of the low doped substrate *(*$Nd = 6.10^{14}$ cm^{-3}*)* and with the SiC_{11} layer (curve a in **Figure 5.7**), the current onset is measured at $V_0 = 1.37$ *V*, and the second step shows up at $V_1 = 1.87$ *V* (see **Table 5.1** for an overview of the relevant experimental values). According to the

theory developed for Coulomb phenomena on metals[70,68], the step position is given by $V_n = (2n + 1)e^2/2C$: the current onset is expected at a potential that is the half of the step width. Obviously this is not the case in the present experiments since $V_0 \neq 1/2(V_1 - V_0)$. In order to understand the reason for this apparent discrepancy, the doping of the substrate was increased to $Nd = 7.10^{17}\ cm^{-3}$, keeping the same molecular insulating layer and the same nanoparticle diameter. In this case the current onset was lowered to $V_0 = 0.85\ V$, and the first step is measured at $V_1 = 1.22\ V$ (curve b in **Figure 5.7**). The difference between the measured and theoretical onset is due to the strong band bending effect occurring in silicon substrates and particularly in those that are low doped. These effects are qualitatively shown in **Figure 5.8** where the energy profile is drawn as a function of the distance away from the silicon surface. This scheme clearly shows the two barriers that an electron needs to cross in order to travel from the substrate to the STM tip. In the present case, both barriers are of the order of 1 nm and an electron can tunnel through them.

Figure	doping/ cm^{-3}	organic layer	temp (K)	NP diam (nm)	V_0 onset (V)	V_1 2nd step (V)	V_2 third step	V_3 2nd step (V)	ΔV Step width (mV)	Δi step height (pA)	tunnel conditions
5a	low 6×10^{14}	Si–C_{11}	25	8.2	1.37	1.87	2.39		500	20	20 pA, +2.2 V
5b	high 7×10^{17}	Si–C_{11}	100	8.0	0.85	1.22	1.58	1.92	370	2	5 pA, +2.0 V
5c	high 2×10^{18}	Si–C_7	37	7.5	0.80	1.20	1.65	2.10	420	15	50 pA, −2.0 V

[a]The voltages are obtained with an accuracy of 0.05 V.

Table 5.1: *Electric Characteristics of the Coulomb Staircases Measured with Our Silicon Substrates[a]. From Caillard et al. Langmuir (2013).*

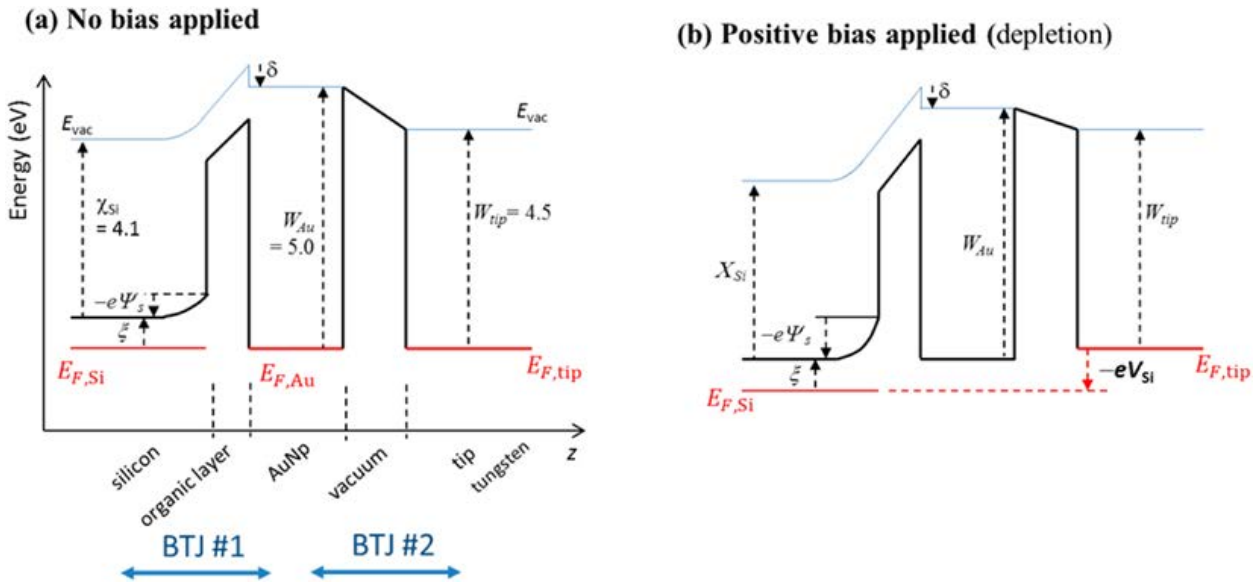

Figure 5.8: *Energy Diagram of the DBTJ. The first barrier tunnel junction is between the silicon and the selected AuNP, and the second BTJ is between this AuNP and the STM tip. From Caillard et al. Langmuir (2013).*

The profile is derived from the work functions of all the materials of the DBTJ, knowing that the Fermi levels should be aligned through the entire structure when no bias is applied[145,146]. For the first barrier tunnel junction (denoted BTJ #1), the work function of silicon W_{Si} is given by the sum of the electron affinity of silicon χ_{Si} and the energy difference $\xi = E_C - E_{F,Si}$ such that $W_{Si} = \chi_{Si} + \xi \approx 4.4\ eV$. χ_{Si} is slightly attenuated by the electrostatic dipole generated by the molecular layer. The molecular dipole δ is independent of the applied bias and was evaluated at around $-0.4\ V$ in similar cases[125,147]. In **Figure 5.8** this dipole shows up as a shift of the vacuum level indicative of an electric field close to the organic surface. The Fermi levels of silicon and gold are aligned at equilibrium, and since the work function of gold is $W_{Au} = 5.1\ eV$, it results in the creation of an electric field between the two materials so that the bands of the semiconductor tend to bend upward even at zero applied bias. As a consequence of this band bending, an

interface potential is generated, denoted ϕ_S in **Figure 5.8**. When a positive bias V_{Si} is applied as depicted in case b of **Figure 5.8**, the band bending is amplified and the electron needs to *roll up this supplemental hill* to reach the tip. As a result, a supplemental amount of energy needs to be provided, which is done by further increasing the applied voltage V_{Si}. This effect is all the more important when the doping is low. This explains why the steps of the Coulomb staircases were detected at higher potential for the low doped samples. Therefore, band bending has two consequences: first, the actual interface potential applied to the silicon/organic layer/AuNP system is much weaker than the external potential applied by the STM tip, and the electrons need to climb this supplemental barrier. Second, the process depends on the thickness of this barrier, which can be very thin in the case of high doping allowing the charges to tunnel through it. This is not the case for low doped substrates due to band bending. The band bending potential at zero bias has been evaluated to be *+0.60 V* for low n-doped substrate (10^{15} cm^{-3}) and *+0.50 V* for highly n-doped silicon (10^{19} cm^{-3}) by Cahen's group[83]. Hacker found a value of *+0.26 V* with low n-doped substrate (4.10^{14} cm^{-3})[125]. Although these two values differ, probably because of the different ways of estimating the molecular interface dipole, they confirm the order of magnitude of the voltage shift observed in our experiments.

Finally, with the shorter SiC_7 monolayer, the Coulomb phenomena are even more pronounced, as shown in curve c of **Figure 5.7**: the steps are clearly visible, and the current is stronger due to a higher conductance of this thinner organic layer. The current onset is detected at *0.80 V*, very similar to curve b, because the doping level and nanoparticle diameters are identical. The step widths are also comparable. It is not possible to compare the step height since

the tunneling conditions were not the same for these three experiments (see last column of **Table 5.1**), and the actual tip−nanoparticle distances differ and are unknown in all three cases.

The inset in **Figure 5.7** illustrates another consequence of working with a low doped substrate. With the high doped substrate, the *i(V)* is almost symmetric with stairs in positive and reverse bias. At positive and reverse biases, the current onset is measured at *+0.80* and *−0.89 V*, respectively. However, for a low doped substrate, no current is detected in reverse bias, and the junction behaves like a Schottky diode.

5.5 Conclusion

For the first time, a self-assembled monolayer made with organic molecules covalently grafted on oxide-free silicon has been used for measuring Coulomb blockade. This grafted organic monolayer consists of a highly ordered 10-carboxydecyl grafted organic monolayer on silicon which is further modified with an amine termination designed for covalently attaching colloidal gold nanoparticles. By using the tip of an UHV-STM system, above a gold nanoparticle, a double barrier tunnel junction was formed and was found to exhibit clear Coulomb staircase, as evident in the I−V plots. The influence of the doping level of the silicon substrates on the electrical behavior of this system has been investigated. Low doped substrates induce a strong band bending near the Si/organic layer/Au junction, so such that the actual interface potential is much lower than the applied bias. The step width of the Coulomb staircases

is therefore increased, compared to the case of highly doped silicon. Finally, the hydrosilylation method for preparing the organic layer was successfully applied for attaching shorter molecules, and we also investigated the influence of monolayer thickness on the step heights. Results suggest that the step heights are found to be higher for the thinner monolayer as expected. These results open a way for using such grafted organic monolayers on oxide-free silicon as active layers for molecular electronics. Now that Coulomb blockade is clearly established, and that the influence of using a semiconducting substrate was qualitatively discussed we will determine the parameters that need to be optimized to obtain more reproductive results (**CHAPTER 6**). In the end **CHAPTER 7** will present how to adjust a proper model for understanding in details this single electron transport.

CHAPTER 6

CONTROLLING THE REPRODUCIBILITY OF COULOMB BLOCKADE PHENOMENA FOR GOLD NANOPARTICLES ON AN ORGANIC MONOLAYER/SILICON SYSTEM

This chapter is the reproduction of a recently submitted paper in Nanotechnology (published by IOP Science):

L. Caillard, S. Sattayaporn, A-F. Lamic-Humblot, S. Casale, P. Campbell, Y. J. Chabal, O. Pluchery. Controlling the reproducibility of Coulomb blockade phenomena for gold nanoparticles on an organic monolayer/silicon system, 2014.

This is a study on the parameters that have an influence on the reproducibility of single electron transport observations using our system.

6.1 Introduction

Molecular electronics emerged as a leading research topic because molecular architectures make possible to engineer structures that inorganic crystalline semiconductor could not produce. The achievements of molecular electronics have made possible the invention of plastic electronics, of printed electronics, of organic LED to cite a few examples[86,148,128]. Molecular assemblies can be engineered so that they form periodic structures, and give rise to macroscopic electrical properties in a similar way as the lattice periodicity in semiconductor according to Bloch theorem. However the coupling of molecular structures with standard silicon technology requires a control down to the atomic level of the interface between molecular layer and a semiconductor substrate. This field of research still requires sustained efforts to reach a high level of liability and reproducibility[108,148,128] At the heart of the problem lies the question of

interface quality between the active molecular layer and the silicon substrate. Interface issues are already well known within the realm of standard inorganic electronics, for which the control of interface state density is a key parameter that drives the device performance. Such control is also needed for organic layers in order to perform reliable electronic functions, such as driving charges with high mobility, storing electrons[120], or providing a controllable electron flow for transistor applications[122,121]. Controlling the interface quality means controlling simultaneously the atomic/molecular organization and the amount of trapped charges[123] or leakage current[84]. In the present study, we investigate the possibility of using hybrid interfaces made of highly ordered molecular layers on semiconductor surfaces for single charge electronics. This next-generation electronics is based on Coulomb blockade and is generated in a structure made of a double-junction tunneling barrier (DBTJ).[70]

Coulomb blockade is a phenomenon where electrons are driven one-by-one through an *island* which is often a metallic nanoparticle. In term of energy, adding one more electron in the island structure costs an electrostatic energy given by $e^2/2C$ where C is the equivalent capacitance of the structure and e the elemental charge. This capacitance depends on the geometry of the architecture such as the nanoparticle diameter, its shape and its distance to the electrodes. The particle must be at the nanometer scale in order to be able to observe this phenomenon at room temperature because the electrostatic energy $e^2/2C$ should be far larger than kT. In a practical way, single electron phenomena are detected as a stepwise increase of the current going through the island, upon increase of the applied potential. These staircase-like I-V curves open the route to a built-in logical electronics where the discrete nature of the current is

used to directly implement logical functions[56,57,59]. Single charge electronics have received a strong interest from the scientific community in the early 2000s[149,150,143] and more recently some single electron transistors have already been fabricated[82,151,152,153] as well as memory cells[154,58]. Notable works have shown that it was possible to obtain single-electron transistors by self assembling gold nanoparticles on a substrate[153] or between metallic electrodes[152]. But there are very few examples of Coulomb blockade obtained with one electrode being semiconducting. Single charge transport was observed in a silicon nanopillar engineered in a way that it includes two tunnel barriers in series.[80] An interesting prototype was obtained on a bulk silicon using photolithography[82], but here also, source and drain were established by metallic contacts (chromium). Moreover, the yield for fabricating operational transistors remained really low (1%). In the literature and to the best of our knowledge two studies describe single charge architectures where one of the electrodes is a semiconductor substrate: Radjokovic *et al.* reported it 1996 but their results are frequency dependent and are then more likely to be artifacts[115] (see **CHAPTER 7.4.1**) and Tedesco *et al.* in 2010 acknowledge the difficulty to observe reliable single electron transport and stress the importance of the depletion layer in SCs[155]. Therefore using silicon substrate as an electrode is needed to move towards the compatibility with CMOS technology. In order to fulfill the requirement of compatibility and of reproducibility at the molecular scale, self assembly methods are probably the most promising way.[156] It is especially true when working with silicon interfaces where the quick uptake of native oxide generates interface trapped charges[5]. Ever since the discovery of atomically flat hydrogen-terminated silicon (111) surfaces in 1989[5] many chemical processes have been developed to graft molecules in lieu and place of the hydrogen, whether by using thermal activation[6,7,8,125], UV

activation[8,9,10,126], electrochemical activation[11,12] or chlorination[8,13,127]. The electrical properties of the resulting surfaces have been investigated in the context of electronic application[128]. For instance, the work function of such surface has been measured and vary from 4 to 5eV depending on the termination[13]. Results also show that surfaces with very few defects can be achieved[14,16,17,51,133,157]. A density of interface states as low as $D_{it}=2.10^{11}$ cm^{-2} eV^{-1} has been measured on (n) Si(111) functionalized surfaces[51]. These Si(111) surfaces are stable for a several hours in ambient conditions and can remain oxide-free after several post chemical treatments for grafting either gold nanoparticles[123] or quantum dots[21]. As a comparison, hydrogen-terminated (SiH) surfaces remain stable only a few minutes in typical ambient air (*i.e.* with some radicals, ozone, and low level corrosive gases), typically leading to levels of surface oxidation that are too high for electrical devices (*e.g.*, the efficiency of silicon solar cells[158] are severely degraded when $Di>10^{13}$ cm^{-2} eV^{-1}). In contrast, organically functionalized surfaces remain stable for several days[15]. The quality of the grafted monolayer is critical for several reasons: it allows the stable attachment of a gold nanoparticle, it provides a protecting layer on top of the silicon in order to prevent the creation of electron traps due to oxidation, and it is used as an insulator with a controlled thickness between the AuNP and the Si bulk

In the present work, we focus on a double barrier tunnel junction where one junction is formed by a molecular layer situated between a gold nanoparticle (AuNP) and a silicon substrate, and the second junction is formed by the gap between the AuNP and the tip of a scanning tunneling microscope (STM) as depicted in **Figure 6.1**a. We review how to obtain reproducible Coulomb blockade behaviors and what are the effects of several key parameters, such as the

nanoparticle size, shape and crystallinity, as well as the quality of the GOM and the effect of aging of the silicon substrate (local oxidation).

Observation of Coulomb blockade and a Coulomb staircase is carried out with an STM in UHV (10^{-11} Torr) at low temperatures (30-40K), as demonstrated earlier.[16] However, as shown in this earlier work, the reproducibility of the single-electron transport measurements is a real challenge. Coulomb blockade is highly sensitive to the actual morphology and electronic properties of the two tunnel junctions. **Figure 6.1**c shows an STS curve with clear Coulomb staircase features obtained on a 6.0 nm AuNP at 40K. However a nearby NP with the same morphological characteristics, exhibit no Coulomb blockade even after several tries of data acquisitions (**Figure 6.1**d). The reasons for this no-show are multiple and seven of them are schematically depicted on **Figure 6.1**b: (1) the size of the NP measured by STM might be biased since STM topography is based on mapping the LDOS; (2) NP might not be spherical; (3) the fact that NP are mono or polycrystalline may also affect the electron transport; (4) the colloidal NP might still be surrounded by ligands which will influence the behavior of the tunnel junctions; (5) the GOM is made of small molecular domains and at the boundaries the electrical properties may fluctuate; (6) the STM tip is not perfectly stable and therefore the second junction also fluctuates; and finally (7) the passivation against substrate oxidation carried out by the GOM is limited in time and local electrical defects progressively arise. Unfortunately, there is no easy experimental setup that allows measuring simultaneously an STS curve and probing the parameters listed above. Therefore we will draw our conclusions on a basis of a statistical approach.

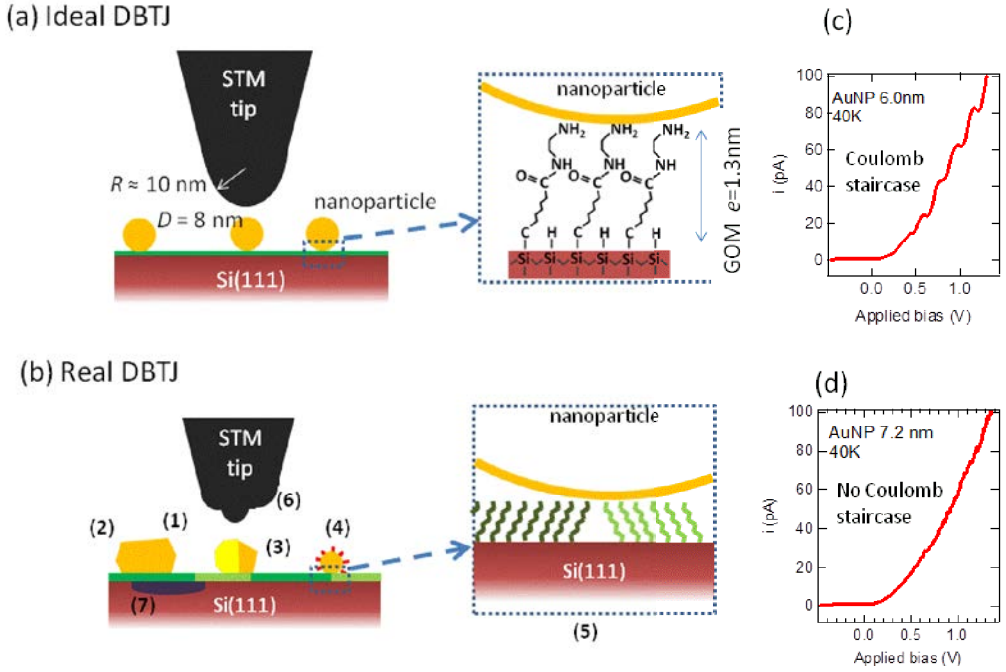

Figure 6.1: *Sketch of the DBTJ used in the present work for measuring Coulomb blockade in the ideal case (a) and in the real experiments where many imperfections may affect the STS measures: (1) inaccurate NP size, (2) non-spherical shape, (3) polycrystalline particles, (4) remains of molecular ligands, (5) molecular domains boundaries (6) tip instabilities and (7) local substrate oxidation. On a same sample, two close-by nanoparticles may exhibit clear Coulomb blockade I-V curves (c) or nothing detectable like in graph (d).*

6.2 Experimental

6.2.1 Sample preparation

Surface preparation

Functionalization of atomically flat, H-terminated Si surfaces has been described previously.[16] Briefly, a 500 micron-thick Si(111) sample is cut into 15x38mm rectangle from a N-doped silicon wafer (polished on both sides) with a resistivity of 0.02Ω.cm. It is cleaned in a

piranha solution (H_2SO_4+H_2O_2 3:2) for 15min at 80°C. The native oxide layer is then stripped using a diluted HF (10%) solution for 30sec. The H-terminated surface is etched in a NH_4F (40%) solution for 2min30 at room temperature to get an atomically flat surface[21]. The oxide-free monohydride-terminated sample is then immersed in a neat solution of 10-carboxydecyl (SiC_{11}, long carbon chain) or in a neat solution of 6-carboxydecyl (SiC_7, short carbon chain). The SiC_{11} grafting is done in a heated solution (200°C), which has been degassed (oxygen free) through three successive freezing-pump-thaw cycles using liquid nitrogen. The reaction lasts for 4 hours. The SiC_7 grafting is done using UV activation in a customized quartz cell where the sample is sandwiched between two quartz slides in a N_2(g)-purged glove box. It is then irradiated (with 253, 350 and 375 nm wavelengths) for 4h. UV activation is used for the SiC_7 molecules to reduce the amount of chemical needed: thermal hydrosilylation requires a higher amount of molecules and would require SiC_7 molecules to be diluted in mesitylene. The latter has a boiling point of 164.7°C, requiring a reaction temperature lower than the preferred 200°C and leading to a lower quality surface.

After the reaction, both samples are rinsed in boiling dichloromethane (40°C). Amine-terminated surfaces are obtained by deprotection for 1min30 in a potassium-tert-butoxide solution using dimethyl sulfoxide (DMSO) as solvent, and activation for 1min in N-ethyl-N'-(3-(dimethylamino)propyl)-carbodiimide (EDC) before adding ethylenediamine to the solution and keeping it at room temperature for 1h30. The resulting surfaces exhibit an amine group on top of the layer as shown in the inset of Fig. 1-a.[17,24,133] The samples are then characterized with X-ray

photoelectron spectroscopy (XPS) and Fourier transform infrared spectroscopy (FTIR) measurements in order to assess their quality.

Gold nanoparticle preparation

Gold nanoparticles can then be chemically attached on the amine head groups. Three different synthesis methods have been used to prepare the AuNPs. All the chemicals were purchased from Sigma-Aldrich.

- **Turkevich method:** The citrate reduction method for synthesizing gold nanoparticles in water was pioneered by Turkevich *et al.* in 1951[134] and modified by Frens in 1973[135]. As of today it is one of the most popular methods to synthesize spherical monodisperse gold nanoparticles. An aqueous solution of HAuCl4 (20 mL, 0.25 mM) is heated up at 100°C with vigorous stirring. Tri-Sodium citrate is quickly added (1 mL, 18 mM), resulting in a change of color from yellow to purple within 4−5 min. In this reaction, citrate is first used as a reducing agent but also tends to adsorb onto the metallic gold clusters. It results in a size regulation of the obtained nanoparticle because the process is slowed down. Moreover, citrate ions are negatively charged such that the nanoparticles repel each other[138,139].

- **Ascorbic acid method:** The method used to synthesize nanoparticles with ascorbic acid is described elsewhere[140]. Typically, 200 µL of an aqueous solution of $HAuCl_4{:}3H_2O$ (10 g L^{-1} of gold) is added to 25 mL of water at around 0°C (ice-cooled) in a beaker. Then, 1.5 mL of a Na_2CO_3 solution (21.2 g L^{-1}) and 1 mL of an ascorbic acid solution (7 g L^{-1}) are added under vigorous stirring. The solution becomes instantaneously dark red.

- **Natan method:** This synthesis is based on the work of Natan and al[159] then modified by Dong and al[160]. It is a modified version of the previously described Turkevich method. 2ml of $HAuCl_4$ (aq) 1% are added to 2ml of sodium citrate (aq) 1% in 100ml of water at 0°C. 1,5ml of a 0.075% solution of $NaBH_4$ is then added, resulting in a spontaneous color change to dark red.

Attachment of gold nanoparticles:

Both Turkevich method and Natan method deposition are performed by simply dipping the functionalized surfaces in the colloidal solutions. Turkevich AuNPs are deposited during a 30 min dipping time whereas 1 min only is needed with the Natan technique. The ascorbic acid gold nanoparticle deposition requires a prior step before dipping that consist of lowering the pH solution to 6 with a 0.1 M hydrochloric acid solution. A deposition of 12 min is then performed to get the desired surface coverage. Several rinsing with deionized water is then needed to remove the loose nanoparticles after each deposition. All samples are then dried with a nitrogen steam. For each method, the attachment relies on the interaction between the $-NH_2$ moiety of the organic layer and the gold surface.

6.2.2 Characterization techniques

XPS analysis is performed with a Quantum 2000 Scanning ESCA Microprobe spectrometer (Physical Electronics, USA) equipped with a concentric hemispherical analyzer under ultrahigh vacuum conditions (10^{-10} mbar) and a monochromatic Al Kα X-ray source

(1.5keV, filament current 20mA). Spectra are recorded at a 45° takeoff angle with respect to the surface. A sample area of 100µm × 100µm is analyzed with a pass energy of 46.95 eV for survey and 11.75eV for detailed elemental scans.

FTIR spectra are acquired using Nicolet 6700 FTIR spectrometer from Thermo Scientific equipped with a DTGS detector. Detection is performed in transmission at an angle of incidence of 74° with respect to the Si surface normal in a dry N_2(g)-purged atmosphere. In transmission, both sides are probed, thus increasing the signal, since both sides receive the same treatment during wet chemical functionalization.

Investigation of gold nanoparticle properties with Transmission electron microscope (TEM): TEM images are collected with a JEOL 2010 microscope operating at 200 kV equipped with a charge-coupled device camera. Particle size measurements are performed with "ImageJ" (Image processing and analysis in Java, Open source). The limit of size detection is about 1 nm.

Atomic Force Microscopy (AFM) images of the attached nanoparticles are recorded using a commercial MultiMode® 8 Scanning Probe Microscope from Bruker Corporation. Silicon tips on nitride cantilevers (with a resonance frequency of ~50-70 kHz and a force constant of 0.4 N/m) are used. The AFM is operated in tapping mode. Images are obtained at a constant speed of 1 Hz with a resolution of 512 lines of 512 pixels each. In our study, AFM was used as the main characterization tool to monitor the density of the gold nanoparticles after deposition on silicon.

Scanning Tunneling microscopy (STM) is carried out with a commercial apparatus (Omicron VT-STM) in which the sample can be cooled down to 30-40 K with a coldfinger in contact with liquid helium. The base pressure of the chamber is 3.10^{-11} mbar. After acquiring an STM image, current−voltage spectra *I-V* are recorded with scanning tunneling spectroscopy (STS) on various AuNP having sufficient separation from neighboring particles. The tip is placed above a given AuNP at a distance determined by the current set point used for imaging (typical values for imaging are from 20 to 50pA). A temperature of 40K is obtained with a constant He flow that leads to a lateral drift of roughly 0.4 nm/min after 1h stabilization time. For each image and before I(V) acquisition, this drift is precisely calculated, and a correction is applied so that the tip does not move more than 0.01 nm over a nanoparticle during data acquisition. Series of 10 sweeps are then acquired for each measurement. Several measurements are done on each AuNP. Each curve however is treated individually since the tip can move or vibrate during a sweep, which sometimes alters the *I-V* curve.

6.3 Results

Observation of single electron transport has been optimally achieved using a short organic monolayer (SiC_7) on AuNP synthesized with Natan method as shown in **Figure 6.1**c and **Figure 6.7**. A nanoparticle will be considered "consistently active" when it exhibits consistent single electron behavior: *i.e.* a characteristic Coulomb staircase behavior is observed for more than two third of the sweeps. In contrast, an AuNP will be considered "occasionally active"

when it only displays single electron behavior on occasion, *i.e*. between one third and two third of the time. Several issues can account for this more "erratic" behavior. The approach adopted in the present study is based on statistics in order to draw some general conclusions on the effects from the parameters listed in the following.

6.3.1 Nanoparticle size and shape

From TEM images we obtain a size distribution of each colloidal solution, as illustrated in **Figure 6.2**. As reported in the literature[136,137] the Turkevich method provides particles with a narrow size distribution and a diameter than can be adjusted at values above 12 nm by changing the ratio of citrate over $HAuCl_4$. A ratio [citrate]/[$HAuCl_4$] = 3 very reproducibly provides 16.6 nm AuNP as measured for solution #5 in **Table 6.1**. Smaller particles are achieved with the ascorbic acid method (8.9 nm) but with a wider standard deviation (3.5 nm). This standard deviation can be narrowed to 1.3 nm by using $NaBH_4$ as reducing agent and citrate as surfactant. This is the Natan method which leads to the production of NPs of intermediate size (6.6 nm). NP size was also assessed after deposition on the functionalized substrate with AFM and STM. A summary is provided in **Table 6.1**. The size measured with all three methods provides similar size distribution. Only with STM, sizes seem to be smaller of 1.0 to 1.5 nm. For example with solution #1 in **Table 6.1**, the same sample is analyzed with AFM provides 9.6 ±1.9 nm and 8.1±2.1 nm with STM. There is no clear reason for a systematic size deviation with STM, even if topography is indirectly measured with STM. However the variation of the typical tip-sample

distance due to scanning over different material (NP to GOM) will not exceed 0.5 nm. Therefore the different sizes are due to the sampling. Numbers given below were obtained after analysis of 30 to 100 AuNPs.

Regarding the NP shape, the most regular NP (spherical) are the Turkevich ones with just 4% of them displaying an aspect-ratio greater than 1.25. The aspect ratio of an ellipsoid is the ratio of the long axis over the short axis of the ellipse. On the other hand, ascorbic AuNPs tend to produce more non-spherical NP with 26% displaying an aspect-ratio greater than 1.25. On the other hand, Natan method produces just 8% of elliptic AuNP. Therefore, since Turkevich AuNP are too large for observing room temperature Coulomb blockade, Natan's method seems to be the best option to have spherical and reproducible nanoparticles.

NP type	***HR-TEM***	***% with A/R >1.25***	***AFM***	***STM***
Asc - solution#1			*9.6±1.9*	*8.1±2.1*
Asc - solution#2	*8.9±1.9*	*26%*		
Natan - solution#3	*6.6±1.3*	*8%*	*6.6±1.3*	*5.5±1.8*
Turkevich - sol. #4			*12.3±1.3*	*12.6±0.9*
Turkevich - sol. #5	*16.6±1.6*	*4%*	*15.6±1.0*	

Table 6.1: *Size distribution of colloidal gold nanoparticles prepared by reduction of $HAuCl_4$ with three agents: ascorbic acid, $NaBH_4$ with citrate (Natan method) or just citrate (Turkevich method). The sizes are measured with TEM, and also after deposition with AFM and STM.*

6.3.2 Crystallinity of nanoparticles

High Resolution TEM allows the identification of the crystalline character of the NP. For monocrystalline particles, parallel atomic planes are visible in the high resolution images. When the particles are polycrystalline, this alignment of planes does not span over the whole nanoparticle and sometimes two or three families of planes are identified. However sometimes, the electron beam cannot travel through the entire particle and this later might look as amorphous although it might be a misaligned single crystal. In this case, when it is not possible to determine the crystallinity of some particles these particles (roughly 20-25% of all the analyzed particles for each method) are labeled as "undefined". As shown in **Figure 6.2** and **Table 2.2**, Turkevich method produces polycrystalline NP exclusively. The preparation method with ascorbic acid produces 31% of monocrystalline particles and Natan synthesis 47%. **Figure 6.2** summarizes this data for the size and crystallinity of nanoparticles.

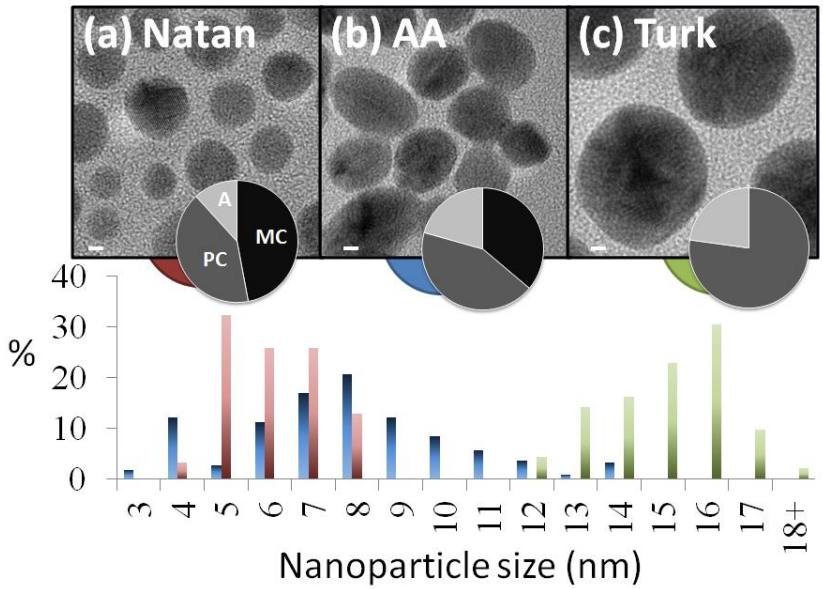

Figure 6.2: *TEM images of gold nanoparticles synthesized with Natan method (a, Natan, red), ascorbic acid method (b,AA, blue) and Turkevich method (c, Turk, green) with the size distribution for each methods. As an inset is added the proportion of monocrystalline (black, MC), polycrystalline (dark grey, PC) and undefined nanoparticles (light grey, A) for each synthesis method. Such distinction between monocrystalline and polycrystalline can be done because of the clear observation of grain boundaries on TEM images. Undefined nanoparticles are the one were crystallinity couldn't be established as they appear featureless. In that case they could be amorphous or the orientation of the gold nanoparticle with respect to the electron beam couldn't allow a proper identification. Scale bars: 2nm.*

6.3.3 Nanoparticle coverage

The nanoparticle coverage after deposition is evaluated with AFM. It must be adjusted so that on the one hand, a typical STM image (50x50nm²) contains a amount of particles large enough to be investigated using STS, and on the other hand the density in not too high for limiting the risk of clusters and electrical interaction between adjacent particles[113]. **Figure 6.3** shows typical AFM images of AuNP deposited with Natan's method on a functionalized SiC_7 surface. Figure shows that one minute dipping of the functionalized silicon substrate in the Natan

NP suspension yields a nanoparticle coverage of $3.4x10^{10}$ NP.cm^{-2}. If the NP were equally distant it would corresponds to an average particle-particle distance of 54 nm. The particle are expected to be well separated which is confirmed in the AFM image (**Figure 6.3**a). Notice that due to the convolution with the AFM tip, the NP diameter appears larger (20 nm typically) than the particle (height estimated with AFM: 6.6±1.3 nm). AFM image for **Figure 6.3**b is obtained after 5 min dipping and the coverage of $1.4x10^{11}$ NP.cm^{-2} produces an average first-neighbor distance of 27 nm. This suggests that an ideal density is around 10^{11} AuNP/cm² for 7 nm particles. Similar results were obtained with ascorbic NP and for a 12 min dipping, a coverage of $7x10^{9}$ NP.cm^{-2} has been measured.

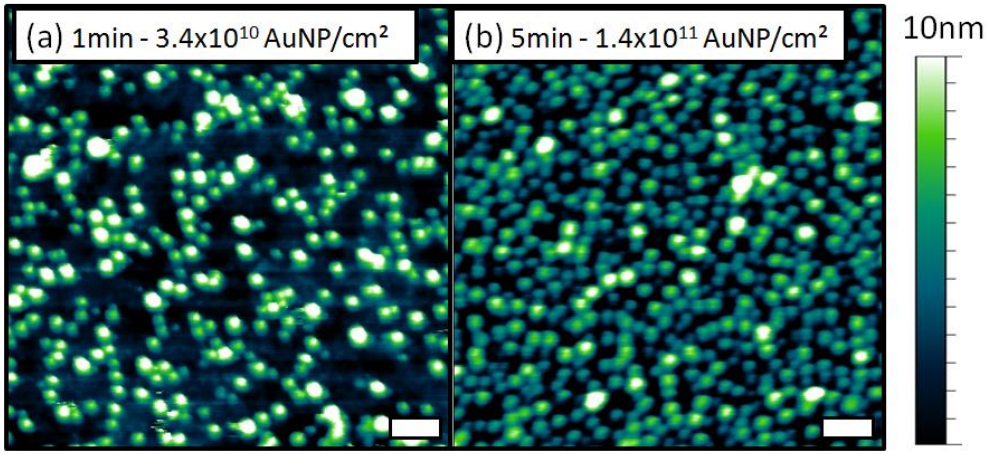

Figure 6.3: *AFM images of Natan AuNP deposited on a functionalized surface. Two deposition times have been tested: 1min (a) and 5min (b). Scale bar: 50nm.*

6.3.4 Removal of ligand by annealing

One origin of STS measurement instabilities might be the presence of ligands around the metallic nanoparticles. Ligands are organic molecules that prevent nanoparticles from

agglomerating when they are in the aqueous solution. However, they act as electric insulators with sometimes hardly predictable properties and this is why their removal is important. The three NP preparations we have selected for the present study are characterized by the ligands with weak adsorption strength: ascorbate for AuNPs prepared with ascorbic-acid and citrate for Turkevich and Natan techniques. Unlike thiol commonly used to stabilize gold nanoparticles, citrate and ascorbate are easily replaced by other adsorbates in solution[161,162]. This is why we investigate the effect of a short annealing in ultra-high vacuum (with temperature from 100 to 250°C) on various samples as a way for removing the organic stabilizing layer.

Regarding the effect on the deposited NP, they were checked with AFM before and after the 150 °C vacuum annealing process. The size distribution was found to be similar, as shown in **Table 6.1**. For a suspension of Ascorbic AuNP the average diameter was found to be 8.2+/-3.9 nm before annealing and 9.6+/-4.4 nm after annealing. These results are in agreement with published results: the melting temperature of 5 nm AuNPs is known to be 800 °C[163]. Moreover no changes in the crystalline structure of the AuNPs was detected upon annealing at temperatures below 300°C[164].

Regarding the effects of annealing on the GOM, a surface is first imaged using our UHV-STM at room temperature without any further treatment. Typical results show instability of the surface and difficulty in obtaining a clean image, in the form of horizontal lines in the images that are characteristic of sudden changes in the tunneling current measurement (**Figure 6.4**a). This is caused by molecules physisorbed on the surface such as water molecules, ligands of the

AuNP or molecules remaining from the deprotection, activation steps. These molecules tend to attach to the tungsten tip and create alternative current paths that result in highly unstable scans. Therefore annealing is a decisive step and three temperatures have been tested for a fixed 30 min annealing time. As shown in **Figure 6.4** after a 250°C annealing, STM images show that the surface is damaged (**Figure 6.4**c): dark areas with almost no AuNPs are detected in many parts of sample. The alkyl chains grafted on silicon are known to be stable up to 400°C[165]. However, since these damaged area exhibit a significant decrease in the number of gold nanoparticles, the alteration must be at the top part of the molecule where the amine group is located. No single electron transport was observed on the few AuNP present in these areas (only 2 AuNP were encountered). **Figure 6.4**b shows a SiC_{11} GOM with Turkevich AuNP after a 200°C annealing. The STM imaging is straightforward and homogenous proving that the surface has not been damaged. For all the other experiments, we carried out an annealing at 150-200°C for 30 min under UHV and it proved to be optimal.

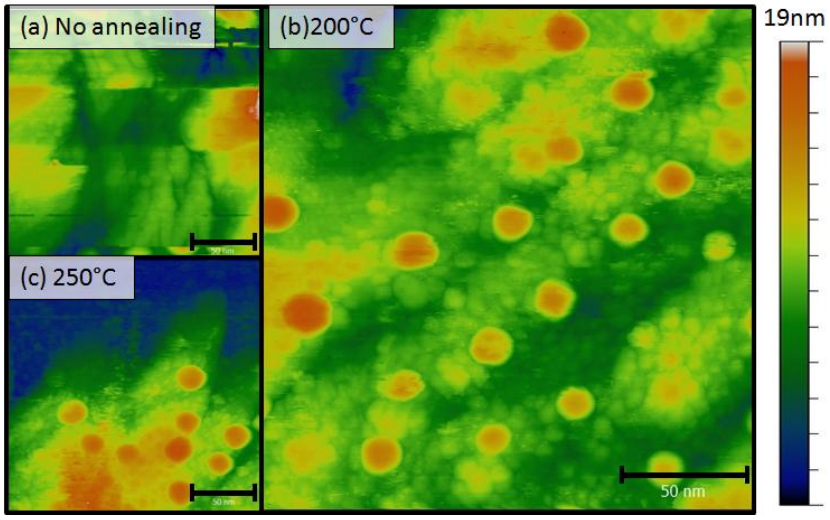

Figure 6.4: *STM images of an activated SiC_{11} surface on silicon with gold nanoparticles deposited on top (using Turkevich technique). With no annealing (a), the surface is difficult to image due to a too high amount of physisorbed contaminants. With a 200°C annealing (b) we have a proper image but 250°C annealing (c) blue area start to appear on the surface that could be due to oxidation or degradation of the organic layer. Scale bar: 50nm.*

6.3.5 Quality of Si/GOM interface:

It is well known that silicon quickly oxidizes[166]: for example the image of a clean Si(100)-2x1 is completely blurred after 5h STM imaging in a 10^{-10} mbar vacuum chamber, which corresponds to 5 sec stability in a 10^{-6} mbar vacuum chamber[167]. Silicon passivation is a serious challenge. The SiC_7 and SiC_{11} surfaces studied in this work successfully take up this challenge and the influence of oxidation was studied as follows: some samples functionalized with SiC_7 were kept for two days in air. FTIR (see **Figure 6.5**) and XPS measurement (see **Figure 6.6**) reveal that oxidation is considerably slowed down as we already discussed in our previous study[16],. In **Figure 6.5**, we show transmission FTIR data for the UV-SiC_7 with the amine terminal group and referenced to the oxide-free H-terminated Si(111) surface. The negative peak

at 2083 cm^{-1} is due to the replacement of Si−H bonds with Si−C bonds during the UV hydrosilylation process. Comparison of the area of this peak with the positive one in the oxide-free Si(111) spectra (referenced to the *oxidized* clean surface, not shown here) provides an estimate for hydrogen coverage of roughly ½ of the surface[15]. Half of the Si-H bonds were replaced by the active molecule in a homogeneous manner. The band at 1713 cm^{-1}, corresponds to the C=O bond of the ester (see **Figure 6.1**a), the vibrations at 1280 and 1410 cm^{-1} correspond to the C-O bond, and 1461cm^{-1} is assigned to the bending mode of the methylene groups of the alkyl chain. The carbon chain is also identified by its 2855 and 2920 cm^{-1} stretch modes (CH_2). The black spectrum corresponds to a pristine sample and the red spectrum to the same sample after two days in air. The latter shows evidence for some oxidation with absorption bands at 1080 and 1240 cm^{-1} (TO and LO modes of SiO_2), which are negligible for the pristine one. The presence of a third carbon peak at 2988cm^{-1} (CH_3) suggests that there is some adventitious hydrocarbon at the surface as well. **Figure 6.6** shows XPS measurements performed only on a UV-SiC_7 sample right before gold attachment, as corresponding measurements on samples prepared by thermal hydrosilylation (SiC_{11}) have already been published[16]. There is no intensity indicative of oxidation (i.e. a peak at 103.1eV) in the black curves, confirming that the sample remains stable when stored in a controlled atmosphere (N_2(g) glove box with <0.1ppm of oxygen and water). The red curve shows that oxidation starts to form at the interface when the sample is placed in air for two days. An estimate of oxidation can be derived from the XPS measurements by comparing the area of the shifted core-level Si 2p peak at 103.1eV, normalized to the bulk Si, with the area of the C1s peak (associated with C=O) of a pristine surface (which represents ½ of

a monolayer). We estimate that the amount of oxidized silicon atoms correspond to 25% of a monolayer.

STM images of the oxidized sample show some dark areas that differ from those observed when over-annealing the sample. They appear “more noisy”, an observation associated with oxidation. The insulating effect of the oxide makes the current less stable leading to this apparent “noise”, and preventing a good imaging of the topology. The images show that the oxidation is not homogeneous on the surface: it is a localized phenomenon, starting with a patch of silicon oxide that spreads with time. It is possible to encounter nanoparticles on these areas, but estimation of their size is inaccurate. Once again, no single-electron transport has been observed on AuNPs on or next to these areas, indicating that a clean oxide-free surface is necessary for devices purposes. For characterization purposes, a sample with some oxidized areas can still be used under UHV for single electron transport if NPs are selected *away* from these altered areas, *i.e.* measurements should only be performed on NPs grafted to oxide-free Si patches.

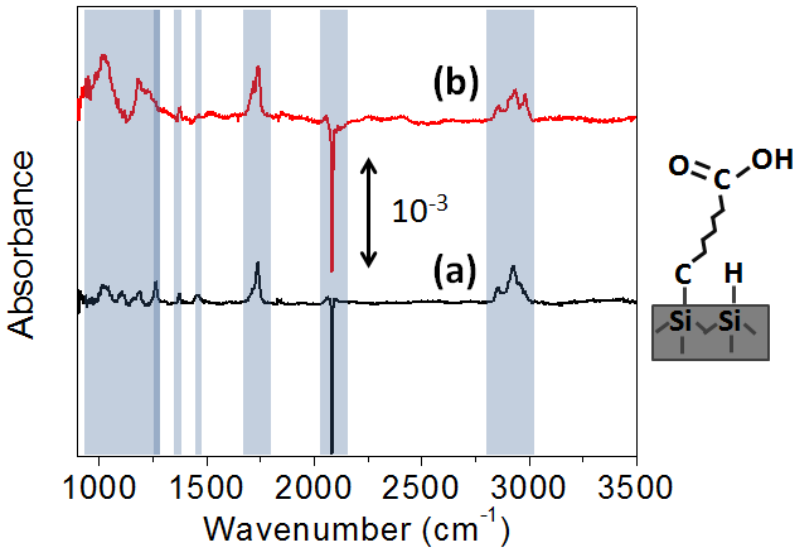

Figure 6.5: *FTIR spectra of the functionalized surface after deprotection of the carboxylic acid for the SiC_7 molecule (b) and after two days in air (a). All the characteristic peaks of the molecule are being identified on both samples. The sample that stayed in air sample shows signs of oxidation with the apparition of the TO an LO peaks and some carbon contamination.*

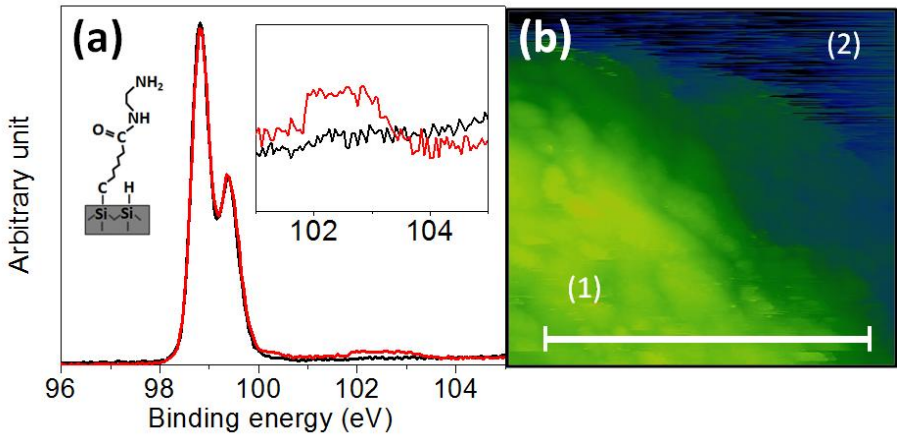

Figure 6.6: *XPS spectra of the Si2P peak (a) taken after activation of the attached SiC_7molecule (black) and after leaving it in air for 2 days (red). The black curve show is characteristic of an oxide free surface whereas the red curve shows the formation of an oxides spot corresponding to roughly ¼ of a monolayer. The insets show a zoom around 103eV where the oxide peak is. STM image (b) of an oxidized sample shows that noisy dark area (2) start to appear near pristine areas (1). The noisy area has been attributed to localized oxidation spots. Scale bar: 50nm.*

6.4 Discussion

In this chapter, we mentioned several reasons that may degrade the single charge behavior of our DBTJ. Single electron transport has only been observed with oxide-free surface that went through a cleaning and ligand-removing process (30min 150ºC annealing). The fact that no positive results have been obtained without annealing can also be explained with recent work from Xu *et al.*in 2009. They have shown that ligands that surround a deposited nanoparticle widen the Coulomb blockade gap: Increasing the concentration of surrounding molecules (hexane) shift the first step to higher bias[168]. With a 6.3nm AuNP on a gold substrate they shift the first step from 0.2V to 1.8V which, if applied to our asymmetrical structure (Silicon substrate instead of gold), should displaced the first step to bias that we have not investigated (>2V). According to results from **Table 6.1** and **Figure 6.2** we conclude that Natan NPs provide the most reproducible nanoparticles and the most spherical: their shape best matches the ideal DBTJ of **Figure 6.1**. Turkevich NP are too large and ascorbic have ill reproducible shape and sizes. However, if no active molecules have been observed with Turkevich AuNP, positive results have been obtained with the two other synthesis techniques and with both linker (SiC_7 and SiC_{11}) as shown in **Figure 6.7**. As stipulated by previous study[68], small NPs are required for single electron transport. In particular, theoretical models recommend a diameter smaller than 5nm for single electron observation *at room temperature* (see **CHAPTER 2**).

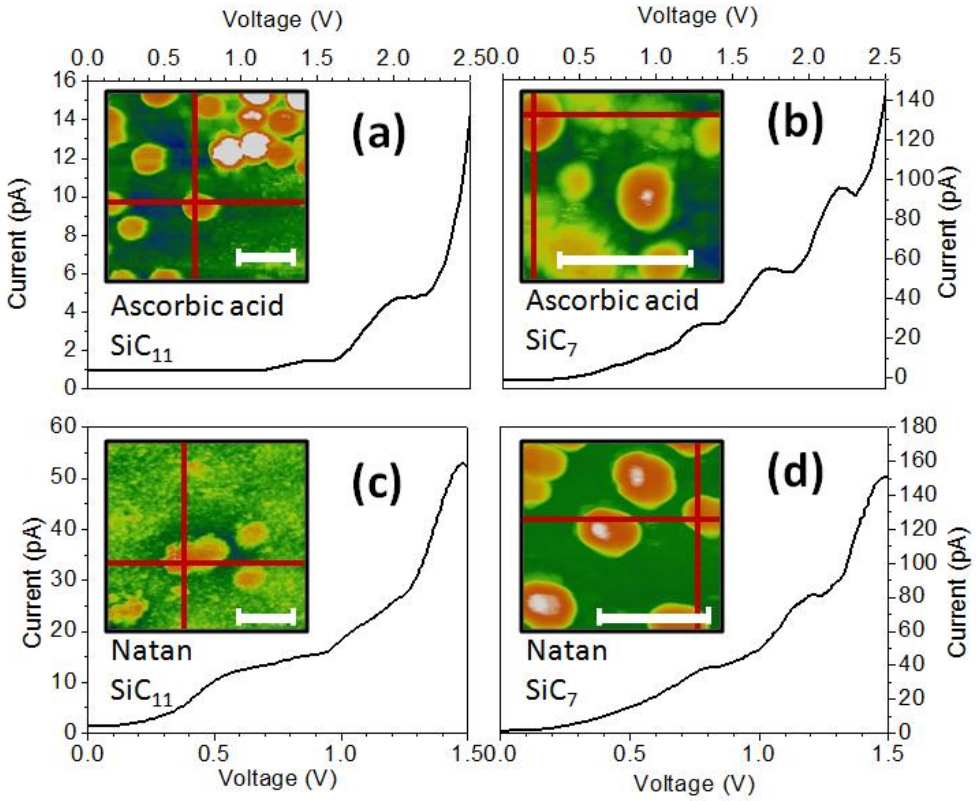

Figure 6.7: *Examples of STS measurements performed on the different surfaces. Silicon surface functionalized with SiC_{11} molecule with an ascorbic acid AuNP of 9nm grafted (a) and a Natan AuNP of 6nm grafted (c). Silicon surfaces functionalized with SiC_7 molecule with an ascorbic acid AuNP of 6nm grafted (b) and a Natan AuNP of 6.5nm grafted (d). Each STS show staircase shape that is characteristic of single electron transport through coulomb staircase phenomena. An inset for each curve shows an STM image of the investigated nanoparticle. All measurements are done at 30K. Scale bar: 50nm.*

We also assess the question of the influence of crystallinity on electron transport. Lu *et al.* report in 2003 specific Coulomb blockade I-V curves on amorphous and monocrystalline palladium NP[144]. They observe additional steps with monocrystalline NP compared to amorphous one and they explain it with discrete resonant tunneling effect that is not visible with amorphous NP because of the shorter lifetime of electronic states. However, they do not discuss reproducibility of results for both types of NP and we propose a statistical approach to tackle this

problem. On the basis of the analysis carried out with HR-TEM we can link crystallinity and STS results. For instance, images shown in **Figure 6.2** shows representative AuNPs obtained by the three different synthesis methods, and the statistical results from a large number of dots (see **Table 6.2**: the total number of AuNP investigated is displayed in the "tot." column) in shaded circles. No particles made by the Turkevich method are single crystal, which may be an important clue to their inactivity. In contrast, 31% and 47% of AuNPs obtained with Ascorbic acid and Natan methods, respectively, are single crystals. **Table 6.2** summarizes these data, including the percentage of occasionally active and consistently active AuNPs for these three fabrication methods. For AuNP particles synthesized with the ascorbic acid method on a SiC_{11}-functionalized surface, 41% of particles are occasionally active and 8% of particles are consistently active (for a total of 12 AuNPs). On a SiC_7-functionalized surface, 52% of particles are occasionally actives and 12% of particles are consistently actives (for a total of 25 AuNPs). With the Natan method, 45% of particles are occasionally actives and 9% consistently actives on SiC_{11} (for a total of 11 AuNP), and 63% occasionally actives and 19% consistently actives on SiC_7 (for a total of 16 AuNP). These results are summarized in **Table 6.2** and suggest that an increase in the monocrystallinity leads to a higher yield reproducibility of single-electron phenomena observation in AuNPs with similar sizes. A possible interpretation is that the quality of the interface between the nanoparticle and the GOM is better when dealing with single crystals. For monocrystalline NPs, the probability that the gold surface faces only one crystallographic plan is higher. In contrast, polycrystalline particles can offer multiple parallel current paths between the gold and the silicon bulk. Single electron transport can still be obtained

with polycrystalline particles if the orientation with respect to the surface is optimum (*i.e.* one plane only), but the likelihood is lower than for single crystals.

	TEM results				STS results			
Synthesis technique	***Average AuNP diameter***	***Standard deviation***	***% mono-crystalline***	***Tot.***	***% Active AuNP SiC_{11}***	***Total***	***% Active AuNP SiC_7***	***Tot.***
Turkevich	*16nm*	*2*	*0*	*92*	*0*	*18*	*0*	*/*
Ascorbic acid	*8nm*	*3.5*	*31*	*213*	*8+41 =49%*	*12*	*12+52 =64%*	*25*
Natan	*7nm*	*2*	*47*	*34*	*9+45 =54%*	*11*	*19+63 =82%*	*16*

Table 6.2: *summary of STS and TEM results on the three different synthesis techniques*

The above results also point to the dependence on the thickness of the GOM. A thicker (*i.e.* SiC_{11}) monolayer appears to yield a lower amount of occasionally and consistently active AuNPs compared with thinner (*i.e.* SiC_7) monolayer. This may be due to the lower tunneling current through thicker organic layers, making it harder to detect single electron phenomena. The measured current is lower and closer to the noise level of the electrical measurements. The current scale for STS measurements is hardly reproducible: it is highly dependent on parameters that are challenging to control such as drift, temperature, quality and shape of the tip (see **CHAPTER 7.5.1**). Typical current for an STS measurement on an AuNP (active or not) on SiC_7 has a value of 174 ± 108pA for V=1.5V at a current setpoint 40pA. On SiC_{11}, this value is 68 ± 41 pA. It shows that, even though the values fluctuate a lot, the typical current for the longer chain is several times lower. Step heights have been measured on a selection of active nanoparticles (both Natan and Ascorbic acid) which have been investigated with the same current setpoint (40pA). Results give a step height of 29±13pA for NP on SiC_7 (total: 41curves)

and 11±7pA for NP on SiC_{11} (total: 26 curves). This shows that, as expected, the typical step height for an active AuNP on SiC_7 is higher than on SiC_{11} even though the value can change a lot from one measurement to another. In the lower end of the step height values for AuNP on SiC_{11} we have current in the order of a few pA: it becomes comparable with the noise level of our STM (2-3pA), therefore the reliability of these value can be questionable and there may be lower scale steps that we couldn't accurately measure. Because of its higher current flux, SiC_7 is a better choice for single electron transport detection. However, one must consider that SiC_{11} GOM is a more stable surface (lifetime: 2 weeks in air) than SiC_7 GOM (lifetime: 3 days in air).

6.5 Conclusion

Our study purpose was to have a better understanding on the parameters that are involved in the making of a reliable and reproducible DBTJ. Our structure is based on the grafting of a molecular layer which would in turn be exposed to uncontrolled environment. Oxidation and cleanness of the sample were assessed and determined to be critical parameters: no single electron can be observed in a reliable way on an unclean or oxidized surface. Three types of AuNP have been tested and results show that Natan method provide the best reproducibility compared to ascorbic acid method and Turkevich method. This is explained by the influence of another parameter: AuNP crystallinity. We have shown that, when the amount of monocrystalline nanoparticles is increased from 31% to 47%, more actives particles are then obtained (from 64% to 82%). The thickness of the GOM has also been identified as an important parameter because of the technical limitation of the detection system. With a longer chain steps

corresponding to the transport of one electron can be in the order of magnitude of only a few picoamperes, which is in the order of the signal to noise ratio of an STM. This is why shorter chains are preferred despite their shorter life time in air. After optimization of our architecture with respect to the described parameters, we observe single electron transport in 82% of the AuNP grafted on our surface. However, consistency of such observation can vary with time in one particle: this is attributed to the use of an STM tip as an electrode. An STM tip should be outperformed by a dedicated metallic contact that would remain stable throughout the whole measurement. On the other hand, it is interesting to compute the average residence time of the electron in the AuNP for both organic layers. In the case of SiC_7, a step height of 29 pA yields an average residence time of an electron of $\tau = \frac{e}{\Delta i_{step}} = \frac{1.6\times10^{-19}}{29\times10^{-12}} = 5$ nsec. In the case of SiC_{11} $\Delta i_{step} = 11$ pA and this residence time is $\tau = 14$ nsec. If the goal were to fabricate single electron memories, the retention time is far too small. But this provides a starting point for designing thicker insulating layers and engineer single electron memories with reasonable storing times. In the next chapter however, we will rather discuss another device, single electron transistors where this quick electron flow is beneficial.

CHAPTER 7

COULOMB BLOCKADE: CORRELATION BETWEEN EXPERIMENTAL AND SIMULATED DATA

7.1 Introduction

In this chapter, we are going to use the structure described in the two previous chapters. We wish to correlate experimental measurements with simulated data. However we are aware that it is challenging to provide accurate interpretation of STS data because several parameters are hardly controlled and therefore difficult to include in a model. We can cite a few: the mechanical drift of the STM tip, the actual shape of the tip, or the presence of contaminants on the tip. STM operates at constant current mode, which means that the distance between the tip and sample can vary depending on the nature of the underlying surface. Its actual value cannot be easily estimated and it is sometimes hard to know whether a change in current is due to a change of conduction of the molecules or a change in height of the tip. Akkerman *et al.* have also shown in a review about molecular conduction 2008 the difficulty of obtaining reliable and reproducible data with organic compounds[87]. In most published work, SIMON, a software based on the orthodox theory (see orthodox theory in **CHAPTER 2**), is used to propose simulation for simple systems[169]. We are going to use a program that has been developed by the Institute for Fundamental Electronics (IEF in Orsay, France) and which was designed to model single electron transport through a metal nanoparticle (NP) between two metal electrodes. This software allows us to modify at ease some parameters such as the barrier height, permittivity or dimensions of the system. However, since its main purpose is to simulate DBTJ with metal contacts it needs to be modified to be applied on our system: one of the electrodes is made out of silicon. One of the main differences regarding the two systems would be the introduction of

another phenomenon, specific to SCs: band bending. This chapter goes over the method we use to tackle this problem.

7.2 IEF's simulation software

7.2.1 Presentation

This simulation program has been developed by Johann Sée and Philippe Dollfus in the IEF[170,171]. It is based on the orthodox theory described in the **CHAPTER 2**. It has been coded using Matlab and can provide an I-V curve depending on several parameters that can be changed depending on the geometry of the system (*e.g.* size of dot, thickness of GOM), the nature of components of the system (*e.g.* electronic affinity, free electron mass) or condition of measurement (*e.g.* temperature). The simulated structure is shown in **Figure 7.1**. This chapter is not going to provide all the details regarding the theoretical calculation that has been done to develop this software. However, it will provide some key elements and approximation that are used.

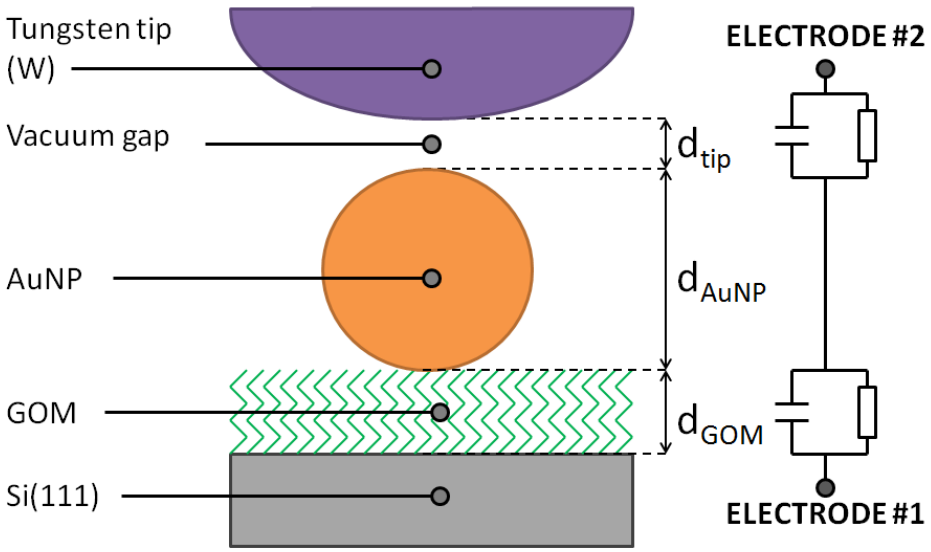

Figure 7.1: *Scheme of the modeled structure with equivalent electronic schematic*

7.2.2 Parameters used

In this software, it is possible to change a lot of parameters depending on the components used and the architecture. These are the one considered

Architecture

Dimension of the system have a huge influence on the electric behavior of the structure: single electron transport is highly dependent on the capacitance of the system and it has been shown in the **CHAPTER 2** that typical length must be in the order of a few nanometers to tenth of nanometer. Parameters that can be changed are:

- ***d_{tip}:*** this is the distance between the tip and the AuNP. The medium in between is considered to be a perfect vacuum. Its value is difficult to estimate experimentally and it was set to be d_{tip}=1 nm.
- ***d_{AuNP}:*** this is the diameter of the AuNP. The gold AuNP is considered to be perfectly spherical and homogeneous. It has no surrounding ligand. This value has been changed from 3 to 10nm depending on the size of the AuNP in the experimental data.
- ***d_{GOM}:*** this is the thickness of the organic layer. The organic layer is considered to be homogeneous and in direct contact with the AuNP. This value has been set to be 1.6nm and 1.3 nm for long chain (SiC_{11}) and short chain (SiC_7) respectively.

Effective electron mass

Effective electron mass is the mass that a single electron seems to have when present in a certain medium. Depending on its surrounding, an electron can be considered as a factor of m_e (9.11×10^{-31} kg), the true mass of an electron ($m^* = A\ x\ m_e$). The factor usually varies from 0.01 to 10. In our case, the free electron mass has an influence on the current density J of the transmitted wave (direct tunneling in **Table 2.2**). Values chosen for the different materials of the system are displayed in **Table 7.1**.

	Effective electron mass	***reference***
GOM (m^*_{GOM})	*0.25 m_e*	*94*
Silicon (m^*_{Si})	*0.26 m_e*	*145,172*
Vacuum (m^*_{Vac})	*1 m_e*	*173*
Gold (m^*_{Au})	*1 m_e*	*/*
Tungsten (m^*_{W})	*1 m_e*	*/*

Table 7.1: *Chosen values for effective electron mass in our system.*

Electronic affinity and work function

Electronic affinity is defined for a given semiconductor as the energy needed to take an electron from the bottom of the conduction band inside the material and drive it to immediate proximity of this material in the vacuum. The work function of a compound on the other hand is defined as the energy needed to remove an electron from the Fermi level of a solid to a point in vacuum in the immediate vicinity (*i.e.* far enough so that the charge is not sensitive anymore to its electrostatic image and close enough so that the surface is homogenous beneath the charge) of the surface. The work function is usually considered to be a property of a surface of a material rather than a property of the bulk. It can be modified depending on doping level or contamination. Values chosen for the different materials of the system are displayed in **Table 7.2**.

	Work function (eV)	***Electronic affinity (eV)***
GOM	W_{GOM} =2.0	/
Silicon	/	χ_{Si} =4.05
Gold	W_{Au} = 5.1	/
Tungsten	W_W = 4.5	/

Table 7.2: *Chosen values for the work functions in our system.*

The values of the work function give the barrier heights of the two tunneling junction using the equations:

- Silicon-AuNP barrier (1): $\begin{cases} right: \varphi_{R1} = W_{Au} - W_{GOM} \\ left: \varphi_{L1} = W_{Si} - W_{GOM} \end{cases}$ Eq 7.1

- AuNP-tip barrier (2): $\begin{cases} right: \varphi_{R2} = W_W \\ left: \varphi_{L2} = W_{Au} \end{cases}$ Eq 7.2

The resulting band diagram can then be deduced and corresponds to the one in **Figure 5.8**a and recalled here in **Figure 7.2**. Silicon work function W_{Si} is obtained as $W_{si} = \xi - \chi_{Si}$ where ξ is the difference between the valence band E_C and the Silicon Fermi level $E_{F,Si}$.

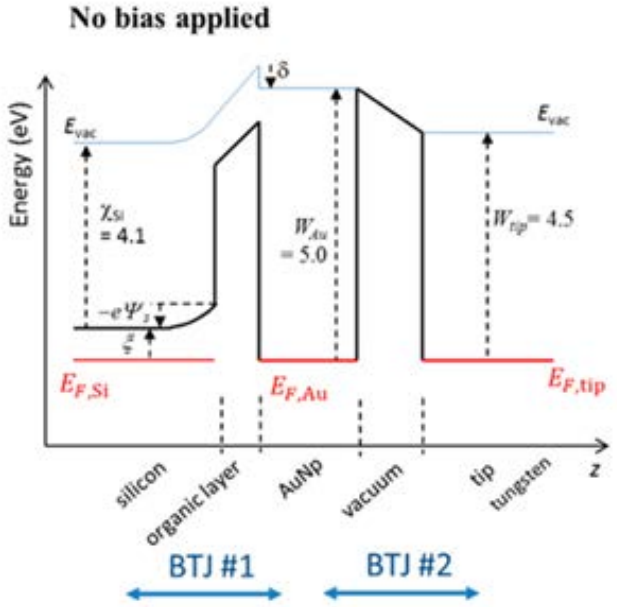

Figure 7.2: *Energy Diagram of the DBTJ. The first barrier tunnel junction is between the silicon and the selected AuNP, and the second BTJ is between this AuNP and the STM tip. From Caillard et al. Langmuir (2013).*

Permittivity

The permittivity is the measure of the resistance in the formation of an electric field in a medium. Basically it shows the influence of an electric field on a medium and how the polarization due to the fixed charges of the medium is opposing it. Especially in the case of dielectrics. It is usually noted $\varepsilon_r\varepsilon_0$ where ε_0 is the vacuum permittivity ($8.854.10^{-12}$ F/m) and ε_r is the relative permittivity of the material. In our case, we set in the case of the GOM ε_{rGOM} = 2.2. This value is typical for organic layers as shown in various publications[83,84,93,174]. Notice that this is the static value of ε_r ; the dynamic value (obtained with ellipsometry for example) is linked to the optical index ($\varepsilon_r = n^2$) and was measured to be 3.9[7] for our organic monolayer.

7.2.3 Capacitances of the system

As seen in **CHAPTER 2** capacitances of the system are critical parameters that have a huge influence on the shape of the Coulomb staircases steps. These capacitances depend on the nature of the chosen components in the system, but mostly on the dimension of the said system. An analytic computation of the two main capacitances of the system is implemented on the software: the capacitance between the tip and the gold nanoparticle (1) and the capacitance between the gold nanoparticle and the silicon substrate (2). The first one is approximated as the capacitance between a sphere and a plane where the plane is the tungsten tip and the sphere is the AuNP. This approximation is based on the assumption that the tip "diameter" is significantly bigger than the AuNP diameter. This approximation is reasonable since AuNP have a typical diameter of 5 nm (radius, 2.5 nm) and the tip radius in our STS experiment is evaluated at 10 nm The second capacitance is also assimilated as the capacitance between an infinite plane and a sphere where the sphere is the AuNP and the plane is the silicon substrate. **Figure 7.3** sums up the assumptions made.

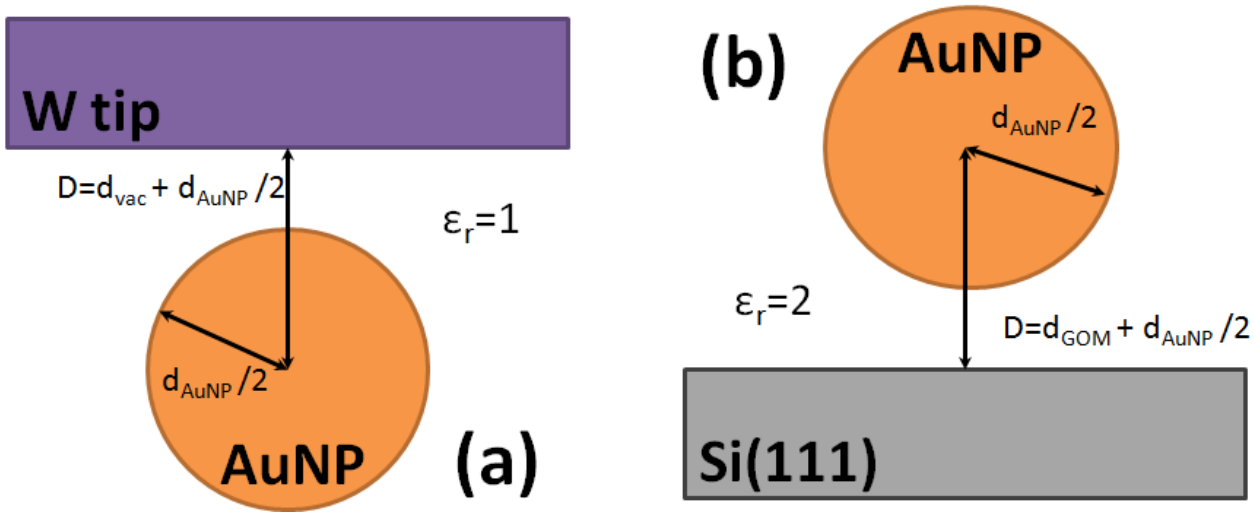

Figure 7.3: *Analytical model used for the computation of the first (a) and the second (b) capacitance.*

The equation that gives the capacitance of a sphere in front of an infinite plan is[175,176]:

$$C = 2\pi\varepsilon_r\varepsilon_0 d_{AuNP} \sum_{n=1}^{\infty} \frac{sinh\left(ln\left(D+\sqrt{(D^2-1)}\right)\right)}{sinh\left(n\, ln\left(D+\sqrt{(D^2-1)}\right)\right)} \qquad \textit{Eq 7.3}$$

Where $D = 2d/d_{AuNP}$.

7.2.4 Current flow approximation

The computation of the current flow through the system is carried out using the probability of an electron to transfer from the tip to the AuNP and from the AuNP to the silicon substrate. The geometry has been approximated to planar surface in order to simplify the calculation. The gold nanoparticle is then assimilated as a cylinder, as seen in **Figure 7.4**, with a

cross section equal to 1/10th of the one of the actual nanoparticle. This approximation is based on the fact that the majority of the current tunnel through the apex of the tip because of the exponential dependence of the barrier transparency with tip-sample distance. Moreover, this parameter sets the order of magnitude of the current flow and the value of 1/10 was adjusted for computing a current in the order of 10 pA. We have then $S_G = S_D = \pi {d_{AuNP}}^2/10$.

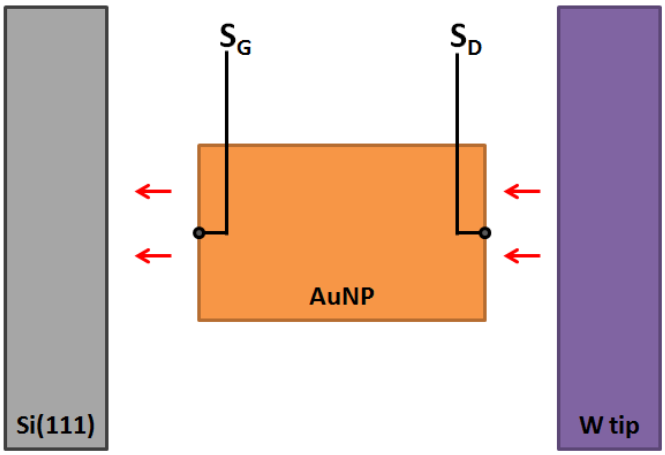

Figure 7.4: *Geometry for calculating the current flow through the nanoparticle. The spherical shapes are replaced with planar surfaces. S_D and S_G are taken as 1/10 of the particle cross section ($4\pi R^2$).*

7.3 Additional consideration regarding simulations

7.3.1 HOMO-LUMO of the GOM

To confirm our approximation that the GOM should behave like a tunneling barrier, conductive AFM in UHV measurements have been done on a Si-C_7 sample using the equipment available in Miquel Salmeron's group at University of California Berkeley (USA). Results of

voltage sweep in contact of the GOM shown in **Figure 7.5** suggest that the HOMO-LUMO gap is around 5-6eV. This is a bit smaller than data found in the literature which reports HOMO-LUMO gap in the order of 7-8eV[84,86]. However this value is high enough for us to consider that the molecular layer is behaving like a tunneling barrier at the voltage bias we are using for this study (-1.5/1.5V). We assume that the transport in the GOM is dominated by neither the HOMO nor the LUMO in the voltage range used. As a consequence the GOM can be modeled as a regular tunnel barrier as predicted in **CHAPTER 2**.

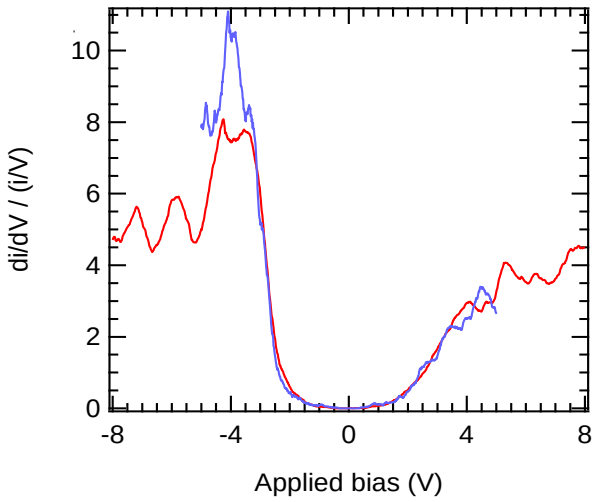

Figure 7.5: *Sweeps of voltage done in contact of two different points on a SiC_7 GOM using a conductive AFM. Each curve is an average of 10 I-V curves. Results suggest a bandgap roughly equal to 5-6eV.*

7.3.2 Band Bending

As shown before, all materials used in our system have different work functions, therefore, once equilibrium is reached at zero bias, a built-in potential is formed. Since the first electrode is made out of a non-degenerately doped SC, silicon, the built-in potential will induce

the creation of an electrostatic field that will create a depletion layer (or space charge region) because of the bending of the bands of the SC[145,146]. This is why once a voltage bias is applied on the system a significant part of the potential is dropped in the depletion region. We must then distinguish the voltage applied on the whole system V_{STM} and the voltage effectively applied at the interface between the silicon bulk and the GOM V_{interf}. Calculations are done to establish a relation between the two potentials.

Most studies done on Coulomb blockade have been carried out using metallic compounds as electrodes and theoretical models have been applied to experimental measurements using standard approach such as the orthodox theory[150,155,177]. To our knowledge, no work has been done on model that takes into account asymmetrical systems where band bending must be considered. We wish to propose a numerical evaluation of the potential V_{interf} as a function of the applied bias V_{STM}.

Principle of the calculation

Using the previously described parameters, we can make a band diagram in **Figure 7.6**. We consider that $\chi_{Si} = 4.05$ eV and the work function can be deduced using the equation:

$$W_{Si} = \chi_{Si} + kTln(N_C/N_D) \qquad Eq\ 7.4$$

Where N_D is the density of donors and N_C is the density of states of the conduction band (a constant of material). It must be noted that the work function depend on the temperature T.

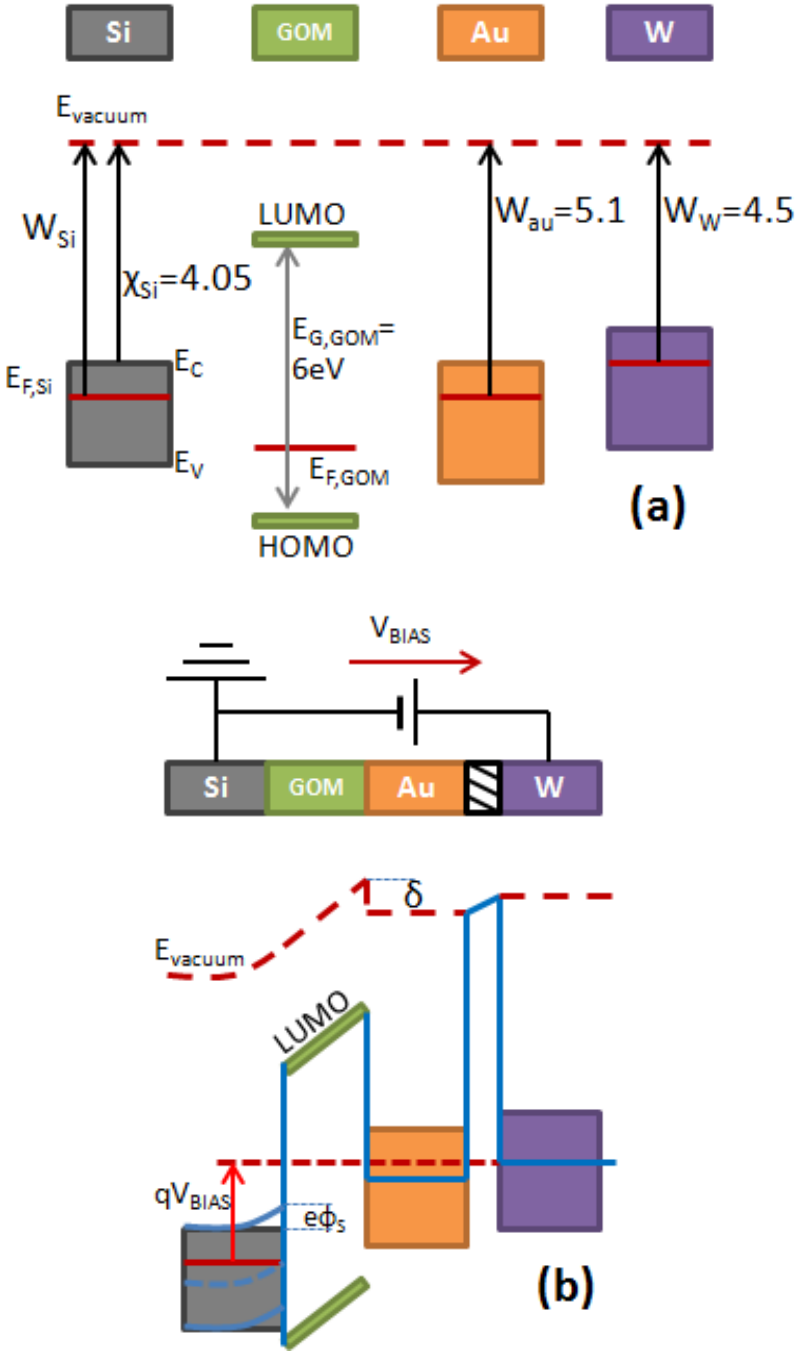

Figure 7.6: *Energetic parameters of the DBTJ, before the electrical contacting of the 4 materials (a) and after contacting when a negative bias of -1 V is applied (b).*

Eq 7.4 works in the framework of the Boltzmann approximation which can be used as long as the doping level is not too high and the temperature not too low. As an example, at room temperature (300K) and with N_D=2.10^{18}cm^{-3} **Eq 7.4** yields W_{Si} = 4.12eV but this is no longer true at 30K. In the case of our STS, which have been acquired at very low temperature, the Fermi Dirac integral must be calculated numerically instead of Boltzmann approximated formula[145]. The silicon substrate is considered grounded as it is the convention in solid state physics. However, it must be noted that in the case of the STM, the convention is inverse: the tips is grounded. Therefore we must make a distinction between V_{STM} and V_{BIAS} (opposite sign). Once the DBTJ is formed, all the Fermi levels align in order to reach a static equilibrium (see **Figure 7.6**a).

Some aspects must be considered:

- When a negative bias V_{BIAS} is applied, the corresponding energy qV_{BIAS} is positive because the charge carriers are electrons (q = -e).
- Because of the difference in work functions between N-doped silicon and gold, electrons will flow from the silicon toward the gold leaving positive holes behind them. An electric field is therefore created (built-in potential) until the electron flow is compensated. In the band diagram it shows up as a positive bending of the silicon bands and is noted $e\phi_S$.
- The built-in potential at the silicon-gold is exactly compensated when we apply the flatband potential on the system. it is given by[145]:

$$V_{fb} = \chi_{Si}/e - W_{Au}/e + (kT/e)ln(N_C/N_D) \qquad Eq\ 7.5$$

- In **Figure 7.6**b, the value δ (in eV) is the molecular dipole of the insulating molecular layer. This parameter takes into account the non uniform charge distribution within the GOM due to difference in electronegativity of the different atoms in the molecules.

Band diagrams in **Figure 7.6** help visualizing the DBTJ. It is important to realize that they are not square but trapezoidal shaped. As pictured, the band bending can have a strong influence on the first tunnel barrier. Therefore it is important to evaluate $e\varphi_S$ and the thickness of the depletion layer, W_{depl}.

Calculation of the potential profile of the DBTJ in a simple case with Southwick model

Free available software can be used to perform preliminary calculations. Southwick *et al.* proposed a model in 2006 that allows the calculation of the electrostatic potential profile at room temperature (T=300K) and without molecular dipole (δ=0)[178]. Results plotted in **Figure 7.7** show a band bending of -0.5V (+0.5V in the energy diagram) with a depletion zone 20 nm thick. It is quite clear that electrons will not be able to tunnel through it but will have to climb it. As a consequence, a voltage of ~0.5V must be applied on top of the potential bias in order to overcome this barrier.

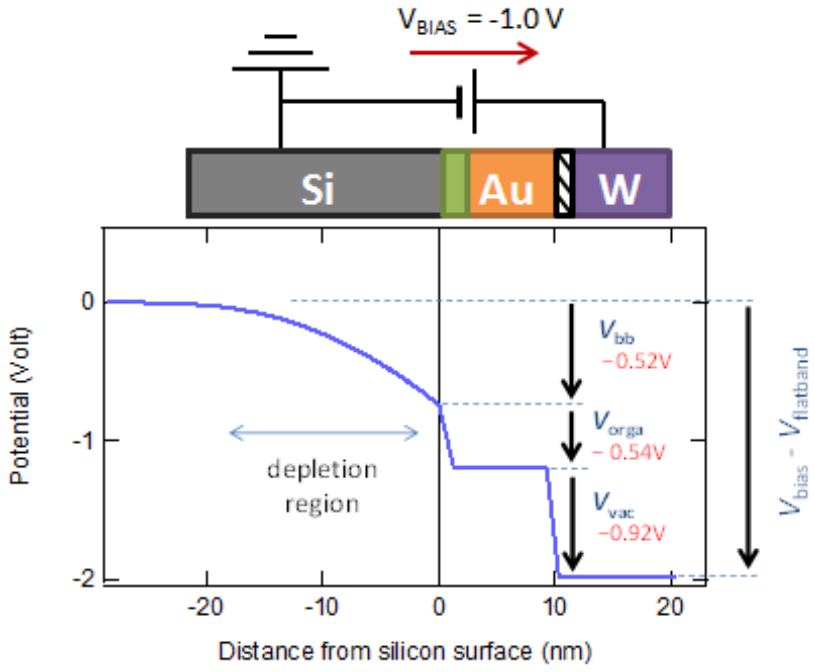

Figure 7.7: *Potential profile of a DBTJ at 300K for a n-doped silicon substrate (N_D = 2.10^{18} cm^{-3}) The values given on the graph correspond to the potential distribution across the different layers when the applied bias is set at -1.0V. The band bending is of -0.52 V and the depletion layer extends over a depth of 20 nm. The flatband potential is V_{fb} = 0.982 V in the present case the molecular dipole was set to 0 in this calculation. Using software from Southwick et al. IEEE (2006).*

Exact calculation for planar DBTJ (1D model)

Despite its usefulness, the model proposed by Southwick and Knowlton[178] is based on the Boltzmann approximation. As a consequence it is only accurate when this approximation is valid: which is not the case when dealing with temperature lower than 100K. Moreover, this model cannot take into account the molecular dipole δ. An alternative model that takes into account these limitations has been programmed with Igor Pro. The Poisson equation is solved in the silicon following the derivation explained by Sze[145] and using the equation:

$$V_{bias} = V_{flatband} + \phi_S + \phi_{GOM} + \phi_{vac} - \delta/e \qquad \textit{Eq 7.6}$$

If we consider only one dimension, the Poisson equation reduces to $d^2V/dx^2 = -\rho(x)/\varepsilon$. In **Eq 7.6** we can see that V_{BIAS} compensates for the potential drop on top of the flatband potential: band bending ϕ_S, the potential across the two barriers (the GOM, ϕ_{GOM} and the vacuum gap ϕ_{vac}) and the molecular dipole δ/e. The calculation principle can be summarized as follows:

- The flatband potential is calculated using **Eq 7.5** or the Dirac integral for low temperatures**.**
- Band bending potential ϕ_S is taken as an input parameter and all other potential are considered as functions of ϕ_S. Once ϕ_S is known, it is possible to derive the electric field at the interface between the GOM and silicon. We assume that the GOM doesn't contain any fixed charges; therefore the electric field is constant across the organic layer. As shown in **Figure 7.7**, the potential depends linearly with the distance from the surface.
- Because of its metallic nature, the electric field in the AuNP is null and the potential is constant. However there are charges located at the surface and that are responsible for an electric field across the gold-vacuum interface. From there, it is possible to evaluate the linear potential across the second barrier (vacuum between the tip and the AuNP).
- The molecular dipole is estimated from the literature[125,174,179,180].

Eq 7.6 therefore gives the bias potential V_{BIAS} as a function of ϕ_S. This can be reversed, giving expressions of ϕ_S, ϕ_{GOM} and ϕ_{vac} as functions of V_{BIAS}. For a simple 1-D case at 300K, our calculation of band bending potential with respect to the applied voltage is in accordance with Southwick model.

Computation of the Fermi-Dirac Integral: cases of high doping and low temperatures

When Boltzmann approximation applies, **Eq 7.4** is obtained with the integration of the following equation of the carrier density in the conductance band:

$$n = \frac{2}{\sqrt{\pi}} N_c \times F_{\frac{1}{2}}\left(\frac{E_F - E_c}{kT}\right) \qquad \textit{Eq 7.7}$$

Where $F_{\frac{1}{2}}$ is the Fermi-Dirac integral given by

$$F_{\frac{1}{2}}(y) = \int_0^{\infty} \frac{\sqrt{x}}{1+e^{x-y}}\, dx \qquad \textit{Eq 7.8}$$

In the case of the Boltzmann approximation, we consider that $\frac{E_F - E_c}{kT} \ll -1$ which simplifies the denominator the integral to $e^{-(x-y)}$. With such simplification, the integral can be calculated by integration by parts and the result is **Eq 7.4**. However, this doesn't hold up in the case of heavily doped SCs and for low temperature: the integral must be calculated.

Approximation to the 3-D geometry

Our calculation were compared with the work done by Feenstra *et al.* on GaAs in 1987 where he calculated the band bending induced by an STM[85] (see in **CHAPTER 2**, **Figure 2.10**). In this simple case of a single tunnel junction, our results are in accordance with Feenstra's (not shown here). However, the case considered here, is a simple one: a 1-D planar tunnel junction. Later, he developed a 3-D model that takes into account the geometry of the end of the STM tip which cannot be approximated as an infinite plane. In his work the tip is considered to have a

hyperbolic shape and that induces a significant change in the band bending[181]. For example the band bending changes from 2.0 eV for the 1-D model, to 0.6 eV when the tip radius is 5nm and has a shank opening of 90°. This calculation was done when the tip was 1 nm away from the sample and with an N-doped SC (N_D = 1.10^{18} cm^{-3}). A FORTRAN program has been made available to calculate these effects in other cases[182]. Unfortunately getting information about the tip shape is challenging and as of today we haven't implemented this 3-D correction. Therefore we make an estimation of the correction factor, using Feenstra's results, and apply this to fit experimental data[181]. The 3-D band bending potential (noted $\phi_{S\,3D}$ is linked to the planar band potential ($\phi_{S\,planar}$) with the relation:

$$\phi_{S\,3D} = \phi_{S\,planar}/\alpha \qquad \textit{Eq 7.9}$$

With α derived from Feenstra's work and indicated in **Table 7.3** below.

NP diameter (nm)	*5*	*7*	*9*	*15*
Corr factor $\boldsymbol{\alpha}$	*3.7*	*3.3*	*3.1*	*2.8*

Table 7.3: *Correction factor for different AuNP diameters.*

7.4 Experimental results analysis

Prior to being able to compare simulated data with experimental one, we need to assess some questions regarding acquired STS data. We need to distinguish actual Coulomb staircase *I-V* characteristics curves from artifacts such as parasitic oscillations occasionally encountered.

Moreover, a statistical study has been carried out so that positions of Coulomb steps are evaluated with various samples and error bars can be calculated. This allows a sound comparison with the calculated Coulomb blockade characteristics.

7.4.1 Parasitic oscillations

As reported in a few amount of publications these past 15 years[113,115,66,183,184], some groups have detected oscillations when dealing with DBTJ. On some of our aging samples, we have experienced the same phenomenon. These oscillations can be mistaken for negative differential resistance because of the decreasing current with increasing voltage. Oscillation period are highly dependent on the overall scanning time of the raster time (time spent by the tip at each voltage in the voltage sweep). Furthermore the frequency is low (multiples of 30Hz)[66] and is not dependent on the size of the AuNPs. Practically speaking, changing the sweeping rate of the STS curve drastically changes the period width of the observed oscillations (see **Figure 7.8**a in our system, and **Figure 7.8**b as reported by Park *et al.* in 2000 when doing STS on silver nanoparticle on a silicon substrate[113]).

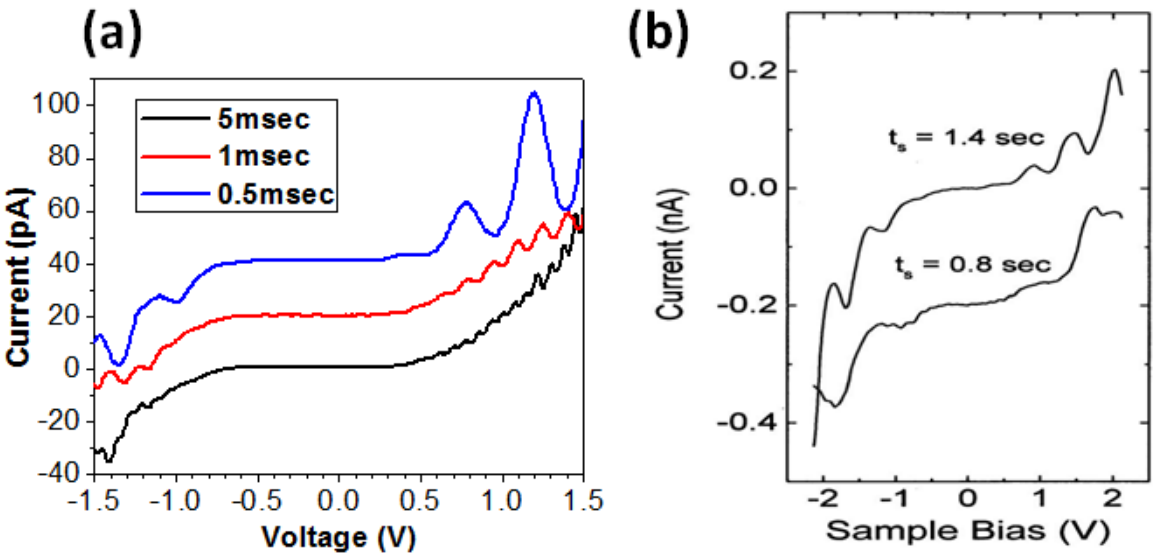

(c) parameters				
Voltage bias	***Current setpoint***	***Sweep voltage***	***Feedback gain***	***Number of points***
-1.5V	40pA	-1.5/1.5V	1.5%	400 pts

Figure 7.8: *(a) STS measurements done on a gold nanoparticle in our system at three different raster times. The other parameters used for these measurements are summarized in (c). (b) Sequentially taken dual I–V curves, on silver nanoparticle deposited on silicon, revealing current oscillations with the different periods, where the scan time t_S is 0.8 and 1.4 sec, respectively. From Park et al. JVST B (2000).*

Origin of theses oscillations is still unknown; they cannot be attributed to Coulomb blockade effect because of their dependence with measurement parameters (raster time). Moreover they are unlikely to be related to the nature of the equipment used (*i.e.* due to electric noise caused by the feedback system of the STM) because of the fact that it is reported by a wide variety of groups with different systems in different area of the world. One group reported it on partially oxidized silicon surface[183]. The attributed the apparition of such oscillations to the

introduction of electron traps due to slow oxidation of their substrate. Xie *et al.* also reported in 2001 that by approaching the tip from the surface, the oscillations tended to disappear[184]: they attributed it to the fact that electrons would tunnel directly to the bulk. They concluded by saying that this phenomenon is closely linked to surface states creation, and approaching the tip allow the electron to not be affected by them. Our case however is a little different since approaching the tip will not change the distance between the AuNP and the silicon substrate at the surface of which electron trap can be formed. Theoretical approach has been considered to model this phenomenon using electron-phonon interaction in electron traps[185]. However it is very complex and, to our knowledge, no recent study has been done to validate it. Nevertheless very recent results obtained by O. Pluchery in M. Salmeron's group in Berkeley tend to show that our samples have the ability to trap electrons for a longer time that initially expected. This phenomenon was detected when doing charging experiments of individual nanoparticles with the tip of a KPFM. This points to some unexpected capacitive phenomena that might show up in the organic layer.

However in the present series of experiments, a systematic method was established to insure that Coulomb blockade is actually detected and not oscillations. A smaller number of acquisition points (around 250 pts for a -1.5/1.5V acquisition compared to 400 points usually) and a faster raster time (1msec instead of 5msec) drastically decrease their occurrence. In order to make sure that the Coulomb staircase observed in our system are not due to this kind of current oscillations, we have decided to use the method proposed by Park *et al.* Once we detect

single electron transport, we change the raster time of the STS measurements and make sure that the step width remain unchanged (see **Figure 7.9**a in our system and **Figure 7.9**b by Park *et al.*).

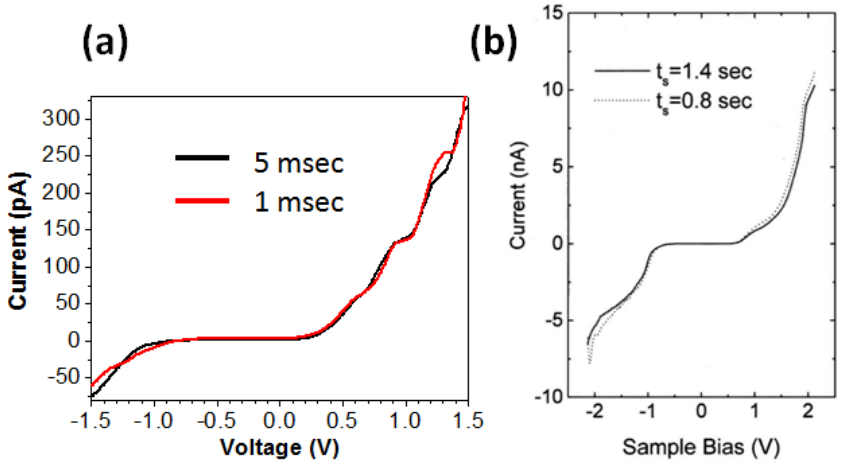

(c) parameters				
Voltage bias	***Current setpoint***	***Sweep voltage***	***Feedback gain***	***Number of points***
-1.5V	40pA	-1.5/1.5V	1.7%	250 pts

Figure 7.9: *(a) STS measurement done on a 5nm AuNP at different voltage raster time (1 and 5msec). Widths of the coulomb staircase's steps remain constant. The other parameters used for these measurements are summarized in (c). (b) Similar observation with STS done on silver nanoparticle from Park et al. JVST B (2000). The time corresponds to the time of the whole acquisition.*

7.4.2 Step width analysis

From the orthodox theory, it is expected that the steps of the Coulomb staircase I-V curves are directly linked to the capacitance of the system and all have the same width for assuming that the system remain stable throughout the whole measurement. A statistical analysis has been done on 30 particles synthesized using Natan techniques (see **CHAPTER 6**) deposited

on a Si(111) SiC_7 functionalized (see **CHAPTER 5**) with a resistivity of 0.02 Ω.cm. Step widths have been measured using the distance between each peaks observed in the derivative of the I-V curve. We have determined that all steps measured on a particle have equidistant width for a positive bias with an error averaged at ±6,8mV. Measurements of step width are plotted in **Figure 7.10** as function of nanoparticles diameter with respective error bars. AuNPs diameter has been estimated using the profile function on STM: this must be noted that this way of evaluating the size of the nanoparticle is not the most accurate as STM is not only influenced by topographic change but also change in density of electronic state. However we can clearly see the linear dependence of step width with respect to AuNP diameter. For example we can see that a AuNP with a diameter of 5nm exhibits Coulomb staircase with equidistant steps and each steps are ~330 ±7mV.

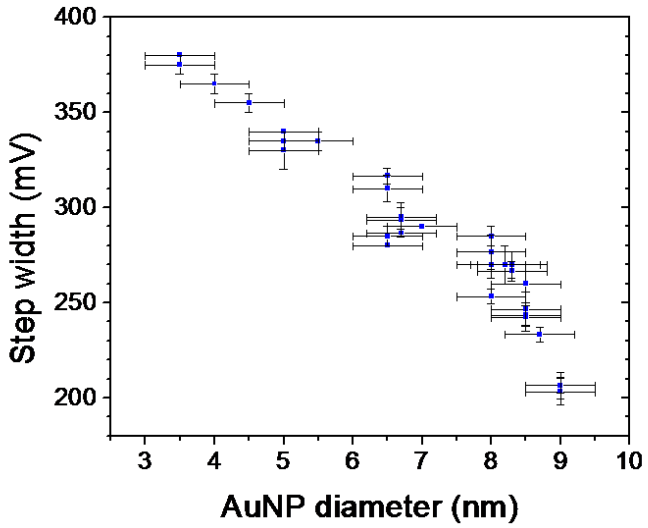

Figure 7.10: *Step width of AuNPs with respect to AuNP diameter. Measurements were done on at 40K 30 AuNP synthesized using Natan technique deposited on a SiC_7 GOM grafted on a N-doped silicon substrate (0.02 Ω.cm). Average error bar: 6.8mV.*

7.5 Simulation results

7.5.1 Example of simulation results using IEF's software

Here are a couple of examples of cases that have been investigated using IEF's software without taking into account the band bending correction.

Influence of tunneling cross section

Influence of varying the tunneling cross section approximation discussed in **7.2.4** can be investigated using IEF's software. The cross section considered for the current flow from the AuNP to the substrate and from the tip to the AuNP is equal to a fraction of the AuNP area. We change it from $S_D = \pi R^2/10$ to $S_D = \pi R^2/7$ in order to check the influence on the Coulomb staircases. Results displayed in **Figure 7.11** for an AuNP with a diameter of 8 nm, suggest that the width of the steps is unchanged but their heights are heavily impacted. This shows that, depending on the geometry of the AuNP, and certainly also the geometry of the tip, the current scale can vary a lot without changing the step width. Therefore we chose to consider the step width to be a more reliable and more reproducible measurement.

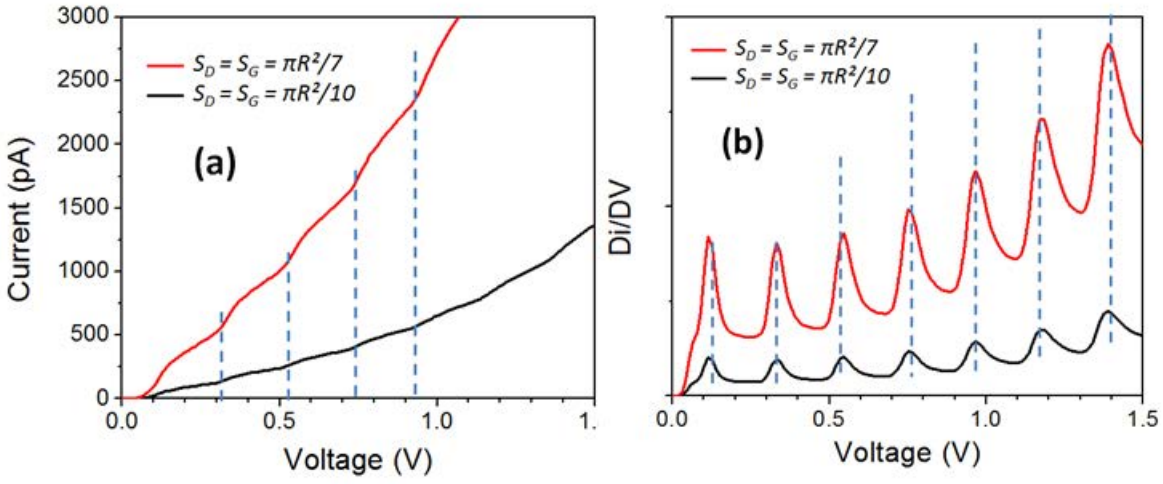

Figure 7.11: *Simulated STS (a) and derivative (b) showing influence of tunneling cross section at T=30K.*

Influence of temperature

We also investigated the influence of temperature on our system. Results showed in **Figure 7.12** for an AuNP with a diameter of 4 nm suggest that the low temperature is critical to observe single electron transport. Even at 30K the steps are quite shallow because the capacitance value of the vacuum gap and the GOM are close (0.8aF and 1.6aF respectively). At 100K the step are barely visible in this simulation and would be hard to be observable in experimental condition because of the noise. At room temperature, no steps are visible.

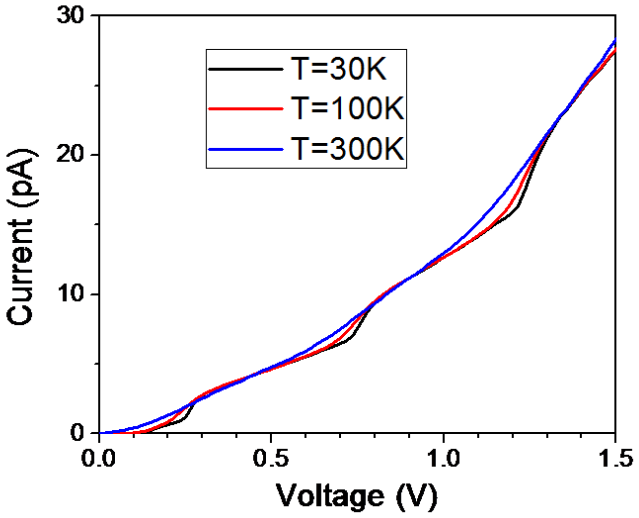

Figure 7.12: *Simulation data showing the influence of temperature on simulated STS on a 4nm AuNP. Temperatures considered are 30, 100 and 300K.*

7.5.2 Band bending calculation results

As shown previously, the band bending is an extra barrier that electron need to climb in order to go through the DBTJ. The reason is that the depletion layer's thickness is around 20 nm for a doping of 2.10^{18} cm^{-3}, which is too wide for electron to tunnel through. We derive the potential effectively applied on the interface (V_{interf}) by subtracting the potential of band bending ϕ_S to the applied bias. We can then plot the V_{interf} as a function of V_{BIAS}.

$$V_{interf} = V_{BIAS} - \phi_S(V_{BIAS}) \qquad \textit{Eq 7.10}$$

It is important to notice that ϕ_S is a function of V_{BIAS}.

Six selected cases for calculating the band bending

Three different doping levels at two different temperatures are considered: low doped N-Si (denoted N), highly doped N-Si (N+) and degenerately doped N-Si (N++). Values of $V_{flatband}$ and V_{thr} are reported in **Table 7.4** and correspond to the boundaries of the three regimes of the SC operation: inversion, depletion and accumulation. Parameters of the simulations are the same as the one reported earlier in this chapter. Columns marked with a (*) correspond to cases where the Boltzmann approximation is not valid and the Fermi-Dirac integral had to be calculated. The correspondence between resistivity and dopant concentration is obtained from an online calculator[186] whose results are based on a 1981 publication[187]. For example, results show that an N+ silicon sample will work in the depletion regime with V_{BIAS} = -1 V at 300K. The regime will change to inversion if V_{BIAS} < -1.427 V. However at 40K, at V_{BIAS} = -1 V, N+ silicon will be in accumulation mode and be in depletion regime if V_{BIAS} < -1.053 V. It will never reach inversion.

Name	***r (Ohm.cm)***	***N_D (cm^{-3})***	***T***	***Ec - Ef***	***$V_{flatband}$***	***V_{thr}***
N	*1-5*	*2.10^{15}*	*300K*	*0.247*	*0.803*	*−0.726*
			*40K **	*0.023*	*1.027*	*−∞*
N+	*0.01-0.02*	*2.10^{18}*	*300K*	*0.068*	*0.982*	*−1.427*
			*40K **	*−0.003*	*1.053*	*−∞*
N++	*0.001*	*7.10^{19}*	*300K **	*−0.046*	*1.096*	*−12.8*
			*40K **	*−0.057*	*1.107*	*−∞*

Table 7.4: *Input parameters for SC used to run our Poisson solver and some results: Ec-Ef is the position of the Fermi level relative to the conduction band. $V_{flatband}$ is the applied potential where the semiconductor is flatband (band bending is null). V_{thr} is the threshold potential at which the semiconductor goes from depletion to inversion. Temperatures marked with a star (*) indicates cases where Boltzmann approximation is not valid and the Fermi-Dirac integral was calculated.*

Application to the STS data

In order to use the simulated data to interpret STS data, we need to identify the correct sign convention. **Figure 7.13** provides a visualization of the SC different states depending on the V_{BIAS}. Two scales are distinguished: one corresponding to the STM convention and the other one corresponding to the usual convention in semiconductor physics. Using the example of a N+ semiconductor at 300K, when a STM bias of +1.2 V is applied, the semiconductor is in depletion. It is in inversion at 2.0V.

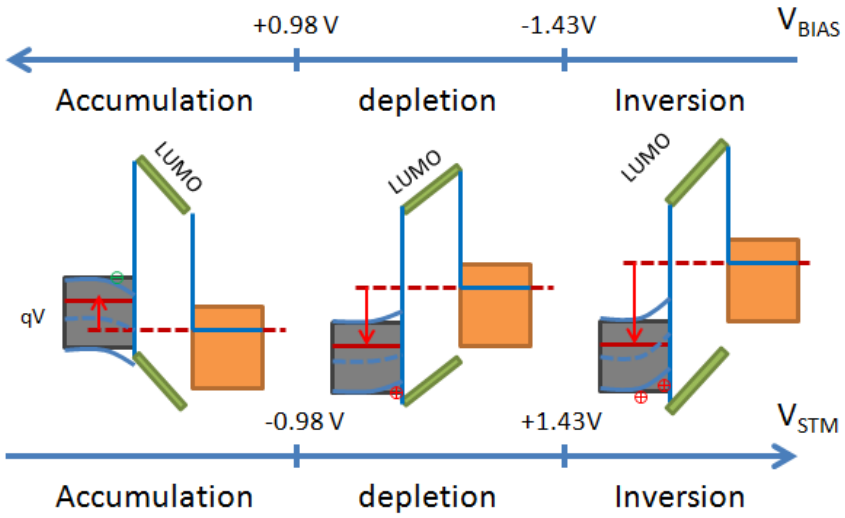

Figure 7.13: *Evolution of the state of the semiconductor with the applied bias. This sketch represents the two scales. Values are given for n-doped Si at 300K taking into account the molecular dipole.*

The six cases reported in **Table 7.4** are considered and their interface potential V_{interf} are plotted in **Figure 7.14** as a function of V_{STM}. For N-doped silicon the interfacial potential depends highly nonlinearly on the applied bias. When no external bias is applied to the sample,

the interface bias at the DBTJ is -0.70 V at 40K. Moreover the two curves are very different at 300K and 40K. However for N+, the temperature dependence is only visible for STM bias higher than +0.8 V, and the two plots tend to be linear. For N++, the semiconductor behaves like a metal (degenerate doping) and the interface potential depends linearly with the applied potential and is not dependent on the temperature. We can also see that the slopes of the curves at 40K are equal to 1 except between from ~ -1.5 V to ~ -1 V for the N sample and from ~ -1.5 V to ~ 0.6 V for the N+ curve. This means that the curve is essentially shifted from the one obtained for metal or degenerated SC.

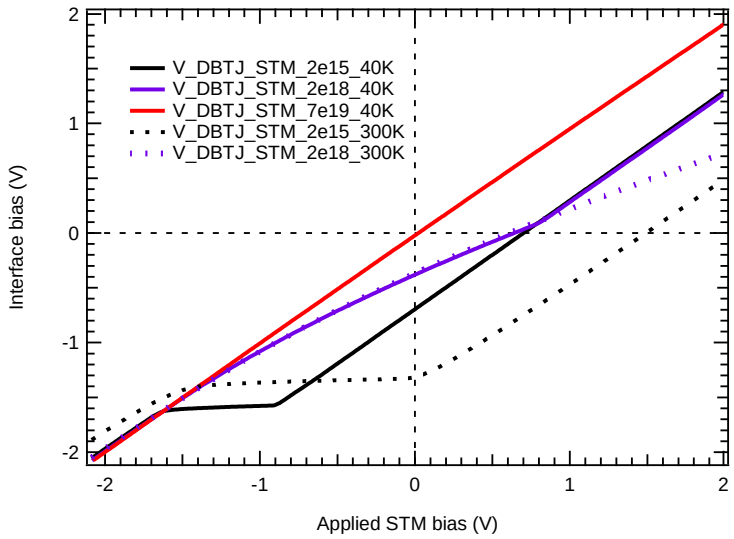

Figure 7.14: *Plot of the interface bias as a function of the applied bias for a DBTJ. The three doping of our experiments are considered.*

7.6 Experimental correlation with simulated data

In light of all the elements discussed in this chapter, we show a comparative study of experimental data obtained using STS on our structure with simulated data obtained using the programs considered in this chapter.

7.6.1 Band bending correction

Experimental data and simulated data were normalized for better viewing in this section: as shown before, the step height is non-reproducible and can change from one curve to another even in the same set of measurements. In this case, experimental data are obtained on a Natan AuNP with a diameter of 9 nm deposited on a SiC_7 GOM grafted on a N+ doped silicon substrate. Temperature during measurement was 40K. Simulated data are obtained using the parameters discussed earlier, corresponding to experimental architecture. It must be noted that the distance between the tip and the AuNP has been estimated using the $I_{setpoint}$ current (40 pA): we adapt the tip-AuNP distance parameters in our software for the current to be roughly 40 pA at a voltage bias 1.5 V which is the one we used for STM imaging. We estimated it to be around 1 nm. The diameter of the AuNP is directly correlated with the step width: from experimental curve we obtain an equivalent capacitance (see orthodox theory in **CHAPTER 2**) equal to C_{eq} = 0.8 aF. This slight discrepancy between the actual measured AuNP diameter with STM (9 nm) and the theoretical estimation (8 nm) may be caused by the error induced by the STM

measurement (STM provide topographical and electronic density information instead of just topographical) and by the approximation in the capacitance calculation in the software. When comparing simulated data with experimental one, the first noticeable difference as outlined by **Figure 7.15**a (black curve is simulated data and red curve is experimental) is evident shift in the voltage scale. At this stage, simulated data do not take into account the voltage drop in the band bending: the effectively applied voltage is therefore lower and an additional bias is needed to overcome the first barrier. V_{interf} is then replaced with V_{STM} in the simulated data following the relationship proposed in **Figure 7.14** and the obtained result is shown in **Figure 7.15**a (blue curve). We can see that the whole curve is shifted toward positive bias as expected but experimental and simulated data still don't match. As discussed earlier we have to apply a 3-D correction factor following the work done by Feenstra *et al.* in 2003[181]: for a 9nm AuNP we apply a correction factor α=3.1 (see **Table 7.3**). Results are displayed in **Figure 7.15**b inset and they show a convincing correlation between simulated and experimental data: in the derivative curve, each peak corresponds to a step and we can clearly see the quality of the alignment between experimental and simulated data. However, the band bending correction is not just a shift, but in low bias there is a dilatation of the simulations. Looking at the derivative of the obtained results (in **Figure 7.15**b) reveals that the first step of the simulated data is elongated. In that range, simulated and experimental data do not fit anymore. More study must be done, but Feenstra *et al.* predicted in 1987 that in low bias, the depletion layer is small enough for the electrons to tunnel through it[85]. This is not implemented yet in this correction but this overlooked phenomenon can have an influence on the experimental data obtained at low bias. The same observation has been done with smaller AuNP as shown in **Figure 7.16**. It must be noted that the

3-D correction factor is smaller when dealing with smaller AuNP, which means that the shift is not as strong from the uncorrected data, and the first step is not elongated as much (see **Figure 7.16**b).

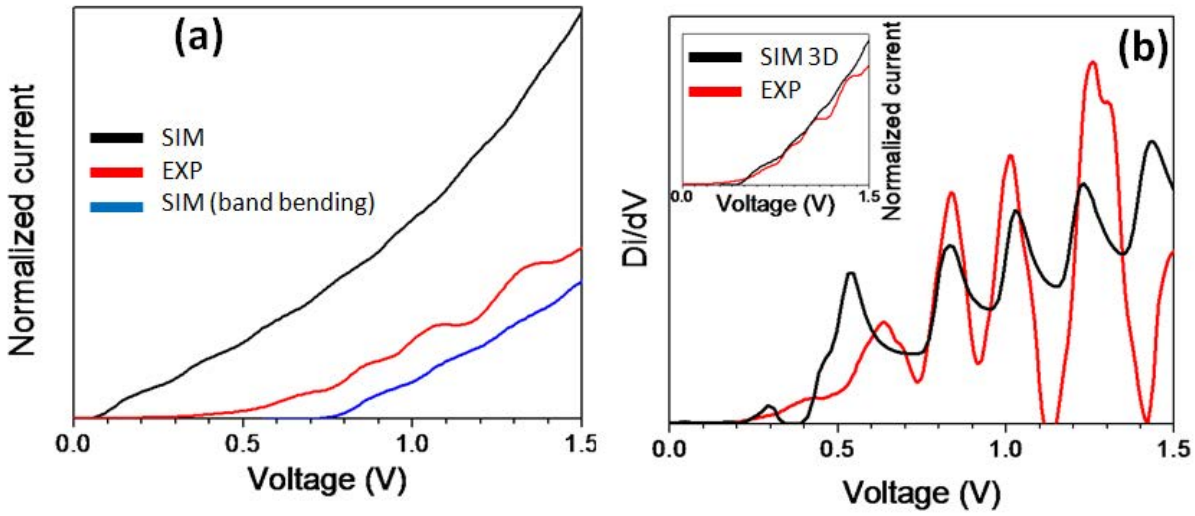

Figure 7.15: *STS curves obtained on a 9 nm Natan AuNP deposited on a SiC_7 GOM grafted on a N+ doped silicon substrate. Experimental data are compared to simulated data and Band bending corrected simulated data (a) and 3-D corrected simulated data (b-inset). Derivative of experimental and 3-D corrected simulated data are shown in (b).*

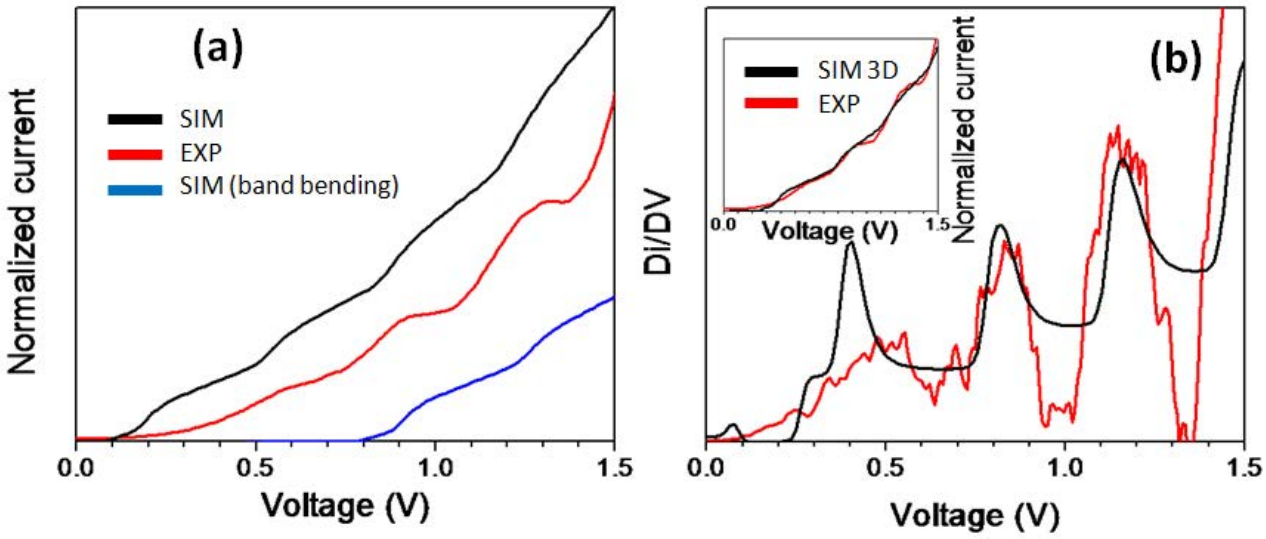

Figure 7.16: *STS curves obtained on a 5 nm Natan AuNP deposited on a SiC_7 GOM grafted on a N+ doped silicon substrate. Experimental data are compared to simulated data and Band bending corrected simulated data (a) and 3-D corrected simulated data (b-inset). Derivative of experimental and 3-D corrected simulated data are shown in (b).*

It is also interesting to see if the correction fits when we are dealing with degenerately doped (N++) silicon sample. We have plotted experimental results done on a 7nm AuNP on **Figure 7.17**a and we can see that the band bending correction doesn't change much, as the expected from **Figure 7.14**, because the bulk behaves similarly to a metal substrate. There is no need in using a 3-D correction factor in this case as the influence of band bending is minimal. It is however interesting to note from the derivative plot (**Figure 7.17**b), that this time, it is not the simulated curve which have an elongated first step, but the experimental one which have a contracted one. As an important point, it must be noted that even though statistical study tends to show that experimental curves have equidistant steps with an error of 6.8mV, for bigger AuNP (the one where we detect the more steps, because they are smaller), their width sometimes increases with voltage bias. This is clearly visible in the example shown in **Figure 7.17**b. it is

important to note that steps observed experimentally are more pronounced than simulated one. Our interpretation of this is the fact that the experimental DBTJ is less symmetric than the simulated one: the difference between the resistances of the two junctions is larger experimentally than the one expected from simulated results. The smaller the differences of resistance and capacitances are, the smoother the steps are (when they are identical, we have a linear *I/V* curve, see **CHAPTER 2**). Another possibility is that there can still be some underlying oscillations (see section **CHAPTER 7.4.1**).

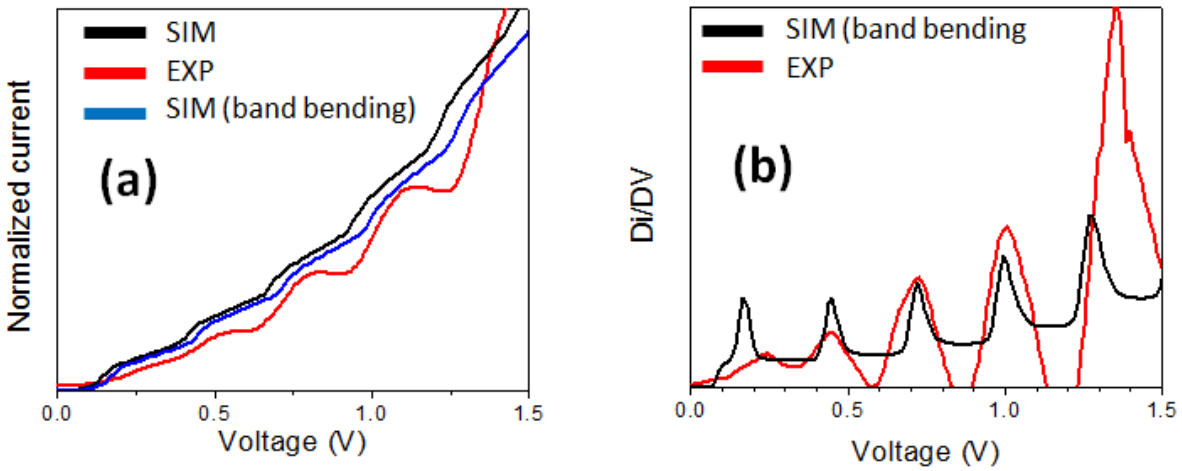

Figure 7.17: *STS curves obtained on a 7 nm Natan AuNP deposited on a SiC_7 GOM grafted on a N++ doped silicon substrate. Experimental data are compared to simulated data and Band bending corrected simulated data (a). Derivative of experimental and band bending corrected simulated data are shown in (b).*

7.6.2 Nanoparticle size dependence

We have seen in **Figure 7.10** that the step width was directly linked with the capacitance of the system which in turns is related to the AuNPs' diameter. According to experimental data

we can extract a linear fit. From simulated data we can extract the step width with respect to the AuNP sizes. An error of 0.5nm in the STM measurements of the AuNP diameter is assumed and represented on the graph. Results are plotted in **Figure 7.18** and show that we have a good fit for AuNP with a diameter higher than 5nm but when the AuNP becomes smaller the fit doesn't match anymore. However, we can see that, for smaller AuNP the step width becomes closer to the maximum of the voltage bias we have applied on our AuNP: this means that for smaller AuNP, we cannot see 2 steps, which is a minimum for us to be able to accurately measure the width. In that case we cannot pretend to propose a perfect match.

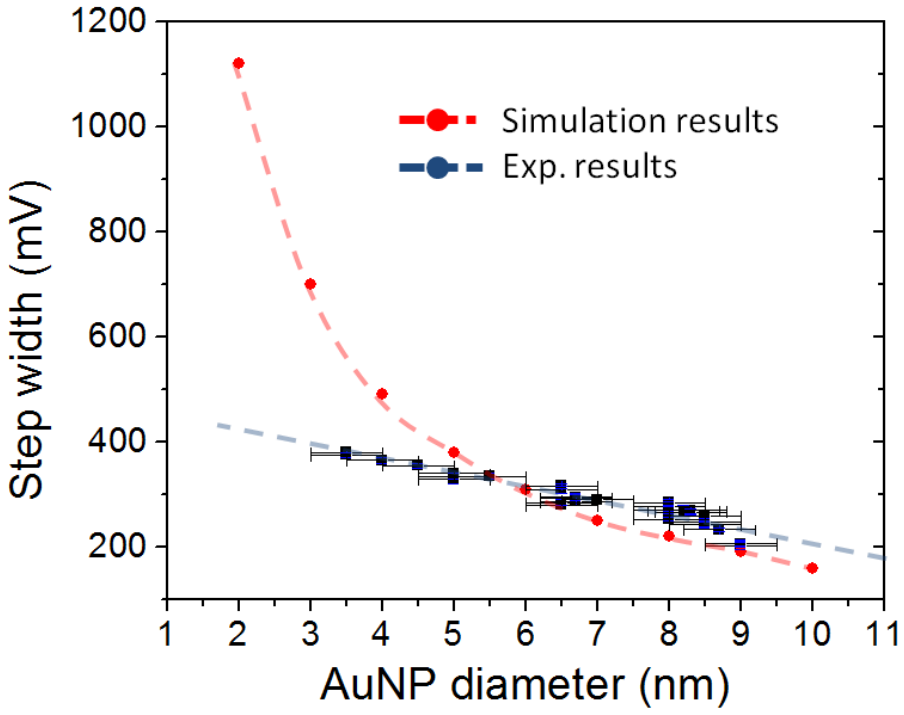

Figure 7.18: *Comparison between experimental fit (blue curve) obtained from* ***Figure 7.10*** *with results obtain from simulated data (red curve). AuNP diameter is estimated with a 0.5nm error with the STM profile and is shown in the experimental fit (blue area).*

7.6.3 Future work for single electron simulation

We have distinguished clear conditions to observe Coulomb blockade using our system and used IEF software to compare obtained results with simulated data. We have added band bending as an external parameter of the software and obtained convincing correlation with experimental data. This correlation was obtained with parameters that are in accordance with the nature of materials used in our structure. This shows that our simulation tool can convincingly predict experimental behavior. However, additional work still needs to be performed to improve the quality of this correlation. We need to implement band bending directly into the IEF program transparency of the tunnel barrier can be estimated accounting the band bending. Doing so will allow a more accurate simulation of band bending effect by taking into account the effect of tunneling through the depletion layer at low bias. The 3D geometry of the tip needs also to be accounted more accurately in the software with the possibility to change parameters such as the tip diameter, the distance between the tip and the AuNP, and between the tip and the surface. It must also be noted that we have not been able to propose simulation that could accurately fit with experimental I/V curve in negative bias. This must be considered in future work. Finally, a better understanding of parasitic oscillations is required to decrease their likelihood of occurrence.

7.7 Toward single electron transistor (SET)

The understanding gained in studying and simulating our DBTJ is a good step toward the fabrication of SET using our system. Several designs for working prototypes have already been proposed and preliminary work toward the fabrication of these structures has been done. Two different structures have been considered, both of them using an STM tip.

7.7.1 Gold strip transistor

In order to build a functioning SET it is necessary to introduce a third contact on our system. This can be achieved by building a gold stripe on half of the sample using UV-lithography. Process flow and final structure are shown in **Figure 7.19**. A 5nm layer of Al_2O_3 are deposited using atomic layer deposition (ALD) on a COOH terminated GOM using the same process designed in Y. Chabal's group and described by Peng *et al.* in 2012[51]. A resist is spin coated in the sample and half of it is exposed to UV light using a chromium mask. Half of the resist is then removed with a developer and a 30 nm thick gold layer can be evaporated on the surface. half of the gold is then lifted off using boiling acetone and the underlying Al_2O_3 layer can be removed with a quick HF 10% dip. The unprotected GOM can then be activated (grafting of the diamine as discussed in **CHAPTER 5**) and AuNP can be deposited.

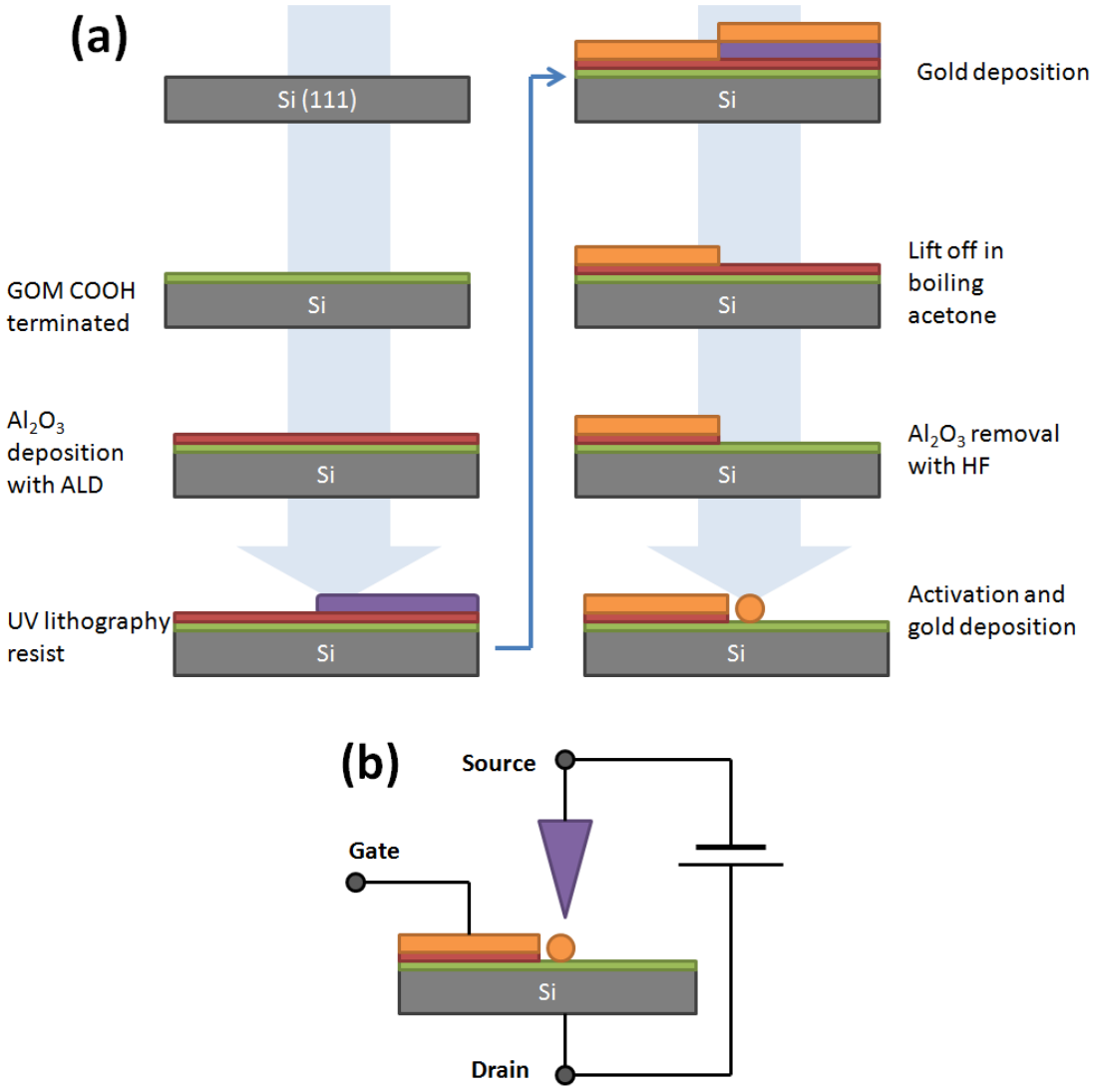

Figure 7.19: *Process flow (a) and final structure (b) of the gold strip transistor.*

Integrity of the GOM has been monitored using XPS after Al_2O_3 removing (see **Figure 7.20**). The fact there is no significant peak at 103.1eV shows that little to no oxidation is detected suggesting that the GOM's integrity is preserved throughout the whole process. Three main peaks are detected on the C1s area: 285eV for the carbons of the alkyl chain, 286eV for carbon contamination and 290eV for the carbon of the carboxylic acid. These results are very similar to

the XPS results shown in **Figure 5.3** in **CHAPTER 5** except for the fact that there is no peak at 288eV because the carboxylic acid is deprotected. A peak at 284.5eV that correspond to the Si-C is not detected because these spectra are not high resolution.

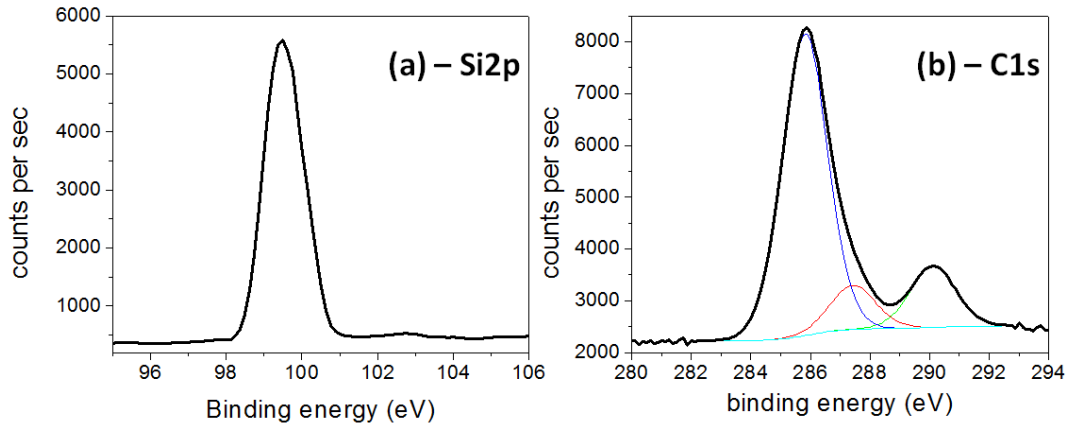

Figure 7.20: *XPS measurements done on the GOM after Al_2O_3 removal. Selected areas correspond to the Si2p peaks (a) and C1s peaks (b).*

The interface between the gold stripe area and the GOM can be observed using SEM and STM. SEM images are easily achievable with successive zoom-in and are displayed in **Figure 7.21**a showing that the interface is well defined compared with a bad interface obtained using a Kapton® tape instead of a UV lithography resist (**Figure 7.21**b). STM image of the interface is trickier to obtain because of the impossibility to zoom on several order of magnitude size scales. We proceeded as follow: the tip was placed on top of the GOM and on STS acquisition was performed. The tip was then moved 10 micrometers toward the gold strip and another STS was acquired on the reached area. This process is repeated up until the STS acquired correspond to STS acquired on gold instead of on GOM (**Figure 7.22**b shows the noticeable difference). Once the gold layer is reached, the process is repeated but the tip is displaced on the other direction

with smaller steps (*e.g.* 1µm) up until we reach the GOM. By decreasing the distances by which we move the STM tip, we can reached the interface and image it as shown in **Figure 7.22**a. This technique must be used in order to position the tip for the transistor architecture to be complete.

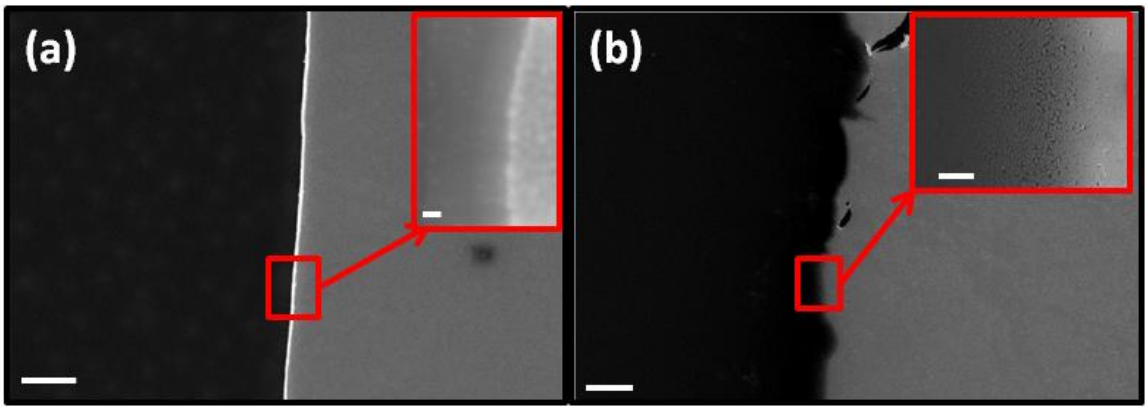

Figure 7.21: *SEM images of the interface between the GOM and the gold layer obtained with UV lithography (a) and with a kepton tape (b). Scale bars are 1µm and 20 nm for (a) and 10 µm and 1 µm for (b).*

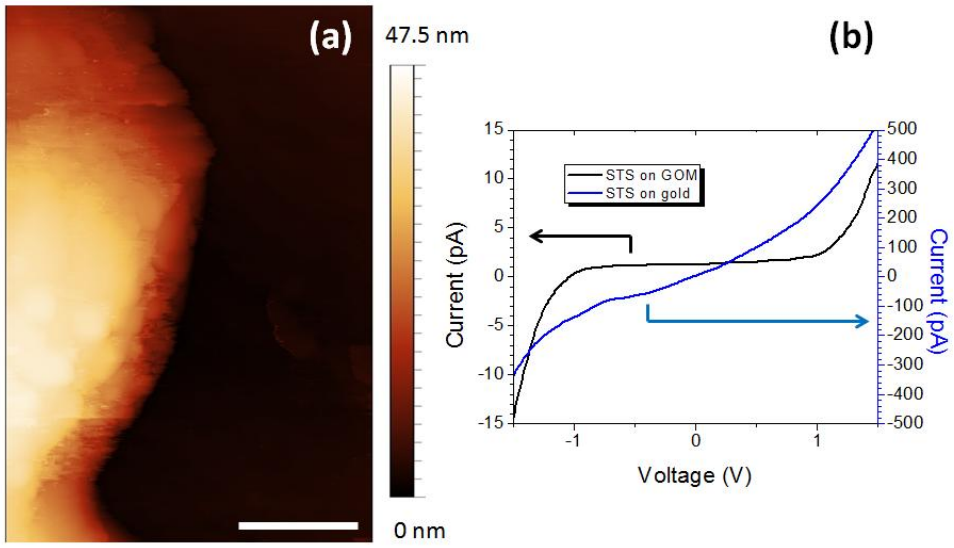

Figure 7.22: *STM image of the interface between the GOM and the gold layer obtained with UV lithography (a) with STS measurements on gold and GOM (b). The current scale for the STS on GOM is on the left, the current scale for STS on gold is on the right.*

We have shown that we are capable of producing the wanted sample in order to build an SET architecture using a gold strip on the GOM. We can also reach a wanted area using the STM tip on our sample. However, as of this day we have not been able to obtain conclusive data and this will be the object of further study.

7.7.2 Silicon on insulator (SOI) based transistor

A simpler architecture has been considered using a functionalized SOI silicon sample. The STM has been modified in order to be able to image the surface of the SOI wafer when the bias voltage is applied with respect the silicon membrane instead of the silicon bulk. Applying a gate voltage on the silicon bulk is expected to force a different SC regime on the silicon membrane in order to shift the Coulomb staircase I-V characteristic curve as shown in the previous section. Some prototypes have been built following the architecture shown in **Figure 7.23** in order to be able to prove that imaging on the membrane is possible. However, dimensions of the SiO_2 box and Si membrane and the doping level of the membrane and the bulk must be optimized for single electron transport observation. In our case we used a lowly doped bulk (500µm thick) with a low doped silicon membrane. The box (oxide layer) was 100 nm thick and the silicon membrane was 65 nm thick. In this case it is expected that all the gate voltage is lost on the bulk: a highly doped bulk is required.

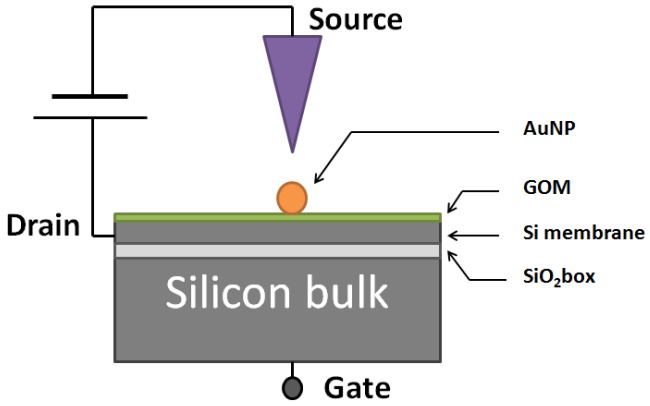

Figure 7.23: *Architecture of the SOI based SET.*

7.8 Conclusion

In this chapter we have shown that it is possible to correlate experimental data with simulation. IEF's software, with band bending modification allowed us to accurately predict electrical behavior on AuNP deposited on the GOM. A 5nm and a 9nm AuNP deposited on a highly doped functionalized substrate (r = 0.02 Ω.cm) have been successfully modeled and simulated results show convincing correlation with experimental one. The shift of the I-V curve toward higher bias is explained by the band bending effect that is highly dependent on the 3-D shape of the structure. With degenerately doped substrate (r = 0.001 Ω.cm) our simulations tools predict a behavior that is similar to the one using metallic substrate. This has been confirmed experimentally with a 7nm AuNP. We have also shown experimentally that the diameter of AuNP influence the shape of the steps in the Coulomb staircase characteristic I-V curve. Simulated data are consistent with experimental one for AuNP bigger than 5nm. For smaller AuNP, model predicts a strong increase of the Coulomb steps with decreasing AuNP size that

has not been confirmed experimentally. It is important to stress that our fits are not perfect because of the relative instability of any system using an STM and because of some uncovered phenomena (such as tunneling through the depletion region at low bias) that we still need to quantify in order to have a better understanding of our overall structure. This work is a step toward the development of a working model for SET. We also propose design along with experimental protocol to make working prototypes of SET. These proposed SET designs are direct follow up of the achievement done using our architecture.

CHAPTER 8

SILICON PATTERNING: AN OPTIMIZATION PROCESS FOR HYBRID PHOTOVOLTAICS

8.1 Introduction:

Finding ways to improve solar cells efficiency has been a leading technological issue. Among all the solutions being investigated, changing the architecture of solar cells has been seen as one of the most promising approaches[188,189,190]. Designing tailored structures at the interface of active material can have several beneficial effects for light trapping [117], increasing charge collection [116] or, like on our case, increasing in the amount of active material on the surface by increasing the surface area[133]. Silicon is the most common substrate used in solar cells technology and micro-processing technology. Consequently, the technologies involved in the fabrication of patterned silicon are mature. Examples of fabrication techniques are UV lithography[191], E-beam lithography[62], interference lithography[192] or nanoimprint lithography[64]. Each of them has its own advantages and drawbacks, so that the most appropriate technology can be selected depending on the goals. In this case, we decided to fabricate silicon nanopillars. A cheap and efficient way to produce this kind of pattern is to use nanosphere lithography[193,194,195] that can provide a wide array of repetitive nanoscale feature using minimal equipment and time, as described below.

SEM and AFM images in this chapter have been obtained using the equipment described in **CHAPTER 4** unless specified.

8.2 Fabrication of silicon nanopillars

The goal is to fabricate silicon nanopillars with a diameter in the range of several hundreds of nanometer. In order to do so, the process pictured in **Figure 8.1** is followed.

The first step consists in cleaning a wafer (with its native oxide) using a piranha solution (H_2SO_4+H_2O_2 3:2) for fifteen minutes. Wafers with (100) and (111) orientations can be used but the orientation does influence the etching direction during the metal-assisted etching step[196]. The second step is the self assembly of polystyrene beads on top of the clean silicon wafer. 200nm and 500nm beads, purchased from Sigma Aldrich, have been deposited with two auto assembly techniques: spin coating and fishing. Once adsorbed on the surface, the beads are reduced in size in step 3 with Reactive Ion Etching (RIE): O_2 plasma is used because it does not etch the underlying silicon for the doses used. The resulting polystyrene mask, with open areas developed during the plasma etching, is used to pattern metal deposition in between the beads in step 4. The beads are then removed by sonicating the sample in methyl ethyl ketone (MEK) in step 5 (Note: this step is optional). A gold pattern is obtained defined by the ordered holes in it. Silicon nanopillars are produced using metal-assisted etching (step 6), and the gold film removed in an aqua regia solution (HNO_3+HCl 1:3) for 15min.

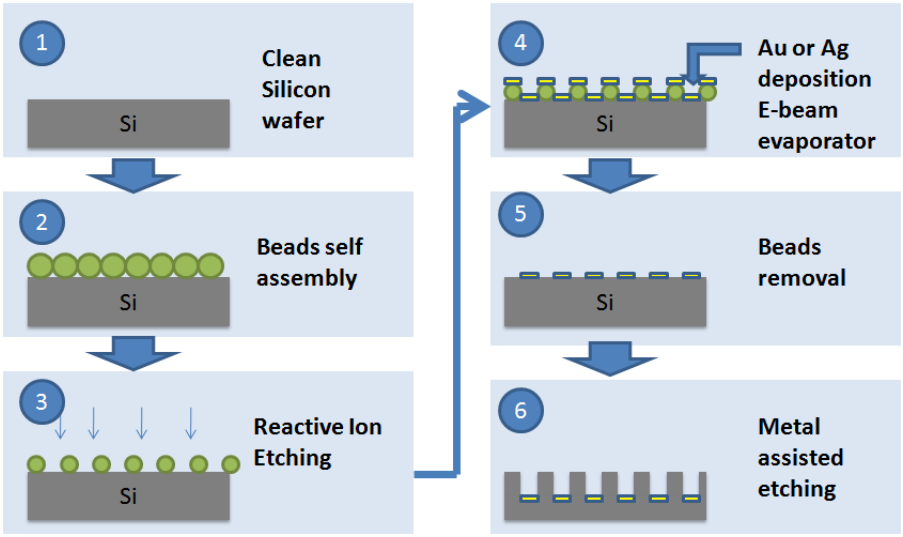

Figure 8.1: *overview of the process used for silicon nanopillars fabrication.*

8.3 Nanosphere lithography

Nanosphere lithography is based on the self assembly of polystyrene nanoparticles. In order to achieve this, two techniques have been investigated. For both techniques a critical parameter for a good coverage is the size distribution of the purchased polystyrene beads. As the beads get smaller, the coefficient of variation (CV) of diameter gets worse and it becomes harder to self assemble them. Typically the one used here have a CV lower than 5%.

8.3.1 Spin-coating

We initially followed the protocol found in the literature[193]: a solution of beads is prepared by mixing 350µl of the purchased solution (sigma Aldrich) with a 50µl solution of

surfactant (triton X-100 diluted in methanol 1:400). The solution was then spin coated on a 2x2cm clean silicon sample using a commercial spin coater with a two-step program. *step1*: spin with 300rpm to evenly disperse the solution on the sample for 10sec; *step2:* increase spin to 800 rpm for 2 minutes to remove the excess solution from the sample. The resulting surface is then examined with SEM to determine the beads coverage on the sample (see **Figure 8.2**). The bead assembly was typically good in localized areas only, with large open areas elsewhere. The coverage varied from ~10 to 40% depending on the sample. Even with our best samples, this coverage was not deemed sufficient to proceed any further. This is why we looked into an alternative self-assembly technique.

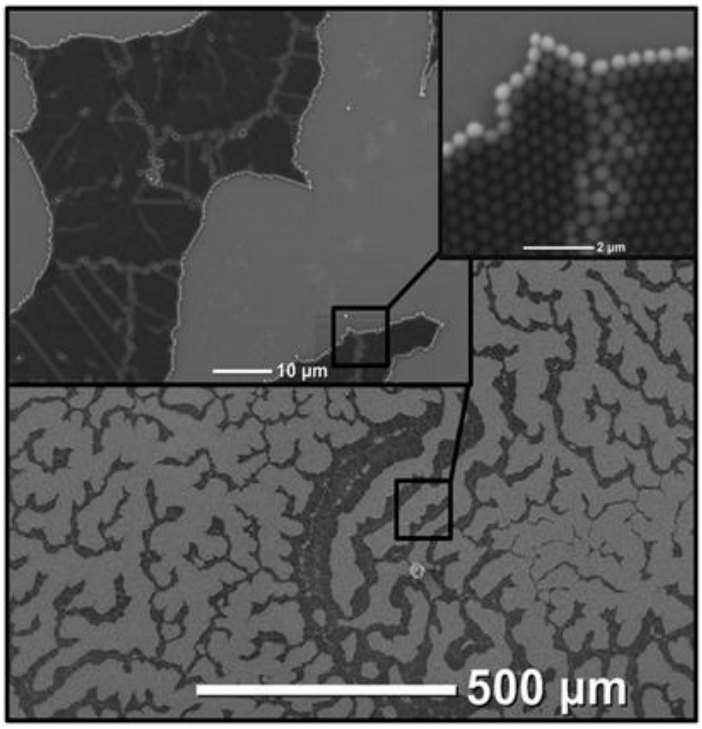

Figure 8.2: *SEM images of a silicon substrate with a layer of polystyrenes nanoparticles with a diameter of 500nm deposited with spin coating. Insets show several zoom-in that gives indication of a good localized assembly of the beads despite a low coverage (~15%). Note: the image has been taken with a low resolution JEOL tabletop SEM.*

8.3.2 Fishing

In order to achieve a better coverage, an alternative method has been used, based on a modified version of what has been described in the literature[197,198]. The process, summarized in **Figure 8.3**, is as follows: several droplets of a mixture of beads solution with methanol (1:1) are drop cast on a large and clean silicon wafer. As the solution dries, it spreads evenly on the surface providing a disperse monolayer of particles on the surface. A water bath is prepared using clean distilled water (18 MΩ), in which a small amount of ammonium dodecylsulfate (ADDS) (60 µl at 2% for a surface area of ~700 cm^2) is introduced. The ADDS, used as a surfactant to lower the surface tension of the water bath, keeps the beads in a semi-compact layer and prevent them from spreading everywhere on the water surface. The beads layer is then slowly transferred at the surface of the water by dipping the wafer into the liquid. The layer remains at the surface but is very fragile. So, more ADDS (200 µl at 2% for a surface area of ~700 cm^2) is added to the water densify the layer enough for the next step. Another clean wafer is then used to fish the layer in suspension on top of the water and let to dry.

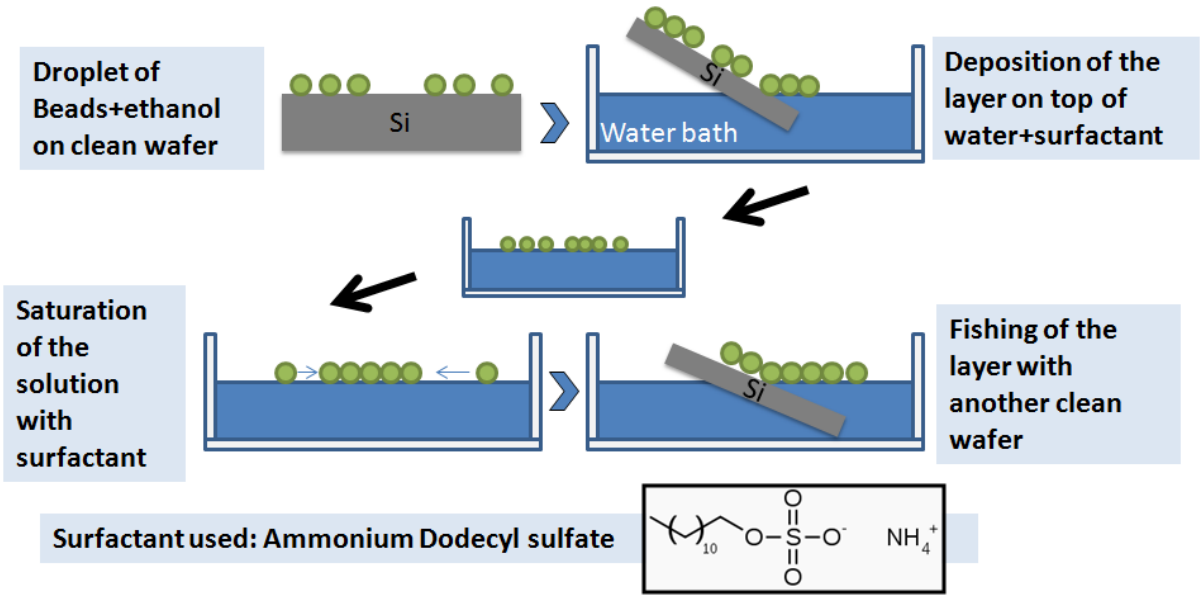

Figure 8.3: overview of the fishing process.

This process results in a dense monolayer of beads on the surface, as confirmed by SEM (**Figure 8.4**). Images show a ~95% coverage at the surface. The monolayer is divided in individual "grains" of perfect packing. Grains have a typical size between 5 to 30μm^2. There are defects on this surface but the overall coverage is acceptable and produces good size samples (up to 5x5cm, potentially higher).

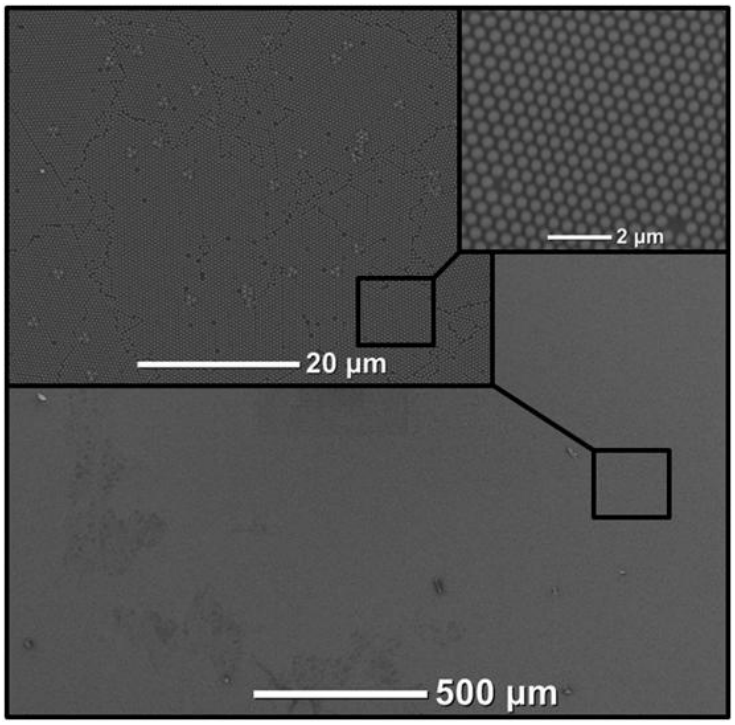

Figure 8.4: *SEM images of a silicon substrate with a layer of polystyrenes nanoparticles with a diameter of 500nm deposited through fishing. Insets show several zoom-in that give indication of a good coverage of the surface (~95%). Beads are organized in 5 to 30µm^2 grains. Note: the image has been taken with a low resolution JEOL tabletop SEM.*

8.3.3 Plasma etching and metal deposition

In order to build a proper mask with nanosphere lithography, we need to modify the shape of the nanobeads. This is done using O_2 plasma etching at low power: 60mTorr of O_2 with a power of 50W. The low power allows us to have a good control over the resulting size of the etched beads. Several different times have been tested as shown in **Figure 8.5** (top part). The shape of the etched beads determines the size of the holes in the metal film, and therefore the diameter of the final nanopillars. The metal deposited in our case is gold: it is a good catalyst for

the next step, *i.e.* for metal-assisted etching. Silver has also been tried, but it gives us worse results because of the relative instability of the silver in the metal-assisted etching solution. A layer of 40nm gold is therefore deposited with an e-beam evaporator under high vacuum (10^{-6} Torr). The lower part of **Figure 8.5** shows the resulting gold masks after gold deposition and beads removal with sonication. A standard time of 120 sec of RIE has been selected with a variation of +/- 15sec depending on how thick the pillars need to be. When RIE step is skipped, the surface is covered with triangular shaped gold nanoparticles that can be harvested in a solution after strong Sonication[195].

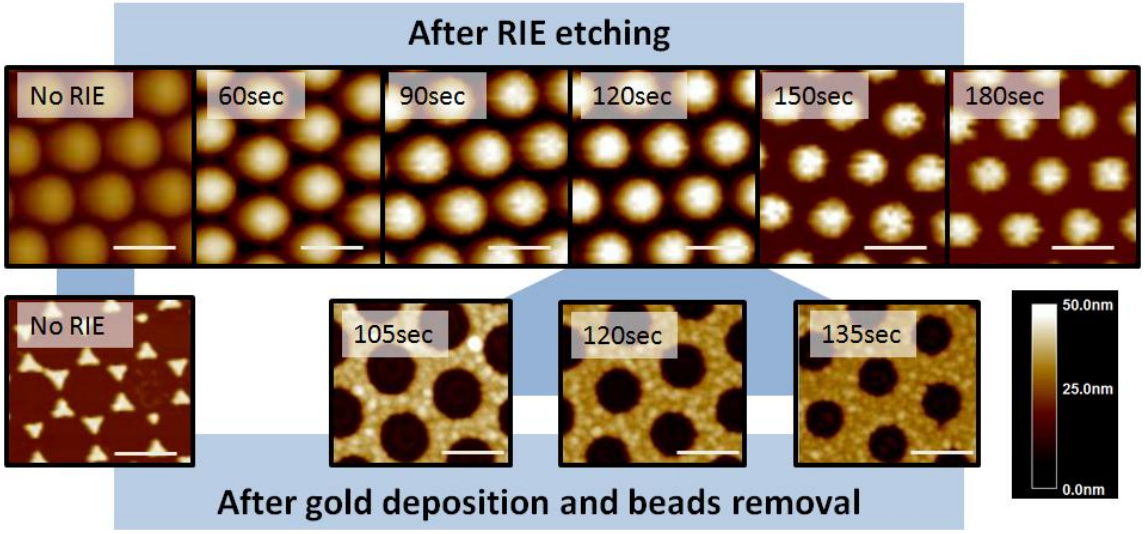

Figure 8.5: *AFM images of a silicon substrate with a layer of polystyrenes nanoparticles with a diameter of 500nm deposited through fishing. Upper part corresponds to the resulting surface after different times of RIE. Lower part corresponds to resulting surface after gold deposition and beads removal for some selected times. Scale bars are 500nm.*

8.4 Metal assisted etching

8.4.1 Basic principle

Metal assisted etching is a chemical process used to etch silicon, which is based on selective oxidation and etching in the presence of a metal catalyst. The process consists of immersing a sample in a solution of hydrofluoric acid (HF) and hydrogen peroxide (H_2O_2) diluted in a solvent (in our case, ethanol, EtOH). The overall concept relies on the reduction of the H_2O_2 compounds in the presence of metal. This allows the oxidation of the underlying silicon. The underlying oxidized silicon is then etched away in a HF solution: the silicon is therefore etched in the direct proximity of the metal which means that a metal negative mask can be used to transfer a pattern to the silicon bulk. The chemical reactions involved in the process are[196]:

Oxidation of hydrogen peroxide on the metal:

$$H_2O_2 + 2H^+ \rightarrow 2H_2O + 2h^+ \qquad \textit{Eq 8.1}$$

Dissolution of silicon:

$$Si + 6HF + 3h^+ \rightarrow H_2SiF_6 + 3H^+ + \frac{1}{2}H_2(g) \qquad \textit{Eq 8.2}$$

Leading to the following overall reaction:

$$Si + \frac{3}{2}H_2O_2 + 6HF \rightarrow H_2SiF_6 + 3H_2O + \frac{1}{2}H_2(g) \qquad \textit{Eq 8.3}$$

The etching process is still not fully understood but can be described this way (see **Figure 8.6** from Huang and al.[196]): (1) The hydrogen peroxide is reduced at the surface of the noble metal

due to its catalytic activity. (2) The holes generated during this previous reaction then diffuse through the metal to reach the silicon that is in contact. (3) The injected holes induce the oxidation of the silicon that is then dissolved by the HF present in the solution. By products are extracted through diffusion around the metal. (4) The reaction is fastest in the direct vicinity of the metal because this is where there is the highest concentration of holes. The pattern of the metal is then transferred onto the silicon. (5) If the rate of holes injection in the silicon is faster than the dissolution of the silicon, holes can diffuse anywhere on the sample: the silicon can be etched anywhere and it can result in the fabrication of microporous silicon[199].

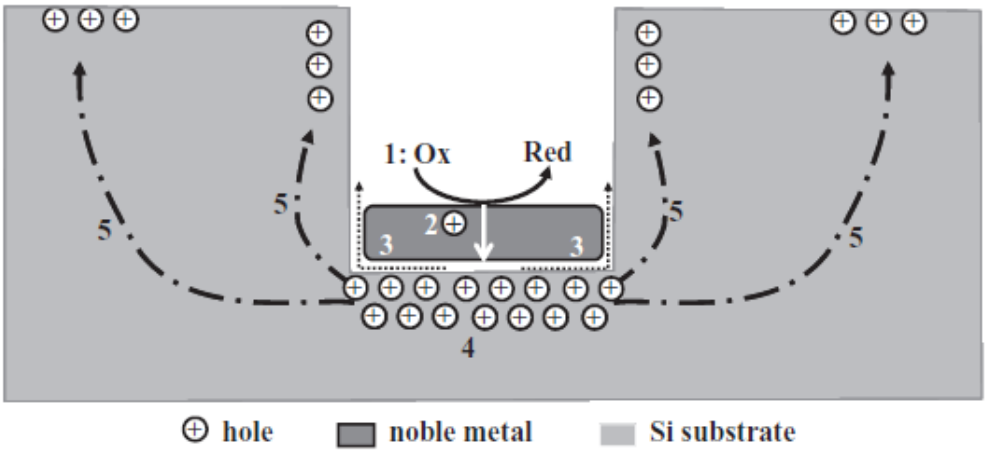

Figure 8.6: *Scheme of processes involved in metal-assisted chemical etching. The numbers are explained in the text. From Huang et al. Adv. Mater. (2011).*

8.4.2 Selected recipe

We decided to use gold as a noble metal. However, gold does not stick well on oxidized silicon surfaces. As shown in the previous part, metal-assisted etching releases gaseous

dihydrogen as a byproduct. Therefore, the reaction induces the formation of bubbles that can slowly make the gold mask pop out. To stabilize the gold mask, a low concentration of H_2O_2 has to be used at first. After some time, the concentration can and needs to be increased because the gold mask is buried in the silicon and remains stable enough for the reaction to continue. The standard recipe is as follows:

1. 8 min with a volumetric ratio of HF/EtOH/H_2O_2 : 1/1/0.01
2. 2 min with a volumetric ratio of HF/EtOH/H_2O_2 : 1/1/1

The obtained structure is displayed in **Figure 8.7** and clearly shows that the shift in the H_2O_2 concentration had an effect on the direction of the etching.

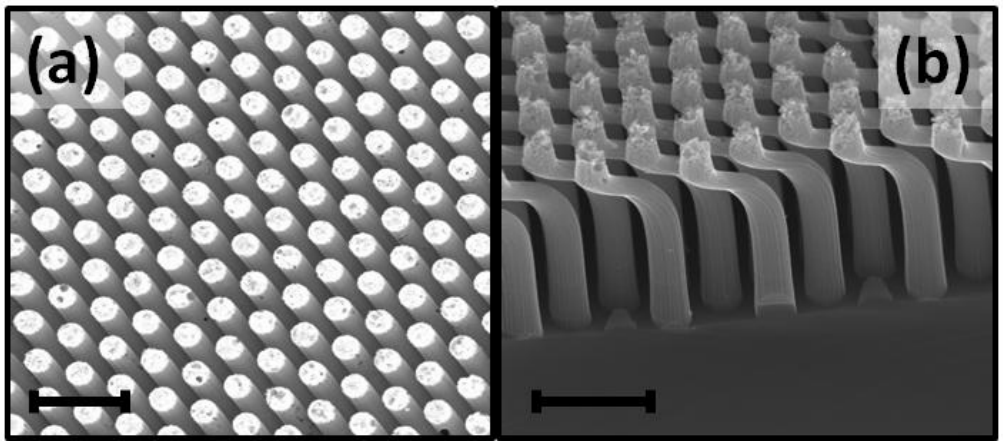

Figure 8.7: *SEM images of silicon nanowires. Top view (a) and side view (b) of Straight pillars obtain with 500nm beads. Scale bars: 1µm.*

8.4.3 Effect of H_2O_2 concentration

As mentioned earlier, the hydrogen peroxide concentration has an influence on the direction of the etching. The gold mask is loosely attached to the silicon and a high concentration

of H_2O_2 can make it pop out. It is then possible for the gold mask to move laterally during the etching process as reported in the literature[196,199]. The reason for such instability remains unclear but can be controlled by varying the hydrogen peroxide concentration as shown in **Figure 8.8**. Experimentally, the maximum instability occurs when the volumetric ratio is around HF/EtOH/H_2O_2 : 1/1/0.1. It is then necessary to quickly increase the H_2O_2 concentration to reach 1/1/1 to ensure that the etching direction remains straight. Another way to obtain fully straight pillars is to keep a very low ratio (1/1/0.01) throughout the whole process. With a low H_2O_2 concentration, a 1h etching is needed to etch 3µm long pillars.

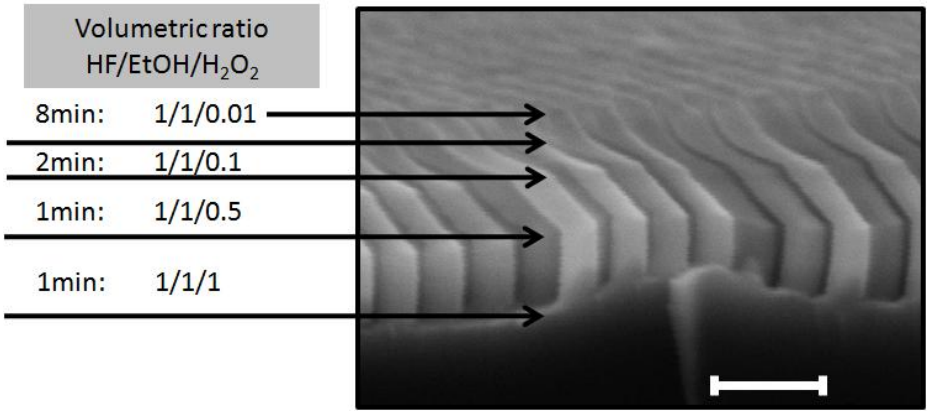

Figure 8.8: *SEM image of silicon nanowires with H_2O_2 concentration variation during the metal assisted etching. The change in concentration has a visible effect on the shape of the silicon nanowires. Scale bar: 1µm. Note: the image has been taken with a low resolution JEOL tabletop SEM.*

8.5 Achievable structures

Using nanosphere lithography combined with metal-assisted etching makes it possible to fabricate a wide variety of shapes for silicon structures.

8.5.1 Silicon nanopillars

The shape of the silicon nanopillars can be tuned with the control over several parameters:

- **RIE time:** changing the O_2 etching time will change the diameter of the silicon pillars. But it will not change the density of the pillars on the surface: so to have a denser array of smaller pillars it is necessary to start the process with smaller beads.
- **Beads size:** Only two sizes have been investigated: 500 and 200nm. There is limit on how much this can be done: when dealing with smaller beads, there is an increased difficulty in obtaining a good self-assembled monolayer. Also, the thinner the pillars are, the more fragile they are and their size must be adapted accordingly
- **Metal-assisted etching time:** the heights of the pillars are set by the metal assisted etching time. It is a trade-off between an optimized surface area increase and a good stability of the pillars in liquid environment. If the pillars are long, they tend to collapse because of capillarity effect. A way to avoid such effect would be to use supercritical drying. But with the extensive amount of wet chemical processes used on the pillars (functionalization, NQDs deposition,…), that option was not selected.
- SEM images of examples of some possible shapes obtained with varying some of the parameters are displayed in **Figure 8.9**.

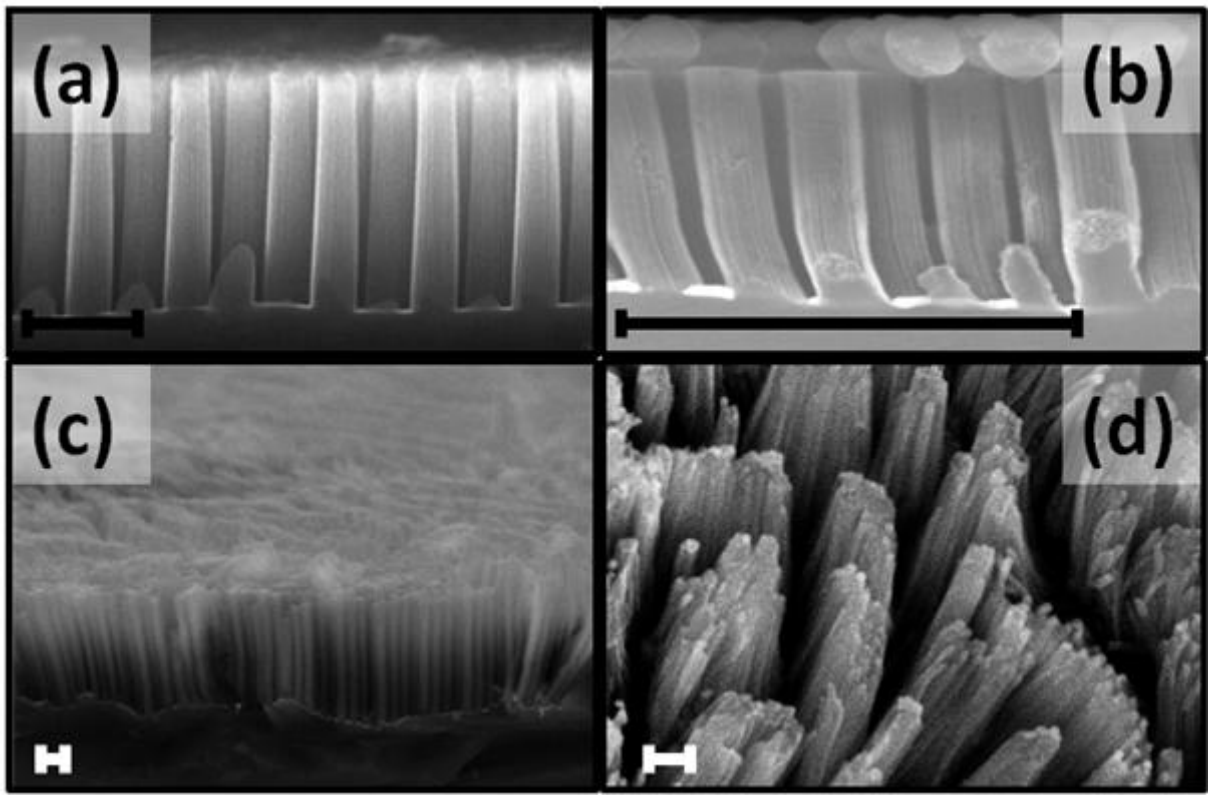

Figure 8.9: *SEM images of silicon nanowires. Side-view of Straight pillars obtained with 500nm beads (a) and 200nm beads (b). Pillars can be etched for a longer time which gives them a more slender aspect (side-view, c) but it makes them collapse when it is overdone (top view, d). Note: images (c) and (d) have been taken using a low resolution JEOL tabletop SEM. Scale bars: 1µm.*

8.5.2 Bent Silicon nanopillars

As seen before, the metal assisted etching step is strongly dependent on the hydrogen peroxide concentration in the solution. This can lead to bent nanopillars as seen in **Figure 8.7** and **Figure 8.8**. Increasing the etching time at the intermediary concentration can lead to some more extreme nanopillars structures. The metal assisted etching process flow is as follow:

Etch 1: 8min with a volumetric ratio of EtOH/HF/H_2O_2: 1/1/0.01

Etch 2: 4min with a volumetric ratio of EtOH/HF/H_2O_2: 1/1/0.1

Etch 3: 2min with a volumetric ratio of EtOH/HF/H_2O_2: 1/1/1

Figure 8.10 illustrate the main resulting structures. They display very long and thin membrane between the upper and lower straight extremities. A top-view, near the edge of the cut sample, allows us to estimate size of the thin part.

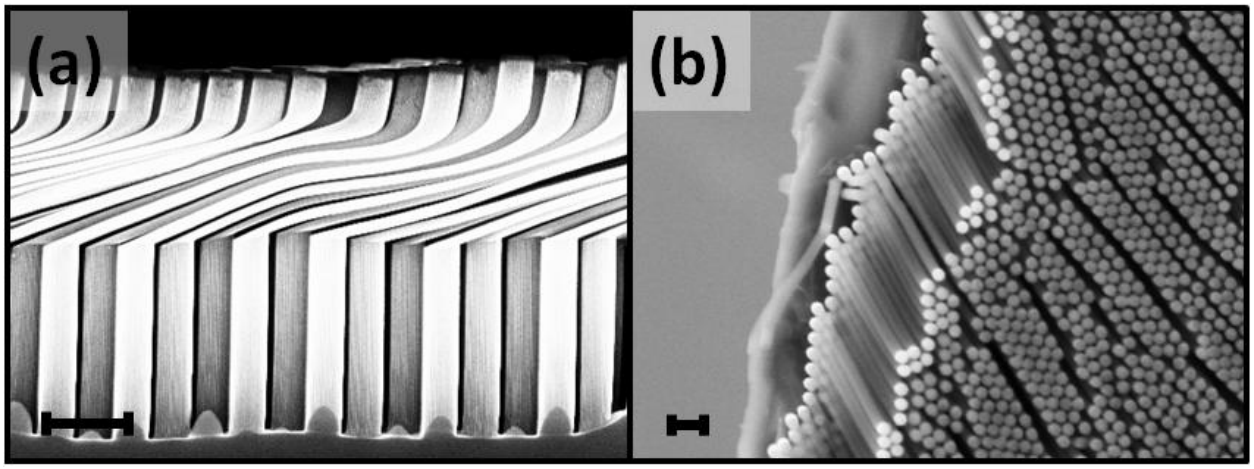

Figure 8.10: *SEM images of bended silicon nanowires. Side-view (a) and top view (b). Scale bars: 1µm.*

But to properly characterize it, we sonicated the sample in EtOH for 30 min for the pillars to break down and go into the solution which was drop cast on another sample. Dimensions are display in **Figure 8.11**. We can also see that the process can be repeated at will so we can have staircase-shaped pillars (**Figure 8.11**a). These repeated steps seem to provide a better stability of the overall structure compared to simple nanopillars of the same size because each pillars supports its neighbor.

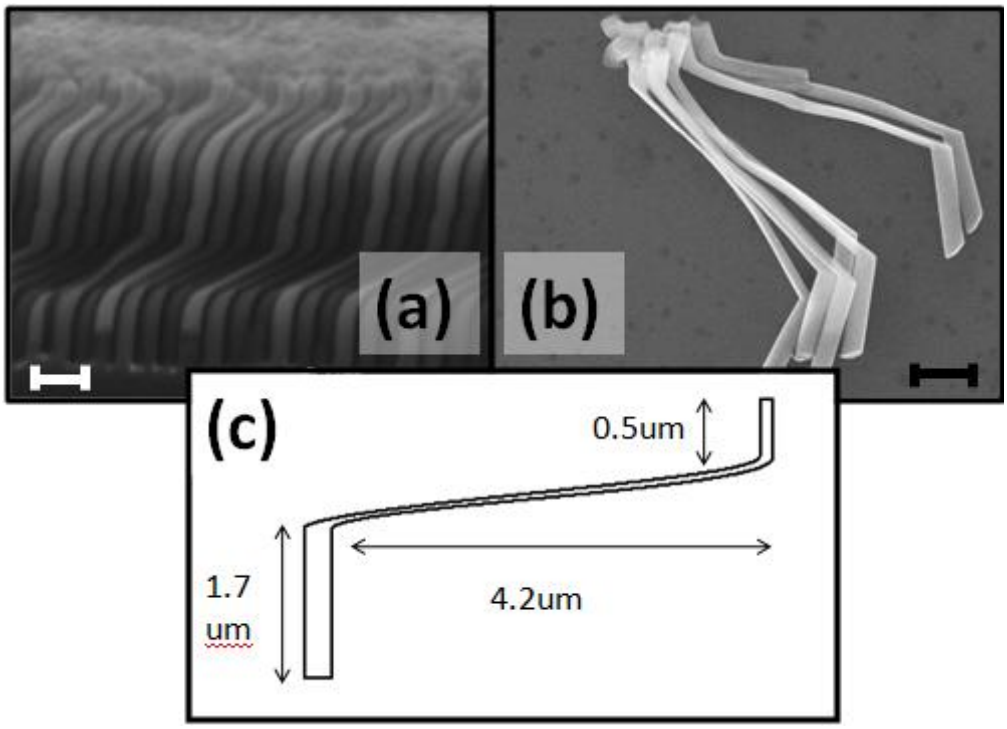

Figure 8.11: *SEM images of bended silicon nanowires. Double bended silicon nanowires are the result of repeating the process twice (a). When broken down with Sonication, pillars can be drop casted on a flat surface (b) where we can estimate more accurately the dimensions (c) the thickness of the thin part is estimated to be 80nm. Note: picture (a) have been taken using a low resolution JEOL tabletop SEM. Scale bars: 1µm.*

8.5.3 Silicon polydiameter pillars

Dual diameter pillars have received some attention in the context of solar-cell optimization because their shape can minimize surface reflectivity (smaller flat area at the top) and enhance the surface area (bigger pillars at the bottom) while remaining relatively sturdy[118]. We propose an alternative way of building such structure out of silicon using nanosphere lithography and metal assisted etching shown in **Figure 8.12**. Samples with a gold mask are prepared with nanosphere lithography using the same protocol as previous experimental work

except for a higher RIE etching time. A RIE etching time of 135sec is used and provide a gold mask with bigger holes than for standard nanopillars. A slow metal assisted etching (with a concentration of EtOH/HF/H_2O_2: 1/1/0.01 for 20 min) is then performed to build the upper part of the dual diameter pillars. We then decrease their diameter by slowly etching them with a KOH solution (30%) for 30sec at room temperature. As mentioned before, the gold mask does not stick well to the silicon and is likely to be removed of the surface during the KOH etch because KOH etches under it. However, the fact that it is stuck at the bottom of the pillars stabilizes it. KOH etching is an anisotropic etching technique so the resulting structure has some faceting of the upper part of the pillars. A second etch is then performed (with a concentration of EtOH/HF/H_2O_2: 1/1/0.01 for 30 min) in order to form the base of the pillars.

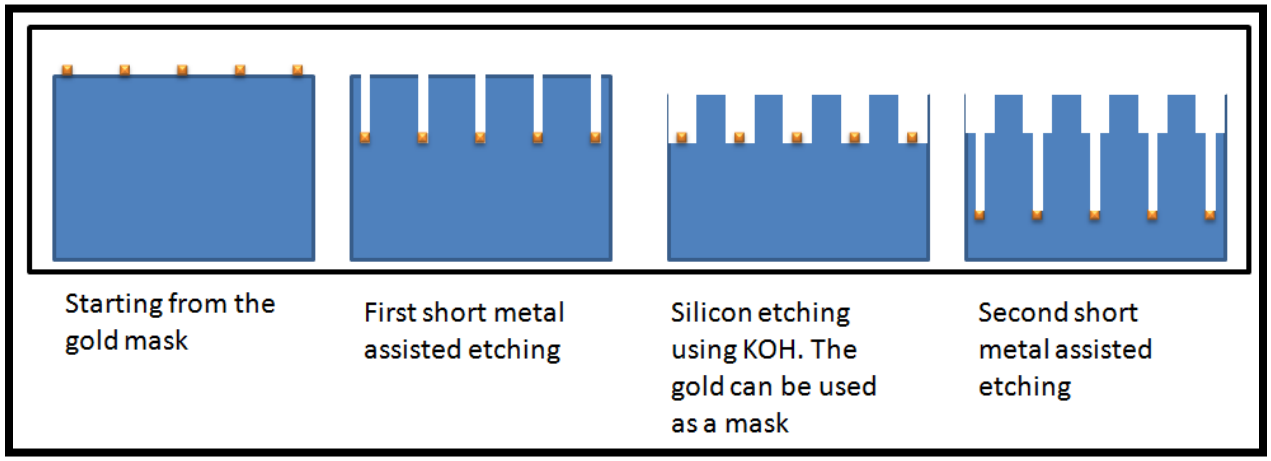

Figure 8.12: *Protocol overview of the fabrication of the silicon dual diameter pillars.*

By adjusting the KOH time (*e.g.* 10sec instead of 30sec), it is possible to do several KOH etching cycles to build polydiameter pillars in order to smooth the transition between the top part less reflective, and the lower part which have a higher surface area. SEM images of obtained

surfaces are displayed in **Figure 8.13** and show the general shape of the obtained structures. Having a smooth transition between upper pillar part and lower pillar part can have the advantage of making the pillars sturdier.

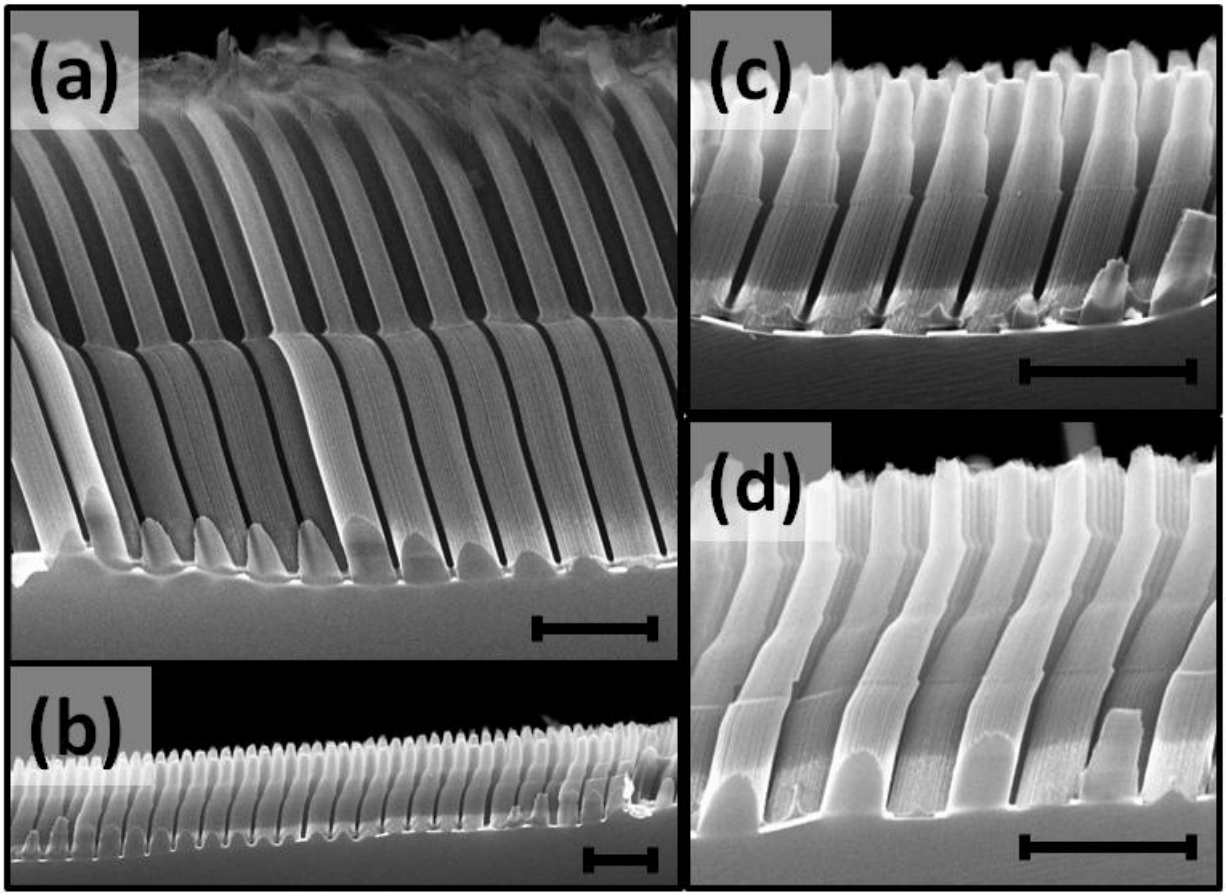

Figure 8.13: *SEM images of the structure obtain with KOH etching. Dual diameter silicon pillars (a) are obtained after one cycle. Triple diameter (b and c) and quadruple diameter (d) are respectively obtained after 3 and 4 KOH etching cycles. All structures are obtained using nanosphere lithography with 500nm beads. Scale bars: 1µm.*

8.6 Optimizing NRET in hybrid NQDs/silicon structures by controlled nanopillar architectures

This section is a direct reproduction of a study that has been published in Applied Physics Letter in 2013[133]:

O. Seitz., L. Caillard, H. M. Nguyen, C. Chiles, Y. J. Chabal, and A. V. Malko. "Optimizing Non-Radiative Energy Transfer in Hybrid Colloidal-Nanocrystal/silicon Structures by Controlled Nanopillar Architectures for Future Photovoltaic Cells." Applied Physics Letters 100, no. 2 (January 9, 2012): 021902.

This publication is providing experimental evidence for the optimization of PL counts from grafted NQDs using patterned silicon. Standard silicon nanopillars have been used as described in this chapter. I initially worked with a postdoc, Oliver Seitz, to fabricate the patterned surface (Si nanopillars), following the method described in this chapter. I was solely responsible for the fabrication of nanopillars, and then for all functionalization after Oliver Seitz left.

8.6.1 Introduction

Silicon-based solar cells are still dominating the market, despite impressive progress in organic bulk-heterojunction systems that involve high photon absorption and cheaper production costs as compared with traditional crystalline Si-based technology. The primary issues faced by

organic-based photovoltaic (OPV) cells are their limited stability and poorly controlled interface quality, leading to insufficient carrier transport and collection. On the other hand, silicon-based PV cells suffer from weak absorption, requiring thick Si films.

A mechanism alternative to direct charge generation and separation is offered by non-radiative energy transfer (NRET) in hybrid nanostructures comprising of strongly absorbing components, such as organic molecules or inorganic nanocrystal quantum dots (NQDs) and highly conductive, ultra-thin and potentially flexible semiconductor (SC) layers. Light absorption in such structures is followed by longer-range energy transfer into SC layers[21,200], in which charge separation and collection are easily accomplished via the built-in electric fields, thus entirely avoiding interface charge separation issues inherent to traditional organic devices. In all cases, substrate nanostructuring improves the performance by providing a larger absorption due to the increased surface-to-volume ratio and benefits to enhanced exciton extraction. Several nanostructure architectures have been considered, such as one dimensional nanostructures (nanowires and nanorods)[116,190,117]. Particularly useful are OPV devices made in the form of nanopillars that can be fabricated by several methods, such as nanoimprinting (applicable to soft, organic based devices) or by controlled etching of the underlying inorganic substrate. Such nanopillars can be easily doped to form radial p-n junctions. These structures have been shown to have an advantage in carrier collection and device efficiency over planar devices because the shorter distance minority carriers must travel to reach p-n junction[188,189]. Additionally, such structures have improved optical absorption through photon scattering/reabsorption within the nanostructured substrate as well as due to potential for light coupling in photonic structure. High

concentrations of nanopillars would increase the effective absorption in both the active material (NQDs) due to higher concentration per unit area, and in the underlying thin Si substrate by efficient energy transfer into the thin film, ultimately increasing the light conversion efficiency.

Despite the potential advantages of one dimensional structures, light conversion efficiencies that are obtained with organic nanoimprinted solar cells are presently lower than their planar versions due to difficulties in controlling the surface passivation of the nanostructures, leading to exciton trapping and recombination[24]. Further, ordinarily used dropcast or spin-cast NQD films on unpassivated surfaces provide poor control of the placement at and chemical bonding to the surface[200]. The situation is particularly difficult when the substrates are not well chemically passivated by a stable oxide (as is the case for oxide-free silicon). Yet, the attachment of NQDs on high quality surfaces with low interface state density is required for advanced applications. Methods for functionalizing and stabilizing defect-free surfaces have been developed[7,17,24], but surfaces may not always remain chemically stable during the NQD attachment process. Substrate oxidation and formation of trapping sites that occur on the outer NQD ligands[201] may open an effective channel for electron scavenging that may hinder NRET related phenomena.

In this work, we controllably prepare large area, high aspect ratio Si nanopillar structures and demonstrate the grafting of dense monolayers of colloidal CdSe/ZnS NQDs positioned at well-controlled distances from Si interfaces[21]. For oxide-free silicon surfaces, we show that a grafted organic monolayer completely passivates the Si surface through the formation of a Si-C

bond (*i.e.*, prevents subsequent oxidation)[7], as clearly demonstrated on flat silicon surfaces[17], and leads to an amount of interface states that remains negligible for most applications (*i.e.*, comparable to what is typically seen with thermally grown silicon oxide)[17], while providing functional headgroups for attachment of NQDs[21]. In addition to passivating the interface, a linker assisted deposition guides the creation of a single, tightly controlled monolayer of NQDs at pre-determined distances that densely covers the side facets of the Si nanopillars. High-resolution SEM analysis of nanopillars reveals a close packing of nanocrystals on the vertical sides on the nanopillars with densities similar to those on planar Si surfaces. Using photoluminescence (PL) spectroscopy we register ~35 fold increase of NQD surface coverage as compared to the planar Si/NQD structures This increase is consistent with the increase in surface area obtained by forming the nanopillars and available for dense NQD monolayer grafting. Importantly, time-resolved PL measurements reveal that the NQD PL decay is much faster (~15 fold) compared to NQD/glass reference samples. Comparison with planar NQD/Si samples indicates that NRET into Si nanopillar substrate continues to be the dominant mechanism of energy transfer. The possible coupling of the NQD emitted light into the waveguiding modes within Si nanopillars and/or the change in the NQD radiative lifetime due to photonic crystal structure further contribute to the enhanced exciton depopulation dynamics.

8.6.2 Preparation:

Silicon nanopillars preparation is initiated by using polystyrene monodisperse microparticle 0.5 μm size in water (Sigma-Aldrich), following previously described

procedures[196,197,198]. Briefly, a mixture of ethanol/microparticle (1/1, v/v) is dispersed on a clean Si wafer by drop casting and drying. The layer of particles is then lifted off the wafer by inserting into a water bath containing a small amount of ADDS. The layer is then transferred on a clean silicon substrate and left dry in ambient. Prior to deposition of 40 nm gold layer via e-beam evaporation the microparticle size is reduced using O_2 Reactive Ion Etching (RIE) plasma. The pillars are formed by leaving the structure for 10 min in a mixture of ethanol (98%), HF (49%) and H2O2 (30%) with a volumetric ratio of 1/1/0.01, then more of H_2O_2 is added to bring the ratio to 1/1/1 and left for 2 min. Finally, the gold is removed from the sample by using an aqua regia solution (15 min) and the remaining microparticles are washed away by using a piranha solution (20min).

Surface functionalization is based on two approaches depending on the starting surfaces (oxide-free Si or pure glass) and is described elsewhere[16,21]. Note that in the present study, the silane used is 0.2% of C11-Ald instead of AUTES due to the use of water soluble quantum dots. Water soluble colloidal NQDs are purchased from Invitrogen (Qdot 565 ITK amino (PEG), # Q21531MP) and used as received. NQDs attachment is performed differently depending on the head group: (a) for carboxyl terminated head groups, the sample is immersed in an MES (2-morpholinoethanesulfonic acid) solution containing EDC (1-ethyl-3-(3-dimethylaminopropyl) carbodiimide) (0.8 mg/ml) and with NQD concentration of ~15 nM; (b) for aldehyde terminated head groups, the sample is exposed to NQD solution containing some sodium cyanoborohydride (5 mM). (Note: for the thin glass slides, a homemade holder is used to perform the adsorption

only on one side of the slide.) The samples are left 40 min for adsorption, rinsed at least twice with Deionized water and dried under N_2 gas.

8.6.3 Results and discussion

To characterize the surface structure as well as the NQDs coverage, we performed SEM imaging on the nanorodes. **Figure 8.14** shows a picture and SEM top view images of the nanopillars structure. This protocol results in the formation of highly uniform, large area (~5 cm^2 in the shown case), close-packed formation of upright standing, ~300 nm diameter, ~500 nm pitch (center to center separation), Si nanopillars on Si substrate. After GOM functionalization and attachment of NQDs at higher concentration (~250 nM) used for PL measurements, the SEM cross section of the structure at different magnifications is shown in **Figure 8.15**a and **Figure 8.15**b. The resultant nanopillars are isolated and close-packed, with a change of direction observed along the pillar axis (**Figure 8.15**a). This reproducible change is explained earlier in this chapter. Using the SEM scaling, the length of the pillars can be estimated between 3.5 and 4.0 μm, leading to an estimated increase of surface area of ~20 times, as compared to the starting flat silicon substrate. Note that this increase does not take in account the increase of surface area induced by the increase of the surface roughness due to the etching process. At higher magnification (**Figure 8.15**c), the HR-SEM picture reveals the presence of a homogeneous, close-packed NQD monolayer wrapped around the nanopillars with a size distribution in the 4-6 nm range. The presence of this layer confirms the realization of the NQDs/nanopillar attachment

process and implies the presence of a dense GOM on oxide free Si nanorods with a predetermined distance of 1.6 nm between the dots and the Si substrate.

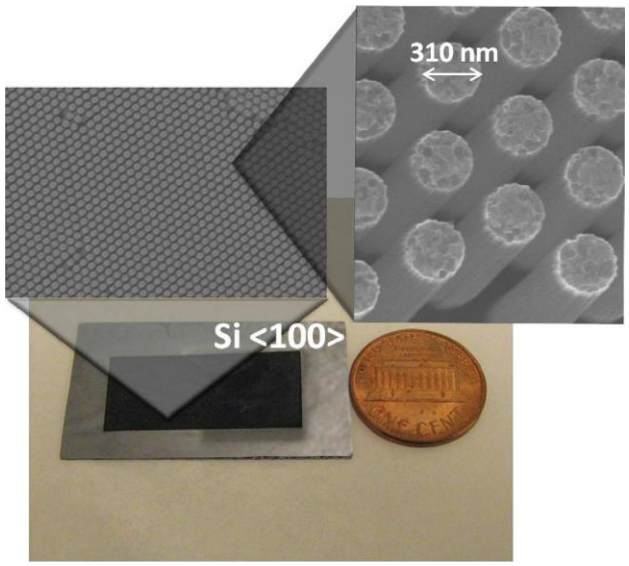

Figure 8.14: *Digital camera picture and SEM top view imaging of Si nanorods. From Seitz et al., Applied physics letter (2012).*

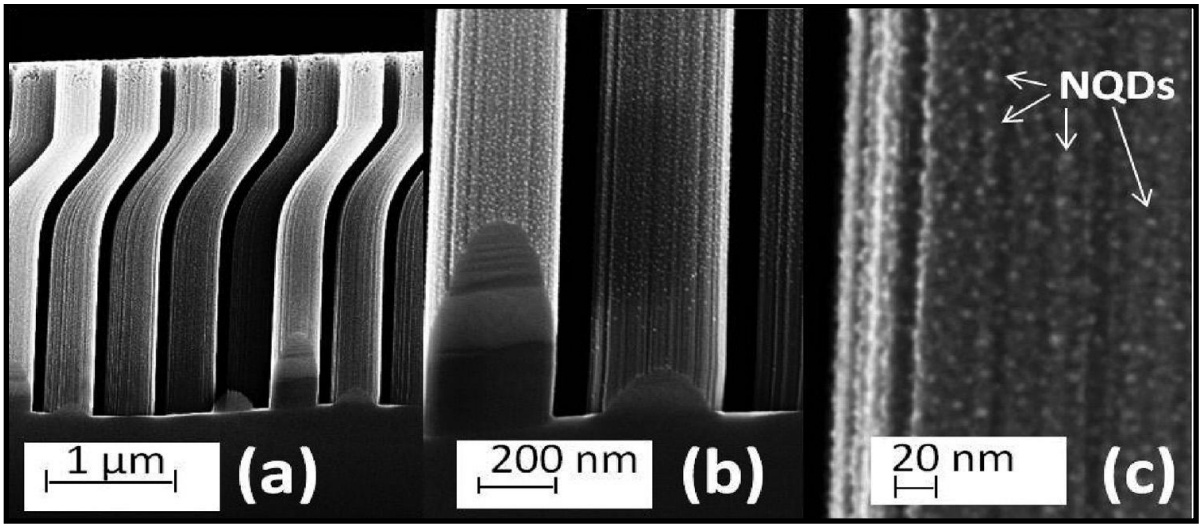

Figure 8.15: *(a)-(c) SEM cross-sectional images of Si nanorods' structure at different magnifications after functionalization and attachment at high concentration of NQDs. Well resolved individual NQDs are seen on panel (c). From Seitz et al., Applied physics letter (2012).*

To characterize the surface coverage and study the effects of energy transfer, we used typical microscope-based μPL that has the required single-photon sensitivity[21]. Measurements of the PL intensity (**Figure 8.16**a) confirm dense packing, monolayer arrangement of NQDs on the side walls of the nanopillars. The PL intensity measured for the Si nanopillar sample is approximately 35 times larger than PL intensity of the planar Si/NQD sample, which is prepared using the same concentration of NQDs for grafting. This number compares well to the expected increase of the surface area, with some discrepancy that may come from incomplete NQD coverage of the trenches between the pillars, thus increasing the proportion of the PL coming from the densely covered side surfaces vs. the flat substrate (see the inset to **Figure 8.16**a).

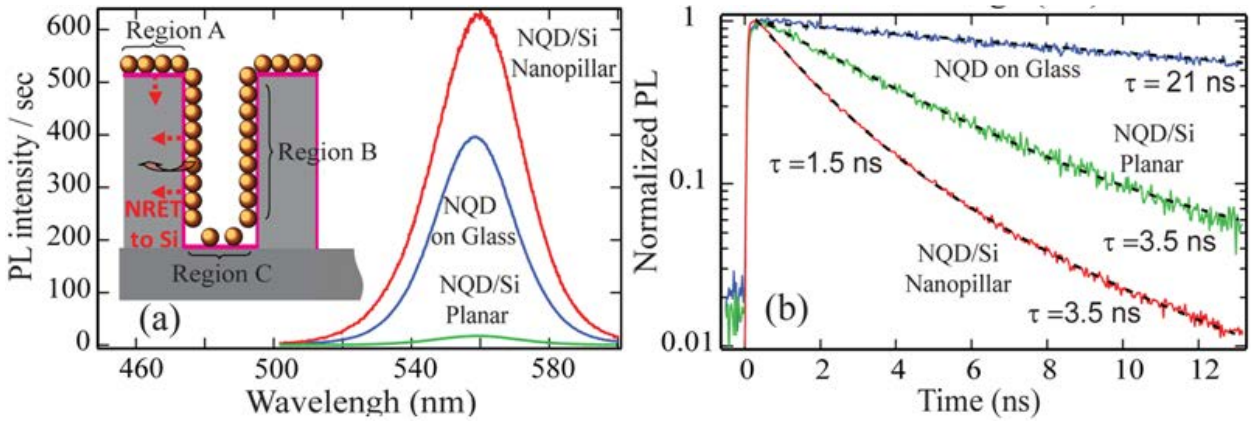

Figure 8.16: *(a) PL spectra of NQDs grafted on glass, planar Si and Si-nanopillars for similar starting NQD concentrations. Inset: Schematics of nanopillar structure (b) PL decays for the same set of samples. Dashed lines are fits to monoexponential decays (top and middle curves) and to biexponential decay (bottom curve).From Seitz et al., Applied physics letter (2012).*

Further, we recorded time-resolved PL dynamics for (i) the Si/NQD nanopillar sample, (ii) the planar Si/NQD sample, and (iii) the NQDs grafted on a glass substrate, used as a reference. All samples were prepared using the same starting NQD concentration (*i.e.*, 15 nM)

for grafting to ensure similar surface coverages. The NQD PL dynamics (recorded at the peak position, *i.e.*, λ~570 nm) differ greatly, with those on the Si nanopillar sample being the fastest as seen in **Figure 8.16**b. A monolayer of NQDs deposited on glass has a monoexponential PL transient with decay time $\tau_{glass}=21\ ns$, attesting to the high quality of the commercial NQDs. The NQD dynamics on the planar Si/NQD sample also exhibit a nearly monoexponential decrease, with much faster dynamics, $\tau_{Si}=3.5\ ns$, as compared to the reference on glass. In previous work[21], our team characterized the PL decay rates for NQDs grafted at well defined distances from planar Si surfaces. The large observed difference in PL dynamics is fully described by modification of the radiative and non-radiative decay rates for an emitting dipole placed near high refractive index ($n_{Si}\sim4$), weakly absorbing ($Im(\varepsilon)\sim0.3$) Si surface. The observed ratio of total decay rates $\Gamma_{Si}/\Gamma_{glass}=(21/3.5)=6$ is in excellent agreement with the theoretical calculations that predict (i) the NRET contribution accounting for a factor of 2.5, and (ii) the change in the radiative rate due to presence of highly polarizable Si substrate accounting for a factor of 2.4.

The observed fast decay component $\tau_{fast}=1.5\ ns$ is, therefore, indicative of additional/enhanced decay channels that are responsible for exciton depopulation when NQDs are placed on nanopillars. Two possible mechanisms are possible: (1) further modification of NQD radiative rates when placed in the photonic crystal structure, and (2) coupling of the NQD emission into quasi-waveguide modes of the nanopillars, thus further reducing the PL decay times. The former mechanism has been extensively studied in different photonic structures for both colloidal NQDs as well as for epitaxial quantum dots grown in situ in microcavities (so called Purcell effect)[202,203]. The later mechanism has been recently discussed in the context of the

plasmonic-based light coupling[204]. Further optical experiments are currently being performed to clarify these mechanisms in Si nanostructures.

8.7 Conclusion

Nanosphere lithography, combined with metal assisted etching provides a relatively easy and cheap way to fabricate silicon nanowires with a wide variety of shape and size. In the frame work of the enhancement of quantum dots based solar cells it has been decided to use standard silicon nanowires. We have then prepared large-area, regular arrays of 3D Si nanopillars and grafted monolayers of colloidal CdSe/ZnS quantum dots. Such 3D nanopillar structures gave an effective increase in surface area of ~20 fold without compromising the interface quality and without detectable evidence of surface states (if created) that typically hamper the performance of composite nanostructured devices. We have clearly demonstrated that in such hybrid architecture, NQDs' grafting still produces close to ideal monolayer coverage similar to what is achieved on planar Si substrates. PL spectroscopy measurements have revealed considerable acceleration of the PL dynamics of NQDs positioned on the nanopillars due to the combined effects of the non-radiative and radiative energy transfers. Such a photon harvesting architecture would potentially allow the combination of effective exciton collection from NQDs to Si via energy transfer mechanisms and improved carrier extraction via built-in electric fields of radially doped p-n junctions. This approach may prove useful for the development of thin-film, flexible Si solar cells with power conversion efficiencies approaching the efficiencies of thick, crystalline Si devices[205], but at much lower production costs and higher throughput.

CHAPTER 9

DITHIOL AND DIAMINE BASED MULTILAYER CDSE NANOCRYSTAL QUANTUM DOTS FABRICATION

9.1 Introduction

Considerable progress has been done in the field of organic bulk heterojunction systems, whether it is in photon absorption or in optimization of cost fabrication. But despite all this work, traditional Si-based PV cell technology still dominates the market. It is mainly due to the fact that OPVs have limited time stability in typical ambient environments and poorly controlled interface quality, all of which have a direct influence on carrier transport and collection. However, silicon itself in silicon-based PV cells has a weak absorption, requiring thick Si films, further increasing the production cost.

Energy transfer from organic molecules or inorganic nanocrystal quantum dots (NQDs) to a semiconductor (SC) layer through non-radiative energy transfer (NRET) is believed to be an interesting method to increase efficiency. The light absorbed in the NQDs is transferred to a conductive and thin SC layer where excitons are generated and charges separated via a built-in electric field (in p-i-n junctions). Along with NQDs stability compared to organic materials, one of the main advantages is that charges do not need to be transferred from the NQDs to the silicon layer, thus avoiding interface charge capture issues typically occurring in traditional OPVs. It has been demonstrated that a dense monolayer of CdSe/ZnS NQDs can be attached on passivated silicon substrate using self assembled monolayer[21]. Efficiency has been improved by increasing surface area through patterning by taking advantage of the widespread knowledge on silicon patterning[133]. Study has also been performed suggesting that potentially cheaper thin silicon should provide better efficiency than thick bulk because of introduction of additional radiative

energy transfer routes through wave-guiding in the thin silicon membrane[206]. In order to further improve the efficiency, the number of layers attached to silicon needs to be increased as well to fully capture the solar radiation. Doing so increases the number of NQDs on the surface in turn improving the light absorption, thus maximizing the energy transferred to the bulk through NRET. Such improvement can also open the road to the ordered attachment of successive monolayers of NQDs with a tailored absorption profile. A wider spectral range can be absorbed by the NQDs and transferred to the silicon bulk. Such enhancement is possible because of the relatively long-range nature of NRET (compared to charge transfer) and RET and by inter-dot energy diffusion[21,200].

The fabrication of ultrathin films of quantum dots or nanoparticles has already been achieved on several substrates (silicon, metal, glass,…)[207] using different techniques such as layer-by-layer assembly[207,208,209], spin casting[210] or Langmuir-Blodgett deposition[211]. Multilayer quantum dots systems, fabricated using layer-by-layer assembly techniques with polymer films, have been shown to enhance luminescence of NQDs[207]. Such systems have also been obtained with self-assembly of polyelectrolytes, such as, positively charged poly(diallyldimethylammonium chloride) (PDDA), polyallylamine hydrochloride (PAH), and quaternaryammoniumion cationic starch (QAICS), stacked with negatively charged NQDs[212]. These techniques offer possibilities to build thick films of NQDs on a flat surface which in turns allow tuning fluorescence intensities and quantum yield by changing NQDs sizes (aka wavelength emission). It also takes advantage of fluorescence resonance energy transfer. Multilayers of CdSe/ZnS QDs have been controllably fabricated through layer-by-layer chemical

grafting using dithiols, and characterized using XPS and PL measurement[213]. XPS measurements offer a good estimate of the density of NQDs attached on the surface by performing measurements between each grafting cycle. PL measurements also provide an estimate of the converage and determine, through decay-time measurements, the mechanisms involved in energy transfer.

Our approach is to build similar systems using dithiol and diamine and characterize them with XPS and time-resolved photoluminescence measurements. The use of dithiol has been motivated by the fact that thiol group –SH has a good affinity with ZnS protective shell and therefore allow a stable attachment of the NQDs. The interaction between thiol and zinc atoms has been modeled and shows that a liaison is created between them[33,34]. It is also the case with sulfur atoms, but with a lower binding energy[33,34]. Amine has a similar affinity albeit not as strong. It has been shown that amine could lead to an increase in photoluminescence counts[214,215], leading to their description as "perfect ligands" for Cd/Se NQDs[216]. Some negative influence on photoluminescence has been reported for both thiol[217] and amine[218] ligands. In constrast to the previously mentioned study, our work is based on ZnS-capped CdSe NQDs. We focus on the influence of dithiol and diamine groups on the energy transfer between NQDs and determine the most promising fabrication method.

9.2 Experimental method

9.2.1 Surface preparation

The starting surface, corresponding to the first step in the **Figure 9.1**a, is prepared as follows. A thick thermal oxide (2µm) is first grown on top of the silicon substrate. This oxide layer needs to be of high quality (see **CHAPTER 1.2.1**) to ensure that no energy can be transferred from grafted NQDs to the substrate[206]. The SiO_2 film is then functionalized in order to build a dense monolayer[23]. To do so, SiO_2 surfaces are initially cleaned using piranha solution (1:2 volumetric ratio of hydrogen peroxide / sulfuric acid) and dipped into a solution of 20ml of toluene with 40µl of active molecule for 12 hours at 70°C. The functionalization is done in a dry N_2(g)-purged atmosphere (in a UNIlab Glovebox Workstation MBRAUN). What we call active molecule here are the molecules that we intend to graft on the surface. Two such molecules have been tested in order to have two different active groups on our surface: 11-aminoundecyltriethoxysilane (AUTES)[23] to get a terminated amine group and 11-mercaptoundecyltrimethoxysilane (MUTS) to get a thiol terminated group. Both samples are then rinsed and sonicated in toluene for 30sec. The resulting surfaces are used to attach NQDs[21,213,108].

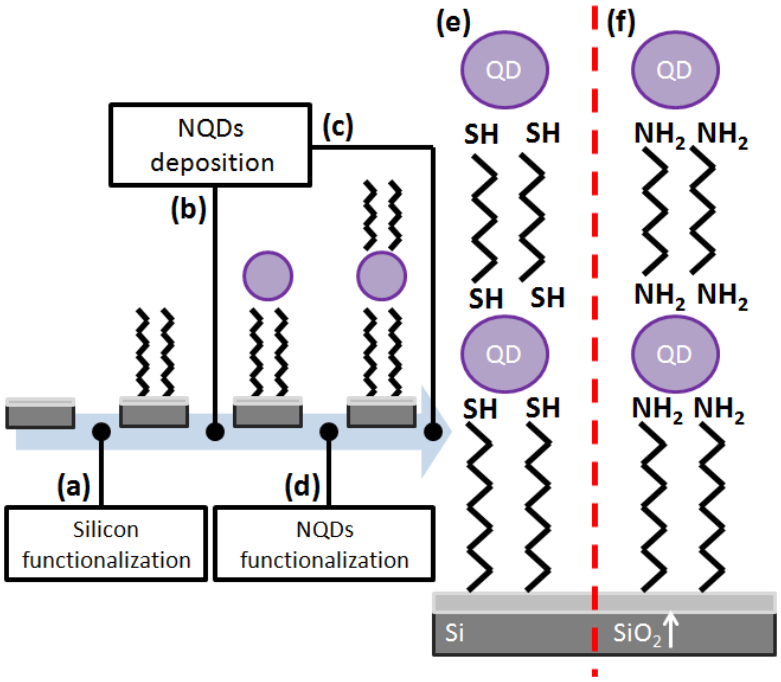

Figure 9.1: *The successive steps for preparing the two kinds of multilayers (DT based and DA based) considered in this study.*

9.2.2 Multilayer fabrication

The surface prepared in the previous paragraph is used as a starting surface for the growth of multilayer samples. These steps are shown in **Figure 9.1**b-f. NQDs (CdSe core with ZnS protective layer, purchased from Invitrogen) are then attached on the surface by leaving the samples 90min in a solution of 20µl of colloidal NQD605 diluted in 2ml of hexane and then rinsed twice and sonicated in hexane for 30sec (b). Multilayers are obtained by dipping the previous surfaces in either a solution of 1,6-hexanedithiol (DT, various concentration from 10^{-1}Mol/L to 10^{-4} Mol/L in ethanol) for 60 min for MUTS functionalized surface or 1,6-hexanediamine (DA, with various concentration from 10^{-2} Mol/L to 10^{-7} Mol/L in toluene) for

60min for amine terminated surfaces (c). All surfaces are then rinsed twice and sonicated for 30sec in their respective solvent (ethanol and toluene). NQD605 deposition can then be performed again using previous technique (d). At the end of the process, depending on the starting active molecule, we obtain multilayer of NQDs functionalized with thiol (e) or amine (f). NQDs deposition and diamine/dithiol attachment are repeated to add extra layers on the surface.

9.2.3 Characterization

Several techniques are used in this chapter to characterize the resulting surfaces including XPS, microphotoluminesence (PL) time-resolved spectroscopy, UV-vis absorption measurements, atomic force microscopy and scanning electron microscopy. All the equipments and techniques use for this work have been described in **CHAPTER 4.**

- **XPS characterization:** Cd $d_{5/2}$ peak (405.3eV) area is compared to Si 2p peak (at 103.1eV, because we are dealing with silicon oxide), which is used as normalizing reference for the whole process. Ratios are plotted with the number of multilayer grafted.
- **Microphotoluminesence (PL) time-resolved spectroscopy**: Such apparatus allows us to identify emission wavelength of deposited quantum dots with PL measurement. Decay measurement, in combination with PL measurement allows us identify energy transfer: slow radiative transfer or fast decay which is usually attributed to non radiative energy transfer.
- **UV-vis absorption measurement:** Grafting of up to 10 layers of NQDs absorbing at 565nm is performed on a thin glass sample using the same method as the one described in the

surface preparation section. This is done in order to monitor the growth of a thick photoactive film with UV absorption measurement.

- **Microscopy measurement:** In order to obtain a good estimate of topography of the surface, AFM and SEM are used. Images of a monolayer of NQD deposited on an oxide substrate have been obtained to investigate the density of the starting monolayer. For better images with SEM, oxide free silicon is used instead of silicon oxide (because SiO_2 is an insulator); the oxide free functionalization method is the same as the one described in **CHAPTER 5** (SiC_{11}).

9.3 Results and discussion:

9.3.1 Multilayer grafting

The fabrication of multilayer can be monitored with XPS and UV-vis absorption measurements. **Figure 9.2** displays the ratio between the ratio between the cadmium Cd3d peak and the silicon Si2p peak after each layer being grafted on a surface up to 3 layers. A linear increase of the ratio is observed using DA and DT showing that materials are added on the surface. It is therefore assumed that we are successively adding more layers of quantum dots as depicted in **Figure 9.1**. A similar observation can be made by looking at **Figure 9.3** that displays UV-vis absorbance as a function of grafting cycles of NQDs on a thin glass substrate only with DA (no DT). We can see that more and more quantum dots are attached on the surface even when we are dealing with an extended number of grafting cycles (up to 10 cycles).

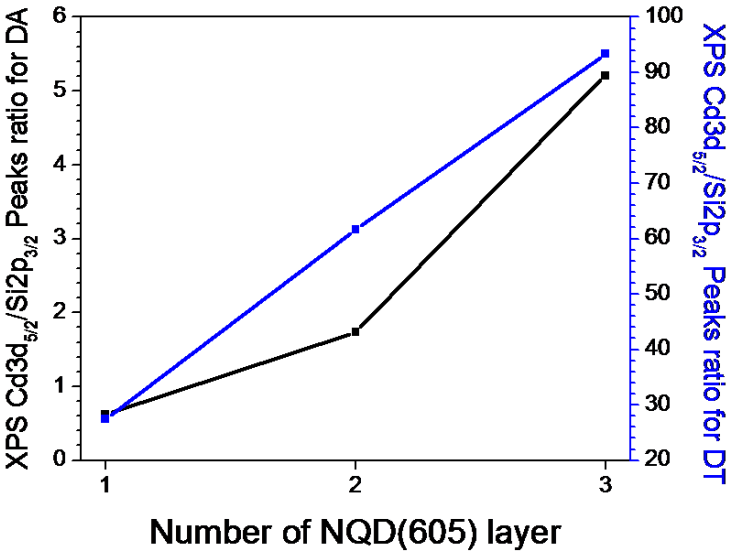

Figure 9.2: *Ratio of $Cd3d_{5/2}$ on $Si3d_{3/2}$ peaks obtained using XPS measurements done on NQDs multilayers fabricated using DA (black) and DT (blue).*

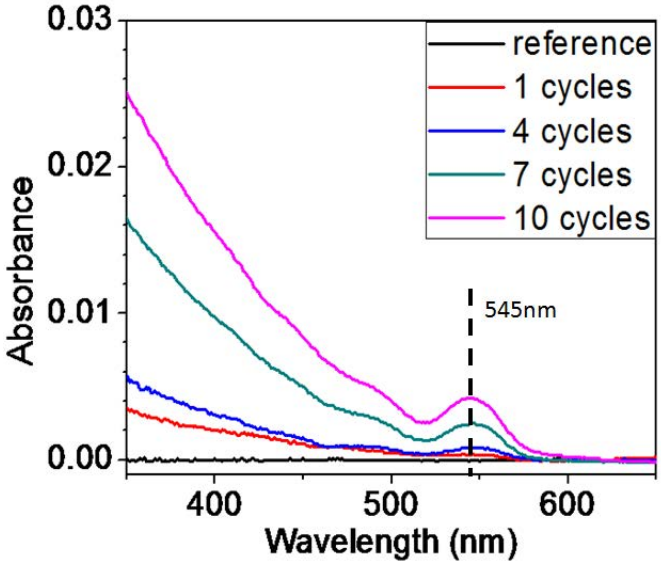

Figure 9.3*: Absorption measurements done on a thin glass substrate on which up to 10 cycles of NQDs 545 grafting have been performed.*

9.3.2 Effect of NQDs functionalization on PL measurement

Before doing any PL measurement on a multilayer, we need to investigate the effect of DA and DT on the photoluminescence of one monolayer of NQDs. Monolayers are exposed to different concentrations of DT in ethanol and DA in toluene. Time-resolved PL and measurements of PL count are performed on each samples in order to study the possible effect on the photoluminescence (thus the decay mechanisms).

Effect of Dithiol:

In order to investigate the effect of DT in our system, a monolayer of NQDs deposited on a MUTS surface (see **Figure 9.1** after step b) is exposed to several solutions of DT in ethanol with concentration varying from 1 to 10^{-4} mol.L^{-1}.Using the reference with no exposure to DT, the results are displayed in **Figure 9.4**. The functionalization of CdSe NQDs induces a big drop in the photoluminescence count (see inset **Figure 9.4**). It is strongly related to the concentration of the DT solution in ethanol as the loss in PL count scales with DT concentration. The reference yields a maximum of roughly 9300 counts/sec, which is ~6 times higher than the maximum obtained with a surface exposed to a solution with a low concentration of DT (10^{-4} mol/L). It can go up to 60 times higher when compared with surface exposed to high DT concentration (1 mol/L). Such trend cannot be attributed to the loss of NQDs attached on the surface as the ratio between $Cd3d_{5/2}$ and $Si2p_{3/2}$ is roughly the same for each DT concentration and for the reference (see **Figure 9.5**, the slight decrease in the ration can be attributed to the screening of the NQDs

on the surface by the amount of DT on top of it: an increase in the probability of photoelectrons to be absorbed by the layer of DT ligands). Time-resolve spectroscopy (see **Figure 9.4**, recorded at the peak position, *i.e.*, λ=605nm) shows that the decay is much faster after functionalization and correlates with DT concentration. The decay time for the reference sample is ~12.3nsec. This value drops and remains quite stable (~6nsec) for low DT concentrations (10^{-4} to 10^{-2} mol/L). For high DT concentrations, the drop is larger (to ~2nsec for 1mol/L). It is then assumed that there are fast mechanisms that are becoming dominant mechanisms for photoluminescence decay when we functionalize NQDs with DT. It has been shown that typically thiol groups have a big influence on NQDs CdSe[217,219,220]. It is due to a photocatalysed oxidation process: when a hole is formed due to the formation of an exciton, it is captured by a thiol which leads to the creation of a thiol radical. The latter can be stabilized with another thiol radical while creation a disulfide bond. This process is the favored one because the thiol redox energy is lower than the semiconductor valence band[217]. Time-resolved PL results suggest the dominance of this more efficient relaxation process, which interferes with any study of subtle phenomena such as NRET.

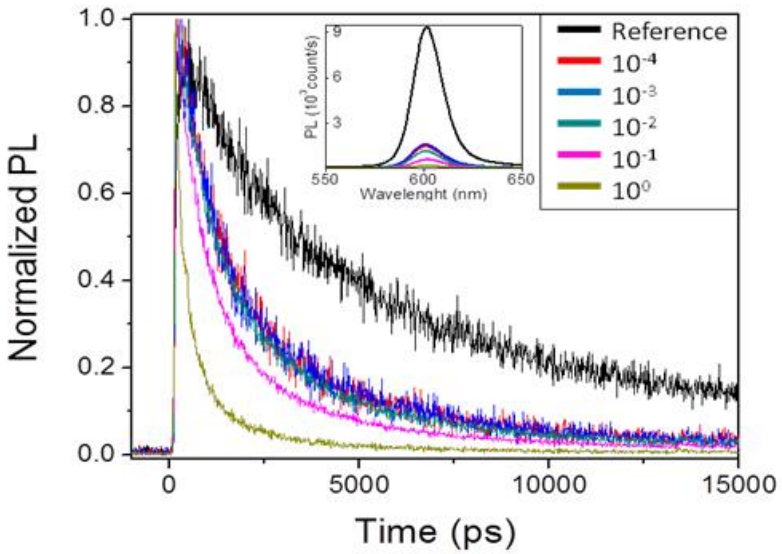

Figure 9.4: *Influence of DT concentration, varying from 1 to 10^{-4}mol/L in ethanol, on a monolayer of NQDs grafted using MUTS. The influence is investigated through time-resolved spectroscopy and Photoluminescence counts (inset). We observe a big loss in the PL count and a much faster decay compared to the reference data (no DT).*

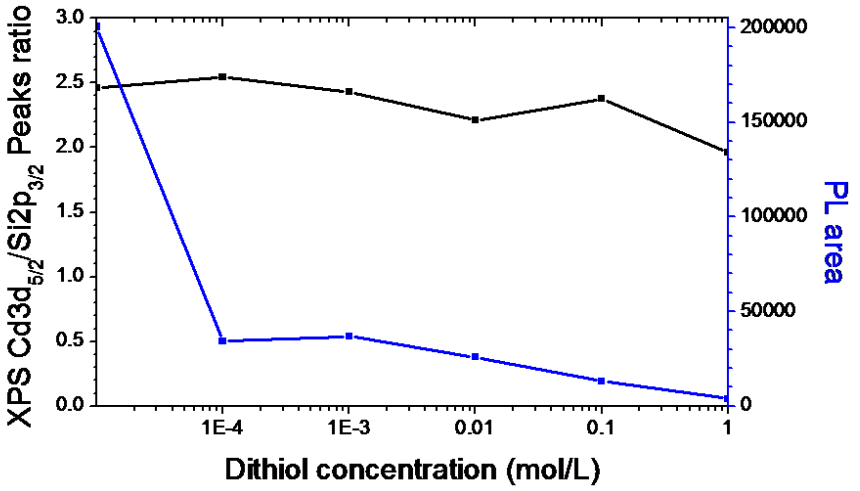

Figure 9.5: *Evolution of $Cd3d_{5/2}$ on $Si3d_{3/2}$ peaks ratio obtained with XPS with the DT concentration (black) compared to the evolution of PL count (blue). The evolution of the ratio suggests that the DT passivation has little to no influence on the number of quantum dots present on the surface.*

Effect of diamine:

Similar experiments have been done using DA instead of DT: a monolayer of NQDs deposited on a silicon surface functionalized with AUTES is exposed to several solutions of DA in toluene with different concentration. The results are displayed in **Figure 9.6**. NQDs functionalized with DA show an increasing PL count. The maximum PL count is around 6000counts/sec for the reference sample. This number can reach 10000 counts/sec after functionalization with a 10^{-5} mol/L DA solution in toluene. With higher concentration (10^{-2} mol/L) the PL count reaches 14000 counts/sec. The photoluminescence decay (recorded at λ=605nm) remains relatively slow and stable with the DA concentration below 10^{-4} mol/L: we measure a value around 12.1nsec. When the concentration reaches 10^{-3} mol/L, the decay time is even slower suggesting that the radiative energy transfer is becoming an even more predominant energy transfer mechanism. The decay time increase up to 12.8nsec and 13.6nsec for 10^{-3} mol.L^{-1} and 10^{-2} mol.L^{-1} respectively. It is assumed here that the DA functionalization effectively passivates the surface of the NQDs, removing recombination sites and traps. This passivation is a necessary enhancement for energy transfer characterization.

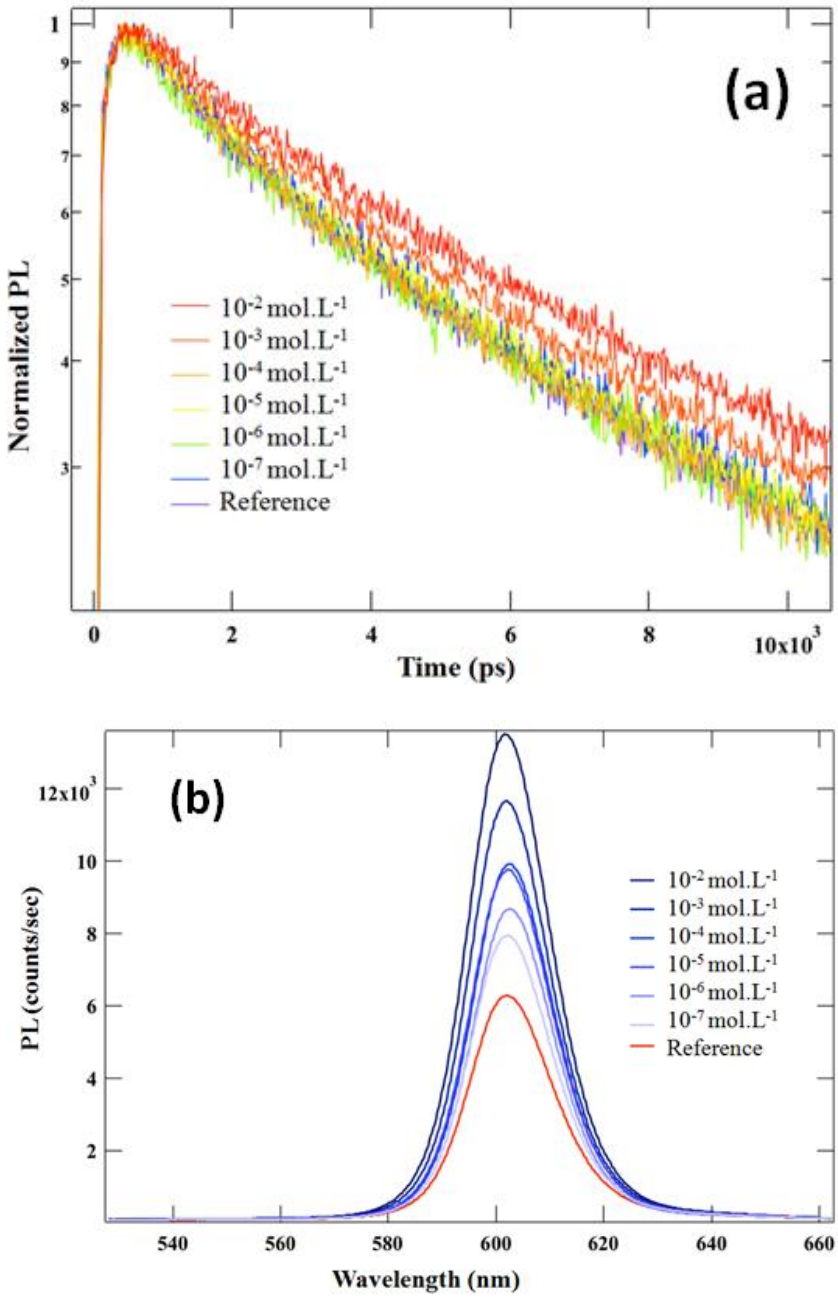

Figure 9.6: *Influence of DA concentration, varying from 10^{-2} to 10^{-7} mol/L in toluene, on a monolayer of NQDs grafted using AUTES. The influence is investigated through time-resolved spectroscopy (a) and Photoluminescence counts (b). We observe a big gain in the PL count and a stable decay time compared to the reference data (no DA).*

9.3.3 Photoluminescence measurements of multilayers

Multilayers have been fabricated on silicon oxide using DA with a concentration of 5.10^{-2} mol/L in toluene as a double linker between each NQDs layers. Up to three layers have been stacked this way and the different steps have been monitored with PL measurements (**Figure 9.7**). All PL measurements have been done after DA passivation of the last NQDs layer deposited. The results show an increase in the maximum count with the number of layers added. The maximum PL count at ~605nm varies from 15000 ± 300 counts/sec with only the first layer to 18500 ± 300 counts/sec after adding the second layer and 19500 ± 300 counts/sec after adding the third and last layer. The PL gain is noticeable with the second layer, but it is not double and certainly not triple when adding the third layer. This can be explained by the fact that the second and third layers do not have the same quality as the first one as every defect on a layer has a huge influence on the quality of the next layer. Another reason can be that a non-negligible part of the energy does not decay radiatively but can be transferred non-radiatively (NRET) between each layer (see inter-dot energy transfer in **CHAPTER 3**). It is possible because of the size distribution of the NQDs: transfer can only be done from one NQD to another with a lower energy (higher wavelength). The density of NQDs in a monolayer is such that the distance between each NQDs is big enough to prevent NRET between them as shown in a previous study[21]. But there can be transfer between NQDs of each layer (which will be the topic of **CHAPTER 10**). Time resolved spectroscopy measurements (see inset **Figure 9.7**) show that the decay is faster as the number of layers increases: there is a decay of 13.2nsec with one layer, 10.4nsec with two layers and 10.2nsec with three layers. These numbers suggest that a fast

mechanism is being more important the more NQDs layers we add on our surface. This fast mechanism has been associated with the NRET between two NQDs of different layers.

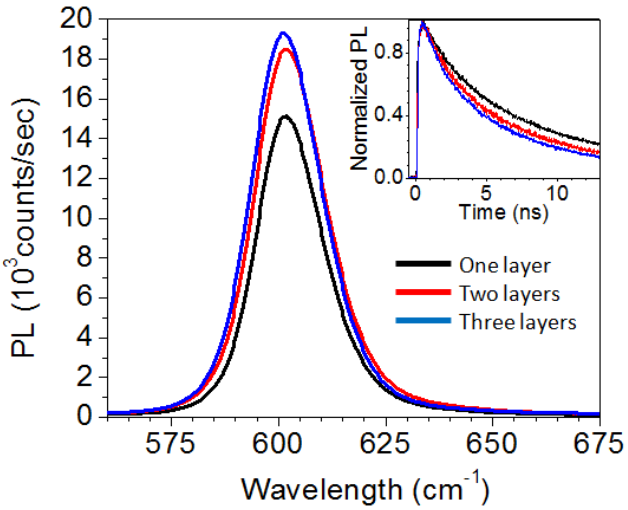

Figure 9.7: *PL measurement evolution with increasing number of layers grafted on an AUTES functionalized silicon substrate. The PL count increase with additional layers but the PL gain decrease after the second layer. µPL measurements (inset) show a faster decay time as we add layers on the sample suggesting that faster energy transfer mechanism are being more prevalent.*

9.3.4 Density of layers

We have shown that we can add more material on the surface. The more grafting cycle being done, the more quantum dots are being attached on the surface. Here we investigate whether we add additional layers on the surface or just keep adding material in the first imperfect monolayer. AFM images of a monolayer of NQD deposited on an oxide substrate have been obtained to investigate the density of the starting monolayer as shown in **Figure 9.8**. Monolayers deposited on AUTES and on MUTS are of similar density (10^{12} NQD/cm^2) according to AFM

images (**Figure 9.8**). But this microscopy technique cannot provide an accurate representation of the actual density. SEM pictures can more clearly and quantitatively give the coverage of the first layer. We use a monolayer of NQDs with known density for comparison. For better images, oxide-free silicon surfaces need to be used instead of silicon oxide; the functionalization method is done with a SiC_{11} molecule. **Figure 9.9** shows the comparison with a monolayer obtained through assembly method (work done by Sara Rupich in UT Dallas in the Spring 2014). From this comparison, we see that we have a poor coverage with the grafting method: roughly 30% of the surface is covered with NQDs (which correspond to roughly 3.10^{12} NQD/cm^2 for 4nm NQDS).

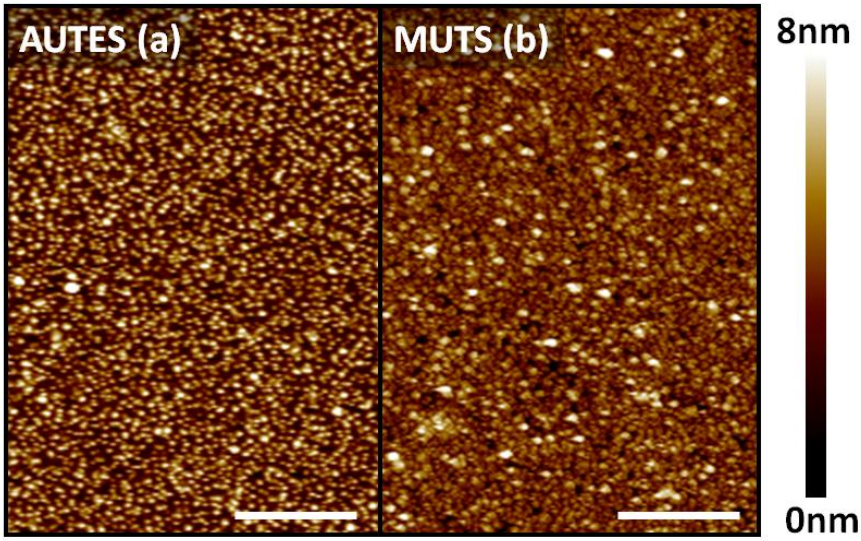

Figure 9.8: *AFM image in tapping mode of a NQD monolayer deposited on AUTES (a) and MUTS (b). The density is roughly estimated around 20 000 part/μm^2 for both surfaces. Scale bars: 500nm.*

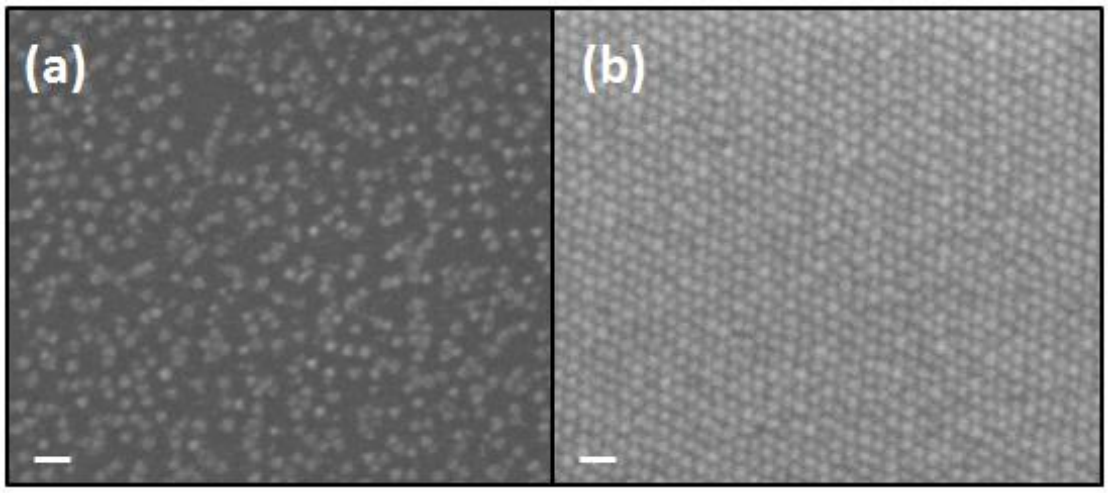

Figure 9.9: *SEM images of NQDs deposited on amine terminated functionalized silicon. The deposition has been done through usual grafting (a) and through self assembly technique (b). Scale bars: 20nm.*

According to these results, it is then assumed that each grafting cycle does not produce a full monolayer, but just about a third of a monolayer. But, since absorption measurements in **Figure 9.3** show an increase in counts bigger than three times of the initial deposition, it is then assumed that, with successive cycles, we can grow more than only one layer. Therefore, although this technique can build multilayers of quantum dots, it is not efficient as more than one cycle is needed to graft each layer. Other techniques need to be considered for applications such as solar cells. For instance, auto assembly seems more reliable as shown by Sara Rupich's recent work.

9.4 Conclusion

We have successfully demonstrated that we can fabricate NQDs multilayers using DT and DA as double ligand between each layer. XPS and UV-absorption results support the

conclusion that multilayers can be grown. Photoluminescence measurements suggest that DA is more suited for a controlled light harvesting because of its passivating effect of the NQDs interface with atmosphere. In contrast, DT introduces new transfer mechanisms that are not suitable for an efficient and reliable system. While these depositon techniques can be use in order to study the mechanisms of energy transfer (like the cascade effect in **CHAPTER 10**), they are not, however, reliable enough to build a high amount of defect-free layers on silicon for solar cells fabrication.

CHAPTER 10

EFFICIENT DIRECTED ENERGY TRANSFER THROUGH SIZE-GRADIENT NANOCRYSTAL LAYERS INTO SILICON SUBSTRATES

This chapter is a direct reproduction of a study that has been published in the Langmuir journal in 2013:

De Benedetti, William J. I., Michael T. Nimmo, Sara M. Rupich, Louis M. Caillard, Yuri N. Gartstein, Yves J. Chabal, and Anton V. Malko. "Efficient Directed Energy Transfer through Size-Gradient Nanocrystal Layers into Silicon Substrates." Advanced Functional Materials, May 1, 2014.

This work gives experimental evidence of optimization of the energy transfer between NQD and silicon with taking advantage of the multilayer fabricated in **CHAPTER 9.** Bilayers of NQDs are grafted on a functionalized surface where each layers is made NQDs with a different wavelength. Energy transfer between different NQDs and between NQDs and the substrate are studied. Along with De Benedetti W. and Rupich S., I was in charge of the fabrication of the samples following the method described in **CHAPTER 9**.

10.1 Introduction

There has been a significant interest in nanostructured photovoltaics[221] as a broad platform that can potentially enable cost-effective production of efficient and flexible solar cell modules. A multitude of structures utilizing different materials and architectures have been studied and while substantial progress has been achieved, their specific challenges and limitations are well recognized (see a well-referenced review article[221]). Since some of those limitations stem from the functional demands placed on the materials involved, it becomes important to understand if those demands could be alleviated by employing different operational

principles. Such an opportunity may arise in energy transfer (ET) based hybrid nanostructures[222,103] that seek a clear separation of the functionalities of the different materials components: one component of the hybrid structure is chosen for its strong light-matter interaction while the other for its high charge carrier mobilities. The strong near-field electromagnetic interaction is responsible for inter-conversion of neutral excitations, excitons and electron-hole pairs, between the components. In the photovoltaic (PV) mode of operation, solar light is harvested in the highly absorbing component followed by exciton diffusion and ET across the interface with the subsequent separation and transport of charge carriers entirely within the high-mobility semiconductor component. This separation of functionalities is conceptually reminiscent of photosynthesis[223], where solar energy is absorbed in light-harvesting antennae and then relayed to reaction centers that enable charge separation. Hybrid architectures operating on ET principles should thus be contrasted with conventional[221] charge transfer based PV nanostructures. Many charge transfer based structures, for example, rely on exciton fission at the interface resulting in charge carriers on both sides and therefore place high demands on carrier mobilities in both components as well as on the microscopic quality of the interface.

We have recently shown[108,206] that a combination of colloidal NQDs with ultrathin crystalline Si layers could be an attractive practical realization of ET-based hybrids for thin-film solar cells that would take advantage of the beneficial properties of both components. On the one hand, Si layers in such devices are effectively sensitized via ET from NQDs. Hence, the issue of weak solar light absorption in Si is no longer a defining factor in the overall design of the solar

cell and the thickness of the crystalline Si layer can be substantially reduced to fractions of a micron in our experiments[206]. On the other hand, NQDs, well-known as good light absorbers and emitters, are no longer required to exhibit good charge carrier transport in their assemblies. We have experimentally demonstrated very efficient (close to 90%) ET coupling between individual proximal NQDs and Si substrates over a wide spectral range as enabled via both non-radiative (NRET) and radiative (RET) mechanisms[21,108,109,206]. Hybrid structures with ET coupling can also be realized in different three-dimensional geometries[133200224]. Given the maturity of Si technology and chemical processability of colloidal NQDs, NQD/Si hybrid structures are expected to be manufacturable without major new developments.

Further assessment of the practical viability of NQD/Si hybrids requires fabrication and analysis of energy flows in structures with optically thick, multi-layer NQD arrays that would provide sufficient absorption of the incident solar light. While significant research has been carried out on various "NQD solids" due to the NQD's unique physicochemical properties of band-gap tunability, photostability and solution processability attractive for optoelectronic applications, most of the effort has focused on the improvement of carrier mobilities in these arrays[225]. For example, lead chalcogenide NQDs have been employed in conventional PV nanostructures[97,221] due to their superior performance in the near-infrared (NIR) spectral region in comparison with organic dyes; however, low charge carrier mobilities hinder progress in such NQD based solar cells. While sharing the requirement of good light absorption with conventional architectures, ET-based structures, in contrast, do not use charge transport within the NQD arrays and therefore are amenable to different property optimizations.

It is worthwhile to recall that charge and energy transfer processes have very different relevant spatial scales. Charge transfer relies on the overlap of the electronic wave functions and is therefore determined by angstrom-scale interactions; the ligands on NQDs can strongly influence charge transport in NQD solids. On the other hand, ET processes rely on relatively long-range electromagnetic interactions: the typical length scales are several nanometers for NRET and are even longer ranged for radiative transfer processes. RET from NQDs into Si substrates is expected to be efficient over distances of tens of nanometers[108,109,206].

One of the important requirements for assembling NQDs in our structures is to minimize the number of energy (exciton) scavenging events and thereby preserve their high quantum yields (QYs). This is a significant practical issue as it is known that the deposition of densely-packed NQD films commonly leads to substantial reductions in the photoluminescence (PL) QYs as compared to QYs in solutions[226]. Contributing to the deterioration of the PL QY in dense arrays is the NRET-mediated diffusion of excitons towards "defective" NQDs that act as excitonic traps where "dark-state" excitations are irrecoverably lost. One can envision various approaches to battle such energy losses. The direct approach is the reduction of the dark-exciton traps by appropriate chemical and growth routes that would tightly control the resulting structure and passivate defect sites. Recent work[227] demonstrating low-threshold lasing with dense NQD films illustrates that issues of high-QY arrays can be successfully addressed via proper fabrication.

One can also utilize accelerated directed migration of excitons from their generation locations towards the high-mobility semiconductor substrate. This design would mitigate exciton scavenging that is more frequently encountered in the random diffusion process. The idea of exciton drift can be naturally pursued in assemblies with engineered NQD size (band-gap) gradients. Indeed, several groups have demonstrated this effect in bilayer[104] and multilayer[228,229] configurations where different size NQDs are arranged in layer-by-layer geometries on neutral glass substrates. Since quantum confinement in NQDs results in larger exciton energy for smaller diameter dots (of the same composition), the NRET processes enable fast directed migration of relaxed excitons towards the layer with the largest dots. While short interlayer NRET times of fractions of a nanosecond were reported, the graded films in previous studies[104,228,229] were not optimized to maintain high overall QYs and no attempts were made to convert excitons into accessible excitations inside conducting media.

In this chapter, we explore these two approaches *via* a detailed spectroscopic study of energy relaxation pathways in size-gradient, dense NQD bilayer structures carefully grafted on planar Si and SiO_2 substrates. NQD grafting via grafted organic monolayers (GOMs) of functionalized molecules assures both the electronic purity of the underlying substrate[51] and the uniform placement of NQDs allowing for the ET processes to be studied unobscured. Additionally, the linker strategy enables us to carefully build up the subsequent NQD monolayers in a controlled manner. By using time-resolved PL measurements of the donor and acceptor NQD emission, we find that energy is unidirectionally transported into the Si substrate via sequential exciton NRET migration and direct RET coupling to the Si substrate. Based on the

analysis of the experimentally measured ET times between NQD layers and Si substrates, we estimate the overall transfer efficiency of the donor excitons in the outmost layer into Si substrate approaching ~90%. Our measurements and observations are in a good agreement with theoretical analysis of NRET- and RET-mediated energy transport in the absence of detrimental energy-scavenging mechanisms. These results suggest that linker-assisted assembly can enable the fabrication of defect-free NQD multilayer structures with unimpeded energy flows into the underlying semiconductor substrate. This further supports the concept of ET-based hybrid nanocrystal/Si thin film PV devices, where bandgap-engineered optically thick NQD layers are used as primary solar photon absorbers to further funnel excitons into high-charge-mobility ultrathin Si substrates.

10.2 Preparation method

The preparation of bilayers on SiO_2 was done following the method detailed in the **CHAPTER 9**: an AUTES functionalization of the glass was done before attachment of NQDs. different kind of quantum dots were used for each layer. Linkers between each layer were amine based (DA). Bilayers done on oxide free silicon were done using the long chain GOM (SiC_{11}) described in **CHAPTER 5** instead of the AUTES functionalization. The rest of the process is similar with the process done on SiO_2 sample. The last layer for each sample was passivated with amine based linker. Two DA have been tested ethylenediamine (C2 short chain) and 1,6-hexanediamine (C6, long chain).

10.3 Results and discussion

10.3.1 Bilayer on glass

We studied and compared the time-resolved decay of excitons in photoexcited NQDs in monolayer and bilayer arrangements on SiO_2 and Si substrates as schematically shown in **Figure 10.1**a and **Figure 10.4**a. NQD monolayers were attached to the substrates via amine terminated GOMs. In the bilayer samples, a second layer of NQDs was linked to an underlying monolayer of NQDs via short alkyldiamines. We have used two different sizes of CdSe/ ZnS core shell NQDs, whose PL emission spectra are centered approximately at 545 nm and at 585 nm. We refer to them as donor (D) and acceptor (A) NQDs, respectively, as they act in the capacity of energy donors and energy acceptors in the bilayer configuration. The experimental PL data for NQDs on SiO_2 substrates are collected in **Figure 10.1** and the data for NQDs on Si substrates in **Figure 10.4**. With the selected NQDs, the emission spectra of Ds and As are well separated as is clear from the figures. Moreover, the ~0.16eV difference in energy of the respective excitons is large enough to prevent thermally activated exciton transfer from A to D at room temperature. Under this condition, the simplest linear kinetic model describing the time evolution of the number of donor, N_D , and acceptor, N_A , excitons from their original quantities $N_D(0)$ and $N_A(0)$ at time t = 0 is given by equations[230]:

$$\frac{dN_A}{dt} = -\gamma^A N_A + wN_D; \qquad \textit{Eq 10.1}$$

$$\frac{dN_D}{dt} = -\gamma^D N_D - wN_D. \qquad \textit{Eq 10.2}$$

Here, w is the rate of the exciton transfer from the excited donor NQD to the acceptor NQDs, while γ^D and γ^A are the decay rates of the D and A excitons due to all other radiative and non-radiative processes. (It should be kept in mind that γ^D and γ^A rates can themselves depend on the configuration under study.) The solutions to **Eq 10.1** and **Eq 10.2**

$$N_D(t) = N_D(0)e^{-(\gamma^D+w)t}, \qquad \textit{Eq 10.3}$$

$$N_A(t) = N_A(0)e^{-\gamma^A t} + \frac{wN_D(0)}{\gamma^D+w-\gamma^A}(e^{-\gamma^A t} - e^{-(\gamma^D+w)t}), \qquad \textit{Eq 10.4}$$

can be exploited in the analysis of the experimental data in the bilayer samples. When compared with the PL dynamics of the monolayers, the important qualitative features of the solutions are the acceleration of the D decay in **Eq 10.3** due to exciton transfer to A (here it is a mono-exponential decay), and the appearance of the corresponding energy "in-flow" in the acceptor dynamics in **Eq 10.4**. These salient features are exhibited by the experimental data in panels (c) and (d) of **Figure 10.1**.

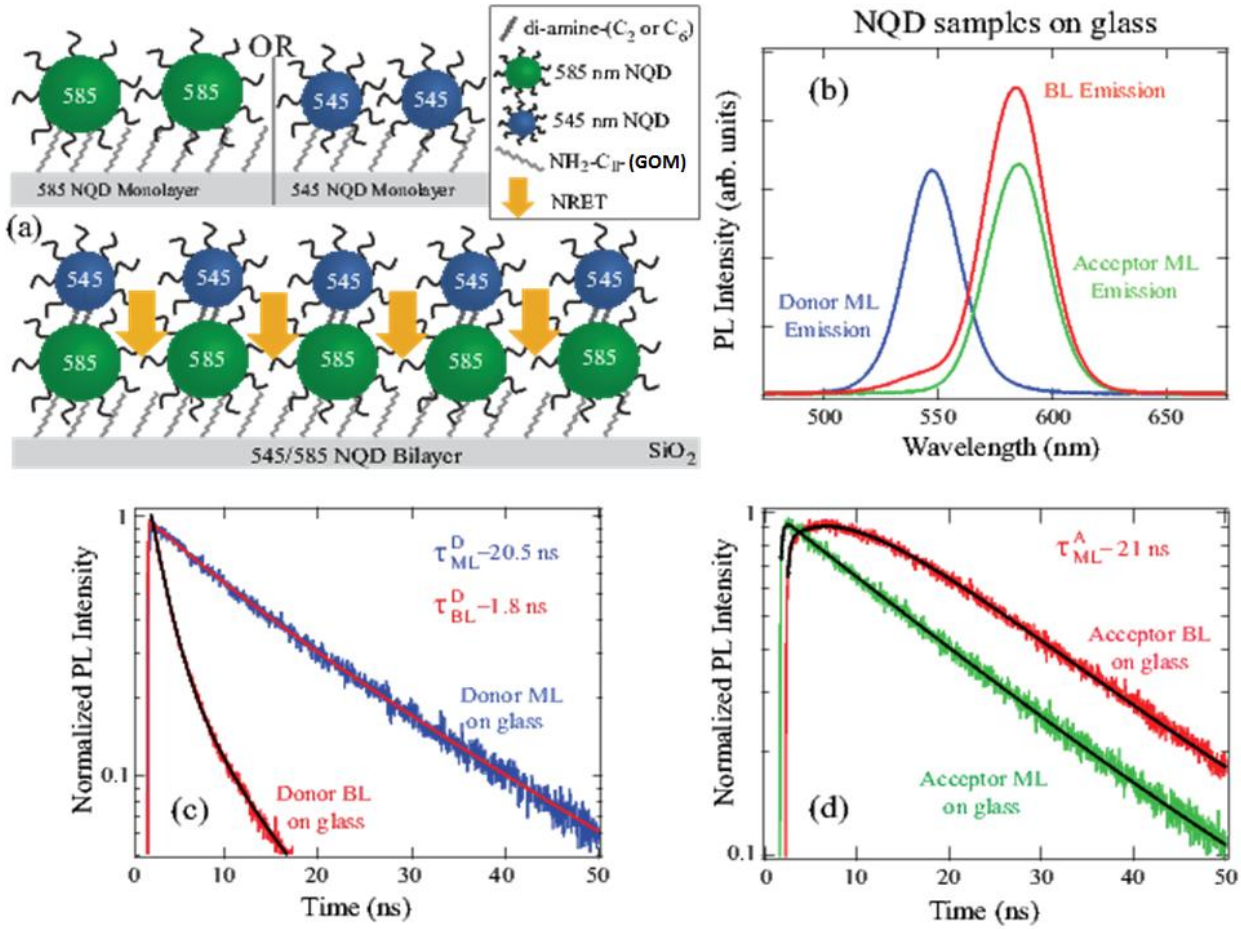

Figure 10.1: *(a) Schematics of the monolayer and bilayer placement on SiO_2 substrate. (b) PL emission spectra for donor monolayer (NQD-545, ML), acceptor monolayer (NQD-585, ML) and bilayer (NQD-545 on NQD-585, BL) samples grafted on SiO_2. The spectra represent three different samples. (c) PL dynamics at donor emission peak (545 nm) for donor monolayer (top trace) and bilayer (bottom trace) samples. Traces are shown along with the fitting curves. (d) PL dynamics at acceptor emission peak (585 nm) for acceptor monolayer (bottom trace) and bilayer (top trace) samples. Fitting curves are also displayed for panels (c) and (d). From De Benedetti et al., Adv. Funct. Mater. (2014).*

Figure 10.1b shows the PL spectra of D and A emission in monolayer and bilayer samples grafted on SiO_2 substrates. It is clearly seen that in the bilayer sample, the relative PL intensity from the donor NQDs is much smaller than the PL from the acceptor NQDs. This is indicative of efficient ET from the donor to the acceptor layer as characteristic of short-distance

NRET processes[229]. It may be unreliable to make quantitative assessments of the efficiency and rates of the NRET process from PL intensity (or photon count) measurements as, for instance, varying NQD surface coverage would inherently affect the comparison between samples. A direct and much more reliable quantitative approach is to study changes in the PL dynamics which are unaffected by the number of photo-excitations and rather are determined only by the rates of the relevant processes[109]. **Figure 10.1**c shows a drastic acceleration of the donor PL intensity decay in the presence of acceptors in the bilayer configuration (bottom trace, BL) as compared to the donor decay in the monolayer configuration (top trace, ML): the respective decay times are found as $\tau_{BL}^{D} = 1.8nsec$ and $\tau_{ML}^{D} = 20.5nsec$. The faster donor PL decay in the bilayer structure clearly demonstrates the presence of an additional decay channel, which is NRET from the donor to the acceptor layer. A good estimate of the interlayer rate *w* can be derived already from the raw data. Indeed, in the case of the SiO_2 substrates, the D decay rate γ^D into other channels can be approximated by its value $\gamma_{ML}^{D} = 1/\tau_{ML}^{D}$ in the donor monolayer configuration. This arises from the fact that these other decay channels for samples on the SiO_2 substrate are presumed to be purely radiative[108,206]. The distance from the donor layer to the SiO_2 substrate in the bilayer, while larger than in the donor monolayer, is still only about 10nm so that the change in the donor radiative rates between the bilayer and monolayer samples is small[108,206]. In this approximation, the interlayer NRET time $\tau_w = 1/w$ is then found from $w = 1/\tau_{BL}^{D} - 1/\tau_{ML}^{D}$ to be τ_w~2.0 nsec. The efficiency of the interlayer NRET (defined as a fraction of the overall decay rate) is correspondingly evaluated as $w/(\gamma^D + w) = \tau_{BL}^{D}/\tau_w \sim 0.91$. This result strongly suggests that NRET from the donor to acceptor NQD layers is highly efficient. A more accurate analysis taking into account that

bilayer's $\gamma < \gamma_{ML}^{D}$ would lead to a slightly shorter interlayer NRET time and a bit higher efficiency.

An important counterpart in the detection of the interlayer NRET is the observation of the energy "in-flow" in the A layer. To this aim, in **Figure 10.1**d we directly compare the time evolution of the PL of the acceptor layer in the bilayer structure (top trace, BL) to the PL of an acceptor monolayer on SiO_2 (bottom trace, ML), where no ET would occur. It is clearly seen that the A emission rises slower in the bilayer sample, consistent with ET from the D to A layer. For a clearer demonstration of the changes in the acceptor PL emission, we selected a bilayer sample with a somewhat higher concentration of donor NQDs. Indeed, as per **Eq 10.4**, changes in the rise time of the acceptor can be obscured if the initial number of excitons in the A layer, $N_A(0)$, is appreciably greater than the initial number $N_D(0)$ of donors excitons. Since the laser excitation of the donor NQDs also creates excitons in the acceptor NQDs and the absorption cross-section of the bigger-sized NQDs is larger, a larger number of excitons could be created in the acceptor layer. This is why samples with higher D concentrations are more desirable when probing acceptor rise times (**Figure 10.1**d).

While the simple kinetic **Eq 10.1** and **Eq 10.2** feature single values of various rate constants resulting in the monoexponential D decay in **Eq 10.3**, the real samples are well known to frequently exhibit more variations. In fact, in several instances, we observed the presence a relatively weak second exponent in the D decay in bilayer structures as seen in **Figure 10.1**c. The second component may arise from a distribution of distances between the donor and

acceptor NQDs, *e.g.* due to some small inhomogeneities in the NQD placement. In such cases, the experimental data is processed for fitting with weighted contributions from two rates: $w = C_1 w_1 + C_2 w_2$, where coefficients $C_{1,2}$ satisfy $C_1 + C_2 = 1$ and $w_{1,2}$ are NRET rates derived from biexponential fits to the donor decay traces.

The experimental traces in **Figure 10.1** are overlayed with fitting curves from the kinetic model showing satisfactory agreement. In particular, the solid black curve in **Figure 10.1**d fits the acceptor dynamics in the bilayer configuration using **Eq 10.4**. All of the kinetic rate parameters for this equation (the donor and acceptor decay rates in the monolayers and the NRET rate in the bilayer) were first independently measured, thus leaving the relative initial number of D and A excitons, $N_D(0)/N_A(0)$, as a fit parameter. The displayed agreement between the model fit and experimental data is achieved for the ratio of $N_D(0)/N_A(0) \sim 1.2$. This value appears reasonable given the ratio of the D and A monolayer PL intensities in **Figure 10.1**b although we cannot make a direct comparison. The satisfactory quantitative characterization of the bilayer configuration on SiO_2 substrates can be used to extract information on the interlayer NRET interactions for analysis and comparisons with hybrid configurations on Si surfaces.

From **Figure 10.1**d, it is also clear that the acceptor exciton decay rates in the bilayer and monolayer configurations are very close: $\gamma^A \sim \gamma^A_{ML}$; moreover, the observed decay time of $\tau^A_{ML} \sim 21 nsec$ is very similar to the previously measured decays[108] in submonolayer samples. The latter observation is also true for the donor exciton decay in **Figure 10.1**c, where the measured decay time τ^D_{ML} closely matches our measurements in submonolayer samples. As the

exciton decay in submonolayer samples is largely determined by the spontaneous decay rates of individual NQDs, our measurements of the PL kinetics in mono- and bilayers strongly indicate that no substantial detrimental exciton-scavenging channels were introduced when we fabricated dense NQD samples with our linking approach.

10.3.2 Theoretical model

This model is essentially the product of Malko *et al.* and Gartstein *et al.* work.

It is interesting and instructive to discuss the experimentally observed trends in the context of a related simpler theoretical model system which is depicted in **Figure 10.2**a. The theoretical analysis of the modification of the electromagnetic decay rate of an electric dipole emitter in the vicinity of stratified dissipative and non-dissipative substrates is well known[231,232] and we described details of its applications for similar systems in several recent publications[108,109,206,233,234]. Comparing exciton decay times τ_1 and τ_2 (without and with the acceptor layer, respectively) in model configurations of **Figure 10.2**a should be similar to comparing donor decay times τ_{ML}^{D} and τ_{BL}^{D} in the experimental monolayer and bilayer configurations. The computational results displayed in **Figure 10.2**b and **Figure 10.2**c clearly illustrate how ET from the donor exciton into the acceptor layer is sensitively dependent on both the distance *z* to the layer and on the layer's dielectric/optical parameters *n* and *a* .

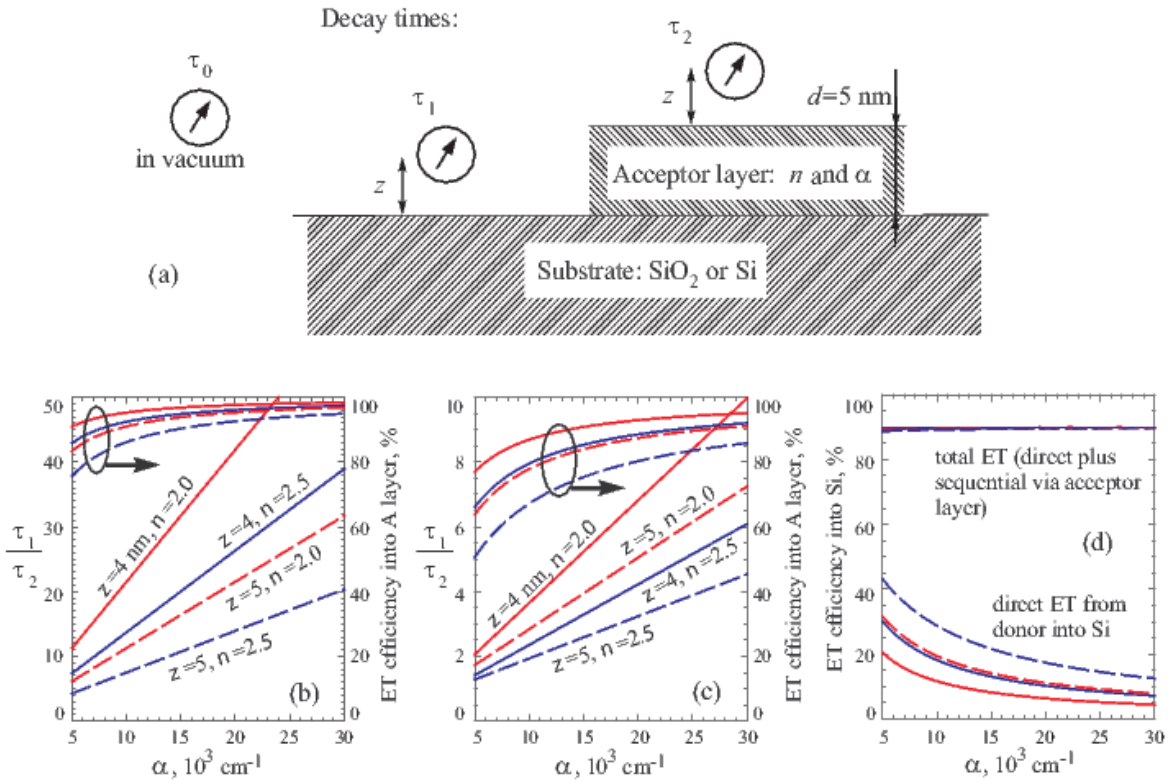

Figure 10.2: *(a) Schematics of a related simpler model system where a single randomly oriented electric-dipole donor exciton decays in different configurations: when in vacuum, its radiative decay time is τ_0, when in the vicinity (at distance z) of a substrate, the decay time is τ_1, and when at the same distance z from the acceptor layer on top of the same substrate, the decay time is τ_2. In calculations, the acceptor layer is a macroscopic slab of thickness d = 5 nm that is characterized by its absorption coefficient a and refraction index n. Panels (b) and (c) show the results of computations for the ratio of decay times τ_1/τ_2 as a function of the absorption coefficient a of the A layer in the model system. This ratio can be compared to experimental ratios τ^D_{ML}/τ^D_{BL} for the donor decays in the monolayer and bilayer configurations. Results in panel (b) are for the SiO_2 substrate with a refraction index n_G = 1.5, results in panel (c) are for the Si substrate whose complex dielectric function at the emission wavelength λ_0 = 545 nm is as reported by Aspnes and Studna[108,107]. Each panel features results calculated for two different distances z of 4 and 5 nm, and for two different values of n = 2 and 2.5 as indicated. Also shown in panels (b) and (c) are the corresponding coordinated ET efficiencies into the A layer defined as a fraction of the overall decay into all channels (upper curves referring to the right axes). (d) ET efficiency from donor NQDs into the Si substrate in the bilayer configurations. Different style curves are coordinated with the lines in panel (c). The lower group of curves shows the direct ET into Si as a fraction of the donor decay into all channels. For the total ET (the upper group of curves), the direct ET is complemented by the sequential ET process via the acceptor layer. Here, the efficiency of the ET into the acceptor layer is taken from panel (c), and 90% of the acceptor excitons are assumed[108] to be further transferred into Si. From De Benedetti et al., Adv. Funct. Mater. (2014).*

We show the results calculated for a range of values of these parameters that we expect to find in our experimental systems. The diameters of the NQDs used are about 4.7 nm and 5.3 nm for NQD-545 and NQD-585, respectively. The length of different linker molecules is assessed to be between 1 and 2 nm. The chemistry of our linkers ensures their direct attachment to the NQD body and to the substrate surface. One can thus estimate distances z from the centers of spherical NQDs (associated with the position of the point-like electric-dipole emitter) to the underlying (effective) surface[108]. For the effective absorption coefficient a of the acceptor layer that is treated in calculations as a continuum slab of thickness d = 5 nm, in **Figure 10.3** we also provide the results of our measurements on a monolayer of the acceptor NQDs. The experimentally measured optical density was converted here into the absorption coefficient assuming that the monolayer constitutes an absorbing slab of the same thickness d.

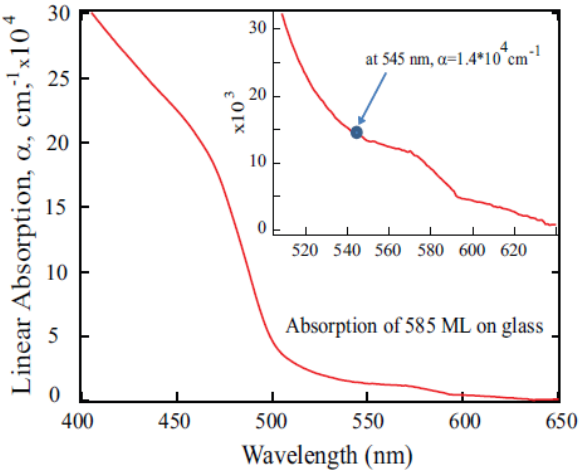

Figure 10.3: *The wavelength dependence of the effective absorption coefficient of the acceptor layer as derived from the measured raw data on optical density of the monolayer of acceptor NQDs under the assumption of layer thickness of 5 nm. From De Benedetti et al., Adv. Funct. Mater. (2014).*

The results of **Figure 10.3** yield a value of $a \sim 1.4 \times 10^4$ cm^{-1} at the donor emission wavelength λ_0 = 545 nm. We consider this value only as representative—we are not pursuing actual fits with the computational data in this chapter and rather concentrate on semi-quantitative understanding. Overall, the experimentally observed value of $\tau_{ML}^D/\tau_{BL}^D \sim 11.4$ on SiO_2 substrates (**Figure 10.1**) can be rationalized in the context of computational results in **Figure 10.2**b, particularly given the fact that extra dielectric screening takes place in experimental samples due to the presence of the donor layer, which is absent in the model system. The same theoretical panel (b) also shows that the ET efficiency into the acceptor layer is very high, in excess of 80% for all the curves shown and at or above 90% in the expected experimental region. Here, efficiency is defined as a fraction of the overall decay rate of the donor exciton. Indeed, the rate of NRET into the A layer here should dominate with respect to the rates of otherwise radiative processes. The latter are only modestly accelerated from the spontaneous vacuum value in the vicinity of SiO_2 substrates: the computations yield $\tau_1/\tau_0 \sim 1.63$ at z = 4 nm and $\tau_1/\tau_0 \sim 1.55$ at z = 10 nm. This weak distance dependence of the radiative processes has already been mentioned earlier in this chapter.

On the other hand, the exciton decay is expected to be greatly affected in the vicinity of Si substrates: the computations give $\tau_1/\tau_0 \sim 9.96$ at z = 4 nm, which reduces to $\tau_1/\tau_0 \sim 6.95$ at z = 5 nm and falls to $\tau_1/\tau_0 \sim 3.63$ at z = 10 nm. The main reason for this strong distance dependence is that NRET into Si is a very substantial contributor whose rate drops precipitously within several nanometers[21,108,109,206]. However, even weakly distance-dependent RET process have

much higher rates into Si than into SiO_2 due to higher refraction index of Si. With stronger competition from ET into Si, the ET efficiency for the donor exciton into the A layer should be lower on Si substrates than on SiO_2 substrates. This is quantitatively illustrated in **Figure 10.2**c. The computational data in this panel suggests that the ratio $\tau_{ML}^{D}/\tau_{BL}^{D}$ of the decay rates in the monolayer and bilayer configurations on Si substrates should be substantially smaller than that measured on SiO_2 substrates: for this model, we expect values within the 2–3 range.

10.3.3 Bilayer on Silicon

Comparison of the experimental data for the monolayer and bilayer configurations on Si substrates is shown in **Figure 10.4**. Similar to samples on SiO_2 substrates, the PL intensity of the donor emission in bilayers on Si is strongly reduced in comparison with the acceptor emission (**Figure 10.4**b). The quantitative results for samples on Si substrates are however quite different from samples on SiO_2 substrates. First, the donor decay time in the monolayer configuration on Si is much faster (**Figure 10.4**c): $\tau_{ML}^{D} \sim 3.3 nsec$, about 6.2 times as fast as the decay in monolayers on SiO_2 . This agrees well with our previous measurements[108] at the donor wavelength and the computational results from the model system. The acceleration of the decay is caused by the combined effects of NRET and RET into the Si substrate[21,206]. Second, an even faster donor decay is observed in the bilayer samples: $\tau_{BL}^{D} \sim 1.1 nsec$ (the value is derived from a double exponential fit to the decay curve in **Figure 10.4**c), but the ratio of the decay times: $\tau_{ML}^{D}/\tau_{BL}^{D} \sim 3$, is now substantially smaller than the value obtained for the samples on SiO_2

substrates. With a single exponential fit to the decay curve, the extracted value $\tau_{BL}^{D} \sim 1.6 nsec$ results in an even smaller ratio $\tau_{ML}^{D}/\tau_{BL}^{D} \sim 2.1$. These smaller values are very much in line with the theoretical expectations of the τ_1/τ_2 ratio shown in **Figure 10.2**c for the model system. As discussed above, the smaller ratio is a result of a decreased ET rate from the donor into the Si substrate in the bilayer configuration: at such distances from the substrate, NRET does not add significantly to the RET contribution. (For smaller distances from the donor to the Si substrate in the monolayer configuration, NRET is a major decay channel.) On the other hand, NRET from donor NQDs into the acceptor layer would have practically the same rate *w* on either substrate—if no changes in the acceptor layers exist—and it is tempting to use the information extracted from samples on SiO_2 substrates for the analysis of the experimental data on Si substrates. Equating the donor decay rate $\gamma^D + w$ in Eq.3 with the observed inverse decay time $1/\tau_{BL}^{D}$ in the bilayer configuration and taking $\tau_w \sim 2.0$ ns from measurements on SiO_2, one would arrive at the efficiency $w/(\gamma^D + w)$ of ET into the acceptor layer equal to $\sim$ 55% for $\tau_{BL}^{D} \sim 1.1 nsec$ and $\sim$ 80% for $\tau_{BL}^{D} \sim 1.6 nsec$. While the former efficiency estimate appears too low to be consistent with the model predictions in **Figure 10.2**c , the latter estimate is in good agreement with the range of expectations from the model guidelines. The self-consistency of the second estimate can further be verified by evaluating the rate $\gamma^D = 1/\tau_{BL}^{D} - 1/\tau_w$ and comparing it to the rate $\gamma_{ML}^{D} = 1/\tau_{ML}^{D}$, where we find $\gamma_{ML}^{D}/\gamma^D \sim 2.4$ for $\tau_{BL}^{D} \sim 1.6 nsec$, a very reasonable ratio from the theoretical view point. On the other hand, if $\tau_{BL}^{D} \sim 1.1 nsec$ is used with the same values of *w* and τ_{ML}^{D} that would lead to an obviously incorrect value γ_{ML}^{D}/γ^D. Given the variations in linkers and grafting procedures on different surfaces, some variations in the acceptor layers on different substrates are possible, and then the interlayer NRET rate *w* could be somewhat different in the

configurations on SiO_2 and on Si. With these uncertainties, it appears unwarranted at this stage to look for a more detailed quantitative agreement with the computational results obtained for an approximate model system.

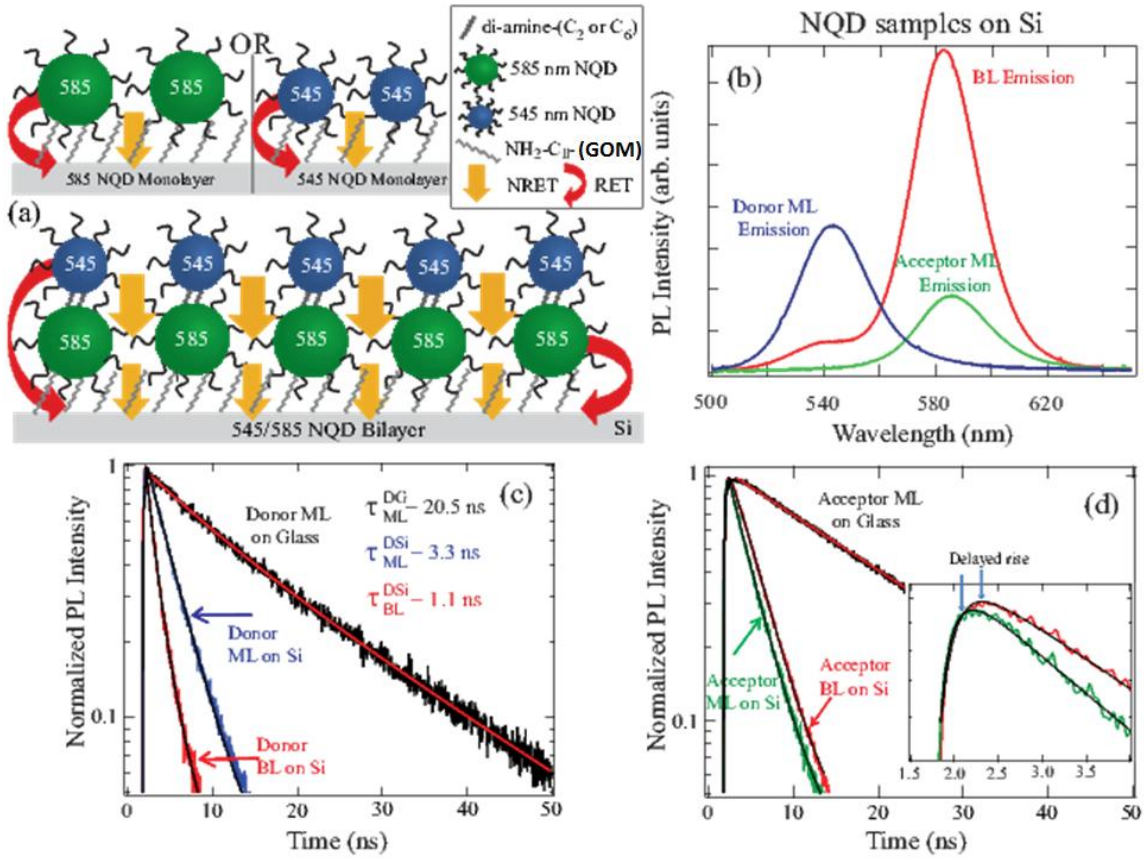

Figure 10.4: (*a) Schematics of the monolayer and bilayer NQD placements and of the relevant ET processes on Si substrates.* (*b) PL emission spectra of donor monolayer (NQD-545, ML), acceptor monolayer (NQD-585, ML) and bilayer (NQD-545 on NQD-585, BL) samples grafted on the Si substrates.* (*c) Compared are the PL dynamics at the donor emission peak (545 nm) for the donor monolayer on SiO_2 (top trace), donor monolayer on Si (middle trace) and donor in the bilayer on Si (bottom trace) configurations. Traces are shown along with the fitting curves.* (*d) Comparison of the PL kinetics at the acceptor emission peak (585 nm): acceptor monolayer on SiO_2 (top trace), acceptor monolayer on Si (bottom trace), and acceptor in the bilayer on Si (middle trace). The inset more clearly shows the delayed rise time and the fitting curves. From De Benedetti et al., Adv. Funct. Mater. (2014).*

We further ascertain ET from the donor to the acceptor layer by comparing the acceptor PL kinetics curves. **Figure 10.4**d and its inset clearly show a delayed rise time of the acceptor PL in the bilayer configuration – as expected from **Eq 10.4**. As we discussed above, the evolution of the PL dynamics curves can strongly depend on the interplay of the kinetic rates (w, γ^A) as well as on the initial ratio $N_D(0)/N_A(0)$ of photogenerated excitons. With much higher decay rates on Si substrates, the resulting decay of the acceptor PL is much faster, which often complicates a quantitative delineation of the rise and fall pattern; however, a delayed rise-time pattern is still clearly observed for the bilayer configuration. Additionally, a visually satisfactory fitting can be done, as the inset shows for the particular fit that resulted in the values of $N_D(0)/N_A(0) \sim 2.4$ and $\tau_w \sim 3$nsec. While these may be reasonable estimates by themselves, their precise quantitative consistency with the donor-decay results is not as clear and we do not rely on them for any firm quantitative conclusions. Once again, this may be reflective of the delicate nature of the linking and grafting procedures that may result in variations between different samples. However, it is reassuring that the kinetic parameters derivable from different fitting routines appear to be within reasonable variation ranges. As an example, different estimates that we extracted for interlayer NRET rates in different samples vary at most by a factor of 2.

Just as in the case for samples on SiO_2 substrates, we stress that the decay times for acceptors in the monolayer and bilayer configurations on Si surface are evidently very close to each other, see **Figure 10.4**d. Moreover, they are close to the donor decay times and to our earlier results[108] for the submonolayer samples. This indicates that the grafting and linking procedures we used allowed us to avoid the formation of any appreciable number of energy

trapping and scavenging sites, otherwise the PL lifetimes would have become even shorter due to additional PL quenching channel(s). In support of this conclusion is the rather faithful correspondence between experimental data and theoretical expectations from the simple model system that does not invoke any detrimental energy scavenging processes but incorporates only well-characterized radiative and non-radiative processes of ET and photon emission.

10.3.4 Efficiency

The experimental data we obtained can thus allow for full rationalization on the basis of well-defined ET pathways without a need to invoke poorly characterized non-radiative exciton trapping/scavenging mechanisms discussed for NQD solids. The good correspondence between our experimental observations and the theoretical expectations from the simple model system in **Figure 10.2** suggests to use the model's help in the further analysis. We are particularly interested in the efficiency of ET from the donor NQDs into the Si substrate in the bilayer configuration, an important measure for photovoltaic applications. **Figure 10.2**c shows the efficiency of NRET from the donor exciton into the acceptor layer as a fraction of the overall donor decay. Consistent with our experimental data for the bilayers on Si substrates, it is clear that the majority of the photoexcitations created in the donor NQD layer are first transferred into the acceptor NQD layer, the precise quantity being dependent on values of system parameters. In addition, a portion of the donor excitons are transferred directly into the Si substrate. At this distance ≈10 nm from the substrate, this direct ET is mainly realized via the longer-range RET coupling but there is still some contribution from NRET[108,109,206]. The lower group of curves in

Figure 10.2d shows the computational results for the efficiency of the direct ET as fraction of the overall donor decay. The precise quantity here is also evidently dependent on the values of the system parameters. The excitons that are first transferred into the A layer would, in turn, be efficiently transferred into the Si substrate via the combined effects of NRET and RET[108, 206] from the acceptor NQDs. Our prior studies[108] showed that the efficiency of this ET is close to 90%. Using this number we calculate the total efficiency of direct and sequential ET from donor NQDs into Si shown in **Figure 10.2**d as the upper group of curves. These curves are nearly on top of each other and remarkably display an efficiency approaching 90% with practically no dependence on the system parameters. The assumption of 85% efficiency of ET from the acceptor NQDs into Si results in the total ET efficiency close to 85% and also showing very little dependence on the values of system parameters.

Figure 10.2c and **Figure 10.2**d illustrate that the weakly varying total efficiency can be seen as a result of the complementary characters of the direct and sequential processes. This can also be understood from another viewpoint: by recalling that the only losses for ET in our model correspond to NQD excitons decaying via photon emission, the process responsible in particular for the PL used in experimental measurements. The photon emission process is suppressed in the vicinity of the interface and is only weakly distance-dependent at the distances studied. In fact, approximately half of such photons[109] would be emitted in the direction of Si and additionally absorbed in thick enough substrates. We however follow our definition of ET in references[108, 206] and do not include such photons in the calculation of radiative ET efficiency. The efficiency of

ET into Si is thus evaluated as only due to near fields (NRET and RET into evanescent/waveguiding modes) that would be applicable even for ultrathin substrates[206].

10.4 Conclusion

In this work, we have extended our grafting and linker-assisted strategies to fabricate dense NQD bilayers on Si and SiO_2 substrates. We performed a detailed comparative study of the NQD PL decays in monolayer and bilayer configurations. Our experimental results and their good agreement with theoretical expectations from a basic electrodynamics model indicate that the resulting NQD structures do not possess any appreciable number of exciton/energy scavenging defects. We also showed that bandgap-gradient NQD structures can assist in efficient directional "funneling" of NQD excitons into the underlying Si substrate. This demonstration of very efficient (nearly 90%) ET into Si from the outer NQD layer in the bilayer configuration complements our earlier findings of highly efficient ET from the proximal NQDs to validate the concept of excitonic sensitization of ultrathin Si layers from the adjacent NQD assemblies. The efficacy of the fabrication approach we used is expected to be maintainable in building multi-layer optically thick NQD solids with little or no energy scavenging losses. It is conceivable that high efficiencies of overall ET from such multi-layer structures into Si substrates are possible to achieve by further enhancing the interlayer NRET through appropriate linking and optimization of the bandgap-gradient NQD structures. ET processes and efficiencies could likely be improved by utilizing NQDs of various compositions and sizes. The reported results thus further support

our proposition that NQD/Si nanostructures are attractive materials systems for practical realization of energy-transfer-based thin-film photovoltaic devices.

GENERAL CONCLUSION AND PERSPECTIVE

In this thesis we have shown the advantages and the potential of using a GOM in two different applications. As demonstrated, grafted organic monolayers offer good perspectives in terms of stability and electronic properties. Along their physical properties, GOM also have the advantage of being a relatively easy, cheap and versatile process. We have mainly used GOM on oxide free silicon and on thermally grown silicon oxide which can be used in technologies that are CMOS compatible. The first part of this thesis gives an overview and a theoretical background on the topics tackled in this work. We provide an overview on oxide free silicon and silicon oxide in **CHAPTER 1**. Succinct theoretical background and state of the art on single electron transport is summed up in **CHAPTER 2**. In this chapter we also provide theoretical tools to understand challenges that are inherent in the architecture we propose. In **CHAPTER 3** we explain the different phenomena involved in NQD solar cells. We also give an overview of achievement already done in this topic. **CHAPTER 4** reports a list of the characterization techniques used in this work as well as the kind of information each technique can provide. Significant achievements were obtained in both projects I have worked on.

In the framework of single electron transport, we have used a GOM on oxide free silicon for three main reasons:

- It is an insulator with a controllable thickness
- It is a protective layer in that ensure the quality and the stability of the silicon surface
- It can be used as an anchor for colloidal AuNP grafting.

We have proposed an experimental protocol and we have successfully observed single electron transport using this structure and a STM in UHV as detailed in **CHAPTER 5**. We have also

provided a study in order to identify parameters that are critical to the reproducibility of the observation of single electron transport using our architecture in **CHAPTER 6**. The level of contamination and oxidation were reported to be important parameters as well as AuNP size and crystallinity. From this study we could deduce an optimal recipe from which we could extract exploitable data. These positive results were then analyzed and compared with a theoretical model based on the "orthodox" theory in **CHAPTER 7**. We adapted a software that was originally designed for structure with only metals as contacts. Since we use silicon as one of the contact, we had to take into account additional phenomena such as band bending. We also provided new design that can be exploited for fabrication of future prototypes of SET. In light of all these achievements, our theoretical model must be improved in order to take into account effect that we have not considered yet such as tunneling through the depletion layer at low bias. One of the goals is to expand our model to be able to simulate a whole SET structure. STM is a very useful characterization tool and allow us to obtain a significant amount of interesting data. However, our aim must be to design prototypes that do not rely on the use of STM as one of the contact. This necessary step toward implementation of this technology to concrete application could also largely simplify the model and increase reproducibility of fabricated prototypes. Indeed, we could remove a significant amount of uncertainties that is inherent in an STM (shape of the tip, drift, contamination, temperature gradient …).

The second part of our work also took advantage of the use of the GOM, but in the framework of quantum dots solar cells. Once again the GOM was used as a passivating layer to protect the underlying silicon surface. It was also an anchor for NQDs grafting which allow the

precise geographical situation of NQDs with respect to the surface. Recent work made in our lab already proved that energy absorbed by grafted NQDs could be transferred to a silicon substrate through different mechanism using our GOM. In this work we have shown that we could not only use a GOM on a planar surface, but also on a patterned silicon surface such as silicon nanopillars. We proposed a protocol process to build the patterned surface and our experimental results in **CHAPTER 8**. The photoluminescence counts were greatly improved on the patterned surface because there were more NQDs grafted on the surface and because of light trapping effect. We have also been able to identify the different transfer mechanisms involved in this process. Another way to graft more NQDs on the surface is to fabricate multilayer of quantum dots on a planar surface. We proposed in **CHAPTER 9** an experimental protocol to build such structure. We have shown with the help of XPS and photoluminescence results that our resulting surface had a significant increase in photoluminescence count. This improvement can be optimized when grafting multilayer of NQDs with a gradient of size so that energy could be transferred between NQDs all the way to silicon. We have shown, in **CHAPTER 10,** experimental evidences for such directed transfer between different NQDs and from NQDs to silicon. We also provided a comprehensive analysis of the energy transfer mechanisms involved when the substrate is oxide free silicon and silicon oxide. Results were found to be in accordance with theoretical expectation. These results are important steps for NQDs solar cells fabrication. In order to push forward this project we need to improve our multilayer technique in order to make it more reproducible and more reliable. The density of the layers must also be improved and positive results have already been obtained by Rupich *et al.* in 2014. An improved multilayer fabrication technique could then be used to build thick multilayers of NQDs with a size gradient

that could greatly optimize the photoluminescence count, and increase the range of the absorbed light to the NIR. In our lab we have also recently shown evidence for optimized RET from NQDs to a 70nm thin silicon membrane using waveguiding[206]. This shows that all the improvement discussed in this project can be applied on a thin silicon membrane to avoid the use to an expensive thick monocrystalline silicon bulk. Thick multilayer of NQDs must be combined with silicon membrane patterning (using an SOI wafer) to design of a promising solar cell prototype based on our achievement.

ABBREVIATIONS

A: Acceptor

ADDS: Ammonium dodecylsulfate

AFM: Atomic Force Microscopy

ALD: atomic layer deposition

APTES: 3-Aminopropyltriethoxysilane

AuNP: Gold nanoparticle

AUTES: 11-aminoundecyltriethoxysilane

BL: Bilayer

BTJ: Barrier Tunneling Junction

C11-Ald: Triethoxysilyl undecanal

C2: Ethylenediamine

C6: 1,6-hexanediamine

CMOS: Complementary metal-oxide-semiconductor

CV: Coefficient of variation

D: Donor

DA: Diamine

DBTJ: Double Barrier Tunneling Junction

DMSO: Dimethyl Sulfoxide

DT: Dithiol

EDC: N-ethyl-N'-(3-(dimethylamino)propyl)-carbodiimide

EtOH: Ethanol

FRET: Forster resonant energy transfer

FTIR: Fourier Transform Spectroscopy

GOM: Grafted Organic Monolayer

HOMO: Highest occupied molecular orbital

IEF: Institut de l'électronique fondamentale

INSP: Institut des NanoSciences de Paris

KPFM: Kelvin Probe Force Microscopy

LDOS: Local density of states

LUMO: Lowest unoccupied molecular orbital

MEK: Methyl Ethyl ketone

MES: 2-morpholinoethanesulfonic acid

ML: Monolayer

MOSFET: metal oxide semiconductor field effect transistor

MUTS: 11-mercaptoundecyltrimethoxysilane

NIR: Near Infra-Red

NP: nanoparticle

NQD: NanoQuantum Dot

NRET: Non-Radiative Energy Transfer

OPV: Organic Photovoltaic cells

PV: Photovoltaic

QY: Quantum Yield

RET: Radiative energy transfer

RIE: Reactive Ion Etching

SAM: Self Assembled Monolayer

SC: Semiconductor

SEM: Scanning Electron Microscopy

SET: Single Electron Transistor

SiC_{11}: Ethyl undecylenate

SiC_7: Ethyl 6-heptenoate

SOI: Silicon on insulator

STM: Scanning electron microscopy

STS: Scanning Tunneling Spectroscopy

TEM: Transmission electron microscopy

UHV: Ultra High Vacuum

UPMC: Université Pierre et Marie Curie

UTD: University of Texas at Dallas

XPS: X-ray Photoelectron Spectroscopy

REFERENCES

1. Helms, C. R. & Poindexter, E. H. The silicon-silicon dioxide system: Its microstructure and imperfections. *Rep. Prog. Phys.* **57,** 791 (1994).
2. Pasternack, R. M., Rivillon Amy, S. & Chabal, Y. J. Attachment of 3-(Aminopropyl)triethoxysilane on Silicon Oxide Surfaces: Dependence on Solution Temperature. *Langmuir* **24,** 12963–12971 (2008).
3. Hanson, E. L., Schwartz, J., Nickel, B., Koch, N. & Danisman, M. F. Bonding Self-Assembled, Compact Organophosphonate Monolayers to the Native Oxide Surface of Silicon. *J. Am. Chem. Soc.* **125,** 16074–16080 (2003).
4. Chabal, Y. J., Higashi, G. S., Raghavachari, K. & Burrows, V. A. Infrared spectroscopy of Si(111) and Si(100) surfaces after HF treatment: Hydrogen termination and surface morphology. *J. Vac. Sci. Technol. A* **7,** 2104–2109 (1989).
5. Higashi, G. S., Chabal, Y. J., Trucks, G. W. & Raghavachari, K. Ideal hydrogen termination of the Si (111) surface. *Appl. Phys. Lett.* **56,** 656–658 (1990).
6. Linford, M. R., Fenter, P., Eisenberger, P. M. & Chidsey, C. E. D. Alkyl Monolayers on Silicon Prepared from 1-Alkenes and Hydrogen-Terminated Silicon. *J. Am. Chem. Soc.* **117,** 3145–3155 (1995).

7. Aureau, D., Varin, Y., Roodenko, K., Seitz, O., Pluchery, O. & Chabal, Y. J. Controlled Deposition of Gold Nanoparticles on Well-Defined Organic Monolayer Grafted on Silicon Surfaces. *J. Phys. Chem. C* **114,** 14180–14186 (2010).

8. Li, Y., Calder, S., Yaffe, O., Cahen, D., Haick, H., Kronik, L. & Zuilhof, H. Hybrids of Organic Molecules and Flat, Oxide-Free Silicon: High-Density Monolayers, Electronic Properties, and Functionalization. *Langmuir* **28,** 9920–9929 (2012).

9. Miramond, C. & Vuillaume, D. 1-octadecene monolayers on Si(111) hydrogen-terminated surfaces: Effect of substrate doping. *J. Appl. Phys.* **96,** 1529–1536 (2004).

10. Voicu, R., Boukherroub, R., Bartzoka, V., Ward, T., Wojtyk, J. T. C. & Wayner, D. D. M. Formation, Characterization, and Chemistry of Undecanoic Acid-Terminated Silicon Surfaces: Patterning and Immobilization of DNA. *Langmuir* **20,** 11713–11720 (2004).

11. Teyssot, A., Fidélis, A., Fellah, S., Ozanam, F. & Chazalviel, J.-N. Anodic grafting of organic groups on the silicon surface. *Electrochimica Acta* **47,** 2565–2571 (2002).

12. Fellah, S., Teyssot, A., Ozanam, F., Chazalviel, J.-N., Vigneron, J. & Etcheberry, A. Kinetics of Electrochemical Derivatization of the Silicon Surface by Grignards. *Langmuir* **18,** 5851–5860 (2002).

13. Puniredd, S. R., Assad, O., Stelzner, T., Christiansen, S. & Haick, H. Catalyst-Free Functionalization for Versatile Modification of Nonoxidized Silicon Structures. *Langmuir* **27,** 4764–4771 (2011).

14. Seitz, O., Böcking, T., Salomon, A., Gooding, J. J. & Cahen, D. Importance of Monolayer Quality for Interpreting Current Transport through Organic Molecules: Alkyls on Oxide-Free Si. *Langmuir* **22,** 6915–6922 (2006).

15. Thissen, P., Seitz, O. & Chabal, Y. J. Wet chemical surface functionalization of oxide-free silicon. *Prog. Surf. Sci.* **87,** 272–290 (2012).

16. Caillard, L., Seitz, O., Campbell, P. M., Doherty, R. P., Lamic-Humblot, A.-F., Lacaze, E., Chabal, Y. J. & Pluchery, O. Gold Nanoparticles on Oxide-Free Silicon–Molecule Interface for Single Electron Transport. *Langmuir* **29,** 5066–5073 (2013).

17. Seitz, O., Fernandes, P. G., Mahmud, G. A., Wen, H.-C., Stiegler, H. J., Chapman, R. A., Vogel, E. M. & Chabal, Y. J. One-Step Selective Chemistry for Silicon-on-Insulator Sensor Geometries. *Langmuir* **27,** 7337–7340 (2011).

18. Bearda, T., Beaudouin, S. P. & Mertens, P. W. *Handbook of Silicon Wafer Cleaning Technology*. (K. A. Reinhardt and W. Kern, 2007).

19. Crabtree, G. W. & Lewis, N. S. Solar energy conversion. *Phys. Today* **60,** p. 37–42 (2007).

20. Green, M. . Third Generation Photovoltaics: Assessment of progress over the last decade. in *2009 34th IEEE Photovolt. Spec. Conf. PVSC* 000146–000149 (2009). doi:10.1109/PVSC.2009.5411708

21. Nguyen, H. M., Seitz, O., Aureau, D., Sra, A., Nijem, N., Gartstein, Y. N., Chabal, Y. J. & Malko, A. V. Spectroscopic evidence for nonradiative energy transfer between colloidal CdSe/ZnS nanocrystals and functionalized silicon substrates. *Appl. Phys. Lett.* **98,** 161904 (2011).

22. Morita, M., Ohmi, T., Hasegawa, E., Kawakami, M. & Ohwada, M. Growth of native oxide on a silicon surface. *J. Appl. Phys.* **68,** 1272–1281 (1990).

23. Seitz, O., Fernandes, P. G., Tian, R., Karnik, N., Wen, H.-C., Stiegler, H., Chapman, R. A., Vogel, E. M. & Chabal, Y. J. Control and stability of self-assembled monolayers under biosensing conditions. *J. Mater. Chem.* **21,** 4384–4392 (2011).

24. Seitz, O., Dai, M., Aguirre-Tostado, F. S., Wallace, R. M. & Chabal, Y. J. Copper−Metal Deposition on Self Assembled Monolayer for Making Top Contacts in Molecular Electronic Devices. *J. Am. Chem. Soc.* **131,** 18159–18167 (2009).

25. Sagiv, J. Organized monolayers by adsorption. 1. Formation and structure of oleophobic mixed monolayers on solid surfaces. *J. Am. Chem. Soc.* **102,** 92–98 (1980).

26. Netzer, L. & Sagiv, J. A new approach to construction of artificial monolayer assemblies. *J. Am. Chem. Soc.* **105,** 674–676 (1983).

27. Onclin, S., Ravoo, B. J. & Reinhoudt, D. N. Engineering Silicon Oxide Surfaces Using Self-Assembled Monolayers. *Angew. Chem. Int. Ed.* **44,** 6282–6304 (2005).

28. Rozlosnik, N., Gerstenberg, M. C. & Larsen, N. B. Effect of Solvents and Concentration on the Formation of a Self-Assembled Monolayer of Octadecylsiloxane on Silicon (001). *Langmuir* **19,** 1182–1188 (2003).

29. Wang, Y. & Lieberman, M. Growth of Ultrasmooth Octadecyltrichlorosilane Self-Assembled Monolayers on SiO2. *Langmuir* **19,** 1159–1167 (2003).

30. Bluemel, J. Reactions of Ethoxysilanes with Silica: A Solid-State NMR Study. *J. Am. Chem. Soc.* **117,** 2112–2113 (1995).

31. Rye, R. R., Nelson, G. C. & Dugger, M. T. Mechanistic Aspects of Alkylchlorosilane Coupling Reactions. *Langmuir* **13,** 2965–2972 (1997).

32. Miller, J. B., Schwartz, J. & Bernasek, S. L. The importance of ligand kinetic basicity on the preparation of surface-supported zirconium complexes by proton transfer from hydroxylated aluminum or silicon. *J. Am. Chem. Soc.* **115,** 8239–8247 (1993).

33. Pong, B.-K., Trout, B. L. & Lee, J.-Y. Modified Ligand-Exchange for Efficient Solubilization of CdSe/ZnS Quantum Dots in Water: A Procedure Guided by Computational Studies. *Langmuir* **24,** 5270–5276 (2008).

34. Green, M. The nature of quantum dot capping ligands. *J. Mater. Chem.* **20,** 5797–5809 (2010).

35. Vega, A., Thissen, P. & Chabal, Y. J. Environment-Controlled Tethering by Aggregation and Growth of Phosphonic Acid Monolayers on Silicon Oxide. *Langmuir* **28,** 8046–8051 (2012).

36. DeBenedetti, W. J. I. & Chabal, Y. J. Functionalization of oxide-free silicon surfaces. *J. Vac. Sci. Technol. A* **31,** 050826 (2013).

37. Weinberger, B. R., Peterson, G. G., Eschrich, T. C. & Krasinski, H. A. Surface chemistry of HF passivated silicon: X-ray photoelectron and ion scattering spectroscopy results. *J. Appl. Phys.* **60,** 3232–3234 (1986).

38. Ubara, H., Imura, T. & Hiraki, A. Formation of Si-H bonds on the surface of microcrystalline silicon covered with SiOx by HF treatment. *Solid State Commun.* **50,** 673–675 (1984).

39. Michalak, D. J., Amy, S. R., Aureau, D., Dai, M., Estève, A. & Chabal, Y. J. Nanopatterning Si(111) surfaces as a selective surface-chemistry route. *Nat. Mater.* **9,** 266–271 (2010).

40. Hines, M. A., Chabal, Y. J., Harris, T. D. & Harris, A. L. Measuring the structure of etched silicon surfaces with Raman spectroscopy. *J. Chem. Phys.* **101,** 8055–8072 (1994).

41. Hines, M. A., Chabal, Y. J., Harris, T. D. & Harris, A. L. Raman studies of steric hindrance and surface relaxation of stepped H-terminated silicon surfaces. *Phys. Rev. Lett.* **71,** 2280–2283 (1993).

42. Dumas, P., Chabal, Y. J. & Higashi, G. S. Coupling of an adsorbate vibration to a substrate surface phonon: H on Si(111). *Phys. Rev. Lett.* **65,** 1124–1127 (1990).

43. Hines, M. A. IN SEARCH OF PERFECTION: Understanding the Highly Defect-Selective Chemistry of Anisotropic Etching. *Annu. Rev. Phys. Chem.* **54,** 29–56 (2003).

44. Zhang, X., Garfunkel, E., Chabal, Y. J., Christman, S. B. & Chaban, E. E. Stability of HF-etched Si(100) surfaces in oxygen ambient. *Appl. Phys. Lett.* **79,** 4051–4053 (2001).

45. Yablonovitch, E., Allara, D. L., Chang, C. C., Gmitter, T. & Bright, T. B. Unusually Low Surface-Recombination Velocity on Silicon and Germanium Surfaces. *Phys. Rev. Lett.* **57,** 249–252 (1986).

46. Linford, M. R. & Chidsey, C. E. D. Alkyl monolayers covalently bonded to silicon surfaces. *J. Am. Chem. Soc.* **115,** 12631–12632 (1993).

47. Zhang, Y., Zhao, L., Patra, P. K. & Ying, J. Y. Synthesis and Catalytic Applications of Mesoporous Polymer Colloids in Olefin Hydrosilylation. *Adv. Synth. Catal.* **350,** 662–666 (2008).

48. Salonen, J., Laine, E. & Niinistö, L. Thermal analysis of hydrosilylation of 1-dodecene on porous silicon surface. *Phys. Status Solidi A* **197,** 246–250 (2003).

49. Jin, H., Kinser, C. R., Bertin, P. A., Kramer, D. E., Libera, J. A., Hersam, M. C., Nguyen, S. T. & Bedzyk, M. J. X-ray Studies of Self-Assembled Organic Monolayers Grown on Hydrogen-Terminated Si(111). *Langmuir* **20,** 6252–6258 (2004).

50. Porter, M. D., Bright, T. B., Allara, D. L. & Chidsey, C. E. D. Spontaneously organized molecular assemblies. 4. Structural characterization of n-alkyl thiol monolayers on gold by optical ellipsometry, infrared spectroscopy, and electrochemistry. *J. Am. Chem. Soc.* **109,** 3559–3568 (1987).

51. Peng, W., Seitz, O., Chapman, R. A., Vogel, E. M. & Chabal, Y. J. Probing the intrinsic electrical properties of thin organic layers/semiconductor interfaces using an atomic-layer-deposited Al2O3 protective layer. *Appl. Phys. Lett.* **101,** 051605 (2012).

52. Bansal, A., Li, X., Lauermann, I., Lewis, N. S., Yi, S. I. & Weinberg, W. H. Alkylation of Si Surfaces Using a Two-Step Halogenation/Grignard Route. *J. Am. Chem. Soc.* **118,** 7225–7226 (1996).

53. Rivillon, S., Chabal, Y. J., Webb, L. J., Michalak, D. J., Lewis, N. S., Halls, M. D. & Raghavachari, K. Chlorination of hydrogen-terminated silicon (111) surfaces. *J. Vac. Sci. Technol. A* **23,** 1100–1106 (2005).

54. Rivillon Amy, S., Michalak, D. J., Chabal, Y. J., Wielunski, L., Hurley, P. T. & Lewis, N. S. Investigation of the Reactions during Alkylation of Chlorine-Terminated Silicon (111) Surfaces. *J. Phys. Chem. C* **111,** 13053–13061 (2007).

55. Michalak, D. J., Amy, S. R., Estève, A. & Chabal, Y. J. Investigation of the Chemical Purity of Silicon Surfaces Reacted with Liquid Methanol. *J. Phys. Chem. C* **112,** 11907–11919 (2008).

56. Likharev, K. K. Hybrid CMOS/Nanoelectronic Circuits: Opportunities and Challenges. *J. Nanoelectron. Optoelectron.* **3,** 203–230 (2008).

57. Inokawa, H., Fujiwara, A. & Takahashi, Y. A multiple-valued logic and memory with combined single-electron and metal-oxide-semiconductor transistors. *IEEE Trans. Electron Devices* **50,** 462–470 (2003).

58. Chan, K. C., Lee, P. F. & Dai, J. Y. Mesoscopic phenomena in Au nanocrystal floating gate memory structure. *Appl. Phys. Lett.* **95,** 113109 (2009).

59. Lientschnig, G., Weymann, I. & Hadley, P. Simulating Hybrid Circuits of Single-Electron Transistors and Field-Effect Transistors. *Jpn. J. Appl. Phys.* **42,** 6467 (2003).

60. Gwyn, C. W., Stulen, R., Sweeney, D. & Attwood, D. Extreme ultraviolet lithography. *J. Vac. Sci. Technol. B* **16,** 3142–3149 (1998).

61. Heuberger, A. X-ray lithography. *J. Vac. Sci. Technol. B* **6,** 107–121 (1988).

62. Carr, D. W. & Craighead, H. G. Fabrication of nanoelectromechanical systems in single crystal silicon using silicon on insulator substrates and electron beam lithography. *J. Vac. Sci. Technol. B* **15,** 2760–2763 (1997).

63. Brown, W. L., Venkatesan, T. & Wagner, A. Ion beam lithography. *Nucl. Instrum. Methods Phys. Res.* **191,** 157–168 (1981).

64. Chou, S. Y., Krauss, P. R. & Renstrom, P. J. Nanoimprint lithography. *J. Vac. Sci. Technol. B* **14,** 4129–4133 (1996).

65. Silver, R. M., Ehrichs, E. E. & Lozanne, A. L. de. Direct writing of submicron metallic features with a scanning tunneling microscope. *Appl. Phys. Lett.* **51,** 247–249 (1987).

66. Xie, F. & Blanckenhagen, P. von. Observation of harmonic current oscillations on partially oxidized Si(111) surfaces by scanning tunneling microscopy. *Appl. Phys. Lett.* **75,** 3144–3146 (1999).

67. See, J. Thesis: Theorie du blocage de Coulomb appliquee aux nanostructures semi-conductrices: modelisation des dispositifs a nanocristaux de silicium. (2003).

68. Mullen, K., Ben-Jacob, E., Jaklevic, R. C. & Schuss, Z. I-V characteristics of coupled ultrasmall-capacitance normal tunnel junctions. *Phys. Rev. B* **37,** 98–105 (1988).

69. Fulton, T. A. & Dolan, G. J. Observation of single-electron charging effects in small tunnel junctions. *Phys. Rev. Lett.* **59,** 109–112 (1987).

70. Likharev, K. K. Single-electron devices and their applications. *Proc. IEEE* **87,** 606–632 (1999).

71. Nakamura, Y., Chen, C. & Tsai, J.-S. 100-K operation of Al-based single-electron transistors. *Jpn. J. Appl. Phys.* **35,** (1996).

72. Klein, D. L., Roth, R., Lim, A. K. L., Alivisatos, A. P. & McEuen, P. L. A single-electron transistor made from a cadmium selenide nanocrystal. *Nature* **389,** 699–701 (1997).

73. Ralph, D. C., Black, C. T. & Tinkham, M. Gate-Voltage Studies of Discrete Electronic States in Aluminum Nanoparticles. *Phys. Rev. Lett.* **78,** 4087–4090 (1997).

74. Altmeyer, S., Hamidi, A., Spangenberg, B. & Kurz, H. 77 K single electron transistors fabricated with 0.1 μm technology. *J. Appl. Phys.* **81,** 8118–8120 (1997).

75. Matsumoto, K., Ishii, M., Segawa, K., Oka, Y., Vartanian, B. J. & Harris, J. S. Room temperature operation of a single electron transistor made by the scanning tunneling

microscope nanooxidation process for the TiOx/Ti system. *Appl. Phys. Lett.* **68,** 34–36 (1996).

76. Takahashi, Y., Namatsu, H., Kurihara, K., Iwadate, K., Nagase, M. & Murase, K. Size dependence of the characteristics of Si single-electron transistors on SIMOX substrates. *IEEE Trans. Electron Devices* **43,** 1213–1217 (1996).

77. Shirakashi, J., Matsumoto, K., Miura, N. & Konagai, M. Single-electron charging effects in Nb/Nb oxide-based single-electron transistors at room temperature. *Appl. Phys. Lett.* **72,** 1893–1895 (1998).

78. Jacobsen, V., Zhu, T., Knoll, W. & Kreiter, M. Current-Voltage Characterisation of Monolayer-Supported Au-Nanoclusters by Scanning Tunnelling Microscopy under Ambient Conditions. *Eur. J. Inorg. Chem.* **2005,** 3683–3690 (2005).

79. Negishi, R., Hasegawa, T., Tanaka, H., Terabe, K., Ozawa, H., Ogawa, T. & Aono, M. Size-dependent single electron tunneling effect in Au nanoparticles. *Surf. Sci.* **601,** 3907–3911 (2007).

80. Walavalkar, S., Latawiec, P. & Scherer, A. Coulomb blockade in vertical, bandgap engineered silicon nanopillars. *Appl. Phys. Lett.* **102,** 183101 (2013).

81. Tan, Y. T., Kamiya, T., Durrani, Z. a. K. & Ahmed, H. Room temperature nanocrystalline silicon single-electron transistors. *J. Appl. Phys.* **94,** 633–637 (2003).

82. Ray, V., Subramanian, R., Bhadrachalam, P., Ma, L.-C., Kim, C.-U. & Koh, S. J. CMOS-compatible fabrication of room-temperature single-electron devices. *Nat. Nanotechnol.* **3,** 603–608 (2008).

83. Yaffe, O., Scheres, L., Segev, L., Biller, A., Ron, I., Salomon, E., Giesbers, M., Kahn, A., Kronik, L., Zuilhof, H., Vilan, A. & Cahen, D. Hg/Molecular Monolayer−Si Junctions: Electrical Interplay between Monolayer Properties and Semiconductor Doping Density. *J. Phys. Chem. C* **114,** 10270–10279 (2010).

84. Lenfant, S., Guerin, D., Tran Van, F., Chevrot, C., Palacin, S., Bourgoin, J. P., Bouloussa, O., Rondelez, F. & Vuillaume, D. Electron Transport through Rectifying Self-Assembled Monolayer Diodes on Silicon: Fermi-Level Pinning at the Molecule−Metal Interface. *J. Phys. Chem. B* **110,** 13947–13958 (2006).

85. Feenstra, R. M. & Stroscio, J. A. Tunneling spectroscopy of the GaAs(110) surface. *J. Vac. Sci. Technol. B* **5,** 923–929 (1987).

86. Cuevas, J. C. & Scheer, E. *Molecular Electronics: An Introduction to Theory and Experiment*. (WORLD SCIENTIFIC, 2010).

87. Akkerman, H. B. & Boer, B. de. Electrical conduction through single molecules and self-assembled monolayers. *J. Phys. Condens. Matter* **20,** 013001 (2008).

88. Von Hippel, A. R. *Molecular Science and Molecular Engineering*. (Technology Press of MIT, Cambridge, USA and Wiley, New York, USA, 1959).

89. Wang, W., Lee, T. & Reed, M. A. Mechanism of electron conduction in self-assembled alkanethiol monolayer devices. *Phys. Rev. B* **68,** 035416 (2003).

90. Chen, F., Li, X., Hihath, J., Huang, Z. & Tao, N. Effect of anchoring groups on single-molecule conductance: comparative study of thiol-, amine-, and carboxylic-acid-terminated molecules. *J. Am. Chem. Soc.* **128,** 15874–15881 (2006).

91. Polymeropoulos, E. E., Möbius, D. & Kuhn, H. Monolayer assemblies with functional units of sensitizing and conducting molecular components: Photovoltage, dark conduction and photoconduction in systems with aluminium and barium electrodes. *Thin Solid Films* **68,** 173–190 (1980).

92. Venkataraman, L., Klare, J. E., Tam, I. W., Nuckolls, C., Hybertsen, M. S. & Steigerwald, M. L. Single-Molecule Circuits with Well-Defined Molecular Conductance. *Nano Lett.* **6,** 458–462 (2006).

93. Akkerman, H. B., Naber, R. C. G., Jongbloed, B., van Hal, P. A., Blom, P. W. M., de Leeuw, D. M. & de Boer, B. Electron tunneling through alkanedithiol self-assembled monolayers in large-area molecular junctions. *Proc. Natl. Acad. Sci. U. S. A.* **104,** 11161–11166 (2007).

94. Tomfohr, J. K. & Sankey, O. F. Complex band structure, decay lengths, and Fermi level alignment in simple molecular electronic systems. *Phys. Rev. B* **65,** 245105 (2002).

95. McEvoy, A., Castaner, L. & Markvart, T. *Solar Cells: Materials, Manufacture and Operation*. (Newnes, 2012).

96. Baskoutas, S. & Terzis, A. F. Size-dependent band gap of colloidal quantum dots. *J. Appl. Phys.* **99,** 013708 (2006).

97. Ip, A. H., Thon, S. M., Hoogland, S., Voznyy, O., Zhitomirsky, D., Debnath, R., Levina, L., Rollny, L. R., Carey, G. H., Fischer, A., Kemp, K. W., Kramer, I. J., Ning, Z., Labelle, A. J., Chou, K. W., Amassian, A. & Sargent, E. H. Hybrid passivated colloidal quantum dot solids. *Nat. Nanotechnol.* **7,** 577–582 (2012).

98. Chuang, C.-H. M., Brown, P. R., Bulović, V. & Bawendi, M. G. Improved performance and stability in quantum dot solar cells through band alignment engineering. *Nat. Mater.* **13,** 796–801 (2014).

99. Stavola, M., Dexter, D. L. & Knox, R. S. Electron-hole pair excitation in semiconductors via energy transfer from an external sensitizer. *Phys. Rev. B* **31,** 2277–2289 (1985).

100. Dexter, D. L. Two ideas on energy transfer phenomena: Ion-pair effects involving the OH stretching mode, and sensitization of photovoltaic cells. *J. Lumin.* **18–19, Part 2,** 779–784 (1979).

101. Stryer, L. Fluorescence Spectroscopy of Proteins. *Science* **162,** 526–& (1968).

102. Stryer, L. & Haugland, R. P. Energy transfer: a spectroscopic ruler. *Proc. Natl. Acad. Sci.* **58,** 719–726 (1967).

103. Agranovich, V. M., Gartstein, Y. N. & Litinskaya, M. Hybrid Resonant Organic–Inorganic Nanostructures for Optoelectronic Applications. *Chem. Rev.* **111,** 5179–5214 (2011).

104. Achermann, M., Petruska, M. A., Crooker, S. A. & Klimov, V. I. Picosecond Energy Transfer in Quantum Dot Langmuir−Blodgett Nanoassemblies. *J. Phys. Chem. B* **107,** 13782–13787 (2003).

105. Crooker, S. A., Hollingsworth, J. A., Tretiak, S. & Klimov, V. I. Spectrally Resolved Dynamics of Energy Transfer in Quantum-Dot Assemblies: Towards Engineered Energy Flows in Artificial Materials. *Phys. Rev. Lett.* **89,** 186802 (2002).

106. Holme, T. P., Chao, C. C. & Prinz, F. B. Energy transfer between quantum dots of different sizes for quantum dot solar cells. in *2009 34th IEEE Photovolt. Spec. Conf. PVSC* 85–89 (2009).

107. Aspnes, D. E. & Studna, A. A. Dielectric functions and optical parameters of Si, Ge, GaP, GaAs, GaSb, InP, InAs, and InSb from 1.5 to 6.0 eV. *Phys. Rev. B* **27,** 985–1009 (1983).

108. Nimmo, M. T., Caillard, L. M., De Benedetti, W., Nguyen, H. M., Seitz, O., Gartstein, Y. N., Chabal, Y. J. & Malko, A. V. Visible to Near-Infrared Sensitization of Silicon Substrates via Energy Transfer from Proximal Nanocrystals: Further Insights for Hybrid Photovoltaics. *ACS Nano* **7,** 3236–3245 (2013).

109. Nguyen, H. M., Seitz, O., Gartstein, Y. N., Chabal, Y. J. & Malko, A. V. Energy transfer from colloidal nanocrystals into Si substrates studied via photoluminescence photon counts and decay kinetics. *J. Opt. Soc. Am. B* **30,** 2401–2408 (2013).

110. Herres, W. & Gronholz, J. *Understanding FT-IR data processing. Part 1: data acquisition and Fourier transformation.* (Instruments and Computers (Reprint), 1984).

111. Ibe, J. P., Jr, P. P. B., Brandow, S. L., Brizzolara, R. A., Burnham, N. A., DiLella, D. P., Lee, K. P., Marrian, C. R. K. & Colton, R. J. On the electrochemical etching of tips for scanning tunneling microscopy. *J. Vac. Sci. Technol. A* **8,** 3570–3575 (1990).

112. Hu, X., Sarid, D. & Blanckenhagen, P. von. Nano-patterning and single electron tunnelling using STM. *Nanotechnology* **10,** 209 (1999).

113. Park, K.-H., Ha, J. S., Yun, W. S., Shin, M. & Ko, Y.-J. Coulomb staircases by lateral tunneling between adjacent nanoclusters formed on Si surfaces. *J. Vac. Sci. Technol. B* **18,** 2365–2370 (2000).

114. Wang, B., Wang, K., Lu, W., Wang, H., Li, Z., Yang, J. & Hou, J. G. Effects of discrete energy levels on single-electron tunneling in coupled metal particles. *Appl. Phys. Lett.* **82,** 3767–3769 (2003).

115. Radojkovic, P., Schwartzkopff, M., Enachescu, M., Stefanov, E., Hartmann, E. & Koch, F. Observation of Coulomb staircase and negative differential resistance at room temperature by scanning tunneling microscopy. *J. Vac. Sci. Technol. B* **14,** 1229–1233 (1996).

116. Kelzenberg, M. D., Boettcher, S. W., Petykiewicz, J. A., Turner-Evans, D. B., Putnam, M. C., Warren, E. L., Spurgeon, J. M., Briggs, R. M., Lewis, N. S. & Atwater, H. A. Enhanced absorption and carrier collection in Si wire arrays for photovoltaic applications. *Nat. Mater.* **9,** 239–244 (2010).

117. Garnett, E. & Yang, P. Light Trapping in Silicon Nanowire Solar Cells. *Nano Lett.* **10,** 1082–1087 (2010).

118. Fan, Z., Kapadia, R., Leu, P. W., Zhang, X., Chueh, Y.-L., Takei, K., Yu, K., Jamshidi, A., Rathore, A. A., Ruebusch, D. J., Wu, M. & Javey, A. Ordered Arrays of Dual-Diameter Nanopillars for Maximized Optical Absorption. *Nano Lett.* **10,** 3823–3827 (2010).

119. Hayes, G. r. & Deveaud, B. Is Luminescence from Quantum Wells Due to Excitons? *Phys. Status Solidi A* **190,** 637–640 (2002).

120. Vuillaume, D. & Lenfant, S. The metal/organic monolayer interface in molecular electronic devices. *Microelectron. Eng.* **70,** 539–550 (2003).

121. Dubey, G., Rosei, F. & Lopinski, G. P. Modulation of flat-band voltage on H-terminated silicon-on-insulator pseudo–metal–oxide–semiconductor field effect transistors by adsorption and reaction events. *J. Appl. Phys.* **109,** 104904 (2011).

122. Clément, N., Pleutin, S., Guérin, D. & Vuillaume, D. Relaxation dynamics in covalently bonded organic monolayers on silicon. *Phys. Rev. B* **82,** 035404 (2010).

123. Aureau, D., Rappich, J., Moraillon, A., Allongue, P., Ozanam, F. & Chazalviel, J.-N. In situ monitoring of the electronic properties and the pH stability of grafted Si(1 1 1). *J. Electroanal. Chem.* **646,** 33–42 (2010).

124. Tao, F., Bernasek, S. L. & Xu, G.-Q. Electronic and Structural Factors in Modification and Functionalization of Clean and Passivated Semiconductor Surfaces with Aromatic Systems. *Chem. Rev.* **109,** 3991–4024 (2009).

125. Hacker, C. A. Modifying electronic properties at the silicon–molecule interface using atomic tethers. *Solid-State Electron.* **54,** 1657–1664 (2010).

126. Faucheux, A., Gouget-Laemmel, A. C., Henry de Villeneuve, C., Boukherroub, R., Ozanam, F., Allongue, P. & Chazalviel, J.-N. Well-Defined Carboxyl-Terminated Alkyl Monolayers Grafted onto H−Si(111): Packing Density from a Combined AFM and Quantitative IR Study. *Langmuir* **22,** 153–162 (2006).

127. Webb, L. J., Rivillon, S., Michalak, D. J., Chabal, Y. J. & Lewis, N. S. Transmission Infrared Spectroscopy of Methyl- and Ethyl-Terminated Silicon(111) Surfaces. *J. Phys. Chem. B* **110,** 7349–7356 (2006).

128. Vilan, A., Yaffe, O., Biller, A., Salomon, A., Kahn, A. & Cahen, D. Molecules on si: electronics with chemistry. *Adv. Mater. Deerfield Beach Fla* **22,** 140–159 (2010).

129. Salomon, A., Boecking, T., Chan, C. K., Amy, F., Girshevitz, O., Cahen, D. & Kahn, A. How Do Electronic Carriers Cross Si-Bound Alkyl Monolayers? *Phys. Rev. Lett.* **95,** 266807 (2005).

130. Thieblemont, F., Seitz, O., Vilan, A., Cohen, H., Salomon, E., Kahn, A. & Cahen, D. Electronic Current Transport through Molecular Monolayers: Comparison between Hg/Alkoxy and Alkyl Monolayer/Si(100) Junctions. *Adv. Mater.* **20,** 3931–3936 (2008).

131. Ogawa, H., Ishikawa, K., Inomata, C. & Fujimura, S. Initial stage of native oxide growth on hydrogen terminated silicon (111) surfaces. *J. Appl. Phys.* **79,** 472–477 (1996).

132. Allongue, P. Molecular Imaging and Local Density of States Characterization at the Si(111)/NaOH Interface. *Phys. Rev. Lett.* **77,** 1986–1989 (1996).

133. Seitz, O., Caillard, L., Nguyen, H. M., Chiles, C., Chabal, Y. J. & Malko, A. V. Optimizing non-radiative energy transfer in hybrid colloidal-nanocrystal/silicon structures by controlled nanopillar architectures for future photovoltaic cells. *Appl. Phys. Lett.* **100,** 021902 (2012).

134. Turkevich, J., Stevenson, P. C. & Hillier, J. A study of the nucleation and growth processes in the synthesis of colloidal gold. *Discuss. Faraday Soc.* **11,** 55–75 (1951).

135. Frens, G. Controlled Nucleation for the Regulation of the Particle Size in Monodisperse Gold Suspensions. *Nature* **241,** 20–22 (1973).

136. Diegoli, S., Mendes, P. M., Baguley, E. R., Leigh, S. J., Iqbal, P., Garcia Diaz, Y. R., Begum, S., Critchley, K., Hammond, G. D., Evans, S. D., Attwood, D., Jones, I. P. &

Preece, J. A. pH-Dependent gold nanoparticle self-organization on functionalized Si/SiO2 surfaces. *J. Exp. Nanosci.* **1,** 333–353 (2006).

137. Kimling, J., Maier, M., Okenve, B., Kotaidis, V., Ballot, H. & Plech, A. Turkevich Method for Gold Nanoparticle Synthesis Revisited. *J. Phys. Chem. B* **110,** 15700–15707 (2006).

138. Roucoux, A., Schulz, J. & Patin, H. Reduced Transition Metal Colloids: A Novel Family of Reusable Catalysts? *Chem. Rev.* **102,** 3757–3778 (2002).

139. Ji, X., Song, X., Li, J., Bai, Y., Yang, W. & Peng, X. Size Control of Gold Nanocrystals in Citrate Reduction: The Third Role of Citrate. *J. Am. Chem. Soc.* **129,** 13939–13948 (2007).

140. Stathis, E. & Fabrikanos, A. Preparation of Colloidal Gold. *Chem. Ind.* 860–861 (1958).

141. Horcas, I., Fernández, R., Gómez-Rodríguez, J. M., Colchero, J., Gómez-Herrero, J. & Baro, A. M. WSXM: A software for scanning probe microscopy and a tool for nanotechnology. *Rev. Sci. Instrum.* **78,** 013705 (2007).

142. De Smet, L. C. P. M., Pukin, A. V., Sun, Q.-Y., Eves, B. J., Lopinski, G. P., Visser, G. M., Zuilhof, H. & Sudhölter, E. J. R. Visible-light attachment of SiC linked functionalized organic monolayers on silicon surfaces. *Appl. Surf. Sci.* **252,** 24–30 (2005).

143. Zabet-Khosousi, A. & Dhirani, A.-A. Charge Transport in Nanoparticle Assemblies. *Chem. Rev.* **108,** 4072–4124 (2008).

144. Lu, W., Wang, B., Wang, K., Wang, X. & Hou, J. G. Synthesis and Characterization of Crystalline and Amorphous Palladium Nanoparticles. *Langmuir* **19,** 5887–5891 (2003).

145. Sze, S. M. & Ng, K. K. *Physics of Semiconductor Devices*. (John Wiley & Sons, 2006).

146. Brennan, K. F. *The Physics of Semiconductors: With Applications to Optoelectronic Devices*. (Cambridge University Press, 1999).

147. Hunger, R., Fritsche, R., Jaeckel, B., Jaegermann, W., Webb, L. J. & Lewis, N. S. Chemical and electronic characterization of methyl-terminated Si(111) surfaces by high-resolution synchrotron photoelectron spectroscopy. *Phys. Rev. B* **72,** 045317 (2005).

148. Vuillaume, D. Molecular Nanoelectronics. *Proc. IEEE* **98,** 2111–2123 (2010).

149. Asahi, N., Akazawa, M. & Amemiya, Y. Single-electron logic device based on the binary decision diagram. *IEEE Trans. Electron Devices* **44,** 1109–1116 (1997).

150. Davidović, D. & Tinkham, M. Coulomb blockade and discrete energy levels in Au nanoparticles. *Appl. Phys. Lett.* **73,** 3959–3961 (1998).

151. Yang, Y. & Nogami, M. Room temperature single electron transistor with two-dimensional array of Au–SiO2 core–shell nanoparticles. *Sci. Technol. Adv. Mater.* **6,** 71–75 (2005).

152. Khondaker, S. I., Luo, K. & Yao, Z. The fabrication of single-electron transistors using dielectrophoretic trapping of individual gold nanoparticles. *Nanotechnology* **21,** 095204 (2010).

153. Tsai, L.-C., Cheng, I.-C., Tu, M.-C., Chen, C.-D. & Lin, H.-Y. Formation of single-electron-transistors using self-assembly of nanoparticle chains. *J. Nanoparticle Res.* **12,** 2859–2864 (2010).

154. Novembre, C., Guérin, D., Lmimouni, K., Gamrat, C. & Vuillaume, D. Gold nanoparticle-pentacene memory transistors. *Appl. Phys. Lett.* **92,** 103314 (2008).

155. Tedesco, J. L., Rowe, J. E. & Nemanich, R. J. Titanium silicide islands on atomically clean Si(100): Identifying single electron tunneling effects. *J. Appl. Phys.* **107,** 123715 (2010).

156. Homberger, M. & Simon, U. On the application potential of gold nanoparticles in nanoelectronics and biomedicine. *Philos. Trans. R. Soc. Math. Phys. Eng. Sci.* **368,** 1405–1453 (2010).

157. De Benedetti, W. J. I., Nimmo, M. T., Rupich, S. M., Caillard, L. M., Gartstein, Y. N., Chabal, Y. J. & Malko, A. V. Efficient Directed Energy Transfer through Size-Gradient Nanocrystal Layers into Silicon Substrates. *Adv. Funct. Mater.* **24,** 5002–5010 (2014).

158. Rahmouni, M., Datta, A., Chatterjee, P., Damon-Lacoste, J., Ballif, C. & Cabarrocas, P. R. i. Carrier transport and sensitivity issues in heterojunction with intrinsic thin layer solar cells on N-type crystalline silicon: A computer simulation study. *J. Appl. Phys.* **107,** 054521 (2010).

159. Grabar, K. C., Allison, K. J., Baker, B. E., Bright, R. M., Brown, K. R., Freeman, R. G., Fox, A. P., Keating, C. D., Musick, M. D. & Natan, M. J. Two-Dimensional Arrays of Colloidal Gold Particles: A Flexible Approach to Macroscopic Metal Surfaces. *Langmuir* **12,** 2353–2361 (1996).

160. Qu, X., Peng, Z., Jiang, X. & Dong, S. Surface Charge Influence on the Surface Plasmon Absorbance of Electroactive Thiol-Protected Gold Nanoparticles. *Langmuir* **20,** 2519–2522 (2004).

161. Viudez, A. J., Madueño, R., Pineda, T. & Blázquez, M. Stabilization of Gold Nanoparticles by 6-Mercaptopurine Monolayers. Effects of the Solvent Properties. *J. Phys. Chem. B* **110,** 17840–17847 (2006).

162. Basu, S., Ghosh, S. K., Kundu, S., Panigrahi, S., Praharaj, S., Pande, S., Jana, S. & Pal, T. Biomolecule induced nanoparticle aggregation: Effect of particle size on interparticle coupling. *J. Colloid Interface Sci.* **313,** 724–734 (2007).

163. Buffat, P. & Borel, J.-P. Size effect on the melting temperature of gold particles. *Phys. Rev. A* **13,** 2287–2298 (1976).

164. Young, N. P., van Huis, M. A., Zandbergen, H. W., Xu, H. & Kirkland, A. I. Transformations of gold nanoparticles investigated using variable temperature high-resolution transmission electron microscopy. *Ultramicroscopy* **110,** 506–516 (2010).

165. Jaeckel, B., Hunger, R., Webb, L. J., Jaegermann, W. & Lewis, N. S. High-Resolution Synchrotron Photoemission Studies of the Electronic Structure and Thermal Stability of CH3- and C2H5-Functionalized Si(111) Surfaces. *J. Phys. Chem. C* **111,** 18204–18213 (2007).

166. Cahill, D. G. & Avouris, P. Si ejection and regrowth during the initial stages of Si(001) oxidation. *Appl. Phys. Lett.* **60,** 326–328 (1992).

167. Pluchery, O., Coustel, R., Witkowski, N. & Borensztein, Y. Adsorption of Phenylacetylene on Si(100)-2 × 1: Kinetics and Structure of the Adlayer. *J. Phys. Chem. B* **110,** 22635–22643 (2006).

168. Xu, L.-P. & Chen, S. Scanning tunneling spectroscopy of gold nanoparticles: Influences of volatile organic vapors and particle core dimensions. *Chem. Phys. Lett.* **468,** 222–226 (2009).

169. Wasshuber, C., Kosina, H. & Selberherr, S. SIMON-A simulator for single-electron tunnel devices and circuits. *IEEE Trans. Comput.-Aided Des. Integr. Circuits Syst.* **16,** 937–944 (1997).

170. Sée, J., Dollfus, P., Galdin, S. & Hesto, P. From wave-functions to current-voltage characteristics: overview of a Coulomb blockade device simulator using fundamental physical parameters. *J. Comput. Electron.* **5,** 35–48 (2006).

171. See, J., Dollfus, P. & Galdin, S. Theoretical investigation of negative differential conductance regime of silicon nanocrystal single-electron devices. *IEEE Trans. Electron Devices* **53,** 1268–1273 (2006).

172. Green, M. A. Intrinsic concentration, effective densities of states, and effective mass in silicon. *J. Appl. Phys.* **67,** 2944–2954 (1990).

173. Nordling, C. & Osterman, J. *Physics Handbook for Science and Engineering*. (Studentlitteratur Ab, 2006).

174. Magid, I., Burstein, L., Seitz, O., Segev, L., Kronik, L. & Rosenwaks, Y. Electronic Characterization of Si(100)-Bound Alkyl Monolayers Using Kelvin Probe Force Microscopy. *J. Phys. Chem. C* **112,** 7145–7150 (2008).

175. Maxwell, J. C. *A treatise on electricity and magnetism*. (Oxford : Clarendon Press, 1873). at <http://archive.org/details/electricandmagne01maxwrich>

176. Durand, E. *lec trostatique. 2, Probl m es g n raux, conducteurs*. (Masson et Cie, 1966).

177. Schouteden, K., Vandamme, N., Janssens, E., Lievens, P. & Van Haesendonck, C. Single-electron tunneling phenomena on preformed gold clusters deposited on dithiol self-assembled monolayers. *Surf. Sci.* **602,** 552–558 (2008).

178. Southwick, R. G. & Knowlton, W. B. Stacked dual-oxide MOS energy band diagram visual representation program (IRW student paper). *IEEE Trans. Device Mater. Reliab.* **6,** 136–145 (2006).

179. Maldonado, S., Plass, K. E., Knapp, D. & Lewis, N. S. Electrical Properties of Junctions between Hg and Si(111) Surfaces Functionalized with Short-Chain Alkyls†. *J. Phys. Chem. C* **111,** 17690–17699 (2007).

180. Gleason-Rohrer, D. C., Brunschwig, B. S. & Lewis, N. S. Measurement of the Band Bending and Surface Dipole at Chemically Functionalized Si(111)/Vacuum Interfaces. *J. Phys. Chem. C* **117,** 18031–18042 (2013).

181. Feenstra, R. M. Electrostatic potential for a hyperbolic probe tip near a semiconductor. *J. Vac. Sci. Technol. B* **21,** 2080–2088 (2003).

182. Feenstra, R. M. SEMITIP, program for calculating the tip induced band bending. (2001). at <http://www.andrew.cmu.edu/user/feenstra/semitip_v6/>

183. Xie, F., Sun, M. & von Blanckenhagen, P. Comparative study of harmonic oscillations of tunneling current on partially oxidized Si(100) and Si(111) surfaces by scanning tunneling microscopy and spectroscopy. *Surf. Sci.* **454–456,** 1031–1037 (2000).

184. Xie, F. & Blanckenhagen, P. von. Time-dependent oscillations of tunneling current on partially oxidized Si (111) surfaces. *Appl. Phys. A* **72,** S217–S221 (2001).

185. Dalidchik, F. I., Kubarev, S. I. & Ponomarev, O. A. Quantum beats of nanocontact tunnel conductivity. *Russ. J. Phys. Chem. B* **3,** 727–736 (2009).

186. Solecon-Laboratories. The Relationship Between Resistivity and Dopant Density for Phosphorus-and Boron-Doped Silicon. (2014). at <http://www.solecon.com/sra/rho2ccal.htm>

187. Thurber, W. R., Mattis, R. L., Liu, Y. M. & Filliben, J. J. The Relationship Between Resistivity and Dopant Density for Phosphorus-and Boron-Doped Silicon. *Natl. Bur. Stand. Spec. Publ.* 400–464 (1981).

188. Kayes, B. M., Atwater, H. A. & Lewis, N. S. Comparison of the device physics principles of planar and radial p-n junction nanorod solar cells. *J. Appl. Phys.* **97,** 114302 (2005).

189. Zhang, Y., Wang & Mascarenhas, A. 'Quantum Coaxial Cables' for Solar Energy Harvesting. *Nano Lett.* **7,** 1264–1269 (2007).

190. Garnett, E. C. & Yang, P. Silicon Nanowire Radial p−n Junction Solar Cells. *J. Am. Chem. Soc.* **130,** 9224–9225 (2008).

191. Moran, J. M. & Maydan, D. High resolution, steep profile resist patterns. *J. Vac. Sci. Technol.* **16,** 1620–1624 (1979).

192. Choi, W. K., Liew, T. H., Dawood, M. K., Smith, H. I., Thompson, C. V. & Hong, M. H. Synthesis of Silicon Nanowires and Nanofin Arrays Using Interference Lithography and Catalytic Etching. *Nano Lett.* **8,** 3799–3802 (2008).

193. Cheung, C. L., Nikolić, R. J., Reinhardt, C. E. & Wang, T. F. Fabrication of nanopillars by nanosphere lithography. *Nanotechnology* **17,** 1339 (2006).

194. Hulteen, J. C. & Duyne, R. P. V. Nanosphere lithography: A materials general fabrication process for periodic particle array surfaces. *J. Vac. Sci. Technol. A* **13,** 1553–1558 (1995).

195. Haynes, C. L. & Van Duyne, R. P. Nanosphere Lithography: A Versatile Nanofabrication Tool for Studies of Size-Dependent Nanoparticle Optics. *J. Phys. Chem. B* **105,** 5599–5611 (2001).

196. Huang, Z., Geyer, N., Werner, P., de Boor, J. & Gösele, U. Metal-Assisted Chemical Etching of Silicon: A Review. *Adv. Mater.* **23,** 285–308 (2011).

197. Cheng, S. L., Chen, C. Y. & Lee, S. W. Kinetic investigation of the electrochemical synthesis of vertically-aligned periodic arrays of silicon nanorods on (001)Si substrate. *Thin Solid Films* **518,** S190–S195 (2010).

198. Rybczynski, J., Ebels, U. & Giersig, M. Large-scale, 2D arrays of magnetic nanoparticles. *Colloids Surf. Physicochem. Eng. Asp.* **219,** 1–6 (2003).

199. Lee, C.-L., Tsujino, K., Kanda, Y., Ikeda, S. & Matsumura, M. Pore formation in silicon by wet etching using micrometre-sized metal particles as catalysts. *J. Mater. Chem.* **18,** 1015–1020 (2008).

200. Lu, S., Lingley, Z., Asano, T., Harris, D., Barwicz, T., Guha, S. & Madhukar, A. Photocurrent Induced by Nonradiative Energy Transfer from Nanocrystal Quantum Dots to Adjacent Silicon Nanowire Conducting Channels: Toward a New Solar Cell Paradigm. *Nano Lett.* **9,** 4548–4552 (2009).

201. Klimov, V. I., McBranch, D. W., Leatherdale, C. A. & Bawendi, M. G. Electron and hole relaxation pathways in semiconductor quantum dots. *Phys. Rev. B* **60,** 13740–13749 (1999).

202. Purcell, E. Spontaneous Emission Probabilities at Radio Frequencies. *Phys. Rev.* **69,** 681–681 (1946).

203. Englund, D., Fattal, D., Waks, E., Solomon, G., Zhang, B., Nakaoka, T., Arakawa, Y., Yamamoto, Y. & Vučković, J. Controlling the Spontaneous Emission Rate of Single Quantum Dots in a Two-Dimensional Photonic Crystal. *Phys. Rev. Lett.* **95,** 013904 (2005).

204. Atwater, H. A. & Polman, A. Plasmonics for improved photovoltaic devices. *Nat. Mater.* **9,** 205–213 (2010).

205. Peters, C. H., Guichard, A. R., Hryciw, A. C., Brongersma, M. L. & McGehee, M. D. Energy transfer in nanowire solar cells with photon-harvesting shells. *J. Appl. Phys.* **105,** 124509 (2009).

206. Nguyen, H. M., Seitz, O., Peng, W., Gartstein, Y. N., Chabal, Y. J. & Malko, A. V. Efficient Radiative and Nonradiative Energy Transfer from Proximal CdSe/ZnS Nanocrystals into Silicon Nanomembranes. *ACS Nano* **6,** 5574–5582 (2012).

207. Zimnitsky, D., Jiang, C., Xu, J., Lin, Z. & Tsukruk, V. V. Substrate- and Time-Dependent Photoluminescence of Quantum Dots Inside the Ultrathin Polymer LbL Film. *Langmuir* **23,** 4509–4515 (2007).

208. Zimnitsky, D., Jiang, C., Xu, J., Lin, Z., Zhang, L. & Tsukruk, V. V. Photoluminescence of a Freely Suspended Monolayer of Quantum Dots Encapsulated into Layer-by-Layer Films. *Langmuir* **23,** 10176–10183 (2007).

209. Halaoui, L. I. Layer-by-Layer Assembly of Polyacrylate-Capped CdS Nanoparticles in Poly(diallyldimethylammonium chloride) on Solid Surfaces. *Langmuir* **17,** 7130–7136 (2001).

210. Konstantatos, G. & Sargent, E. H. PbS colloidal quantum dot photoconductive photodetectors: Transport, traps, and gain. *Appl. Phys. Lett.* **91,** 173505 (2007).

211. Gole, A., Jana, N. R., Selvan, S. T. & Ying, J. Y. Langmuir−Blodgett Thin Films of Quantum Dots: Synthesis, Surface Modification, and Fluorescence Resonance Energy Transfer (FRET) Studies. *Langmuir* **24,** 8181–8186 (2008).

212. Lin, Y.-W., Tseng, W.-L. & Chang, H.-T. Using a Layer-by-Layer Assembly Technique to Fabricate Multicolored-Light-Emitting Films of CdSe@CdS and CdTe Quantum Dots. *Adv. Mater.* **18,** 1381–1386 (2006).

213. Rauf, S., Glidle, A. & Cooper, J. M. Layer-by-Layer Quantum Dot Constructs Using Self-Assembly Methods. *Langmuir* **26,** 16934–16940 (2010).

214. Talapin, D. V., Rogach, A. L., Kornowski, A., Haase, M. & Weller, H. Highly Luminescent Monodisperse CdSe and CdSe/ZnS Nanocrystals Synthesized in a Hexadecylamine−Trioctylphosphine Oxide−Trioctylphospine Mixture. *Nano Lett.* **1,** 207–211 (2001).

215. Kalyuzhny, G. & Murray, R. W. Ligand Effects on Optical Properties of CdSe Nanocrystals. *J. Phys. Chem. B* **109,** 7012–7021 (2005).

216. Bullen, C. & Mulvaney, P. The Effects of Chemisorption on the Luminescence of CdSe Quantum Dots. *Langmuir* **22,** 3007–3013 (2006).

217. Wuister, S. F., de Mello Donegá, C. & Meijerink, A. Influence of Thiol Capping on the Exciton Luminescence and Decay Kinetics of CdTe and CdSe Quantum Dots. *J. Phys. Chem. B* **108,** 17393–17397 (2004).

218. Nazzal, A. Y., Wang, X., Qu, L., Yu, W., Wang, Y., Peng, X. & Xiao, M. Environmental Effects on Photoluminescence of Highly Luminescent CdSe and CdSe/ZnS Core/Shell Nanocrystals in Polymer Thin Films. *J. Phys. Chem. B* **108,** 5507–5515 (2004).

219. Aldana, J., Wang, Y. A. & Peng, X. Photochemical Instability of CdSe Nanocrystals Coated by Hydrophilic Thiols. *J. Am. Chem. Soc.* **123,** 8844–8850 (2001).

220. Liu, I.-S., Lo, H.-H., Chien, C.-T., Lin, Y.-Y., Chen, C.-W., Chen, Y.-F., Su, W.-F. & Liou, S.-C. Enhancing photoluminescence quenching and photoelectric properties of CdSe quantum dots with hole accepting ligands. *J. Mater. Chem.* **18,** 675–682 (2008).

221. Lunt, R. R., Osedach, T. P., Brown, P. R., Rowehl, J. A. & Bulović, V. Practical Roadmap and Limits to Nanostructured Photovoltaics. *Adv. Mater.* **23,** 5712–5727 (2011).

222. Belton, C. R., Itskos, G., Heliotis, G., Stavrinou, P. N., Lagoudakis, P. G., Lupton, J., Pereira, S., Gu, E., Griffin, C., Guilhabert, B., Watson, I. M., Mackintosh, A. R., Pethrick, R. A., Feldmann, J., Murray, R., Dawson, M. D. & Bradley, D. D. C. New light from hybrid inorganic–organic emitters. *J. Phys. Appl. Phys.* **41,** 094006 (2008).

223. Ke, B. *Photosynthesis Photobiochemistry and Photobiophysics*. (Springer Science & Business Media, 2001).

224. Chanyawadee, S., Harley, R. T., Henini, M., Talapin, D. V. & Lagoudakis, P. G. Photocurrent Enhancement in Hybrid Nanocrystal Quantum-Dot p-i-n Photovoltaic Devices. *Phys. Rev. Lett.* **102,** 077402 (2009).

225. Talapin, D. V., Lee, J.-S., Kovalenko, M. V. & Shevchenko, E. V. Prospects of Colloidal Nanocrystals for Electronic and Optoelectronic Applications. *Chem. Rev.* **110,** 389–458 (2010).

226. Kagan, C. R., Murray, C. B. & Bawendi, M. G. Long-range resonance transfer of electronic excitations in close-packed CdSe quantum-dot solids. *Phys. Rev. B* **54,** 8633–8643 (1996).

227. Dang, C., Lee, J., Breen, C., Steckel, J. S., Coe-Sullivan, S. & Nurmikko, A. Red, green and blue lasing enabled by single-exciton gain in colloidal quantum dot films. *Nat. Nanotechnol.* **7,** 335–339 (2012).

228. Franzl, T., Klar, T. A., Schietinger, S., Rogach, A. L. & Feldmann, J. Exciton Recycling in Graded Gap Nanocrystal Structures. *Nano Lett.* **4,** 1599–1603 (2004).

229. Klar, T. A., Franzl, T., Rogach, A. L. & Feldmann, J. Super-Efficient Exciton Funneling in Layer-by-Layer Semiconductor Nanocrystal Structures. *Adv. Mater.* **17,** 769–773 (2005).

230. Agranovich, V. M. & Galanin, M. D. *Electronic excitation energy transfer in condensed matter*. (Elsevier , Amsterdam, 1982).

231. Prigogine, I. & Rice, S. A. *Advances in Chemical Physics*. (John Wiley & Sons, 2009).

232. Novotny, L. & Hecht, B. *Principles of Nano-Optics*. (Cambridge University Press, 2012).

233. Roodenko, K., Nguyen, H. M., Caillard, L., Radja, A., Thissen, P., Gordon, J. M., Gartstein, Y. N., Malko, A. V. & Chabal, Y. J. Anisotropic Optical Properties of Thin-Film Thiacarbocyanine Dye Aggregates. *J. Phys. Chem. C* **117,** 20186–20192 (2013).

234. Gordon, J. M. & Gartstein, Y. N. Dielectric polarization, anisotropy and nonradiative energy transfer into nanometre-scale thin semiconducting films. *J. Phys. Condens. Matter* **25,** 425302 (2013).

VITA

Louis M. Caillard finished high school in 2004 and directly entered a Math and Physic preparatory classes program for engineering school in Lycee Charlemagne, Paris, France. In 2007 he joined ENSERG School from Grenoble Institute of Technology, today known as Phelma from which he received his bachelor of engineering in 2008. He then joined the international master of Micro and Nanotechnology for integrated systems which is a joined program between Grenoble Institute of Technology in France, Politecnico Di Torino in Italy and École Polytechnique Fédérale de Lausanne in Switzerland. He graduated in 2010 after completing internships in Korea University in Seoul and in the Massachusetts Institute of Technology in the US. In January 2011 he entered the PhD program under the supervision of Yves Chabal from University of Texas at Dallas and Olivier Pluchery from Institut des NanoSciences de Paris. This co-tutelle program is the first of its kind between the two universities and aims at creating a strong scientific collaboration.

COMMUNICATIONS

Publications:

- *Seitz, O., Caillard, L., Nguyen, H. M., Chiles, C., Chabal, Y. J. & Malko, A. V. Optimizing non-radiative energy transfer in hybrid colloidal-nanocrystal/silicon structures by controlled nanopillar architectures for future photovoltaic cells. Appl. Phys. Lett.* ***100,*** *021902 (2012).*

- *Caillard, L., Seitz, O., Campbell, P. M., Doherty, R. P., Lamic-Humblot, A.-F., Lacaze, E., Chabal, Y. J. & Pluchery, O. Gold Nanoparticles on Oxide-Free Silicon–Molecule Interface for Single Electron Transport. Langmuir* ***29,*** *5066–5073 (2013).*

- *Nimmo, M. T., Caillard, L., De Benedetti, W., Nguyen, H. M., Seitz, O., Gartstein, Y. N., Chabal, Y. J. & Malko, A. V. Visible to Near-Infrared Sensitization of Silicon Substrates via Energy Transfer from Proximal Nanocrystals: Further Insights for Hybrid Photovoltaics. ACS Nano* ***7,*** *3236–3245 (2013).*

- *Roodenko, K., Nguyen, H. M., Caillard, L., Radja, A., Thissen, P., Gordon, J. M., Gartstein, Y. N., Malko, A. V. & Chabal, Y. J. Anisotropic Optical Properties of Thin-Film Thiacarbocyanine Dye Aggregates. J. Phys. Chem. C* ***117,*** *20186–20192 (2013).*

- *De Benedetti, W. J. I., Nimmo, M. T., Rupich, S. M., Caillard, L., Gartstein, Y. N., Chabal, Y. J. & Malko, A. V. Efficient Directed Energy Transfer through Size-Gradient Nanocrystal Layers into Silicon Substrates. Adv. Funct. Mater.* ***24,*** *5002-5010 (2014).*

- *Zhang, Y., Pluchery, O., Caillard, L., Lamic-Humblot, A.-F., Casale, S., Chabal Y.J. & Salmeron, M. Charging effect on the Work Function of Single Gold Nanoparticles. Nanoletters (2014,* ***under revision****)*

- *Caillard, L., Sattayaporn, S., Lamic-Humblot, A.-F., Casale, S., Campbell, P. M., Chabal, Y. J. & Pluchery, O. Controlling the reproducibility of Coulomb blockade phenomena for gold nanoparticles on an organic monolayer/silicon system. Nanotechnology (2014,* ***just submitted****),*

Conferences

- *International Conference on Nanoscience + Technology 2012: Paris, France. From Jul 23 to jul 27 2012. Evidence for single electron tunnel junction using gold nanoparticles.* ***Oral.***

- *AVS 59th International Symposium & Exhibition: Tampa, Florida, USA. From oct 28 to Nov 2 2012. Evidence for Single Electron Tunnel Junction using Gold Nanoparticles on Oxide-Free Si(111).* ***Oral.***

- *Réunion Plénière du Gdr Or-nano. Nantes, France. From april 3 to april 5 2013. Evidence for single electron tunnel junction using gold nanoparticles.* ***Poster.***

- *AVS Texas Chapter Conference 2013: Richardson, Texas, Dallas. From aug 7 to aug 8 2013. Evidence for Single Electron Tunnel Junction using Gold Nanoparticles on Oxide-Free Si(111).* ***Oral.***

- *2nd international Summer school for young scientist. Nanotechnology: from fundamental research to innovations. Bukovel, Ukraine. From aug 25 to sept 1st 2013. Evidence for Single Electron Tunnel Junction using Gold Nanoparticles on Oxide-Free Si(111). 1st price award.* ***Oral.***

- *IVC-19ICSS-15 and ICN+T 2013. Paris, France. From sept 9 to sept 19 2013. Evidence for single electron tunnel junction using gold nanoparticles.* ***Oral.***

THESIS SUMMARY

ENGLISH:

Progresses made in the field of functionalization on oxide-free silicon and SiO_2 allow for promising outcomes in a wide variety of topics. Grafted organic monolayer (GOM) on oxide-free Si have been fabricated using thermal and UV hydrosilylation and characterized using FTIR and XPS. The obtained amine terminated GOM has been used for nanoparticle deposition. Colloidal gold nanoparticles (AuNP) have been deposited and single electron transport measurements have been performed using STM under UHV: A double barrier tunneling junction was formed with the GOM as the first barrier and the vacuum between the scanning tip and the AuNP as the second one. This structure is known to exhibit single electron transport through Coulomb staircase phenomenon. Evidence for its occurrence was obtained at 30K and a study was done in order to determine critical parameters for results' reproducibility. Optimal recipe were obtained and experimental and simulated data were compared. The latter were acquired using a recently developed theoretical model based on the orthodox theory that has been modified to model our system more accurately. Our goal is to develop an alternative technology to build single electron transistors that are compatible with current Si-based technology. Nanoquantum dots (NQDs) were also deposited on the GOM for NQD solar cells applications. Energy transfers through radiative and non-radiative mechanism between NQDs and substrate were observed on plane

surface in recent work using photoluminescence (PL) spectroscopy. We show evidence of optimization of the PL count using GOM on silicon nanopillars and with successive grafting of NQDs to form multilayers. We also show evidence of directed energy transfer from NQDs to the silicon substrate using bilayers of NQDs with a size gradient. All these achievements can be combined for the fabrication of NQDs solar cells prototypes with an enhanced efficiency that could compete with existing technologies.

FRANCAIS:

Les progrès obtenus dans le domaine de la fonctionnalisation du silicium non oxydé offrent de belles perspectives dans de nombreux sujets. Des couches moléculaires greffées (GOM) sur du Si non oxydé ont été fabriquées avec de l'hydrosilylation thermique et UV pour ensuite être caractérisées par XPS et FTIR. Sa terminaison amine permet le greffage de nanoparticles d'or colloïdes (AuNP). Celles-ci ont été déposées et des mesures ont été prises avec un STM sous UHV: une double jonction tunnel est formée avec comme première jonction la GOM, et comme seconde, le vide entre la pointe et l'AuNP. Ce type de structure est connu pour permettre l'observation de transport à un électron grâce au phénomène de blocage de Coulomb. Des preuves de son observation ont été obtenues à 30K et nous proposons une étude pour identifier les paramètres nécessaires à leur reproductibilité. Nous proposons un protocole optimal et nos résultats expérimentaux sont comparés à des résultats obtenus grâce à un simulateur récemment développé, fondé sur la théorie orthodoxe, que nous avons modifié pour correspondre à notre système. Notre but est de développer une technologie alternative pour la fabrication de

transistors à un électron compatible avec la technologie Si actuelle. Pour des applications photovoltaïques, des boîtes quantiques (NQDs) sont aussi déposées sur la GOM. Des transferts radiatifs et non radiatifs d'énergie ont récemment été observés entre NQDs et substrat sur surfaces planes à l'aide de mesure en photoluminescence (PL). Nous améliorons la PL en greffant la GOM sur des nano-piliers de silicium et en déposant des couches successives de NQDs pour former des multicouches. Nous proposons aussi des preuves expérimentales du transfert d'énergie dirigé entre NQDs jusqu'au substrat avec des bicouches de NQDs avec gradient de taille. Combiner tout ces résultats peut donner lieu à la fabrication de prototypes de cellules solaires efficaces pouvant rivaliser avec les technologies actuelles.